# Targeted delivery of anti-cancer drugs by MS2 virus-like particles

Ruiyang Yan

Submitted in accordance with the requirements for the degree of
Doctor of Philosophy

The University of Leeds
Faculty of Biological Sciences

March 2015

The candidate confirms that the work submitted is his/her own, except where work which has formed part of jointly authored publications has been included. The contribution of the candidate and the other authors to this work has been explicitly indicated below. The candidate confirms that appropriate credit has been given within the thesis where reference has been made to the work of others.

Yan, R., Hallam, A., Stockley, P. G. & Boyes, J. 2014. Oncogene dependency and the potential of targeted RNAi-based anti-cancer therapy. Biochemical Journal, 461, 1-13.

The review was written by R.Y. and A.H., and edited and proof-read by P.G.S and J.B. Some contents of this review were used in parts of Chapter 1 of this thesis.

## Acknowledgements

It has been an interesting three and a half years, in which I have grown a lot as a person. I was fortunate enough to have met some amazing people during this time, without whom, my PhD and this thesis would have been infinitely more difficult and less pleasant - if at all possible. I would like to thank:

My supervisor, Prof. Peter Stockley, for his patience, excellent guidance and encouragement throughout my project.

My co-supervisor, Dr. Joan Boyes, for her helpful advice on cell culture, and for her motivational speeches.

My academic assessor/adviser, Dr. Roman Tuma, for his advice in my transfer(s) and for his wonderful BBQs.

My coworkers, past and present: Amanda, Alex, Amit, Amy, Chris, Dave, Emma, Gaël, Meral, Nic, Nikesh, Rob, Simon. I could not have hoped for better people to share a lab/office with - there was truly never a dull moment. I will miss cake club and our fun, often inappropriate banter. Specifically, thank you, Amy for all your help with oligo synthesis; Amanda, our social sec for organising the bowling; Alex, Dave and Rob for helping me through the early days of my PhD; Nikesh and Simon for all your help in general, including but definitely not limited to deciphering Peter's handwriting. A shout out to Rob and Meral, co-members of my successful but short-lived band, 'We Really Are Scientists'. I will always wonder what could have been, if we were not really scientists or if we had any talent.

Prof. Norman Maitland, for his generous provision of prostate cancer cell lines and associated expertise.

Various people in the FBS for their help on different equipment: Dr. Gareth Howell and Dr. Sally Boxall (flow cytometry and deconvolution microscopy), Dr. Peiyi Wang and Martin Fuller (electron microscopy), Dr. Iain Manfield (oligo synthesis and purification).

爸妈，你们给我的一切。

## Abstract

Problems associated with poor pharmacokinetics and biodistribution, as well as toxic off-target effects, limit the curative potential of most anti-cancer drugs. This has prompted the development of nanoparticulate drug delivery systems to impart both more favourable pharmacological properties and precise tumour targeting. The vast number of formulations, ranging from fully synthetic delivery systems to ones derived from natural sources, currently undergoing clinical trials or preclinical testing underlines the significance of this field. This project is a proof-of-concept investigation into the feasibility and effectiveness of a novel drug delivery system, based on virus-like particles (VLPs) of the MS2 bacteriophage.

Doxorubicin (Dox) and an anti-BCL2 siRNA were used as model drug cargos. They were packaged inside MS2 VLPs either by chemical infusion, or via covalent attachment to an MS2 packaging signal, TR, respectively. An average loading of ~10 molecules of siRNA or ~110 molecules of Dox per VLP was achieved. Packaged cargos remained stably encapsidated; the siRNA was protected from nuclease degradation. VLPs were surface decorated with polyethylene glycol (PEG), and tumour-targeting ligands, human transferrin (Tf) or A9L, an RNA aptamer that targets prostate-specific membrane antigen (PSMA). Extensive PEGylation was achieved (~97% of coat proteins), and each VLP displayed on average ~7 molecules of Tf or ~16 molecules of A9L.

PEGylation significantly reduced the non-specific cellular uptake of VLPs, and antibody binding. Further addition of tumour-targeting ligands facilitated the specific delivery of drug cargos to targeted cancer cells in culture, likely via

receptor-mediated endocytosis, and induced significant cytotoxicity with an $LC_{50}$ of ~10 nM for siRNA and ~800 nM for Dox. Importantly, negligible toxic effects were observed in the presence of excess free targeting ligands, or with non-targeted control cell lines. Furthermore, the cellular uptake of VLPs did not appear to induce any off-target effects.

MS2 VLPs continue to show promise as a robust, flexible and effective drug delivery system. This project highlights the versatility of VLPs for displaying a range of useful ligands on their surface, as well as packaging various therapeutic cargos, and demonstrated their ability to specifically deliver drugs to targeted cancer cells. Though further studies are required, the work presented here is an important step towards fully realising the potential of this drug delivery system.

# Contents

# List of figures

## Chapter 1



## Chapter 3

## Chapter 4

## Chapter 5

# List of tables

## Chapter 1



## Chapter 2



## Chapter 3



## Chapter 4



## Chapter 5

# List of abbreviations

| | |
|---|---|
| Ab | Antibody |
| ABL | Abelson murine leukemia viral oncogene homolog 1 |
| AD | Adamantane |
| AIDS | Acquired immune deficiency syndrome |
| ALL | Acute lymphoblastic leukemia |
| AMD | Age-related macular degeneration |
| ATCC | American tissue culture collection |
| AU | Arbitrary unit or procedure defined unit |
| Bcl2 | B cell lymphoma 2 |
| BCR | Breakpoint cluster region |
| bp | Base pair(s) |
| CDP | Cyclodextrin-containing polymer |
| CLL | Chronic lymphocytic leukemia |
| CML | Chronic myelogenous leukemia |
| CP | Coat protein |
| CPMV | Cowpea mosaic virus |
| CyX | Cyanine X |
| DAPI | 4, 6-diamino-2-phenylindole |
| DEPC | Diethylpyrocarbonate |
| DMEM | Dulbecco's Modified Eagles Medium |
| DMSO | Dimethyl sulfoxide |
| DNA | Deoxyribonucleic acid |
| DNase | Deoxyribonuclease |
| Dox | Doxorubicin |
| DPBS | Dulbecco's phosphate buffered saline |
| DPBST | Dulbecco's phosphate buffered saline with Tween |
| ds | Double strand(ed) |
| EB | Ethidium bromide |
| ECE-1 | Endothelin converting enzyme 1 |
| EDTA | Ethylenediaminetetraacetic acid |
| EGFR | Epidermal growth factor receptor |
| EPR | Enhanced permeability and retention |
| FAM | Fluorescein amidite |
| FBS | Foetal bovine serum |
| FDA | Food and Drug Administration |
| FITC | Fluorescein isothiocyanate |
| Freq. | Frequency |
| FSC | Forward scatter |
| GAPDH | Glyceraldehyde-3-phosphate dehydrogenase |
| GCSF | Granulocyte-colony stimulating factor |
| HCC | Hepatocellular carcinoma |
| HEPES | 4-(2-hydroxyethyl)-1-piperazineethanesulfonic acid |
| HIV | Human immunodeficiency virus |

| | |
|---|---|
| HPLC | High performance liquid chromatography |
| Ig | Immunoglobulin |
| IKBKE | I-kappa-B kinase epsilon |
| $K_d$ | Dissociation constant |
| KS | Kaposi's sarcoma |
| KSP | Kinesin spindle protein |
| $LC_{50}$ | Median lethal concentration |
| $LD_{50}$ | Median lethal dose |
| MFI | Mean fluorescent intensity |
| miRNA | MicroRNA |
| MM | Multiple myeloma |
| mRNA | Messenger RNA |
| MS2 | Bacteriophage MS2 |
| MWCO | Molecular weight cut-off |
| NAP | Nucleic acid purification |
| NHS | N-hydroxysuccinimide |
| NSCLC | Non-small-cell lung carcinoma |
| nt | Nucleotide |
| ODN | Oligodeoxynucleotide |
| PAGE | Polyacrylamide gel electrophoresis |
| P-bodies | Processing bodies |
| PCR | Polymerase chain reaction |
| PDR | Proliferative diabetic retinopathy |
| PEG | Polyethylene glycol |
| PEI | Polyethyleneimine |
| Pen Strep | Penicillin Streptomycin |
| PI | Propidium iodide |
| Plk1 | Polo-like kinase 1 |
| PSMA | Prostate-specific membrane antigen |
| RAC | Ricin A chain |
| RCF | Relative centrifugal force |
| RISC | RNA-induced silencing complex |
| RME | Receptor-mediated endocytosis |
| RNA | Ribonucleic acid |
| RNAi | RNA interference |
| RNAP | RNA polymerase |
| RNase | Ribonuclease |
| RONDEL | RNAi/Oligonucleotide Nanoparticle Delivery |
| RRM2 | Ribonucleotide reductase M2 subunit |
| RSV | Rous Sarcoma Virus |
| RT-PCR | Real-time polymerase chain reaction |
| SATA | N-succinimidyl S-acetythioacetate |
| SD | Standard deviation |
| SDC | Sucrose density centrifugation |
| SDS | Sodium dodecyl sulfate |
| SELEX | Systematic evolution of ligands by exponential enrichment |

| | |
|---|---|
| shRNA | Short hairpin RNA |
| siRNA | Small interfering RNA |
| SNALP | Stable nucleic acid lipid particles |
| ss | Single strand(ed) |
| SSC | Side scatter |
| Sulfo-SMCC | Sulfosuccinimidyl 4-(N-maleimidomethyl) cyclohexane-1-carboxylate |
| sxRNA | siRNA or shRNA |
| TBE | Tris, borate, EDTA buffer |
| TBS | Tris-buffered saline |
| TBST | Tris-buffered saline with Tween |
| TEM | Transmission electron microscopy |
| Tf | Transferrin |
| TfR | Transferrin receptor |
| TR | Translational repressor of MS2 RNA genome (19 nt stem loop) |
| TR-Bcl2 | Bcl2 siRNA (ds) extended with TR on one strand |
| TR-siRNA | A siRNA (ds) with a TR sequence extension on one strand |
| TR-X | Any molecule covalently linked to TR |
| UTR | Untranslated region |
| VEGF | Vascular endothelial growth factor |
| VLP | Virus-like particles |

**Units**

| | |
|---|---|
| p (prefix) | pico |
| n (prefix) | nano |
| µ (prefix) | micro |
| m (prefix) | milli |
| c (prefix) | centi |
| k (prefix) | kilo |
| Å | Angstrom |
| $^{o}$C | Degrees centigrade |
| Da | Dalton |
| g | Gram(s) |
| L | Litre(s) |
| v/v | Volume (mL) per volume (mL) |
| w/v | Weight (g) per volume (mL) |
| mol | Mole(s) |
| M | Molar |
| s | Second(s) |
| min | Minute(s) |
| h | Hour(s) |
| m | Metre(s) |

**Bases**

| | |
|---|---|
| A | Adenine |
| G | Guanine |
| C | Cytosine |
| T | Thymine |
| U | Uracil |

**Amino acids**

| | | |
|---|---|---|
| R | Arg | Arginine |
| H | His | Histidine |
| K | Lys | Lysine |
| D | Asp | Aspartic acid |
| E | Glu | Glutamic acid |
| S | Ser | Serine |
| T | Thr | Threonine |
| N | Asn | Asparagine |
| Q | Gln | Glutamine |
| C | Cys | Cysteine |
| G | Gly | Glycine |
| P | Pro | Proline |
| A | Ala | Alanine |
| V | Val | Valine |
| I | Ile | Isoleucine |
| L | Leu | Leucine |
| M | Met | Methionine |
| F | Phe | Phenylalanine |
| Y | Tyr | Tyrosine |
| W | Trp | Tryptophan |

**This page is intentionally blank**

# Chapter 1

Introduction

## 1.1 A history of chemotherapy

'*Although modern chemotherapy has now assumed its role in science and practical experience, it has its origin in histological staining techniques. Hence, it did not happen by chance that the first promising chemotherapeutical experiments used dyes like methylene blue and trypan red. Thus, early chemotherapy can be looked upon as dye therapy* (Ehrlich, 1911).' This quote from Paul Ehrlich's seminal paper, 'Aus Theorie und Praxis der Chemotherapie', outlines the origins of his work in the search for 'magic bullets' to target disease-causing organisms, which would establish the foundations of modern chemotherapy.

The 'magic bullet' theory was conceived following Ehrlich's observation that chemical dyes had differential affinities for specific biological structures (Ehrlich, 1878, Ehrlich, 1911) – it postulated that such targeting mechanisms could be exploited to deliver toxins to microbes. Led by this speculation, Ehrlich's team systematically screened hundreds of novel dyes derivatized with arsenical groups, and, in 1909, successfully identified a compound that had anti-syphilitic effects in mice and rabbits, which became known as Salvarsan (Ehrlich, 1910). The discovery of Salvarsan was significant not only because it validated Ehrlich's hypothesis and was the first synthetic chemotherapeutic, but because it was the first instance of lead compound optimisation, based on principles of drug discovery that remain largely unchanged to this day.

Ehrlich's success inspired numerous groundbreaking studies that led to the discovery of novel treatments for other human diseases. In 1929, the physician Alexander Fleming published his serendipitous discovery that a fungus,

*Penicillium notatum*, grown in certain conditions, would secrete a substance exhibiting antibacterial properties. This substance, named penicillin, was readily diffusable in agar, and able to inhibit the growth of several disease-causing bacteria, such as diphtheria, gonococcus, pneumococcus and staphylococcus (Fleming, 1929). Fleming noted that penicillin was the first substance he had tested which was ‘more antibacterial than it was antileukocytic’, showing signs of a potentially powerful and selective ‘magic bullet’ therapeutic (Fleming, 1945).

Meanwhile, Ehrlich’s early success with dyes such as trypan red in treating trypanosome infections (Ehrlich and Shiga, 1904) prompted further developments of novel dye-based chemotherapeutics. In 1932, after five years of testing on thousands of azo dye derivatives, Gerhard Domagk discovered the sulphonamide drug, prontosil rubrum, which effectively treated haemolytic streptococci and staphylococci infections (Domagk, 1935). Prontosil rubrum became the first commercially available antibacterial drug, and its discoverer was awarded the 1939 Nobel Prize in Physiology or Medicine. Subsequently, thousands of sulphonamide-related compounds were produced, giving rise to improved formulations for treating a broad range of bacterial diseases.

### 1.1.1 Cancer chemotherapy: first strides

The success and rapid emergence of antibiotic drugs from the early 1900’s is reflected by the general decline in infectious disease-caused mortalities (Figure 1.1). With this observation, Domagk stated in his Nobel lecture that the ultimate purpose of chemotherapy was to treat cancers (Domagk, 1947).

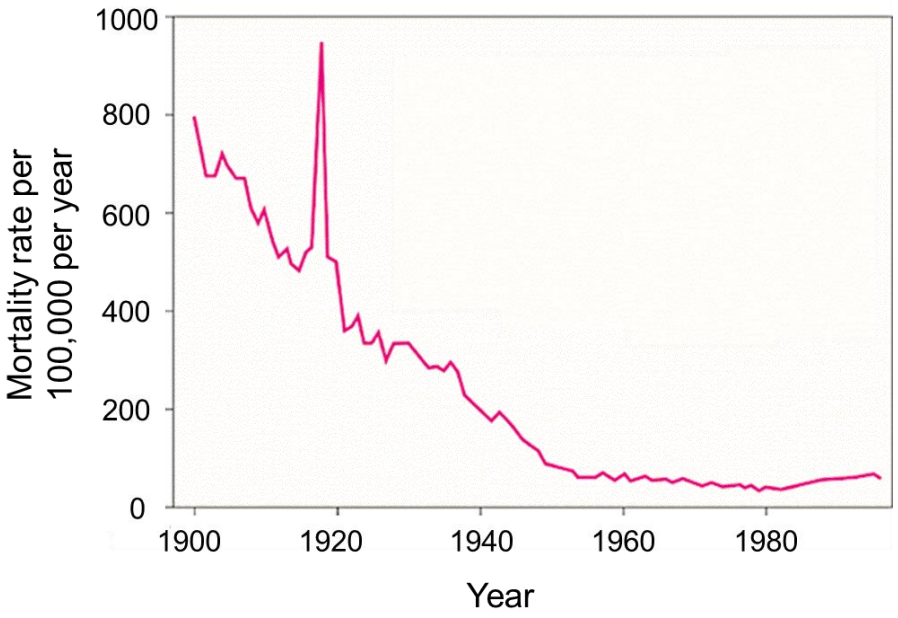


**Figure 1.1. Crude mortality rates caused by infectious diseases in the USA from 1900 to 1996.** The anomalous peak from 1918 to 1920 refers to deaths caused by the Spanish flu. Adapted from Armstrong et al. (1999).

Development of the first cancer chemotherapeutics dates back to 1942, when pharmacologists Louis Goodman and Alfred Gilman investigated the therapeutic potential of toxins developed for chemical warfare in World War II. Following the observation that soldiers exposed to one agent, nitrogen mustard, displayed marked myeloid and lymphoid suppression, Goodman and Gilman hypothesised its therapeutic use against lymphoid tumours (Gilman and Philips, 1946). This was validated in experiments in mouse models, where injected nitrogen mustard resulted in significant regression of transplanted lymphoid tumours, prompting further investigation in humans. The same anti-tumour effects were observed when nitrogen mustard was injected into a non-Hodgkin's lymphoma patient and, although the remission was short-lived, this set the precedent for systemic administration of drugs to treat cancer (Gilman, 1963). In

1949, nitrogen mustard became the first FDA-approved cancer chemotherapeutic.

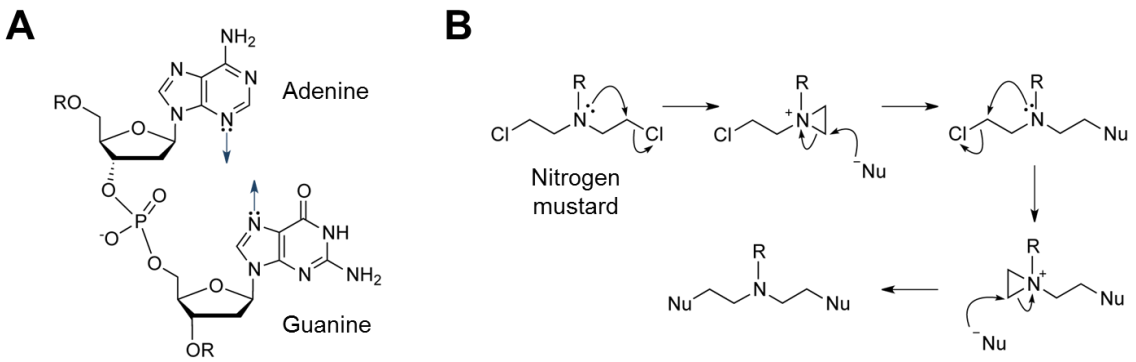


**Figure 1.2. Mechanism of action of nitrogen mustard. (A)** Structures of the purines, adenine and guanine, highlighting their nucleophilic nitrogen atoms (N3 and N7, respectively), which are exposed in the grooves of the DNA double helix. **(B)** Nitrogen mustard forms cyclic aziridinium rings via displacement of a chloride ion by the amine nitrogen. These rings are readily attacked by guanine and adenine on DNA, producing inter- or intra-stand crosslinks.

Studies on its mechanism of action revealed that nitrogen mustard forms covalent bonds with DNA via their alkyl groups, resulting in intra- or inter-strand crosslinks (Figure 1.2), inhibition of transcription and ultimately apoptosis of cancer cells (Goldacre et al., 1949, Masta et al., 1995, Kohn et al., 1987). This led to the subsequent identification of numerous other alkylating and alkylating-like agents for treating cancer, such as chlorambucil, mitomycin C (Crooke and Bradner, 1976), and cisplatin (Siddik, 2003).

### 1.1.2 Anti-metabolites in cancer therapy

Shortly after World War II, another class of cancer chemotherapeutics emerged following Sidney Farber's observation that folic acid – a vitamin previously identified as a deficient factor in megaloblastic anaemia patients (Wills et al., 1937) – stimulated the proliferation of cancer cells in children suffering from acute lymphoblastic leukaemia (ALL). This prompted Farber to synthesise structural analogues of folic acid, first aminopterin and methotrexate (Figure 1.3), to inhibit its pro-tumour action. Intra-muscular injection of aminopterin successfully induced remissions of ALL in patients (Farber et al., 1948). Although these remissions were temporary, they confirmed the tumour suppressive capacity of anti-folates, and paved the way for the development of novel anti-metabolite chemotherapeutics.

It was not until a decade after Farber's original investigation into anti-folates that their mechanism of action was elucidated. In 1958, Osborn and Huennekens identified that aminopterin and methotrexate specifically inhibited the action of dihydrofolate reductase (Osborn and Huennekens, 1958, Osborn et al., 1958), preventing the reduction of dihydrofolic acid to tetrahydrofolic acid. This in turn inhibits the synthesis of thymidine monophosphate and DNA synthesis, ultimately resulting in apoptosis (Jolivet et al., 1983). Since then, methotrexate has demonstrated anti-tumour effects in a wide range of cancers, notably it provided a curative treatment for patients suffering from choriocarcinoma, a malignant trophoblastic cancer typically of the placenta, which became the first solid tumour to be cured by chemotherapy (Li et al., 1958). Methotrexate is currently used in the treatment of various cancers, as well as autoimmune diseases such as psoriasis and rheumatoid arthritis.

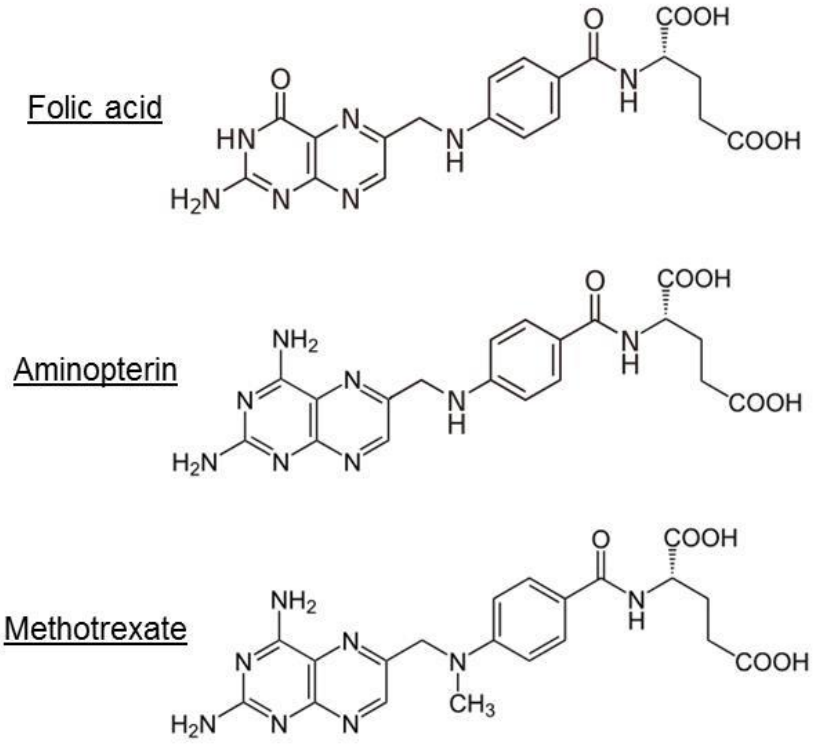


**Figure 1.3. Structures of folic acid and folic acid analogues, aminopterin and methotrexate.** Aminopterin differs from folic acid in the substitution of an amino group for O4; methotrexate contains the same amino group, and also an N-methyl group on its *p*-aminobenzoate moiety.

In 1942, another subclass of anti-metabolite chemotherapeutics surfaced from the work of George Hitchings. Equipped with the knowledge that DNA is composed of purines and pyrimidines, synthesised through a system of anabolic pathways, Hitchings hypothesised that rapidly dividing cells, such as bacterial or cancer cells, depended on modified anabolic pathways that promote DNA synthesis, and that their growth might be inhibited by the use of antagonists of nucleic acid synthesis (Hitchings, 1989). In collaboration with Gertrude Elion, Hitchings screened for purine and pyrimidine analogues using a *Lactobacillus casei* system, which can grow in the presence of adenine,

guanine, xanthine or hypoxanthine provided thymine is present (Elion and Hitchings, 1955). One compound, 2,6-diaminopurine, was able to inhibit the growth of *L. casei*, which was reversible upon the addition of adenine; strains of *L. casei* which displayed resistance to 2,6-diaminopurine grew poorly with adenine as the source of purine. They concluded that 2,6-diaminopurine was anabolised by the same enzyme as adenine, and that its product inhibited purine interconversion (Elion et al., 1953).

Although 2,6-diaminopurine displayed anti-tumour effects in tumour models in mice and in cell culture (Biesele et al., 1951, Burchenal et al., 1949), it also produced off-target toxicities in the form of severe vomiting, nausea and myelosuppression in human patients (Burchenal et al., 1951). This prompted Hitchings and Elion to continue screening for purine analogues in *L. casei* (Balis et al., 1951) – one analogue, obtained by substitution of an oxygen at the 6-position with a sulfur in hypoxanthine, was observed to inhibit purine utilisation. This thiopurine, known as 6-mercaptopurine, demonstrated anti-tumour effects in a broad range of cancers in mouse models (Elion et al., 1951, Biesele et al., 1951) and, in subsequent clinical trials, was able to produce complete remission of acute leukaemia in children (Burchenal et al., 1953). Despite the relapse experienced by many of those patients after treatment, 6-mercaptopurine was sufficiently superior over the previous treatment of methotrexate and steroids, raising the median life expectancy from 4 months to 12 months, to warrant its FDA approval in 1953. It took many more years of research before the mechanism of action of 6-mercaptopurine was elucidated (Figure 1.4).

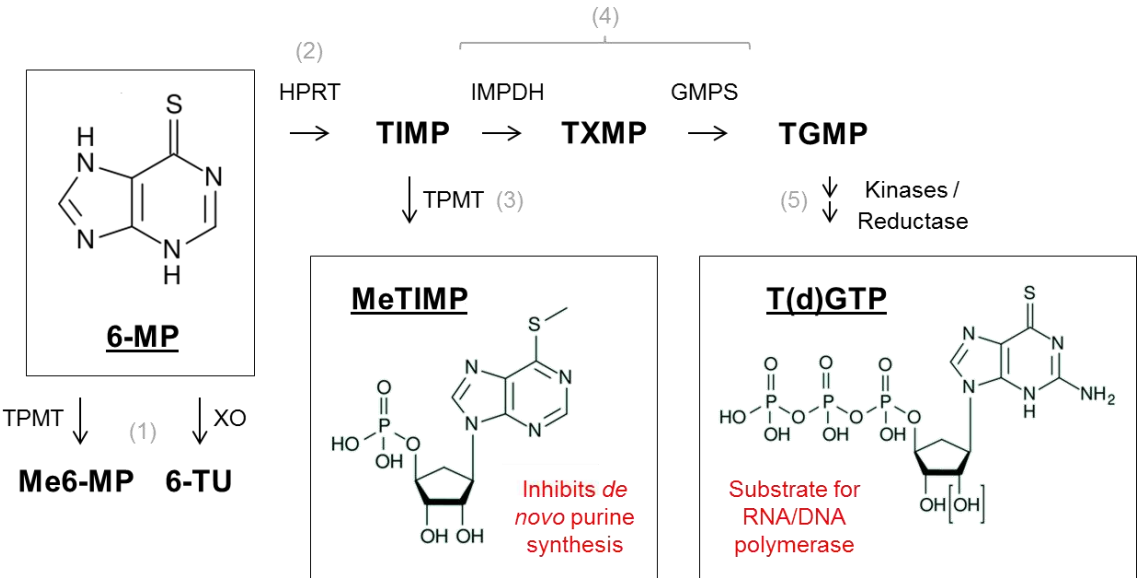


**Figure 1.4. Mechanism of action of 6-mercaptopurine. (1)** 6-mercaptopurine (6-MP) is converted by thiopurine S-methyltransferase (TPMT) or xanthine oxidase (XO) to inactive products, methyl 6-mercaptopurine (Me6-MP) or 6-thiouric acid (6-TU), respectively. **(2)** In a competing reaction, hyphoxanthine-guanine phosphoribosyltransferase (HPRT) converts 6-MP to thioinosine monophosphate (TIMP), **(3)** which can be methylated by TPMT to form methyl TIMP (MeTIMP). MeTIMP inhibits glutamine-5-phosphoribosylpyrophosphate amidotransferase, the rate-limiting enzyme for de novo purine synthesis. **(4)** TIMP can also be converted to thioguanosine monophosphate (TGMP) via thioxanthosine monophosphate (TXMP). **(5)** The sequential action of kinases and reductase converts TGMP to thioguanosine triphosphate (TGTP) and thiodeoxyguanosine triphosphate (TdGTP), which are incorporated into RNA and DNA, respectively. TdGTP in DNA can trigger apoptosis via the mismatch repair pathway. IMPDH = inosine-5′-monophosphate dehydrogenase; GMPS = guanine monophosphate synthetase.

### 1.1.3 Anti-microtubule agents in cancer therapy

One exciting development in chemotherapy came in the late 1950s, with the discovery of the anti-tumour potential of Vinca alkaloids (Johnson et al., 1959,

Noble et al., 1958). These compounds can be extracted from leaves of the periwinkle plant *Catharanthus roseus*, which were originally tested by Robert Noble and Charles Beer for their purported anti-diabetic properties in rabbits and diabetic rats (Noble et al., 1958). The studies revealed that orally administered aqueous extracts of *C. roseus* leaves produced little effects on blood sugar levels and on the disease but, interestingly, reduced the white blood cell count in the test animals, rendering them prone to bacterial infections. This led to the hypothesis that these extracts contained agents that might be of therapeutic use against cancers of the haematopoietic system, such as leukemia and lymphoma. Through fractionation, Beer isolated the compounds vinblastine and vincristine, which dramatically decreased the white blood cell count in rats. In subsequent experiments, vinblastine demonstrated significant anti-tumour effects in rodent models of mammary tumours and leukemias (Cutts et al., 1960), as well as in human patients suffering from Hodgkin's lymphoma, lymphosarcoma and breast cancer (Warwick et al., 1960). Numerous Vinca derivatives have since been developed, which are now FDA approved for treating a range of tumours, including acute leukemia, neuroblastoma, Wilm's tumour, Hodgkin's and other lymphomas.

The mechanism of action of Vinca alkaloids was later identified (Jordan et al., 1991). Vinblastine was shown to bind at the plus ends of microtubules with high affinity (Figure 1.5A): as little as one vinblastine per plus end could significantly suppress treadmilling and dynamic instability of the polymer (Jordan et al., 1986). This stabilisation maintains microtubules in mitotic spindles in an attenuated or paused state, thus blocking mitosis and ultimately triggering apoptosis.

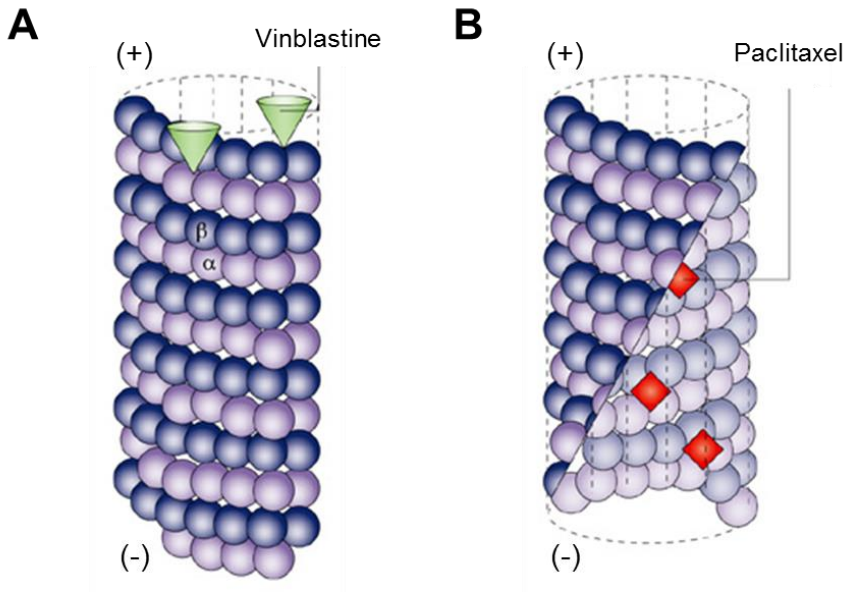


**Figure 1.5. Mechanism of action of anti-microtubule chemotherapeutics. (A)** Vinblastine suppresses microtubule dynamics via high affinity binding to the plus end of microtubules, inducing cell cycle arrest at M phase. **(B)** Paclitaxel suppresses microtubule dynamics by binding at the interior surface, stabilising the polymer from disassembly and ultimately inducing apoptosis. Adapted from Jordan and Wilson (2004).

Another major subtype of microtubule-targeting chemotherapeutics are the taxanes, most notably paclitaxel. Taxanes differ from Vinca alkaloids in their mechanism of action, which involves diffusing through small openings in the microtubule (Nogales, 2001), binding with high affinity to the β-subunit of tubulin along the interior surface (Nogales et al., 1995), stabilising the microtubule and promoting its polymerisation (Schiff et al., 1979) (Figure 1.5B). This effect is likely due to a binding-induced conformational change in tubulin that enhances their affinity for neighbouring subunits (Nogales, 2001). As for the Vinca alkaloids, a small number of paclitaxel molecules are sufficient to significantly reduce the dynamic instability of microtubules (Derry et al., 1995); suppression

of spindle microtubule dynamics blocks mitotic progression from metaphase to anaphase, ultimately leading to apoptosis (Jordan et al., 1996, Yvon et al., 1999). Paclitaxel was approved by the FDA in 1995 and is currently used to treat non-small-cell lung carcinoma (NSCLC), ovarian and breast cancer and Kaposi's sarcoma.

## 1.2 Oncogene-targeted cancer therapy

The discovery of oncogenes and tumour suppressor genes, and the subsequent elucidation of cellular signalling pathways, contributed greatly to our understanding of cancer biology on a molecular level (Hanahan and Weinberg, 2000). The identification of the first oncogene, v-src sarcoma (Schmidt-Ruppin A-2) viral oncogene homolog (*SRC*), took decades to achieve. In 1911, Peyton Rous' demonstrated that cell filtrates from chicken sarcomas could cause cancer in healthy chickens, suggesting the presence of cancer-inducing agents within the tumour, which were found to be the virus that became known as the Rous Sarcoma Virus (RSV) (Rous, 1911).

Six decades later, experiments by David Baltimore and Howard Temin revealed that RSV had an RNA genome that could convert back to DNA and integrate itself within the host's genome (Baltimore, 1970, Temin and Mizutani, 1970). This discovery identified that a genetic element of the viral genome was responsible for transforming cells, which was subsequently narrowed down to a single gene, the *SRC* oncogene (Wang et al., 1976). Homologues of *SRC* were then found in several species of bird and later across all vertebrates (Stehelin et al., 1976), suggesting that the viral oncogene had been acquired from host cells

during evolution, and that normal versions of these genes were present within the host genome which may cause cancer if mutated. These genes were termed ‘proto-oncogenes’ (Varmus, 1990). More than 50 of these have now been identified within the human genome (Vogelstein et al., 2013).

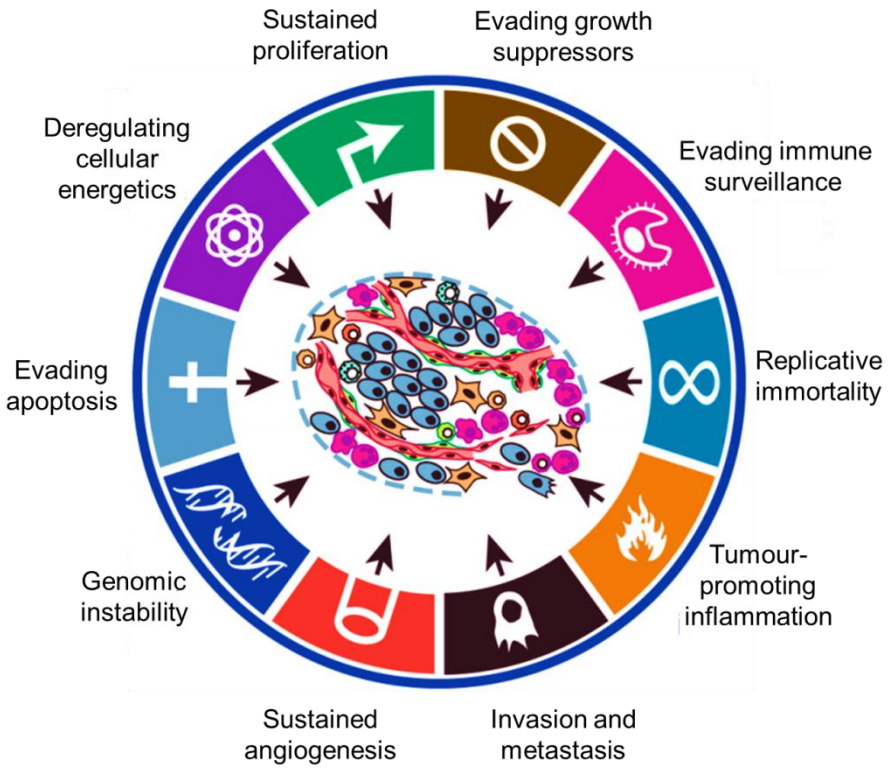


**Figure 1.6. Hallmarks of cancer**. A summary of characteristics exhibited by cancer cells which, collectively, lead to unchecked tumour growth. Adapted from Luo et al. (2009).

It has been reported that as many as 7-10 genetic or epigenetic alterations are necessary to bring about the cancer phenotypes required for tumorigenesis (Figure 1.6) (Renan, 1993, Hanahan and Weinberg, 2000, Brummelkamp et al., 2002). Originally, this notion of a complex network of interacting pathways in

cancers led to the idea that they may be too complicated for simple effective treatments (Li et al., 1997, Hahn and Weinberg, 2002). However, it has since been shown that targeting just one specific gene or its protein product can be sufficient to destroy a cancer. This phenomenon was termed oncogene dependency by Bernard Weinstein in 2000, and has now been identified in numerous cancers (Weinstein, 2002, Weinstein and Joe, 2008, Shaffer et al., 2008, Luo et al., 2009, Yan et al., 2014).

These revolutionary insights led to the identification of many novel therapeutic targets, including growth factors, signalling molecules and a range of proteins involved in apoptosis, angiogenesis or cell cycle regulation (Hanahan and Weinberg, 2000), and spurred on more rational drug designs to specifically target them for cancer therapy. One significant landmark in targeted cancer therapy has been the development of the small molecule drug imatinib (Capdeville et al., 2002). Imatinib is a potent inhibitor of BCR-ABL, a fusion oncoprotein that results from a translocation between chromosomes 9 and 22, and is found in 95% of chronic myelogenous leukemia (CML) (Wada et al., 1995). Wild-type ABL is a highly regulated tyrosine kinase with roles in the cell cycle, genotoxic stress response and integrin signalling (Deininger et al., 2000). The fusion of BCR-ABL results in the loss of the ABL autoinhibition domain, and ultimately leads to its deregulation (Pluk et al., 2002). This constitutively active tyrosine kinase hyper-phosphorylates a vast range of substrates involved in growth, cell adhesion and inhibition of apoptosis, which results in tumorigenesis. Imatinib inhibits BCR-ABL by binding in its active site (Figure 1.7A), locking the kinase in its autoinhibited conformation.

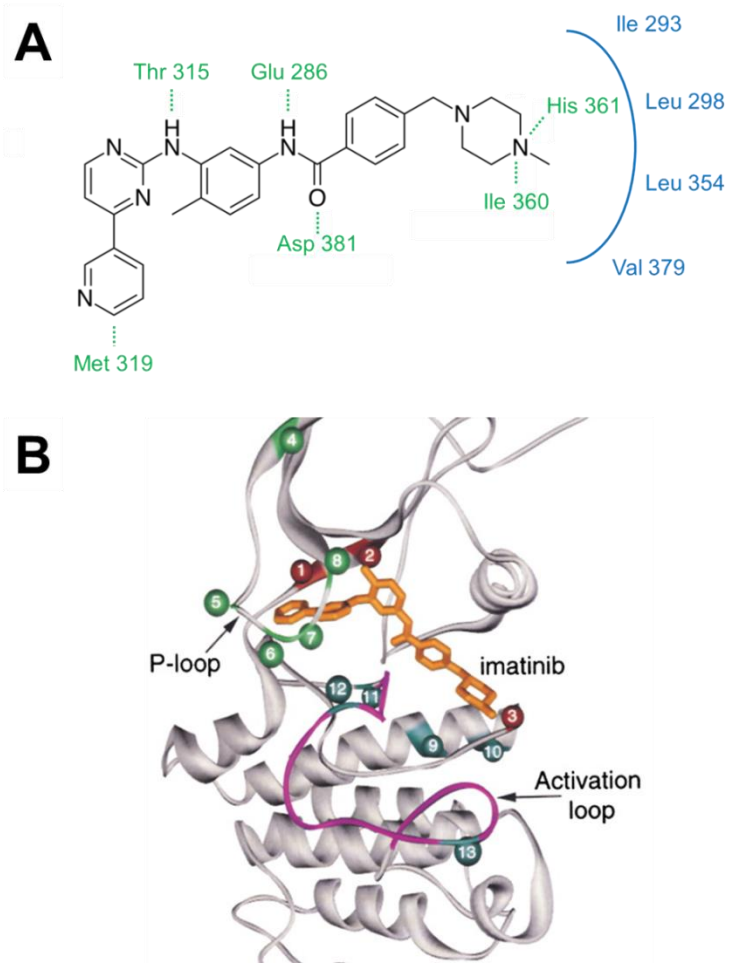


**Figure 1.7. Structure and binding of imatinib. (A)** Schematic showing the structure of imatinib and its interactions with amino acid residues in BCR-ABL. Imatinib binds to the kinase domain of ABL in its inactive conformation, via six hydrogen bonds (green) and numerous van der Waals interactions. Residues shown in blue form a hydrophobic face against which imatinib packs. Imatinib binding stabilises BCR-ABL in its inactive conformation and prevents ATP binding. **(B)** Mutations in ABL which confer resistance to imatinib. These mutations are highlighted as spheres, and include those that directly (1 to 3) or indirectly (4 to 13) perturb imatinib binding. Residues 4 to 8 are present in the P loop; residues 9 to 13 are present within the vicinity of the activation loop (purple) of ABL. Adapted from Shah et al. (2002).

Imatinib demonstrated remarkable efficacy in clinical trials, in which 53 out of 54 CML patients showed hematologic responses and 7 had complete cytogenetic

remissions; this led to the fast-tracked FDA approval of imatinib in 2001 (Druker et al., 2001). However, it has since emerged that drug resistance can develop in CML patients that renders them unresponsive to imatinib treatment, typically through gene amplification of *BCR-ABL* or mutations in its catalytic domain that perturb drug binding (Figure 1.7B) (Gambacorti-Passerini et al., 2003). Such drug resistance is especially prevalent during the later stages of CML, including the accelerated phase or blast crisis (Druker, 2008), and has prompted the development of second generation BCR-ABL inhibitors, such as nilotinib and dasatinib (Weisberg et al., 2007).

Other small molecule kinase inhibitors soon emerged from the clinical pipeline, for instance, gefitinib, which targets the epidermal growth factor receptor (EGFR). EGFR is a receptor tyrosine kinase that is involved in initiating growth and proliferation signalling pathways (Kolch and Pitt, 2010); its overexpression or mutation is a crucial event in the pathogenesis of several cancers, including NSCLC, breast, prostate and ovarian cancers (Ciardiello and Tortora, 2008). Gefitinib inhibits EGFR signalling by competing for ATP-binding sites within its intracellular kinase domain, and exhibited great efficacy in NSCLC patients, leading to its FDA approval in 2003 (Lynch et al., 2004, Pao, 2004). However, as for imatinib, the success of gefitinib was short-lived due to the emergence of drug resistance, often acquired by cancers via mutations in the drug-binding site of EGFR (Tartarone et al., 2013).

### 1.2.1 Exogenous antibodies for cancer therapy

Ehrlich displayed incredible foresight with his early vision of antibodies as "magic bullets that identify their target themselves without harming the organism" (Strebhardt and Ullrich, 2008), and the hypothesis that the immune system can prevent cancers (Ehrlich, 1909). However, this potential was not realised until the identification of cancer cell surface markers, and the emergence of the hybridoma technology (Kohler and Milstein, 1975).

In 1973, Schwaber reported that fusion of human peripheral blood lymphocytes with a mouse myeloma cell line produced hybridomas which secrete monospecific antibodies of both parental types (Schwaber and Cohen, 1973). Based on this work, Cesar Milstein and George Köhler demonstrated in 1975 that B cells isolated from mice immunised with an antigen could be immortalised via fusion with immuno-deficient myeloma cells (Kohler and Milstein, 1975). The resulting hybridomas are diluted and segregated into individual growth chambers, from which clones positive for producing the desired antibodies can be identified by adding the antigen of interest. These can then be grown indefinitely, enabling the large-scale production of monoclonal antibodies.

This revolutionary technology led to the development of the first wave of therapeutic antibodies for cancer, including trastuzumab and rituximab. Rituximab targets the B-cell transmembrane antigen, CD20, and was shown to specifically deplete $CD20^{+}$ B-cells from circulation, the lymph nodes and bone marrow; it was approved by the FDA in 1997 for treating B-cell non-Hodgkin lymphoma (Maloney et al., 1997, McLaughlin et al., 1998). Trastuzumab targets ERBB2, a member of the epidermal growth factor receptor family whose

overexpression has a crucial role in tumorigenesis in breast and ovarian cancers (Slamon et al., 1989), and received FDA approval in 1998 for the treatment of $ERBB2^{+}$ breast cancers (Hudziak et al., 1989).

| Antibody | Target | Format | Indication |
|---|---|---|---|
| Trastuzumab | ERBB2 | Humanised IgG1 | Breast cancer |
| Bevacizumab | VEGF | Humanised IgG1 | Colon and kidney cancer, NSCLC, glioblastoma |
| Cetuximab | EGFR | Chimeric IgG1 | Colorectal cancer, squamous cell carcinoma |
| Panitumumab | EGFR | Humanised IgG2 | Colorectal cancer |
| Ipilimumab | CTLA4 | Humanised IgG1 | Melanoma |
| Rituximab | CD20 | Chimeric IgG1 | Non-Hodgkin lymphoma, chronic lymphoid leukaemia |
| Alemtuzumab | CD52 | Humanised IgG1 | Chronic lymphoid leukaemia |
| Ofatumumab | CD20 | Humanised IgG1 | Chronic lymphoid leukaemia |
| §*Gemtuzumab ozogamicin | CD33 | Humanised IgG4 | Acute myeloid leukaemia |
| *Brentuximab | CD30 | Humanised IgG1 | Hodgkin's lymphoma, systemic anaplastic lymphoma |
| *Ibritumomab tiuxetan | CD20 | Murine IgG1 | Non-Hodgkin lymphoma |
| *Tositumomab | CD20 | Murine IgG2 | Non-Hodgkin lymphoma |

**Table 1.1. List of FDA approved monoclonal antibodies in cancer therapy and their mechanism of action.** Many other antibody-based therapies have been approved by the FDA for treating other diseases, but are not included here. §Gemtuzumab ozogamicin was withdrawn from the market in 2010. *Antibody-drug conjugates.

These antibodies demonstrated anti-tumour efficacy through various mechanisms, including the modulation of signalling pathways, antibody-dependent cellular toxicity, and complement-dependent cytotoxicity (Carter, 2001, Schrama et al., 2006). Their huge clinical success prompted the development of many new therapeutic antibodies targeting a range of cancer-related markers, such as EGFR, vascular endothelial growth factor (VEGF) and epithelial cell adhesion molecule (van Mierlo et al., 2002, Galizia et al., 2007, Chaudry et al., 2007, Hudziak et al., 1989), as well as antibody-toxin conjugates to promote tumour-specific drug delivery (Chari et al., 2014). Many of these have now received FDA approval (Table 1.1).

Despite the significant impact therapeutic antibodies have made on the treatment of cancer, some problems have emerged, mostly related to mechanism-dependent toxicities. For instance, Trastuzumab has been associated with cardiotoxicity due to its binding to receptors in the heart (Seidman et al., 2002); binding of rituximab to healthy $CD20^+$ B-cells has also been reported to induce toxicities (Byrd et al., 1999). Another drug, gemtuzumab ozogamicin, was withdrawn from the market a decade after its FDA approval in 2010, following observations of significantly higher mortality rates in patients compared to standard-of-care chemotherapies (Rowe and Lowenberg, 2013).

### 1.2.2 RNA interference and its therapeutic applications

Since its discovery in the mid-1990s (Fire et al., 1998, Baulcombe, 1996), RNA interference (RNAi) has rapidly transformed from a curious phenomenon in

worms to an invaluable tool in the study of functional genomics. The significance of RNAi technology was underlined by the award of the 2006 Nobel Prize in Physiology or Medicine to Fire and Mello (Bernards, 2006).

RNAi describes the cellular process that occurs in various organisms, including mammals, plants and nematodes, whereby double-stranded (ds) RNAs mediate specific and potent gene silencing (Wilson and Doudna, 2013). RNAi is believed to have evolved from an early immune mechanism against viruses and transposable elements (Obbard et al., 2009). Foreign dsRNAs are recognised and processed by Dicer RNases into 21-24 nt fragments, known as small interfering RNA (siRNA), then loaded onto an Argonaute-containing RNA-induced silencing complex (RISC). One strand of the siRNA (passenger strand) is degraded, whilst the other (guide strand) in complex with RISC searches cytoplasmic RNA for complementary sequences. Once located, Argonaute triggers cleavage of the targeted RNA, thereby silencing expression of the foreign gene. This RNAi pathway forms an important component of innate antiviral immunity in plants, nematodes, fungi and arthropods (Obbard et al., 2009).

Another RNAi pathway, the endogenous microRNA (miRNA) pathway, enables post-transcriptional regulation of gene expression in animals and plants (Figure 1.8) (Carthew, 2006). This pathway commences with the transcription of primary miRNAs (pri-miRNA) from the host genome. These transcripts are typically excised by a microprocessor complex, Drosha, into 65-70 nt precursor miRNAs (pre-miRNA), which are then exported to the cytoplasm by exportin-5 and Ran GTP (Lund and Dahlberg, 2006). Similar to the siRNA pathway, pre-miRNAs are processed by Dicer to form 21-26 nt mature miRNAs, which can be

loaded onto RISC, forming a miRISC complex. Compared to siRNAs, miRNAs only partially base pair with their target sequences in the 3'-untranslated regions (3'-UTRs) of mRNA, mainly via 7-8 consecutive base pairs of the so-called seed region. Binding of miRISCs to 3'-UTRs inhibits 5'-cap dependent translational initiation and can trigger mRNA degradation. Individual miRNAs usually have several different mRNAs as targets. To date, 1,881 miRNA sequences have been identified within the human genome (http://microrna.sanger.ac.uk; accessed March, 2015) which regulate almost a third of protein-encoding genes (Macfarlane and Murphy, 2010). Unsurprisingly, endogenous RNAi plays a critical role in regulating numerous vital processes, including cell growth, cell proliferation, apoptosis and tissue differentiation (Esquela-Kerscher and Slack, 2006).

Cellular RNAi can be exploited to silence a gene of interest by introducing exogenous sxRNA analogues, either siRNA or shRNA, that target its mRNA (Figure 1.8). SiRNAs are competent for RISC loading, and may directly enter the RNAi pathway once delivered to the cytoplasm. For shRNAs, viral vectors are typically used to deliver shRNA-encoding genes into cells for expression. Expressed shRNA undergoes processing to form siRNA, which can then be loaded onto RISC complexes. Many different sxRNA libraries now exist that cover the entire genomes of both mice and humans, enabling high-throughput loss of function analyses and the identification of essential genes for virtually any cellular process (Latterich, 2008).

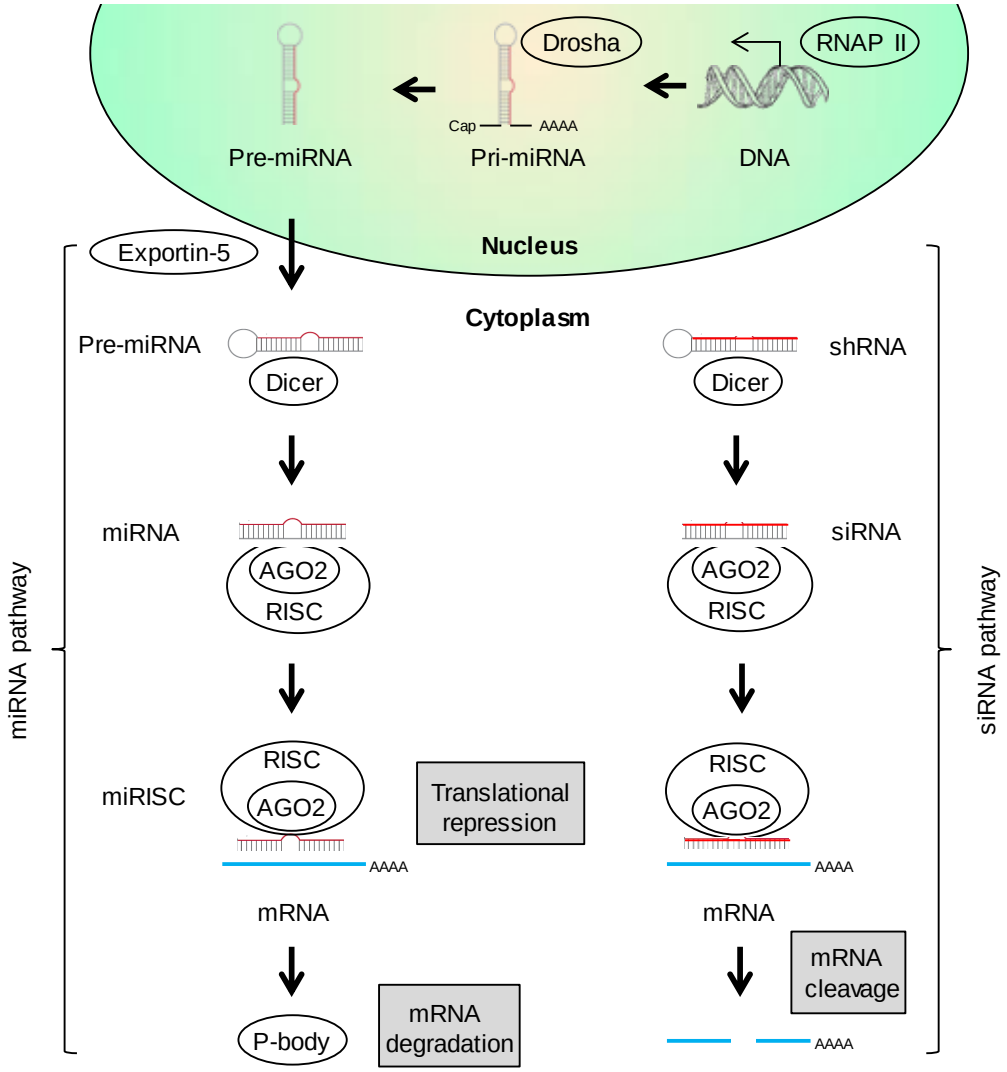


**Figure 1.8. The RNAi pathway.** Endogenous primary miRNAs (pri-miRNA), which are ~80 nt dsRNAs with a hairpin turn, polyA tail and 5´ cap, are transcribed in the nucleus by RNA polymerase II (RNAP II). Pri-miRNA is processed by Drosha and exported out of the nucleus by exportin-5 as 65-70 nt precursor-miRNA (pre-miRNA). In the cytoplasm, pre-miRNA is processed by Dicer to form a 21-26 nt mature miRNA, consisting of a guide strand (red) and a passenger strand (black). The passenger strand is degraded, whilst the guide strand is loaded onto RISC, forming a miRISC complex. The miRNA in miRISC targets mRNA with a near complementary sequence in their in their 3´-UTR for binding, which leads to translational inhibition and degradation of the mRNA by processing bodies (P-bodies). RNAi can also be induced by introducing exogenous small interfering RNA (siRNA) or short hairpin RNA (shRNA). ShRNA requires processing by Dicer to form siRNA. The guide strand of siRNA can be loaded onto RISC to target complementary regions on mRNA for binding, which results in its cleavage by Ago2 within the RISC complex.

RNAi technology has played a key role in the identification of many oncogene-dependent cancers, and the oncogenes on which they rely. One example of this is the identification of the oncogene*, I Kappa B Kinase ε* (*IKBKE*), in breast cancers. A large shRNA library targeting 1,200 genes was used to screen the breast cancer cell line, MCF-7, in which three shRNAs targeting IKBKE were able to reduce proliferation and viability of MCF-7 cells, indicating their dependence on *IKBKE* for maintenance and survival (Boehm et al., 2007). These findings not only added to the accumulating body of evidence for oncogene dependence in cancers, but also highlighted the therapeutic potential of sxRNA-mediated RNAi against them.

SxRNAs have several advantages as novel therapeutic agents. They are synthetic and relatively easy to produce compared to protein-based therapeutics, can be rationally designed to target any oncogene, and can achieve a level of specificity far higher than that of traditional cancer therapeutics. Furthermore, as sxRNAs target oncogenes at the mRNA level, they may exhibit synergistic effects when used with drugs that target at the protein level. For instance, siRNA-mediated silencing of *BCR-ABL* and the gene encoding multidrug resistance protein 1 has been shown to sensitise CML cells to imatinib treatment (Wohlbold et al., 2003, Vasconcelos et al., 2007), highlighting the potential of such combinatorial therapies.

Several barriers have severely hindered the progress of RNAi therapeutics towards clinical approval, including the short plasma half-lives of RNAs, their poor cellular uptake, and the lack of tumour-specific targeting. These issues led to the withdrawal of interest from big Pharma, such as Novartis, Roche and Merck, which in 2010 shut down their billion dollar RNAi programs (Bouchie,

2012). However, there has been a recent resurgence in the development of RNAi therapeutics, fuelled in part by advances in polymeric drug delivery systems which have shown it is possible to overcome or mitigate aforementioned problems (Yan et al., 2014). Numerous promising RNAi-based therapeutics are now under clinical investigation (Table 1.2).

| Product | Description | Indication | Status |
|---|---|---|---|
| SNS01-T | siRNA targeting *eIF-05A1* and a plasmid of *5A1*; systemic delivery via PEI | Multiple myeloma | Phase 1b/2a |
| CALAA-01 | siRNA targeting *RRM2*; systemic delivery by RONDEL | Solid tumours | Phase 1b |
| Atu027 | Modified siRNA targeting *PKN3;* systemic delivery by cationic liposome | Solid tumours | Phase 1 |
| ALN-VSP02 | Modified siRNA targeting *VEGF* and *KSP*; systemic delivery by SNALP | Liver cancer | Phase 1 |
| TKM-PLK1 | siRNA targeting *PLK1*; systemic delivery by SNALP | Solid tumours | Phase 1 |
| siG12D LODER | siRNA targeting *KRAS*; systemic delivery by LODER | Pancreatic Cancer | Phase 2 |

**Table 1.2. Selected examples of siRNA products in clinical trials for treating cancer.** Many other candidates exist, which treat a wide range of diseases, such as Ebola and age-related macular degeneration. eIF = eukaryotic initiation factor; PEI = polyethyleneimine; RRM2 = ribonucleoside-diphosphate reductase subunit M2; RONDEL = RNAi/Oligonucleotide Nanoparticle Delivery; PKN3 = protein kinase N3; VEGF = vascular endothelial growth factor; KSP = kinesin spindle protein; SNALP = stable nucleic acid lipid particles; LODER = local drug eluter. Adapted from Bouchie (2012).

| Problem | Implication | Effect of Drug Delivery |
|---|---|---|
| Poor biodistribution | Drugs with widespread biodistribution can affect normal tissues, causing dose-limiting side effects, such as the cardiotoxicity of doxorubicin. | Drug delivery systems can improve passive targeting of tumour tissues via the enhanced permeability and retention (EPR) effect. |
| Poor selectivity | Low drug concentrations in tumour tissues lead to suboptimal therapeutic effects. Also see 'Poor distribution'. | Delivery systems can utilise EPR to accumulate in tumour tissues, and targeting ligands to preferentially enter tumour cells. |
| Poor solubility | Hydrophobic drugs may precipitate in aqueous media, preventing a convenient pharmaceutical format. Excipients such as Cremophor may be used but can be toxic. | Delivery systems such as micelles offer both hydrophilic and hydrophobic environments, to improve drug solubility. |
| Poor stability *in vivo* | Rapid breakdown of the drug under physiological conditions results in loss of activity, for instance, nuclease degradation of siRNA therapeutics. | Delivery systems can enhance the stability of the drug; lowering the effective dosage. |
| Tissue damage on extravasation | Inadvertent extravasation of drugs can lead to tissue damage, for instance, doxorubicin-induced tissue necrosis. | Regulated drug release from the delivery system can mitigate tissue damage on extravasation. |
| Unfavourable pharmacokinetics | Drug is cleared quickly, for example, by rapid renal clearance, requiring high dosages. | Delivery systems can dramatically alter the pharmacokinetics of the drug, and prevent its rapid renal clearance. |

**Table 1.3. Undesirable properties of drugs and the effect of drug delivery systems.** Adapted from Allen and Cullis (2004).

## 1.3 Drug Delivery Systems

Problems associated with poor pharmacokinetics and biodistribution have affected many cancer drug candidates, which is reflected in their ~95% failure rate (Arrondeau et al., 2010, Kola and Landis, 2004). Many of these problems, however, are not exclusive to novel drugs, but are also common among established and approved formulations. This has prompted the development of drug delivery systems to impart more favourable pharmacological properties to

drugs, such as increased tumour selectivity and prolonged plasma half-lives, to ultimately improve their efficacy whilst mitigating adverse toxicities (Table 1.3).

A large number of systems, based on materials ranging from human viruses to synthetic polymers, have been explored for anti-cancer drug delivery (Figure 1.9). These are highlighted below, attention is paid to the strengths and weaknesses of each delivery system as well as promising examples that are either approved or undergoing pre-clinical or clinical testing.

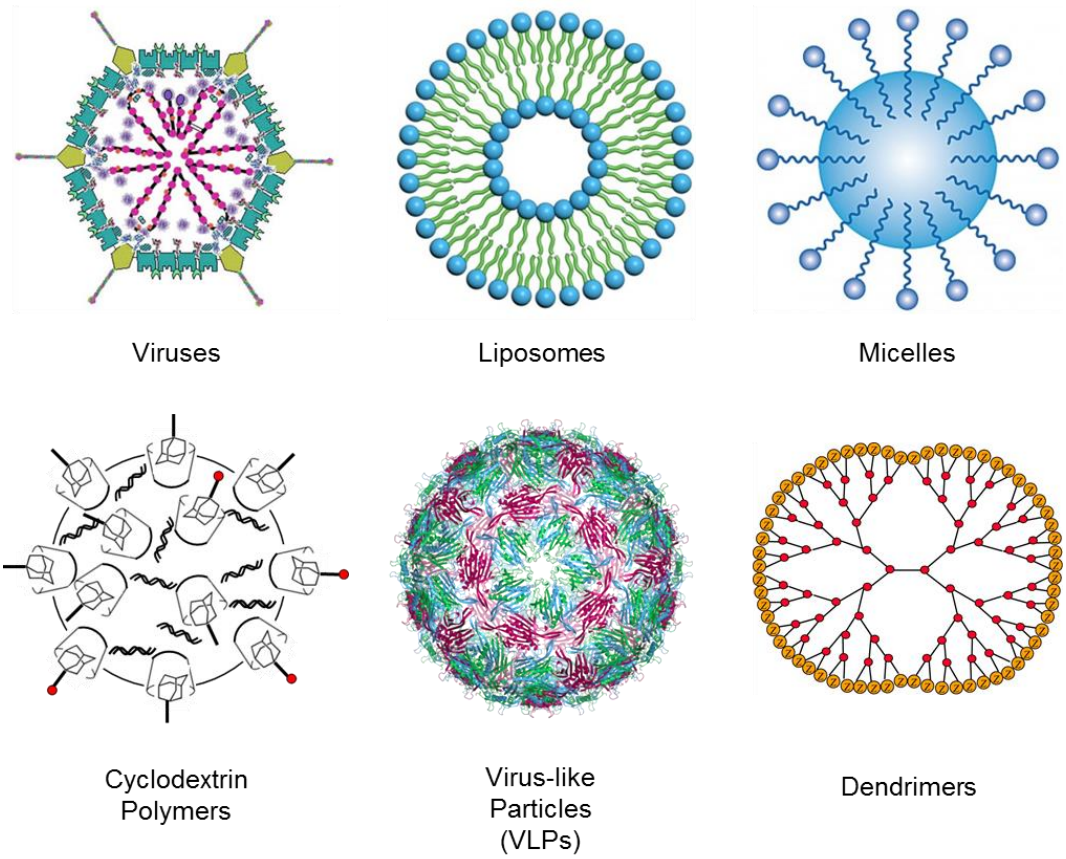


**Figure 1.9. Major classes of polymer-based drug delivery systems.** Schematic presentation of delivery systems which have shown promise in preclinical or clinical testing.

### 1.3.1 Viral Drug Delivery Systems

Eons of evolutionary fine-tuning has given viruses the ability to infiltrate specific cells and deliver genetic material for expression, making them an attractive option for delivering nucleic acid therapeutics, such as RNAi drugs. Viral delivery systems have largely been explored for delivering shRNA expression cassettes (Castanotto and Rossi, 2009). Non-essential regions within the virus genome can be modified to incorporate a promoter and shRNA of interest, to achieve long-term shRNA expression and hence repression of targeted genes in transfected cells. Adenoviruses, adeno-associated viruses, herpesviruses and lentiviruses are among those that have been tested as shRNA delivery vectors (Heilbronn and Weger, 2010).

Adenoviruses are widely used in gene therapy studies due to their ability to incorporate large genes and deliver them to the nucleus (Campos and Barry, 2007). Adenoviral delivery of shRNAs has been demonstrated in several human cancer cell lines, in which delivered shRNAs targeting the mRNA of the tumour suppressor protein, p53, successfully triggered gene silencing (Shen et al., 2003). Despite these encouraging results from *in vitro* studies, the inherent, high immunogenicity of adenoviruses has severely limited their use for shRNA delivery *in vivo* (Liu and Muruve, 2003, Hartman et al., 2008).

Systemic administration of adenoviral vectors to human patients leads to high liver uptake and activation of innate immunity, causing severe acute inflammatory responses and even fatalities (Marshall, 1999). Moreover, the development of neutralising anti-adenoviral antibodies prohibits repeated drug dosing (Yang et al., 1996). These findings seriously questioned the suitability of

adenoviral vectors for *in vivo* applications. However, work is under way to address some of these issues, in particular the immunogenicity and poor targeting of adenoviruses. Various approaches, including addition of polyethylene glycol (PEG) to the virus surface (Wonganan and Croyle, 2010) or liposomal modification (Wan et al., 2013) to mask viral epitopes, and genetic incorporation of tumour-targeting ligands (Campos and Barry, 2007), have shown promising results.

Lentiviruses, of the Retroviridae family, have also been explored for therapeutic shRNA delivery. Lentiviruses are single stranded RNA viruses with the ability to reverse transcribe their RNA genome into DNA, before inserting the viral DNA into the host genome for expression (Sakuma et al., 2012). Brummelkamp and coworkers successfully used lentiviruses to deliver shRNA vectors that targeted an activated *K-RAS* oncogene to pancreatic cancer cells. Effective knockdown of the oncogene was achieved, resulting in the elimination of the tumorigenic capacity of transfected cancer cells in mice (Brummelkamp et al., 2002).

Another lentiviral shRNA delivery system is currently under clinical evaluation for autologous cell therapy against AIDS-related non-Hodgkin's lymphoma (Burnett et al., 2011). This involves *ex vivo* shRNA delivery. Haematopoietic progenitor cells are removed from patients via apheresis, transfected with lentiviral shRNA vectors and then reinfused into the patient. Early results revealed no short-term toxicity associated with the transfected haematopoietic progenitor cells, and two of four patients exhibited persistent expression of the shRNA (DiGiusto et al., 2010).

The major drawback of retroviral shRNA delivery is that random retroviral genome insertion may cause major disruptions to the host genome, resulting in a multitude of problems, including the activation of proto-oncogenes (Yi et al., 2005). This could be particularly dangerous if a large amount of virus is taken up by untargeted healthy tissues. Thus, retroviruses are not ideal candidates for shRNA delivery *in vivo*.

Hong and coworkers demonstrated that *Herpesvirus saimiri* can deliver shRNA targeting the *endothelin converting enzyme 1* (*ECE-1*) into prostate cancer cells (Hong et al., 2011). ECE-1 was selected as the target due to its involvement in the invasion and migration of several cancers, including prostate, lung, breast, colorectal and ovarian (Smollich et al., 2007). The herpesvirus vector was tested *in vitro* in several cell lines and *ex vivo* in primary cells from three different forms of prostate cancer. Significant levels of *ECE-1* knockdown were observed in all cases, which severely limited the capacity of the cancer cells to migrate and invade (Hong et al., 2011). However, much *in vivo* testing is still needed to evaluate the safety of herpesviruses for therapeutic applications, especially considering the well reported tendency of vectors based on herpes simplex virus 1, another member of the herpesviridae family, to trigger severe inflammatory responses in the central nervous system (Wood et al., 1994, McMenamin et al., 1998).

### 1.3.2 Non-viral Drug Delivery Systems

Although viral drug delivery has proven effective *in vitro*, its clinical application has largely been deterred by problems associated with its oncogenic potential, lack of tumour-specific targeting, high immunogenicity and difficulty of large scale production. As a result, non-viral drug delivery systems, which can circumvent or minimise these problems and are able to deliver a diverse range of cargos not limited to nucleic acids, have attracted considerable attention in recent years (Cheng et al., 2012).

Several important parameters need to be considered in the design of a non-viral anti-cancer drug delivery system, including:

- Size: Particles should be 10-100 nm in diameter to avoid rapid renal clearance (Choi et al., 2007), and to accumulate preferentially at disease sites characterised by increased vascular permeability, such as sites of infection or tumour (Matsumura and Maeda, 1986, Tabata et al., 1998).

- Zeta potential: Zeta potential is a measure of the magnitude of the electrostatic attraction or repulsion between particles, and is related to their surface charge. To minimize nonspecific electrostatic interactions with cells, which typically display a zeta potential within the range of -5 to -20 mV (Zhang et al., 2008, Bondar et al., 2012), and to reduce macrophage uptake, a small negative zeta potential is generally desirable for nanoparticles (Zahr et al., 2006).

- Immunomasking: A highly immunogenic delivery system can trigger potentially lethal inflammatory responses in patients, as seen with adenoviruses (Marshall, 1999), and also prohibits repeated dosing. This can be minimised in non-viral delivery systems via surface coverage with PEG molecules, which mask epitopes from the immune system (Knop et al., 2010).

- Targeting: One common problem with many conventional cancer drugs in use today is a lack of specificity. They are readily internalised by healthy as well as cancer cells, thus producing side effects. To this end, ligands that bind cancer cell surface markers can be incorporated into non-viral drug delivery systems. These markers are typically receptors which are overexpressed on cancer cells, such as EGFR, and receptors for transferrin (Tf) and folate (Cheng et al., 2012). Targeting agents can be natural receptor ligands like Tf or synthetic ones like peptide or nucleic acid aptamers (Bunka and Stockley, 2012). Aside from preferential binding to cancer cells, targeting ligands also offer a mechanism of cell entry by receptor-mediated endocytosis (Bareford and Swaan, 2007).

- Endosomal escape: Following endocytosis, delivered drugs must escape the endosome into the cytosol, where many drugs mediate their effect. This may be achieved by incorporating endosomal buffering ligands, such as histidine-rich peptides and polyethyleneimine. These ligands can absorb protons as they are pumped into the endosome, acting as ‘proton sponges’, and promoting further proton influx. This in turn is coupled to an

increased influx of chloride ions and water, resulting in the osmotic swelling and eventual rupture of the endosome, which can then release its contents into the cytosol (Behr, 1997).

A diverse range of non-viral drug delivery systems have been tested; some are already clinically approved or in advanced stages of clinical trials. A selection of some promising formulations is highlighted below; many others exist (Hamidi et al., 2008, Kesharwani et al., 2014, Safari and Zarnegar, 2014, Chari et al., 2014, Alconcel et al., 2011).

**Liposomes**

Liposomes are self-assembling spherical vesicles with a membrane composed of lipid bilayers, and represent a major class of drug delivery systems. Reports of the first liposomes emerged as early as 1965 (Bangham et al., 1965), followed swiftly by speculations over their potential for drug delivery. These were validated three decades later with the FDA approval of Doxil – a PEGylated liposomal formulation of doxorubicin, which was the first FDA approved nanoparticulate drug delivery system, and is now used for treating various cancers including Kaposi's sarcoma, refractory ovarian and breast cancers, and multiple myeloma (Gabizon et al., 2003, James et al., 1994, Blade et al., 2011, Barenholz, 2012). Since then, a large number of liposomal systems have emerged from pre-clinical and clinical testing, that deliver a diverse range of drugs, from established small molecule chemotherapeutics like cisplatin to relatively novel drug entities such as siRNAs (Table 1.4).

| Product | Drug | Indications | Approval | Ref |
|---|---|---|---|---|
| *Approved liposomal drug delivery systems* | | | | |
| Doxil/ Caelyx | Doxorubicin | Kaposi's sarcoma | 1995 | 1-3 |
| | | Ovarian cancer | 1999 | |
| | | Breast cancer | 2003 | |
| | | MM with bortezomib | 2007, (Europe, Canada) | |
| Dauno-Xome | Daunorubicin | Kaposi's sarcoma | 1996 (Europe), 1996 (USA) | 4 |
| Myocet | Doxorubicin | Breast cancer with cyclophosphamide | 2000 (Europe) | 5 |
| Lipo-Dox | Doxorubicin | Kaposi's sarcoma, breast and ovarian cancer | 2001 (Taiwan) | |
| Marqibo | Vincristine | ALL | 2012 (USA) | 6 |
| *Liposomal drug delivery systems in clinical trials* | | | | |
| CPX-351 | Cytarabine: daunorubicin | Acute myeloid leukemia | Phase II | 7 |
| CPX-1 | Irinotecan HCI:floxuridine | Colorectal cancer | Phase II | 8 |
| MM-302 | ErbB2/ErbB3-targeted doxorubicin | ErbB2-positive breast cancer | Phase I | 9 |
| MBP-436 | Tf-targeted oxaliplatin | Gastric cancer | Phase II | 10 |
| Lipo-platin | cisplatin | NSCLC | Phase III | 11 |
| Thermo-Dox | Thermosensitive doxorubicin | Primary hepatocellular carcinoma | Phase III | 12 |
| Endo-Tag-1 | Cationic liposomal paclitaxel | Pancreatic cancer | Phase II | 13 |
| | | Triple negative breast cancer | Phase II | |
| TKM-PLK1 | RNAi targeting polo-like kinase 1 | Liver tumours | Phase I | |
| Stimu-vax | Anti-MUC1 cancer vaccine | NSCLC | Phase III | 14 |

**Table 1.4. Selected examples of liposomal drug delivery systems that are clinically approved or undergoing clinical trials for treating cancer.** References: 1=(James et al., 1994); 2=(Blade et al., 2011); 3=(Barenholz, 2012); 4=(Petre and Dittmer, 2007); 5=(Batist et al., 2001); 6=(Sarris et al., 2000); 7=(Riviere et al., 2011); 8=(Dicko et al., 2010); 9=(McDonagh et al., 2012); 10=(Suzuki et al., 2008); 11=(Fantini et al., 2011); 12=(Poon and Borys, 2011); 13=(Fasol et al., 2012); 14=(Bradbury and Shepherd, 2008). Adapted from Allen and Cullis (2013).

Liposomes can be constituted from a variety of lipid components, including phospholipids, cholesterols, cationic lipids and various lipid-like materials. Lipid composition can greatly influence the physical properties of liposomes (Yitbarek, 2011) and their drug delivery efficiency (Kim et al., 2010). For instance, cholesterols are commonly included to improve liposomal stability, cargo retention and uptake (Gao and Huang, 1995, Allen and Cleland, 1980, Cullis, 1976); some cationic derivatives of cholesterol can also facilitate endosomal escape (Kim et al., 2008). Synthetic phospholipids can be incorporated to confer useful properties to liposomes, for example, thermosensitivity to release their drug cargo only at elevated temperatures to complement hyperthermia therapy (Poon and Borys, 2011, Needham et al., 2000). PEGylated lipids can be incorporated to confer steric stabilisation to the nanoparticle, and prolong its blood circulation by evading the mononuclear phagocyte system (Gabizon and Papahadjopoulos, 1988, Senior et al., 1991). Amino-lipid derivatives containing cleavable ester bonds have recently been developed to improve the biodegradability of liposomes (Maier et al., 2013). A wide range of methods for liposome preparation are available, which can also influence important properties such as the size and dispersity of liposomes (Laouini et al., 2012, Mozafari, 2005).

Significant progress has also been made towards cationic liposomes, in particular for the cellular delivery of nucleic acid therapeutics such as siRNAs. Cationic liposomes self-assemble with siRNA via electrostatic interactions between positively charged lipids and the negatively charged phosphate backbone of siRNA, forming lipoplexes. Lipoplexes can protect encapsulated

siRNA from nuclease degradation, and facilitate their transport across the cell membrane.

Nucleic acid delivery by cationic liposomes is well established, as highlighted by the prevalence of commercially available products such as Lipofectin, Oligofectamine, Lipofectamine and RNAifect, which are commonly used in laboratories to enhance siRNA delivery *in vitro* (Dalby et al., 2004, Baker et al., 2006, Bjorge et al., 2011). Furthermore, nearly half of the most promising siRNA drug candidates currently in clinical trials are formulated with cationic liposomes for delivery (Bouchie, 2012). For example, Alnylam Pharmaceuticals' ALN-VSP02, which is a PEGylated liposome used to treat liver cancer, delivers siRNAs targeted against the mRNAs of vascular endothelial growth factor and kinesin spindle protein, both of which have important roles in tumour proliferation and survival. ALN-VSP02 has suitable physical properties for delivering siRNA *in vivo*, including a diameter of 80-100 nm and a small zeta potential of <6 mV at pH 7.4. Intravenous administration of ALN-VSP02 in patients with advanced cancer and liver metastases gave encouraging results, including siRNA-mediated cleavage of targeted mRNAs in the liver and pronounced tumour regression (Tabernero et al., 2013).

One disadvantage of currently approved liposomal delivery systems, as well as many of the liposomal drug candidates, is the absence of a tumour targeting mechanism. As a result, significant levels of siRNA may be taken up by healthy cells alongside the cancer cells, causing dose-limiting side effects. Recent progress has been made to address this, with several targeted liposomes currently undergoing clinical or pre-clinical testing (Table 1.4). Examples include the Tf targeted PEG-liposome, MBP-436 (Suzuki et al., 2008), and the anti-

HER2 antibody targeted liposome, MM-302 (McDonagh et al., 2012), which displayed markedly improved efficacies *in vivo* compared to their non-targeted versions.

**Micelles**

Polymeric micelles are spherical monolayer vesicles composed of amphiphilic block copolymers, which have a hydrophilic segment and a hydrophobic segment. These copolymers self-assemble into micelles in aqueous solution, with the hydrophobic segments forming a core, which functions as a nanoreservoir for hydrophobic drugs, surrounded by a shell formed by the hydrophilic segments. Polymeric micelles are typically 10-50 nm in diameter (Kwon and Kataoka, 1995, Allen et al., 1999), and thus can fully benefit from the EPR effect to passively accumulate in tumour tissues (Aliabadi and Lavasanifar, 2006, Kwon and Forrest, 2006). Drug cargos can be packaged inside micelles by either physical entrapment, or chemical conjugation. Physical entrapment involves cargo incorporation via hydrophobic interactions between the drug and the micelle core, whilst chemical conjugation involves the covalent attachment of drugs to the hydrophobic core (Gong et al., 2012). Polymeric micelles have been tested for the delivery of various anti-cancer drugs, such as anthracyclines (Nakanishi et al., 2001, Matsumura et al., 2004) and taxanes (Kim et al., 2001, Kim et al., 2004, Kim et al., 2007).

Many important properties of micelle delivery systems, including particle size, drug loading and release, and pharmacokinetics, can be modulated via the chemical composition of constituent block copolymers (Xiong et al., 2011). PEG

is typically used as the hydrophilic block, which sterically stabilises the resulting micelles and also reduces their clearance *in vivo* by the mononuclear phagocyte system (Barratt, 2003). To avoid long-term toxicities, core-forming blocks which can undergo hydrolysis or enzymatic degradation, such as poly(L-amino acids) and polyesters, can be used to confer biodegradability. Copolymers such as poly(N-isopropylacrylamide) and sodium 2-acrylamido-2-methyl-1-propane can also be used to impart additional functions such as temperature- or pH-sensing, to enable degradation of the delivery system and subsequent drug release, upon reaching tissues or cell compartments with different environments – for instance, the acidic microenvironments of tumour tissues and endosomes (Ganta et al., 2008, Liu et al., 2011, Islam and Yasin, 2012). Tumour targeting ligands, such as monoclonal antibodies and nucleic acid aptamers, can be incorporated via attachment to the surface exposed hydrophilic termini of micelles (Xiong et al., 2011).

Several micelle-based drug delivery systems have shown promise *in vivo* for the treatment of cancers. Notably, NK911, a micelle composed of PEGylated poly(aspartic acid) block copolymers, has been tested in phase I clinical trials for delivering doxorubicin to solid tumours (Nakanishi et al., 2001, Matsumura et al., 2004). In a study with 23 patients bearing solid tumours, some dose-limiting toxicity, including neutropenia, alongside mild side effects were observed at higher doses tested. As expected, NK911-delivered doxorubicin displayed longer plasma half-lives in comparison to free doxorubicin. NK911 administration produced a partial response in one patient with metastatic pancreatic cancer, in which the liver metastasis had shrunk by more than 50% post treatment. The current clinical progress of NK911 is unclear.

Another drug, Genexol-PM, delivers the water insoluble, mitotic inhibitor chemotherapeutic, paclitaxel, to patients with advanced and refractory tumours. Genexol-PM is a micelle system composed of PEGylated poly(D,L-lactide) copolymers. In mouse models, significantly improved pharmacological properties were observed when paclitaxel was delivered by Genexol-PM, compared to the free drug, including a three-fold higher maximum-tolerated dose, 2-3 fold higher biodistribution in various tissues and tumours, as well as a markedly improved anti-tumour efficacy (Kim et al., 2001). These promising *in vivo* data lead to the progression of Genexol-PM to clinical trials (Kim et al., 2004, Kim et al., 2007). A phase II trial of Genexol-PM was conducted in 69 patients with advanced NSCLC, in which a 37.7% response rate was achieved and relatively low severity and frequency of toxicities were observed even at high paclitaxel doses.

**Cyclodextrin and Cyclodextrin-containing Polymers**

Cyclodextrins are cyclic oligosaccharides with a lipophilic central cavity and a hydrophilic outer surface (Figure 1.10). They are biocompatible, exhibit low toxicity and immunogenicity in humans, have strong resistance to degradation by human enzymes (Davis and Brewster, 2004). These properties have made cyclodextrin an attractive compound for the application of drug delivery.

One important feature of cyclodextrin is the ability of its hydrophobic cavity to form host-guest complexes with hydrophobic molecules, which is largely driven by hydrogen bonding, van der Waals and charge transfer interactions and the release of water molecules from the cavity (Liu and Guo, 2002). The formation

of these inclusion complexes can greatly improve the aqueous solubility of the guest molecule, this has been shown for a wide range of hydrophobic drugs (Tiwari et al., 2010). In addition to enhanced solubility, cyclodextrin has been demonstrated to impart improved bioavailability (Uekama, 2004), lower toxicity (Nicolazzi et al., 2002), and increased stability (Ueda et al., 1998) to various drugs.

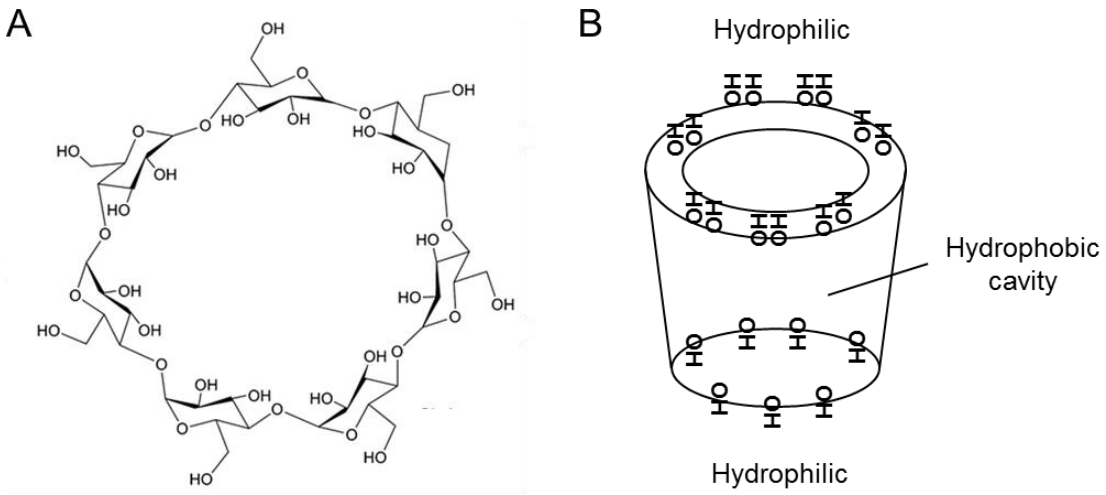


**Figure 1.10. (A)** Structure of β-cyclodextrin. **(B)** Schematic representation of the toroid structure of β-cyclodextrin. Adapted from Raju et al. (2010).

Cyclodextrins can also be incorporated into a cationic linear backbone to form cyclodextrin-containing polymers (CDPs, Figure 1.11A), which can package polyanionic cargos, such as nucleic acid therapeutics, for intracellular delivery. One prominent example of CDP-based drug delivery is the RNAi/Oligonucleotide Nanoparticle Delivery, or RONDEL platform (Heidel and Schluep, 2012). At the heart of RONDEL are CDPs which consist of 5-6

repeating units of β-cyclodextrin coupled to amidine charge centres and terminal imidazoles (Figure 1.10A). These CDPs provide several functions to the delivery system: (1) positively charged amidines enable electrostatic interactions with therapeutic siRNA cargo, (2) CDPs condense siRNAs into nanoparticles and protect them from nuclease degradation, and (3) imidazole groups utilise the proton sponge effect to promote endosomal escape.

CDPs also serve as a structural scaffold onto which additional components can be incorporated, including PEG for steric stabilisation (Bellocq et al., 2003) and immunomasking of the delivery system (Heidel et al., 2007), and Tf for preferential tumour-targeting. By coupling PEG and PEG-Tf to adamantane, a cycloalkane which forms high affinity inclusion complexes with β-cyclodextrin (Pun and Davis, 2002), the CDP-siRNA core can be non-covalently surface decorated with these ligands (Figure 1.11B). Assembled nanoparticles are 70 nm in diameter and thus benefit from EPR, and each contains approximately 10,000 CDPs, 2,000 siRNAs, 4,000 PEG-adamantanes and 100 Tf-PEG-adamatanes (Bartlett and Davis, 2007). Furthermore, the zeta potential of RONDEL particles can be adjusted from +15 mV to -25 mV through incorporation of AD-PEGs modified to contain an anionic charge (Davis, 2009).

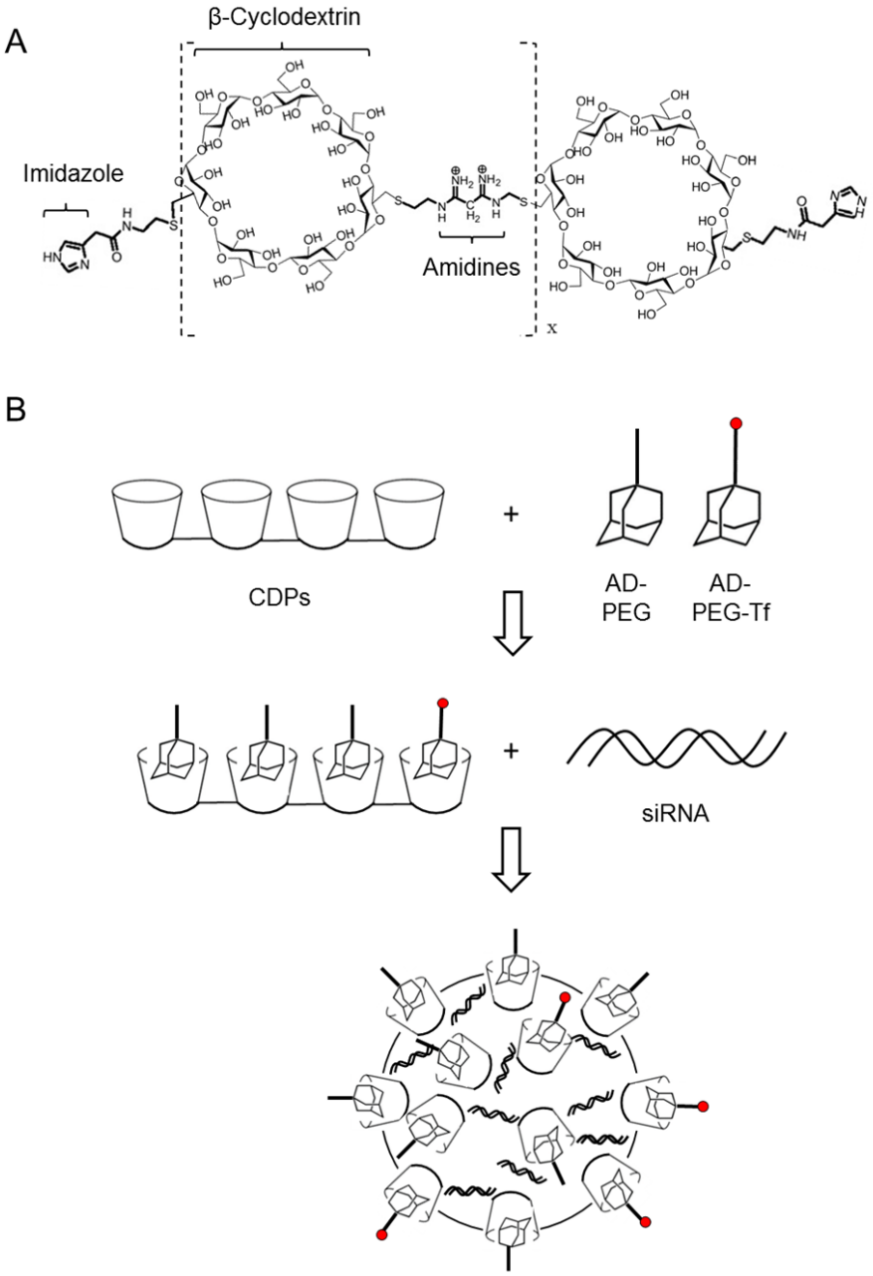


**Figure 1.11. The RONDEL siRNA delivery platform. (A)** Chemical structure of a cyclodextrin-containing polymer (CDP) composed of repeating units of β–cyclodextrin, positively charged amidine centres and terminal imidazoles. **(B)** Schematic illustrating RONDEL assembly. CDPs form high affinity inclusion complexes with adamantane (AD) coupled to PEG or PEG-Tf. Addition of siRNAs triggers compaction of the components via electrostatic interactions between amidines within CDPs and the phosphate backbone of siRNA. The resulting nanoparticle, approximately 70 nm in diameter, contains condensed siRNAs in its core and multiple PEG and PEG-Tf ligands on its exterior. Reproduced from Yan et al. (2014).

RONDEL demonstrated good efficacy when tested in a metastatic murine model of Ewing's sarcoma, in which RONDEL was used to deliver siRNAs that targeted the *EWS/Fli1* fusion oncogene, resulting in effective silencing of the oncogene and significant anti-tumour effects (Hu-Lieskovan et al., 2005). Further, good tolerability of the delivery system was shown in cynomolgus monkeys at dosages of 3 and 9 mg siRNA/kg (Heidel et al., 2007). These promising results led to the advancement of RONDEL into clinical trials. Calando Pharmaceuticals' CALAA-01, a drug candidate currently undergoing phase 1b clinical evaluation (Bouchie, 2012), utilises RONDEL to deliver systemically siRNA targeted against the M2 subunit of ribonucleotide reductase (RRM2) to solid tumours. Ribonucleotide reductase is required for DNA synthesis and is a key component in the proliferation of cancer cells (Cerqueira et al., 2007). CALAA-01 has so far demonstrated promising results in human patients with metastatic melanoma refractory to standard therapies, in which delivered siRNAs localised to tumours, and levels of RRM2 mRNA decreased in a dose-dependent manner (Davis et al., 2010).

**Virus-like particles (VLPs)**

Similar to viruses, RNAi delivery by VLPs relies on capsids for the encapsidation, nuclease protection and intracellular delivery of RNAs. However, several important distinctions exist between the two types of delivery system.

Firstly, VLP delivery utilises capsids of simple viruses, typically bacteriophages, to deliver siRNA, rather than complex, genetically-modified human viruses to deliver shRNA. Because siRNAs can directly enter the RNAi pathway and do

not require expression from a vector, the virus genome can be removed, avoiding problems associated with host genome integration, as seen in retroviral shRNA delivery. Secondly, the components of a VLP delivery system are relatively easy and cheap to prepare. Coat protein subunits that constitute capsids can be produced in large quantities and purified from recombinant *E. coli* expression systems (Mastico et al., 1993, Wu et al., 1995). *In vitro* assembly can then be performed to trigger capsid formation and package a diverse range of therapeutic cargos not limited to nucleic acids (Galaway and Stockley, 2013, Ashley et al., 2011, Wu et al., 1995, Wu et al., 2005, Brown et al., 2002, Destito et al., 2007, Stephanopoulos et al., 2010, Wu et al., 2009) (Figure 1.12). Thirdly, VLPs can be surface-modified to incorporate a range of useful ligands for immunomasking and targeting (Wu et al., 1995, Steinmetz and Manchester, 2009, Cheng et al., 2012, Galaway and Stockley, 2013). Thus, the resultant semi-synthetic particles, whilst retaining desirable viral attributes for drug delivery, exhibit enhanced functionalities.

Much research on VLP-mediated drug delivery has been based on bacteriophage MS2 (Figure 1.12) (Ashley et al., 2011, Galaway and Stockley, 2013). MS2 is a member of the *Leviviridae* family of viruses that infects *E. coli*. Its 3,569 nt ssRNA genome – one of the smallest known – was the first genome to be fully sequenced in 1976 (Fiers et al., 1976), and encodes only four proteins (Figure 1.12A), including the maturation protein (or A-protein), coat protein (CP), lysis protein and replicase protein. The MS2 capsid is a *T=3* icosahedral shell ~26 nm in diameter (Figure 1.12B, C), composed of 180 copies of the CP monomer that associate as 90 non-covalent dimers (Figure 1.12B, C) (Strauss and Sinsheimer, 1963, van Duin, 1988). Each MS2 virion

also contains one copy of the maturation protein, which is implicated in the attachment of MS2 to the F-pilus of *E. coli* and is essential for infectivity (Kozak and Nathans, 1971, Krahn et al., 1972).

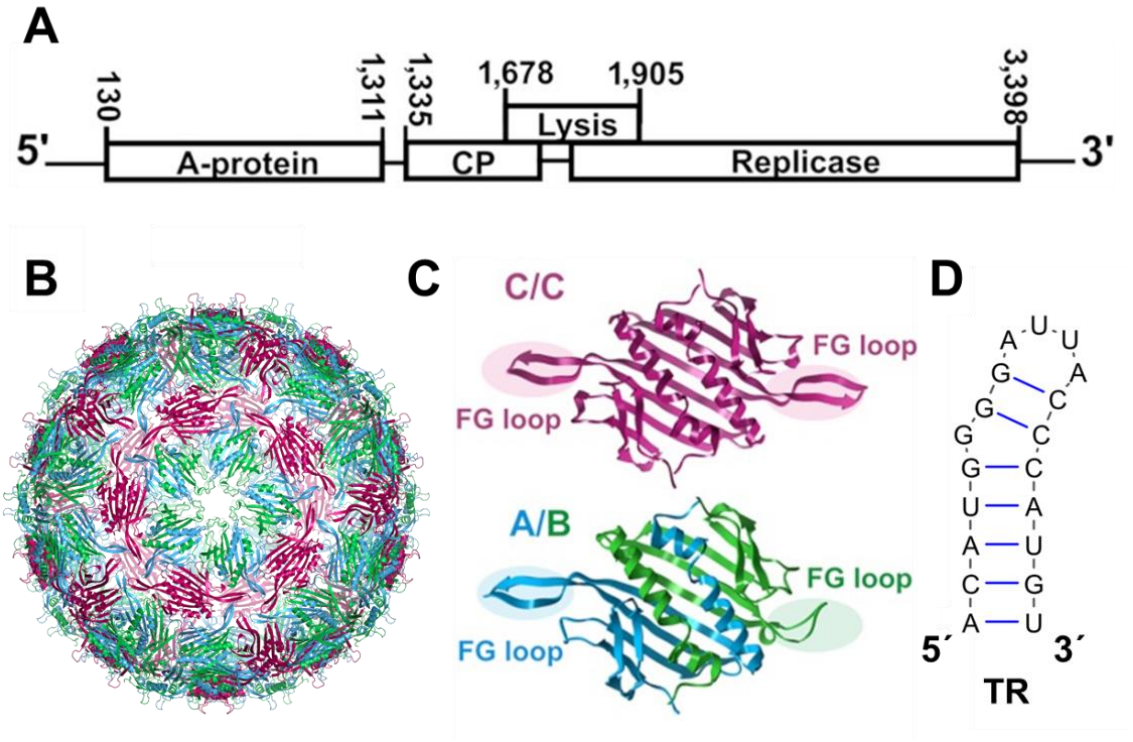


**Figure 1.12. Components of the MS2 bacteriophage. (A)** A map of the MS2 genome (GenBank: NC_001417). **(B)** Structure of the MS2 capsid (PDB: 2ms2). **(C)** Structures of the two quasi-equivalent MS2 coat protein dimers (PDB: 1zdh). Binding of TR to the symmetrical C/C-like dimer triggers a conformational switch, principally in the highlighted FG loops (which connect the F and G β-strands in each monomer), to yield an asymmetrical A/B-like dimer. Both C/C and A/B-like dimers are required for efficient MS2 capsid assembly *in vitro*. **(D)** Structure of the TR RNA stem loop, which encompasses 19 nt of the MS2 genome. Adapted from Borodavka et al. (2012).

MS2 has a positive-sense RNA genome, which can either directly serve as mRNA for translation into viral proteins, or as a template for RNA replication by the viral replicase. Secondary structures within the genome provide a

mechanism to regulate the expression of each of the four viral proteins, ensuring an appropriate number of copies are made (van Duin, 1988). For instance, the gene encoding the CP, which is required in large quantities, is highly accessible to ribosomes and can be immediately translated; whereas the translation start of the gene encoding A-protein is only transiently accessible during replication of the RNA, to limit its expression. Similarly, the start codon for the replicase gene – normally hidden within RNA secondary structure – is transiently accessible as ribosomes traverse the CP gene (Fiers et al., 1976). Lastly, the lysis protein gene is translated upon a +1 ribosomal frameshift during translation of the upstream CP gene, which occurs at a very low frequency. These frameshifted ribosomes terminate at one of two nonsense codons just before the lysis protein cistron, and subsequently initiate translation of the lysis protein gene (Kastelein et al., 1982).

MS2 viral assembly is triggered by a high affinity interaction between a CP dimer ($CP_2$) and TR (Figure 1.12D), a 19 nt stem loop encompassing the start codon of the replicase gene that acts as a packaging signal. TR binding prevents further translation of the replicase gene, and results in a conformational change in the $CP_2$, from a symmetrical C/C-like conformation to an asymmetrical A/B-like conformation (Figure 1.12C) (Stockley et al., 2007). This conformational switch is required for the efficient assembly of MS2 *T=3* capsids (Rolfsson et al., 2008, Stockley et al., 2007), which comprise of 30 C/C-like and 60 A/B-like $CP_2$. There is a growing body of evidence supporting the presence of multiple packaging signals within numerous viral genomes, which facilitate their efficient and high-fidelity packaging into assembling capsids (Bunka et al., 2011, Qin et al., 2003, Goto et al., 2013, Qu and Morris, 1997).

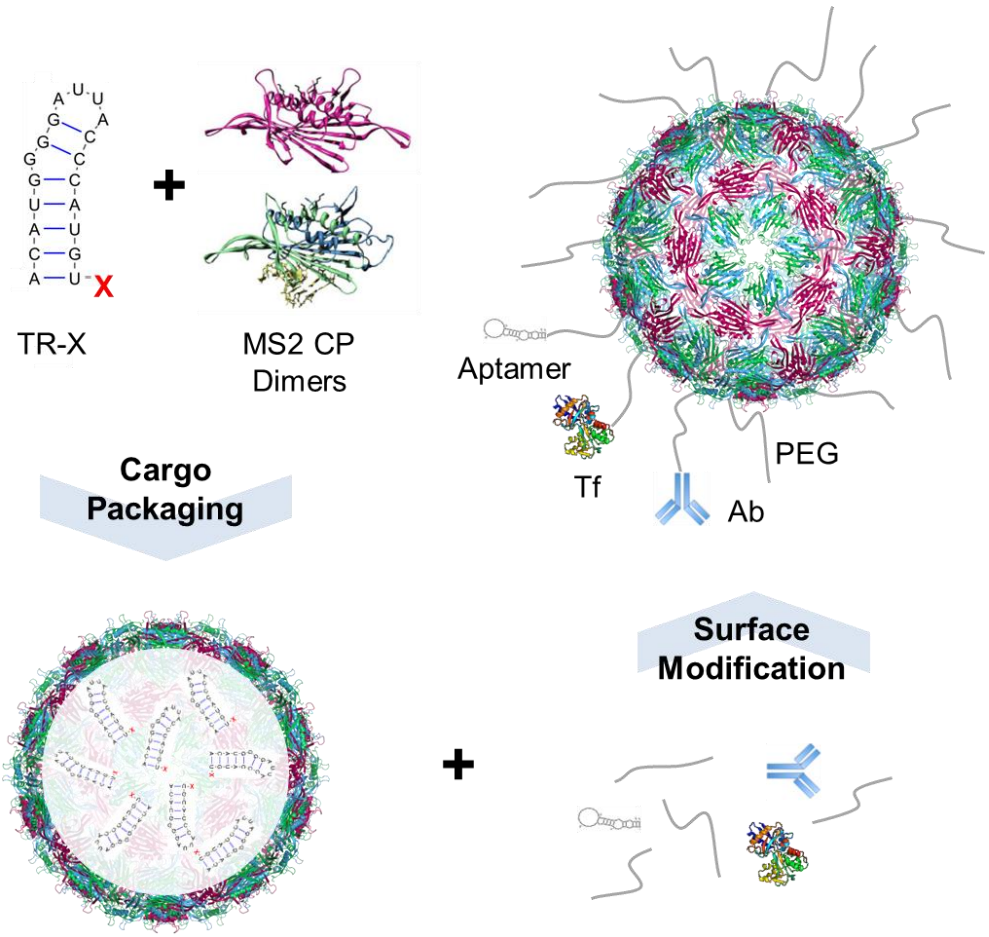


**Figure 1.13. Construction of an MS2 VLP-based drug delivery system.** VLPs can be assembled *in vitro* by mixing $CP_2$ with TR at neutral pH. Drug cargos (X) conjugated to TR can be packaged inside VLPs during assembly. The VLP surface can then be chemically modified to display ligands for immunomasking, endosomal escape or tumour targeting. Examples presented include PEG, a nucleic acid aptamer, Tf and an antibody (Ab). These are not drawn to scale.

MS2 VLPs offer many advantages as a drug delivery system, including (i) they are extremely well-characterised, (ii) the MS2 CP can be recombinantly expressed in large quantities in *E. coli*, (iii) VLPs can be efficiently assembled *in vitro* by mixing dissociated $CP_2$ with TR oligonucleotides at neutral pH; any cargo attached to TR can be packaged inside during assembly (Figure 1.13),

(iv) VLPs are pH-sensitive and can disassemble in the acidic environment of the endosome, thus facilitating drug release, (V) with a diameter of 26 nm, MS2 VLPs fully benefit from EPR, (vi) VLPs have a zeta potential of -25 mV (Pang et al., 2009) and therefore are unlikely to have strong electrostatic interactions with cells; this may also be adjusted via surface modifications if required, and (vii) abundant amines are present on the VLP surface (Figure 1.14) to facilitate multivalent display of useful ligands (Figure 1.13).

Initial work on MS2 VLP-mediated drug delivery began in the Stockley laboratory in the 1990s. TR-conjugated ricin A chain (RAC) was packaged into VLPs during *in vitro* assembly, before Tf was attached to the VLP surface as a tumour-targeting ligand (Wu et al., 1995). RAC is the ribosome-inactivating component of ricin, though its cytotoxicity is limited without the B chain which is required for cellular uptake. VLP(RAC)-Tf successfully delivered RAC to HL-60 promyelocytic leukemia and HeLa cervical cancer cells via Tf receptor-mediated endocytosis, and induced significant levels of cell death with an $LD_{50}$ in the sub nM range (Wu et al., 1995). Other combinations of drugs and targeting ligands were subsequently tested, including the use of the nucleoside analogue, 5-fluorouridine, as the therapeutic cargo and antibodies targeting DF3, a breast cancer marker, as the tumour-targeting ligand (Brown et al., 2002). The resulting VLP particles delivered 5-fluorouridine to ZR-75-1 breast carcinoma cells, and enhanced its cytotoxic effects compared to free 5-fluorouridine. In 2005, VLP-Tf was used to deliver an antisense oligodeoxynucleotide (ODN) to leukemia and bladder cancer cell lines (Wu et al., 2005). The ODN targeted the mRNA encoding P120, a proliferation-linked nucleolar protein overexpressed in

many human tumours. When delivered by VLP-Tf, the ODN induced 8-fold enhanced cytotoxicity in Tf-targeted cancer cells compared to the free ODN.

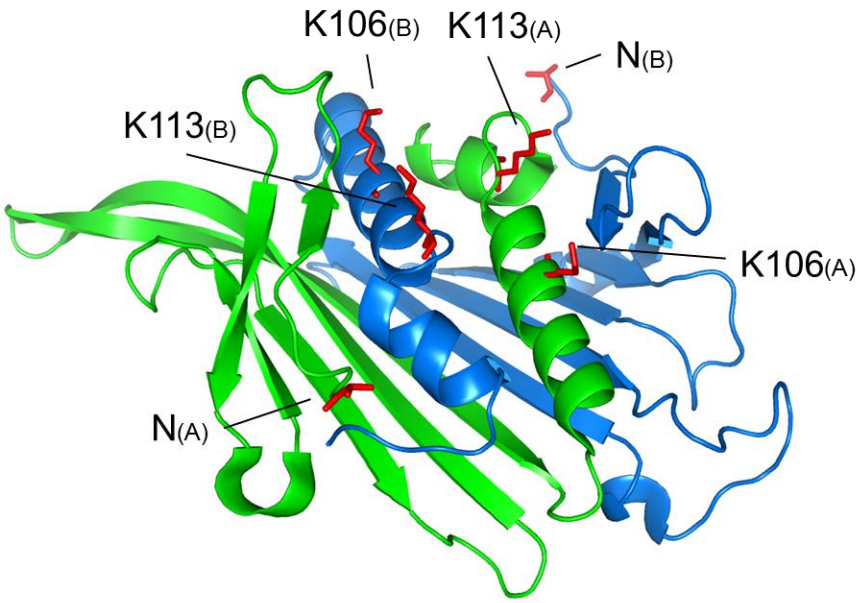


**Figure 1.14. Amine groups exposed on the VLP surface.** Ribbon diagram of an A/B-like MS2 $CP_2$ (A subunit in green, B in blue) is shown. Each monomer consists of three amines (highlighted in red) which are exposed on the surface of assembled VLPs, two present on lysine side chains (K106, K113) and one present at the N-terminus. Therefore, 540 amines are displayed on the surface of each VLP. These amines facilitate N-hydroxysuccinimide (NHS)-based chemistry, which can be used to modify the VLP surface with a range of useful ligands. The same amine groups are also present on C/C-like dimers, which are not shown.

More recently, VLP-Tf was used to deliver therapeutic siRNAs targeted against the mRNA of the apoptotic factor BCL2, and PLK1 (Galaway, 2011, Galaway and Stockley, 2013). The siRNAs were chosen as they were previously demonstrated to retain their function despite being covalently attached to an RNA aptamer (McNamara et al., 2006), and thus should tolerate TR coupling to facilitate their packaging inside VLPs. VLP-Tf successfully delivered the siRNAs

to HeLa cells in a Tf receptor-dependent manner, produced knockdown of the targeted mRNAs and their protein products, and induced significant cytotoxicity at sub nM siRNA concentrations (Galaway, 2011, Galaway and Stockley, 2013).

One potential problem which emerged from these studies was the cellular uptake of unmodified VLPs, possibly due to the presence of VLP surface epitopes that interact with the cell surface and allow internalisation (Wu et al., 1995, Brown et al., 2002, Wu et al., 2005, Galaway, 2011). Although surface modification with Tf improved uptake via Tf receptor-mediated endocytosis, some level of non-specific uptake was still evident – shown through inhibition assays in which high concentrations of free Tf only partially reduced VLP-Tf uptake (Galaway, 2011, Galaway and Stockley, 2013). It was hypothesised that, due to the relatively low levels of surface modification (~15.2 Tf per VLP) (Galaway, 2011) and the lack of control over their spatial distribution, there might be 'naked' regions on the VLP surface with exposed epitopes that allow non-specific uptake. Non-specific uptake is a highly undesirable feature for drug delivery systems, and can severely limit their effectiveness *in vivo* (Peer et al., 2007). High levels of uptake by healthy cells can induce dose-limiting side effects, and also reduce the amount of drugs taken up by cancer cells, thus increasing the effective dosage. Furthermore, prolonged exposure of cancer cells to low levels of drugs can facilitate the development of drug resistance (Holohan et al., 2013). Ultimately, these effects can significantly limit the therapeutic window and efficacy of delivered drugs, therefore non-specific uptake is an important issue that needs to be addressed for the MS2 VLP drug delivery system.

Other groups have since also contributed to the development of this drug delivery system. In 2011, the Peabody group reported the use of MS2 VLPs for the targeted delivery of cargos to hepatocellular carcinoma (HCC) cells (Ashley et al., 2011). A cocktail of siRNAs targeting the mRNA of several cyclins, whose overexpression is associated with hepatocarcinogenesis (Masaki et al., 2003), were packaged inside MS2 VLPs. The VLP surface was then decorated with (i) PEG for immunomasking, (ii) SP94, a targeting peptide previously identified by affinity selection from a phage display library against HCC cell surface targets (Lo et al., 2008), and (iii) a histidine-rich peptide to promote endosomal escape. Gene silencing of targeted cyclins, growth arrest and apoptosis were observed at pM siRNA concentrations in HCC cells, but not in normal hepatocyte cells. Additionally, these VLPs have successfully delivered other cargos, including quantum dots, and a drug cocktail containing doxorubicin, cisplatin and 5-fluorouracil to SP94-targeted HCC cells, selectively killing them at drug concentrations <1 nM (Ashley et al., 2011). This highlighted the potential of MS2 VLPs to facilitate combinatorial therapy, delivering multiple drugs which may demonstrate good synergy *in vitro*, but are severely limited by their different pharmacokinetics and biodistribution *in vivo*.

Preliminary *in vivo* testing of MS2 VLP drug delivery has been carried out by the Wang group (Pan et al., 2012a, Pan et al., 2012b, Li et al., 2013). MS2 VLPs packaging a pre-miRNA, pre-miR146a, were surface-decorated with HIV Tat peptides for cell penetration; no cell-targeting ligands were used. Upon intravenous administration in mice, VLP(pre-miR146a)-Tat particles displayed widespread biodistribution in the plasma, lung, spleen and kidney, where high levels of mature miR146a were detected and knockdown of known targets of

miR146a was observed (Pan et al., 2012b). Systemic lupus erythematosus is an autoimmune disease characterised by the production of pathogenic autoantibodies. Administration of MS2 VLP-delivered miR146a, which is known to act as an inhibitor of autoimmunity and cancer, to lupus-prone mice significantly reduced the expression of autoantibodies and total IgG (Pan et al., 2012a). More recently, MS2 VLPs were adapted for the delivery of mRNA vaccines, which successfully protected mice from prostate cancer, and delayed tumour growth in prostate cancer mice models (Li et al., 2013). Importantly, no off-target toxicities were observed in VLP-treated mice in these studies.

VLPs based on other viruses have also been explored for the delivery of diagnostic or therapeutic agents. It has been reported that VLPs of the cowpea mosaic virus (CPMV) display natural tumour targeting via vimentin (Steinmetz et al., 2011), a type III intermediate filament associated with tumour growth and invasiveness, which is overexpressed on endothelial cells in tumour tissue (van Beijnum et al., 2006). The cellular uptake of fluorescently-labelled CPMV VLPs correlated positively with vimentin expression in four different cancer cell lines; successful targeting was also demonstrated using human tumour xenografts (Steinmetz et al., 2011).

Recently, a non-covalent infusion technique has been utilised to stably package fluorescent and therapeutic cargos which have an affinity for nucleic acids, including 4',6-diamidino-2-phenylindole (DAPI), propidium iodide, acridine orange and proflavin, inside RNA-encapsidated CPMV VLPs (Yildiz et al., 2013). The vimentin-targeted uptake of dye-loaded VLPs by HeLa, HT-29 and PC-3 cancer cells was visualised. VLPs loaded with proflavin, a bacteriostatic agent with known anti-proliferative activity in tumours, demonstrated

comparable $IC_{50}$ to the free drug in the three cancer cell lines; empty CPMV VLPs did not produce an effect on cell viability, indicating the absence of off-target cytotoxicity.

Filamentous VLPs of another plant virus, the Potato virus X, have also been tested as a delivery system. These VLPs exhibited notably enhanced tissue penetration and tumour homing properties compared to the spherical CPMV VLPs (Shukla et al., 2013). This study highlighted the potential of exploiting the shapes of VLPs to achieve better delivery efficiencies.

## 1.4 Summary and aims

More than a century after Ehrlich established the foundations of chemotherapy, several generations worth of effort have failed to fulfil his vision of a magic bullet therapeutic – a *chemotherapia specifica*. One current focus in cancer therapy is the development of nanoparticulate drug delivery systems, which have been shown to improve many aspects of traditional and novel chemotherapeutics; some formulations have already received FDA approval and many more are emerging from laboratories and clinical trials. Despite these advancements, there is a need for more targeted approaches to drug delivery, to enhance tumour selectivity and drug efficacy.

The aim of this project was to build upon a targeted drug delivery system based on MS2 VLPs previously established in the Stockley laboratory. Specific goals were to: (i) mitigate non-specific cellular uptake of VLPs, (ii) test a relatively novel class of targeting ligands, nucleic acid aptamers, to promote tumour-

specific uptake, and (iii) incorporate different drug cargos inside VLPs for delivery.

Chapter 3 explores whether the incorporation of a layer of PEG to the MS2 VLP surface can reduce non-specific cellular uptake. The synthesis and analysis of VLPs surface modified with $PEG_{24}$ (VLP-$PEG_{24}$), or $PEG_{24}$ and Tf (VLP-$PEG_{24}$-Tf), are described. Using HeLa cells, the uptake of VLP, VLP-$PEG_{24}$ and VLP-$PEG_{24}$-Tf are compared. Finally, the cellular effects of siRNA delivery by VLP-$PEG_{24}$-Tf are assessed.

In Chapter 4, the RNA aptamer, A9L, is tested for use as a targeting ligand in the MS2 VLP drug delivery system. A9L specifically binds the prostate cancer marker, PSMA, and allows internalisation into PSMA-expressing prostate cancer cells. The construction and analysis of VLP-$PEG_{24}$-A9L is described. Using two prostate cancer cell lines, $PSMA_{+ve}$ LNCaP and $PSMA_{-ve}$ PC-3, the cellular effects of siRNA delivery by VLP-$PEG_{24}$-A9L are assessed.

Chapter 5 describes the testing of the anthracycline chemotherapeutic, doxorubicin (Dox), as a drug cargo for targeted delivery by VLP-$PEG_{24}$-A9L. The packaging of Dox inside TR-Cy5 encapsidated VLPs is described. The uptake and cytotoxic effects of VLP-$PEG_{24}$-A9L delivered Dox are assessed in LNCaP, PC-3 and HeLa cells.

**This page is intentionally blank**

# Chapter 2

Materials and Methods

# 2.1 Materials

### 2.1.1 General reagents

All chemicals were purchased from Sigma-Aldrich (Gillingham, UK), unless otherwise stated. DEPC-treated water was purchased from Severn Biotech (Kidderminster, UK). Protease/Phosphatase Inhibitor Cocktail (100X) was purchased from Cell Signalling Technology (Leiden, Netherlands). Amicon Ultra 0.5 mL 100 kDa molecular weight cut-off (MWCO) spin concentrators were purchased from Millipore (Feltham, UK).

### 2.1.2 Reagents for the synthesis of surface-modified VLPs

Crosslinking reagents

N-succinimidyl S-acetylthioacetate (SATA) and sulfosuccinimidyl-4-(N-maleimidomethyl)cyclohexane-1-carboxylate (sulfo-SMCC) were purchased from Pierce (Paisley, UK). $SM(PEG)_{24}$ was from Fisher Scientific (Loughborough, UK). EZ-Link NHS-$PEG_{12}$-biotin was purchased from Thermo Scientific (Hemel Hempstead, UK).

Protein

Recombinant human holo-Tf was purchased from Alpha laboratories (Eastleigh, UK).

Nucleic acids

A9L-thiol RNA aptamers were purchased from DNA Technology (Risskov, Denmark). Other RNAs were synthesised at the University of Leeds (with the help of Amy Barker). Syntheses were carried out on an ABI Model 394 DNA

Synthesizer, using UltraMILD reagents purchased from Link Technologies (Bellshill, UK).

| RNA | Sequence (5′->3′) | Modifications | Target |
|---|---|---|---|
| TR | ACAUGAGGAUUACCCAUGU | Cy5 (5′) | - |
| TR-Bcl2 sense | TR-AAAAGUGAAGUCAACAUGCCUGCUU | Cy5 (5′) | - |
| Bcl2 antisense | GCAGGCAUGUUGACUUCACUU | Cy5 (5′) | *BCL2* mRNA |
| TR-Control sense | TR-AAAAUUCUCCGAACGUGUCACGUUU | Cy5 (5′) | - |
| Control antisense | ACGUGACACGUUCGGAGAAUU | Cy5 (5′) | - |
| U6 | UUUUUU | 6-FAM (5′), Thiol-C3 (3′) | - |
| A9L | GGGCCGAAAAAGACCUGACUUCUAUACUAAGUCUACGUCCC | Thiol-C3 (3′) | PSMA |

**Table 2.1. List of RNA oligonucleotides used along with their sequences, modifications, and molecular targets (where relevant).**

### 2.1.3 Biochemical assay reagents

Gel filtration chromatography

The Superose 6 10/300 GL size exclusion column, and Sephadex G25 NAP-5, NAP-10 and NAP-25 columns were purchased from GE Healthcare (Chalfont St Giles, UK).

Gel electrophoresis

Fermentas PageRuler Plus Prestained Protein Ladder was purchased from Thermo Scientific. 10 bp DNA Step Ladder was from Promega (Southampton, UK). Hyperladder I was from Bioline (London, UK). Ethidium bromide was from Severn Biotech.

Western blotting

The anti-MS2 CP antibody was purchased from Millipore. The anti-PSMA antibody was purchased from Abgent Europe Ltd (Maidenhead, UK). Enhanced chemiluminescent Western blotting substrate was purchased from Amersham (Amersham, UK). Nitrocellulose membrane was purchased from Whatman (Little Chalfont, UK). Dried milk powder was from Marvel (St. Albans, UK).

Transmission electron microscopy (TEM)

Ultra-thin carbon coated copper grids were from Agar Scientific (Stansted, UK). Uranyl acetate in pH 4.0 water was provided by Martin Fuller at the University of Leeds.

### 2.1.4 Cell biology reagents

Cell culture

HeLa cervical cancer cells were purchased from ATCC (Manassas, VA, USA) (Galaway, 2011). The prostate cancer cell lines, LNCaP and PC-3, were a gift from Prof. Norman Maitland at the University of York. Dulbecco's Phosphate Buffered Saline (DPBS), Dulbecco's Modified Eagles Medium (DMEM), poly-L-lysine hydrobromide, human serum type AB from male plasma, T75 flasks, and

6 well and 24 well plates were purchased from Sigma-Aldrich. Foetal Bovine Serum (FBS), Penicillin Streptomycin (Pen Strep), Ham's F-12K medium, RPMI-1640 medium, and TrypLE Express were from Life Technologies (Paisley, UK). HiPerFect Transfection Reagent was purchased from Qiagen (Manchester, UK).

Fluorescent dyes

Propidium iodide, FITC-labelled Annexin V and 4,6-diamino-2-phenylindole (DAPI) were purchased from Life Technologies.

| Fluorescent dye | Excitation max (nm) | Emission max (nm) |
|---|---|---|
| DAPI | 358 | 463 |
| FITC | 495 | 517 |
| Fluorescein | 495 | 517 |
| Propidium iodide | 538 | 617 |
| Cyanine 3 | 549 | 562 |
| Cyanine 5 | 646 | 664 |

**Table 2.2. List of fluorescent dyes used, along with their spectral properties.**

Antibodies

FITC-labelled anti-human BCL2 antibody and FITC-labelled isotype control antibody were purchased from BD Biosciences (Oxford, UK). The anti-PSMA antibody was from Abgent Europe Ltd.

### 2.1.5 Buffers

Buffers were prepared with $_{dd}H_2O$ and filter sterilised (0.2 µm filtration).

For the purification of MS2 VLPs:

- λ buffer: 10 mM HEPES, 100 mM NaCl, 1 mM EDTA, adjusted to pH 7.2 with NaOH,
- Ω buffer: 50 mM HEPES, 100 mM NaCl, 10 mM dithiothreitol, 5 mM EDTA, adjusted to pH 7.2 with NaOH.

For the surface modification of MS2 VLPs:

- HEPES buffer: 50 mM HEPES, 100 mM NaCl, adjusted to desired pH with NaOH,
- Iron(III) citrate buffer: 10 mM iron(III) citrate, 200 mM citric acid, adjusted to pH 7.8 with sodium bicarbonate.

For biochemical assays:

- Laemmli loading buffer (2x): 125 mM Tris base, 20% (v/v) glycerol, 4% (w/v) SDS, 10% (v/v) β-mercaptoethanol, 0.02% (w/v) bromophenol blue, adjusted to pH 6.8 with HCl,
- SDS-PAGE Running buffer (10x): 248 mM Tris base, 1.92 M glycine, 1% (w/v) SDS,
- SDS-PAGE Resolving buffer: 1.5 M Tris base, 0.4% (w/v) SDS, adjusted to pH 8.8 with HCl,
- SDS-PAGE Stacking buffer: 0.5 M Tris base, 0.4% (w/v) SDS, adjusted to pH 6.8 with HCl,

- Western blotting transfer buffer: 25 mM Tris base, 190 mM glycine, 0.1% (w/v) SDS, 20% (v/v) methanol,
- Tris-buffered saline (TBS): 50 mM Tris base, 150 mM NaCl, adjusted to pH 7.5 with HCl,
- TBS Tween (TBST): TBS with 0.1% (v/v) Tween,
- BLOCK (5x): TBS with 3.75% (w/v) milk powder,
- TBE: 89 mM Tris base, 89 mM boric acid, 2 mM EDTA, adjusted to pH 8.0 with NaOH.

For cell biology assays:

- Annexin binding buffer: 100 mM HEPES, 1.4 M NaCl, 25 mM $CaCl_2$, adjusted to pH 7.5 with NaOH,
- DPBS/FBS: DPBS with 4% (v/v) FBS,
- DPBS Tween (DPBST): DPBS with 0.1% (v/v) Tween,
- FIX: DPBS with 1% (w/v) paraformaldehyde,
- Permeabilisation buffer: DPBS with 1% (v/v) Triton X-100, 4% (v/v) FBS and 2.5 mM EDTA,
- PSMA Binding buffer: 20 mM HEPES, 150 mM NaCl, 2 mM $CaCl_2$, 0.01% (w/v) BSA, pH 7.4.

## 2.2 Methods

### 2.2.1 Preparation and modification of VLPs

Annealing and purification of TR-siRNAs

Double-stranded siRNAs were prepared by mixing the TR-sense strand (10 µM) and the anti-sense strand (10 µM) in DEPC-treated water. The mixture was briefly heated to 95$^{o}$C, and was allowed to cool to room temperature. The annealing reaction was analysed by gel electrophoresis on a native 15% (w/v) polyacrylamide gel, visualised by ethidium bromide staining and by fluorescence scanning on a Fujifilm FLA-5000. The band corresponding to annealed TR-siRNA was excised, from which the RNA was extracted via electro-elution (80 V for 60 min). The TR-siRNA was then concentrated by isopropanol precipitation, and resuspended in DEPC-treated water.

Purification of MS2 VLPs

Recombinant MS2 VLPs were previously expressed in *E. coli* in the Stockley laboratory, stored as a frozen cell paste. The cell paste was resuspended at room temperature in Ω buffer, and lysed via sonication, with a pulse sequence of 10 on, 10 off for 3 cycles. The cell lysate was centrifuged at 10,000 RCF for 30 min at 4$^{o}$C. The VLP-containing supernatant was collected, treated with DNase I (10 µg.mL$^{-1}$) for 1 h at room temperature, and then centrifuged again at 10,000 RCF for 30 min at 4$^{o}$C. The supernatant was collected, to which ammonium sulfate was slowly added to reach 60% saturation, before it was centrifuged at 10,000 RCF for 30 min at 4$^{o}$C. The precipitate was resuspended in λ buffer, and centrifuged through a 15-45% (w/v) linear sucrose density gradient at 47,000 RCF, 4$^{o}$C for 17 h. Fractions were collected and analysed by

SDS-PAGE to check for MS2 CP content. Fractions containing MS2 CPs (hence VLPs) were pooled, ammonium sulfate precipitated, and purified through a second round of sucrose density gradient centrifugation as before. Pure MS2 VLP-containing fractions were pooled and stored at 4$^{o}$C.

Preparation of MS2 $CP_2$

Purified MS2 VLPs were concentrated using a 100 kDa MWCO spin concentrator, into pH 7.3 HEPES buffer. Concentrated VLPs were dissociated by diluting 1:3 in glacial acetic acid for 1 h at 4$^{o}$C, before brief centrifugation to pellet precipitated nucleic acid material. The supernatant was eluted into 20 mM acetic acid using a Sephadex G-25 NAP-10 column; fractions were collected and analysed by UV spectroscopy and SDS-PAGE for CP content. Fractions with an $A_{260}/A_{280}$ ratio of ≤ 0.8 were considered to contain sufficiently pure $CP_2$; these were pooled, and the concentration was estimated using $\varepsilon_{280nm}$ = 33,240 $M^{-1}.cm^{-1}$. When stored in 20 mM acetic acid at 4$^{o}$C, $CP_2$ remain stable and assembly competent for up to 2 months.

VLP assembly and cargo packaging

Trial experiments to establish optimal reassembly and packaging conditions were performed in 10 µL volumes. Acid dissociated $CP_2$ were mixed with TR-Cy5 at molar ratios of 1:1, 2:1, 10:1, 15:1, 25:1 and 50:1 in pH 7.3 HEPES buffer at room temperature for 5 h. A 10 µM $CP_2$-only control was also used. The concentration of TR-Cy5 was fixed at 1 µM, and that of $CP_2$ varied accordingly. The assembly reactions were then analysed by TEM and native 2% (w/v) agarose gel electrophoresis. The agarose gel was run in TBE buffer at 90 V for 90 min, and then visualised by ethidium bromide and Coomassie

Brilliant Blue R-250 staining. Larger scale assemblies were carried out in 1 mL volumes, in which acid dissociated $CP_2$ (10 µM) were mixed with TR-X (1 µM) in pH 7.3 HEPES buffer at room temperature for 5 h, before the mixture was incubated at 4$^{o}$C overnight. The reactions were analysed by TEM, size exclusion chromatography and native 2% (w/v) agarose gel electrophoresis. Assembled VLPs were concentrated and buffer exchanged into pH 8.3 HEPES using 100 kDa MWCO spin concentrators, then stored at 4$^{o}$C.

Quantification of siRNA and CP content in RNA encapsidated VLPs

To determine the concentration of Cy5-labelled TR or TR-siRNA encapsidated inside VLPs, the Cy5 fluorescence was measured at 649 nm using a Nanodrop 1000 ($\varepsilon_{649nm}$ Cy5 = 250,000 $M^{-1}.cm^{-1}$). To estimate the protein content, the absorbance at 260 nm and 280 nm were measured using a Nanodrop 1000 and the following formula was used (Groves et al., 1968):

$$1.55 \times A_{280} - 0.76 \times A_{260} = [\text{Proteins}]\ (mg.mL^{-1})$$

From this, the concentration of $CP_2$ was calculated using:

$$M_w\ (CP_2) = 27{,}800\ g.mol^{-1}.$$

Synthesis of VLP-Tf

In a 1 mL reaction in pH 8.3 HEPES, TR-Cy5 encapsidated VLPs (333 nM) were reacted with SATA (166.5 µM) at room temperature for 1 h. To deacetylate SATA-modified VLPs, hydroxylamine-HCl (50 $mg.mL^{-1}$ in 100 µL pH 8.3 HEPES) was added to the mixture, and left to react at room temperature for 1 h.

In a separate 1 mL reaction in pH 8.3 HEPES, human apo-Tf (10 µM) was reacted with sulfo-SMCC (1 mM) at room temperature for 1 h. The two reaction mixtures were separately eluted from NAP-25 columns into pH 7.3 HEPES, mixed at room temperature for 2 h, then at 4$^{o}$C overnight. Apo-Tf in the solution was converted to holo-Tf by the addition of 5 µL iron(III) citrate buffer. The mixture was purified by size exclusion chromatography on a Superose 6 10/300 column, equilibrated and eluted with DPBS at a flow rate of 1 mL.min$^{-1}$. The absorbance at 260 nm, 280 nm and 465 nm were monitored and recorded using the ÄKTA FPLC system (GE healthcare). The fraction containing VLP-Tf was collected and concentrated using 100 kDa MWCO spin concentrators into DPBS. VLP-Tf was analysed by size exclusion chromatography, TEM, Western blotting and native 2% (w/v) agarose gel electrophoresis.

Synthesis of VLP-PEG$_{12}$-biotin

In a 200 µL reaction in pH 8.3 HEPES, TR-Cy5 encapsidated VLPs (55.56 nM) were mixed with EZ-Link NHS-PEG$_{12}$-biotin (0.5 mM) at room temperature for 30 min. The mixture was eluted through a NAP-5 column into DPBS – fractions were collected and checked for $A_{260}$, $A_{280}$ and $A_{649}$ using a Nanodrop 1000, those containing VLP-PEG$_{12}$-biotin were pooled and concentrated using a 100 kDa MWCO spin concentrator. VLP-PEG$_{12}$-biotin was then analysed by SDS-PAGE, TEM and native 2% (w/v) agarose gel electrophoresis to confirm successful conjugation and the intact nature of particles.

Synthesis of VLP-PEG$_{24}$

In a 200 µL reaction in pH 8.3 HEPES, TR-X encapsidated VLPs (55.56 nM) were mixed with SM(PEG)$_{24}$ (0.3 mM, 3 mM, 15 mM, 30 mM, or 60 mM) at

room temperature for 30 min. The SM(PEG)$_{24}$ to VLP surface amine molar ratio was 10, 100, 500, 1000 or 2000 to 1, respectively. The mixture was eluted through a NAP-5 column into pH 7.3 HEPES. Fractions were collected and checked for $A_{260}$, $A_{280}$ and $A_{649}$ using a Nanodrop 1000. Those containing VLP-PEG$_{24}$-maleimide were pooled. To quench unreacted maleimide groups, β-mercaptoethanol (7 µL of 14.3 M stock) was added to VLP-PEG$_{24}$-maleimide, and left to react at room temperature overnight. Quenched VLP-PEG$_{24}$ was eluted through a NAP-5 column into DPBS and concentrated using a 100 kDa MWCO spin concentrator. VLP-PEG$_{24}$ was then analysed by SDS-PAGE, TEM, linear 15-45% (w/v) sucrose density gradient centrifugation, size exclusion chromatography and native 2% (w/v) agarose gel electrophoresis to confirm successful conjugation and the intact nature of particles.

Synthesis of VLP-PEG$_{24}$-Tf

In a 200 µL reaction in pH 8.3 HEPES, Tf (1.67 µM) was mixed with SATA (1.4 mM) at room temperature for 30 min. To deacetylate SATA-modified Tf, hydroxylamine-HCl (50 mg.mL$^{-1}$ in 50 µL pH 8.3 HEPES) was added to the mixture, and left to react at room temperature for 1 h. In a separate 200 µL reaction in pH 8.3 HEPES, TR-X encapsidated VLPs (55.56 nM) were mixed with SM(PEG)$_{24}$ (15 mM) at room temperature for 30 min. The SM(PEG)$_{24}$ to VLP surface amine molar ratio was 500 to 1. The two reaction mixtures were separately eluted from NAP-5 columns into pH 7.3 HEPES, fractions were collected and checked for $A_{260}$, $A_{280}$ and $A_{649}$ using a Nanodrop 1000, those containing Tf and VLP-PEG$_{24}$-maleimide were pooled, and mixed together at room temperature for 2 h. β-mercaptoethanol (7 µL of 14.3 M stock) and iron(III) citrate buffer (5 µL) were added to VLP-PEG$_{24}$-Tf to quench unreacted

maleimide groups and to convert apo-Tf to holo-Tf, respectively. The mixture was allowed to react at room temperature overnight.

Quenched VLP-$PEG_{24}$-Tf was purified by linear 15-45% (w/v) sucrose density gradient centrifugation. The fraction containing VLP-$PEG_{24}$-Tf was collected, and then concentrated using a 100 kDa MWCO spin concentrator. VLP-$PEG_{24}$-Tf was analysed by Western blotting, TEM, size exclusion chromatography and native 2% (w/v) agarose gel electrophoresis to confirm successful conjugation and the intact nature of particles.

Synthesis of VLP-$PEG_{24}$-U6-FAM

In a 100 µL reaction in pH 7.3 HEPES, U6-FAM (8.33 µM) was mixed with TCEP (20 mM) at 70$^{o}$C for 2 min, and then at room temperature for 2 h. In a separate 200 µL reaction in pH 8.3 HEPES, TR-Cy5 encapsidated VLPs (55.56 nM) were mixed with $SM(PEG)_{24}$ (15 mM) at room temperature for 30 min. The $SM(PEG)_{24}$ to VLP surface amine molar ratio was 500 to 1. The two reaction mixtures were separately eluted from NAP-5 columns into pH 7.3 HEPES, fractions were collected and checked for $A_{260}$, $A_{280}$, $A_{494}$ and $A_{649}$, using a Nanodrop 1000, those containing U6-FAM and VLP-$PEG_{24}$-maleimide were pooled, and mixed together at room temperature for 2 h, to allow conjugation. To quench unreacted maleimide groups, β-mercaptoethanol (7 µL of 14.3 M stock) was added to VLP-$PEG_{24}$-U6-FAM, and left to react at room temperature overnight. Quenched VLP-$PEG_{24}$-U6-FAM was eluted through a NAP-25 column, and concentrated into DPBS using a 100 kDa MWCO spin concentrator. VLP-$PEG_{24}$-U6-FAM was then analysed by UV-visible spectroscopy, SDS-PAGE, and native 2% (w/v) agarose gel electrophoresis to confirm successful conjugation.

Synthesis of VLP-$PEG_{24}$-A9L

In a 100 µL reaction in pH 7.3 HEPES, A9L (8.33 µM) was mixed with TCEP (20 mM) at 70$^{o}$C for 2 min, and then at room temperature for 2 h. In a separate 200 µL reaction in pH 8.3 HEPES, TR-X encapsidated VLPs (55.56 nM) were mixed with $SM(PEG)_{24}$ (15 mM) at room temperature for 30 min. The $SM(PEG)_{24}$ to VLP surface amine molar ratio was 500 to 1. The two reaction mixtures were separately eluted from NAP-5 columns into pH 7.3 HEPES, fractions were collected and checked for $A_{260}$, $A_{280}$ and $A_{649}$ using a Nanodrop 1000, those containing A9L-SH and VLP-$PEG_{24}$-maleimide were pooled, and mixed together at room temperature for 2 h. To quench unreacted maleimide groups, β-mercaptoethanol (7 µL of 14.3 M stock) was added to VLP-$PEG_{24}$-A9L, and left to react at room temperature overnight. Quenched VLP-$PEG_{24}$-A9L was eluted through a NAP-25 column, and concentrated into DPBS using a 100 kDa MWCO spin concentrator. VLP-$PEG_{24}$-A9L was then analysed by TEM and native 2% (w/v) agarose gel electrophoresis to confirm successful conjugation and the intact nature of particles.

Doxorubicin spectroscopic analysis

Doxorubicin in $_{dd}H_2O$ was analysed by UV spectroscopy to determine the wavelength of maximum absorbance (486 nm). Using this, the absorbance of varying concentrations of doxorubicin was measured to construct a calibration graph, from which the extinction coefficient was calculated. This facilitated the quantification of doxorubicin in downstream packaging experiments.

Doxorubicin packaging inside VLPs

Trial doxorubicin packaging experiments were firstly carried out. In a 10 µL volume, doxorubicin (15 µM, 30 µM, 60 µM, 120 µM, 240 µM, 480 µM or 960 µM) was mixed with VLP(TR-Cy5) (0.278 µM) in pH 8.3 HEPEs for 1 h at room temperature. Two controls were doxorubicin only (960 µM) and VLP(TR-Cy5) only (0.278 µM). The mixtures were concentrated through 100 kDa MWCO spin concentrators three times, washing in between with pH 8.3 HEPES, to 20 µL final volumes. Concentrated solutions were analysed by UV-visible spectroscopy: the absorbance at 649 nm was measured to estimate the concentration of VLP(TR-Cy5) present; the absorbance at 486 nm was measured to estimate the concentration of doxorubicin present. The doxorubicin retained after spin concentration was assumed to be bound to TR-Cy5 within VLPs. For the preparation of VLP(TR-Cy5/Dox)-$PEG_{24}$-A9L, the above protocol was scaled up to using 480 µM doxorubicin and 0.278 µM VLP(TR-Cy5) in a 100 µL volume. VLP(TR-Cy5/Dox) was eluted through a NAP-5 column, and concentrated into pH 8.3 HEPES using a 100 kDa MWCO spin concentrator, prior to surface modification with $SM(PEG)_{24}$ and A9L (as previously described).

### 2.2.2 Biochemical assays

Sucrose density gradient centrifugation (SDC)

Samples were loaded onto a 12 mL (SW 40 rotor) or 38 mL (SW 32 rotor) 15-45% (w/v) linear sucrose gradient made using a Biocomp Instruments gradient station. The gradients were centrifuged in a Beckman Coulter Optima L-80 XP ultracentrifuge at 47,000 RCF, 4$^{o}$C for 17 h. Fractions were collected using a Biocomp Instruments piston gradient fractionator either by 260 nm absorbance

Pharmacia UVM II detector or by eye. Photographs were taken on a camera phone, at a fixed position in front of the gradients.

Western blotting

Protein samples were resolved by SDS-PAGE (15%) in Tris glycine buffer at 160 V for 60 min, and transferred to a 0.2 µm nitrocellulose membrane at 80 V for 60 min. The membrane was washed with TBS, incubated with BLOCK (5x) for 1 h at room temperature, and washed twice with TBST. The primary antibody was incubated with the membrane in TBST for 45 min, before washing once with BLOCK (1x) and twice with TBST. The membrane was incubated with the HRP-conjugated secondary antibody in TBST for another 45 min, and washed once with BLOCK (1x) and twice with TBST. After brief incubation with enhanced chemiluminescent substrate, peroxidase activity was detected using X-ray film. Ghost bands on the film left by a pre-stained protein ladder allowed estimation of the molecular weight of the protein bands

2D Densitometry

The intensities of the bands from SDS-PAGE or Western blotting were measured using AIDA (Astronomical Image Decomposition and Analysis) image analysing software. A mock sample lane containing only loading buffer was used to measure the background intensity, using which the other band intensities were corrected. For VLP-$PEG_{24}$-Tf visualised with anti-MS2 CP antibody, the intensity of the unmodified CP band was compared to the total intensity of the bands to calculate the percentage of CPs that were (not) conjugated to $PEG_{24}$. Likewise, the intensity of the CP-$PEG_{24}$-Tf conjugate band was compared to the total intensity to calculate the percentage of CPs coupled

to $PEG_{24}$ and Tf. For VLP-$PEG_{24}$-Tf visualised with anti-Tf antibody, the intensity of the CP-$PEG_{24}$-Tf conjugate band was compared to that of the free Tf band. As the molarity of free Tf loaded onto the gel was known, the molarity of Tf present in CP-$PEG_{24}$-Tf conjugates was extrapolated. The same method was used to estimate the total molarity of CPs (and hence VLPs) present. These were then used to estimate the average number of Tf coupled to each VLP.

TEM

Samples were applied to the shiny side of charged carbon-coated copper grids and left for 1 min. After gently removing the sample with filter paper, two drops of 2% (w/v) uranyl acetate solution were briefly applied to the shiny side of the grid, and allowed to run off. A third drop of uranyl acetate was then applied to the grid, and allowed to sit for 45 s. A wedge of filter paper, wetted in sterile water, was used to gently remove the uranyl acetate to leave a thin sheen of stain on the surface. The grid was allowed to dry at room temperature for 1 h, before it was visualised using a JEOL 1400 transmission electron microscope at 120 keV.

Ribonuclease digest assay

TR-Cy5, either free in solution or encapsidated in VLPs, were incubated with 50 $ng.mL^{-1}$ RNase A for 30 min at 37°C. Reaction mixtures were analysed by native 2% (w/v) agarose gel electrophoresis, run at 100 V for 90 min. Bands were visualised by ethidium bromide or Coomassie Brilliant Blue R-250 staining.

Antibody binding assay

TR-Cy5 encapsidated VLP or VLP-$PEG_{24}$–A9L were mixed with rabbit polyclonal anti-MS2 CP antibody (0, 1 or 5 µL), and left at room temperature for 30 min. The mixture was analysed by native 2% (w/v) agarose gel electrophoresis, run at 100 V for 90 min. Bands representing VLP or VLP-$PEG_{24}$–A9L were visualised by Cy5 fluorescence scanning, and their intensities quantitated using 2D densitometry.

VLP stability assay in media and human serum

VLP-$PEG_{24}$-A9L was incubated in either of the prostate cancer cell medium (Ham's F-12K or RPMI 1640), or in human serum at 37$^{o}$C for up to 48 h. The mixtures were buffer exchanged into HEPES (pH 7.3) buffer using 100 kDa MWCO spin concentrators, before they were analysed by TEM or native 2% (w/v) agarose gel electrophoresis.

### 2.2.3 Cell biology assays

Cell culture

All cells were cultured in T75 flasks at 37°C with 5% (v/v) $CO_2$, and passaged with TrypLE Express. HeLa cervical cancer cells were grown in Dulbecco's Modified Eagles Medium that was supplemented with 10% (v/v) FBS, penicillin (50 $U.mL^{-1}$) and streptomycin (50 $\mu g.mL^{-1}$). PC-3 cells were grown in Ham's F-12K Medium supplemented with 7% (v/v) FBS. LNCaP cells were grown in RPMI-1640 Medium supplemented with 10% (v/v) FBS. Cell cultures were discarded and renewed from frozen stock roughly once every month.

Poly-L-lysine plate spreading

Poly-L-lysine was dissolved in tissue culture grade water to a final concentration of 0.1 mg.mL$^{-1}$. The cell culture surface was aseptically and evenly coated with 40 µL poly-L-lysine solution per cm$^2$. After 5 min, the solution was removed and the surface rinsed with sterile water, before drying for at least 2 h prior to cell seeding.

Deconvolution microscopy internalisation assay

Cells were seeded on glass coverslips in a 24 well plate and grown to ~70% confluence. After washing with medium, cells were incubated in fresh medium at 4$^o$C for 20 min. The medium was then replaced by fresh 4$^o$C medium containing up to 100 nM encapsidated TR-Cy5, in which cells were incubated at 4$^o$C for 1 h. The cells were washed three times with 4$^o$C medium, and incubated with fresh medium at 37$^o$C for 1 h to allow internalisation of cell surface bound VLPs. Cells were washed three times with DPBST, and incubated in FIX for 15 min at room temperature. After washing with DPBST, cells were incubated in 200 µL DPBS containing DAPI (2 µg.mL$^{-1}$) at room temperature for 10 min. The DPBS/DAPI was removed; coverslips were mounted onto slides using Fluoromount-G and allowed to dry, before visualisation on a Delta Vision deconvolution microscope. Images were acquired using a 60x magnification objective lens. SoftWoRx was used to acquire a Z stack of images for deconvolution analysis.

Flow cytometry analysis

Flow cytometry was carried out on a Becton Dickinson BD-LSRFortessa Cell Analyzer. From each sample, 10$^4$ cell events were collected for analysis. The

355 nm laser was used with a 450/40 detector for DAPI; the 488 nm laser was used with a 525/10 detector for FITC, a 585/15 detector for doxorubicin, and a 630/30 detector for PI; the 633 nm laser was used with a 660/20 detector for Cy5. Compensations were set using Becton Dickinson fluorescent beads in accordance with the manufacturer's instructions. Several gates were established to separate desired and undesired events, and to measure relative cell populations. An initial gate, based on forward and side scatters of untreated cells, was used to distinguish cell events from non-cell events. A second gate was set to distinguish between cells that have taken up TR-X and cells that have not. Untreated cells were used to set the upper Cy5 fluorescence intensity for non-transfected cells – cells with fluorescence higher than 99% of these cells were designated 'transfected'. For the apoptosis assays, a third gate was set up to sort cells into one of four populations, including live, early apoptotic, late apoptotic and necrotic, based on their FITC (Annexin V) and propidium iodide fluorescence emissions.

VLP uptake analysis in test tubes

Cells were harvested using TrypLE at 37$^{o}$C, washed three times with 500 µL DPBS, and counted using a hemocytometer. Following dilution to $0.5 \times 10^5$ cells per mL in cell medium, 400 µL cells were pipetted into test tubes, to which 100 µL medium containing encapsidated TR-Cy5 (to make a final concentration of 10 nM) was added. After brief vortexing, cells were incubated at 37$^{o}$C for up to 24 h. Cells were washed three times with DPBST, and incubated in FIX at room temperature for 10 min. Fixed cells were pelleted with brief centrifugation, then resuspended in 200 µL DPBS and analysed by flow cytometry.

VLP uptake analysis on plates

Cells were harvested using TrypLE at 37$^{o}$C, and counted using a hemocytometer. After diluting to 0.5 x $10^5$ cells.mL$^{-1}$ in cell medium, 340 µL cells were seeded onto wells of a 24 well plate. TR-Cy5 packaged inside various VLP formulations was diluted in cell medium to a total volume of 10 µL, and a concentration of 350 nM. This was added to the seeded cells; hence a final concentration of 10 nM TR-Cy5 was achieved. Cells were incubated in a $CO_2$ incubator at 37$^{o}$C for up to 48 h. Cells were harvested with TrypLE at 37$^{o}$C, and washed three times with 500 µL DPBS. After fixing with 200 µL FIX at room temperature for 10 min, cells were finally resuspended in 200 µL DPBS before analysis by flow cytometry.

Cellular delivery of siRNA by VLPs

Cells were harvested using TrypLE at 37$^{o}$C, and counted using a hemocytometer. After diluting to 0.5 x $10^5$ cells.mL$^{-1}$ in cell medium, 340 µL cells were seeded onto wells of a 24 well plate. TR-siRNA (BCL2 or Control) packaged inside various VLP formulations was diluted in cell medium to a total volume of 10 µL, to a concentration which is 35x the desired final concentration. This was added to the seeded cells. Cells were incubated in a $CO_2$ incubator at 37$^{o}$C for up to 72 h, and prepared for downstream assays.

Liposomal delivery of siRNA

TR-Cy5 or TR-siRNA was mixed with 3 µL HiPerFect Transfection Reagent. The mixture was vortexed and left at room temperature for 10 min, and then added to PC-3 cells in 24 well plates. The cells were incubated for up to 48 h

before flow cytometry analysis of uptake, relative BCL2 expression and apoptosis.

Intracellular anti-BCL2 antibody staining

The cell medium was collected and retained. Cells were washed twice with DPBS and harvested with TrypLE at 37$^{o}$C. Harvested cells were collected with the original medium and centrifuged at 1,000 RCF for 5 min. The cell pellet was resuspended in FIX for 5 min at room temperature, and washed with DPBS, before it was transferred into a clean tube and incubated in permeabilisation buffer at 4$^{o}$C for 20 min. FITC-labelled anti-BCL2 antibody (30 µL per $10^{6}$ cells) was added to the cell suspension, and left at 4$^{o}$C for 1 h. The cells were pelleted and resuspended in 200 µL DPBS, before flow cytometry analysis. A FITC-labelled isotype control antibody was also used to stain untreated cells to determine the background fluorescence, which was subtracted from the mean fluorescence values of anti-BCL2 antibody stained cells. Relative percentage BCL2 expressions were calculated by comparing the mean FITC fluorescence of treated cells with that of untreated cells, assuming 100% expression for the untreated cells.

Apoptosis assay

After siRNA delivery, the cell medium was collected and retained. Cells were washed twice with DPBS and harvested with TrypLE at 37$^{o}$C. The harvested cells were collected with the original growth medium, washed twice with DPBS and once with annexin binding buffer. Cells were then resuspended in 200 µL annexin binding buffer containing annexin V (2 µg.mL$^{-1}$) and propidium iodide (4 µg.mL$^{-1}$), incubated at 4$^{o}$C for 15 min, and analysed by flow cytometry. For

HeLa cells, controls included untreated cells stained with annexin V and propidium iodide; cells exposed to UV radiation for 2 h, stained with propidium iodide (necrotic control); and cells treated with 50 μM cisplatin for 24 h, stained with annexin V (apoptotic control).

PSMA expression on prostate cancer cell lines

The cell surface expression of PSMA on LNCaP and PC-3 cells was determined by flow cytometry. Cells were harvested using TrypLE at 37$^{o}$C, washed three times with 500 μL DPBS, and counted using a hemocytometer. Cells were then resuspended in 500 μL DPBS/FBS (1 x $10^{6}$ cells.mL$^{-1}$), incubated at room temperature for 15 min. After brief centrifugation, pelleted cells were resuspended in 100 μL of DPBS/FBS and 20 μg.mL$^{-1}$ primary rabbit anti-PSMA antibody, incubated at room temperature for 1 h. Cells were then washed three times with 500 μL DPBS/FBS, and incubated in DPBS/FBS containing a 1:500 dilution of secondary antibody (anti-rabbit IgG-FITC conjugate) at room temperature for 30 min. Cells were washed three times with 500 μL DPBS/FBS, resuspended in 200 μL DPBS/FBS and analysed by flow cytometry. Cellular PSMA expression was also analysed by Western blotting. LNCaP and PC-3 cells were collected as described above, resuspended in 1x RIPA buffer containing 1x Protease/Phosphatase Inhibitor Cocktail, and incubated at 4$^{o}$C for 20 min. Cells were pelleted with brief centrifugation, and 25 μg protein from the supernatant was analysed by Western blotting. Antibodies used include a primary rabbit anti-PSMA antibody and a HRP-conjugated secondary anti-rabbit IgG antibody.

PSMA cell surface binding assay

TrypLE harvested LNCaP and PC-3 cells were washed twice with 500 µL DPBS, incubated in 200 µL FIX solution for 10 min at room temperature. Fixed cells were washed twice with 500 µL DPBS, resuspended in PSMA binding buffer, then incubated at 37$^{o}$C for 20 min. Cells were then pelleted, resuspended in 50 µL PSMA binding buffer containing 25 nM encapsidated TR-Cy5, and incubated at 37°C for 1 h. After washing three times in 500 µL PSMA binding buffer, cells were finally resuspended in 200 µL DPBS and analysed by flow cytometry.

Doxorubicin delivery assays

LNCaP, PC-3 and HeLa cells were harvested using TrypLE at 37$^{o}$C, and counted using a hemocytometer. After diluting to 0.5 x $10^{5}$ cells.mL$^{-1}$ in cell medium, 340 µL cells were seeded onto wells of a 24 well plate. Free or encapsidated doxorubicin was diluted in cell medium to a total volume of 10 µL, to a concentration which is 35x the desired final concentration. This mix was added to the cells. Cells were incubated in a $CO_2$ incubator at 37$^{o}$C for 24 h, and analysed by flow cytometry to assess the doxorubicin uptake and cytotoxic effects (as previously described for siRNA treated cells). One variation from the aforementioned apoptosis assay was the substitution of propidium iodide for DAPI as the cell viability dye.

# Chapter 3

Mitigating non-specific cellular uptake of VLPs

# 3.1 Introduction

### 3.1.1 Polyethylene glycol and drug delivery

Polyethylene glycol (PEG) is one of the most widely used synthetic polymers (Figure 3.1A). It can be made via the polymerisation of ethylene oxide – a range of different molecular weights can be achieved, from 300 Da to 10,000,000 Da, to suit a myriad of applications (Yue et al., 2012). They can also be prepared with chemical groups on one or both termini to facilitate conjugation to biomolecules. Some examples, including the commercially available hetero-bifunctional SM(PEG)$_{24}$, and NHS-(PEG)$_{12}$-biotin, are shown in Figure 3.1BC.

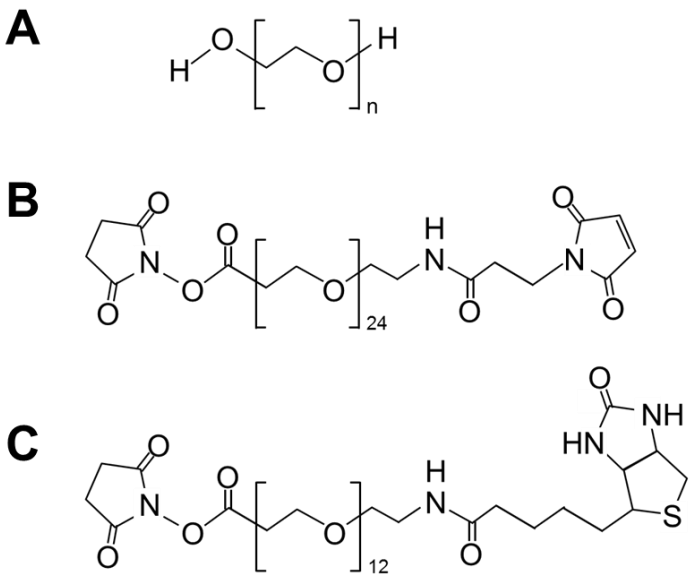


**Figure 3.1. Structure of polyethylene glycol and some possible derivatives. (A)** Structure of polyethylene glycol (PEG). PEG is commercially available over a wide range of molecular weights, with n repeats of ethylene oxide (O-$CH_2$-$CH_2$) resulting in different lengths to suit a myriad of applications. **(B)** Structure of SM(PEG)$_{24}$. The presence of an NHS group and a maleimide group facilitates amine-to-thiol conjugations, whilst incorporating a $PEG_{24}$ linker. **(C)** Structure of NHS-(PEG)$_{12}$-biotin. $PEG_{12}$-biotin can be conjugated to amine presenting molecules.

PEG is highly water soluble, biocompatible, chemically inert, and displays low immunogenicity as well as low toxicity. The versatility and usefulness of PEG has been demonstrated across a range of applications (Yue et al., 2012), for example, it is used in mass spectrometry studies as a calibration compound, in DNA preparations to facilitate precipitation, in food as an anti-foaming agent, and in toothpastes as a humectant.

The first reports of conjugating PEG to proteins emerged in 1977, which revealed that PEGylation could mask bovine serum albumin from the immune system in rabbits (Abuchowski et al., 1977b), and also significantly increase the plasma retention of bovine liver catalase from 12 h to 48 h in mice whilst, importantly, not affecting its enzyme activity (Abuchowski et al., 1977a). These results sparked a huge interest in the therapeutic applications of PEG. Since then, many PEGylated drugs (proteins, nucleic acids and small molecules) have been synthesised and shown to exhibit more favourable properties compared to the non-PEGylated versions (Knop et al., 2010); several of these formulations are now FDA approved for treating a range of diseases (Table 3.1). It is now known that PEG can improve the drug efficacy through multiple mechanisms (Knop et al., 2010), including (i) increasing the hydrodynamic size of small molecule drugs or drug delivery systems, to reduce rapid renal clearance, and enhance their plasma half-lives and passive accumulation in tumour tissues via EPR, (ii) improving drug solubility, (iii) enhancing drug stability and protection from degradation by endogenous proteases or nucleases, (iv) altering their biodistribution, (v) mitigating non-specific cellular uptake, and (vi) reducing immunogenicity by masking surface epitopes.

| Drug | Description | Indication | Approval |
|---|---|---|---|
| Oncospar | mPEG-L-asparaginase | ALL | 1994 |
| Doxil | PEG-liposome | Breast cancer, Kaposi's sarcoma, MM, ovarian cancer | 1995 |
| PEG-Intron | mPEG-interferon α2a | Chronic hepatitis C | 2001 |
| Neulasta | mPEG-GCSF | Febrile neutropenia | 2002 |
| Pegasys | mPEG-interferon-α-2b | Chronic hepatitis C | 2002 |
| Macugen | mPEG-anti-TNFα | Age-related macular degeneration | 2004 |
| Peginesatide | PEG-peptide | Anaemia associated with chronic kidney disease | 2012 |

**Table 3.1. Selected examples of approved drugs that include PEG.** mPEG = methoxy polyethylene glycol; GCSF = granulocyte-colony stimulating factor.

The use of PEG in VLP drug delivery systems has been demonstrated for the CPMV (Destito et al., 2007). Similar to MS2 VLPs, non-surface modified CPMV VLPs carrying fluorescent cargo displayed some levels of non-specific uptake, which was significantly reduced by decorating the VLP surface with PEG chains ($M_w$ ~ 500 Da). Upon further addition of the targeting ligand, folic acid, specific folate receptor-mediated uptake was observed in targeted HeLa and KB cancer cells. Furthermore, the addition of a PEG layer markedly improved folic acid-mediated cell binding and uptake compared to VLPs directly conjugated to folic acid, which was attributed to the added flexibility conferred to the ligands (Destito et al., 2007). More recently, MS2 VLPs surface decorated with $PEG_{24}$ and a tumour-targeting peptide successfully delivered cargos to targeted hepatocellular carcinoma cells, but not normal hepatocyte cells (Ashley et al., 2011). These results suggest that PEGylation might be a suitable strategy for

mitigating the previously observed non-specific uptake of MS2 VLPs (Galaway, 2011). Further addition of a targeting ligand, such as Tf, to the PEG termini should promote tumour-specific delivery of encapsidated cargo.

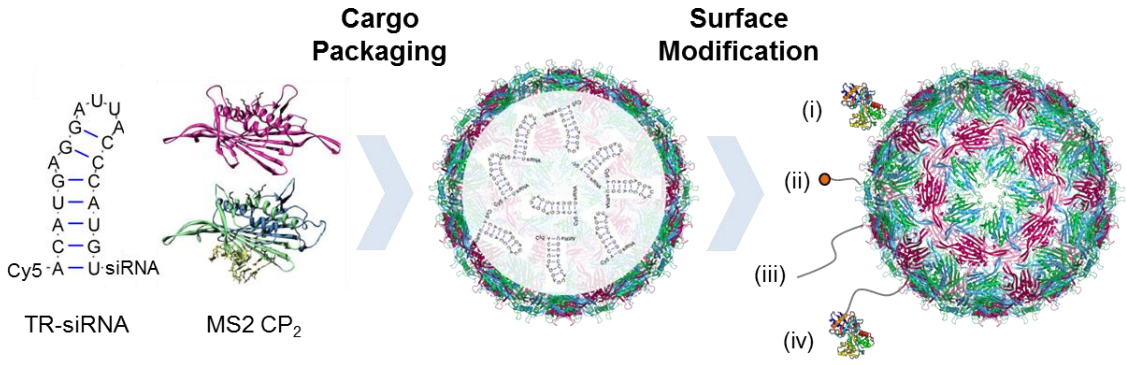


**Figure 3.2. General schematic showing the synthesis of siRNA encapsidated, surface modified VLPs.** Mixing TR-coupled siRNA with dissociated MS2 $CP_2$ at neutral pH triggers VLP assembly and the packaging of siRNA inside. VLPs can then be surface modified using NHS-based conjugative chemistry, to incorporate useful ligands. The modifications used in this chapter are shown (not to scale), including (i) Tf, (ii) $PEG_{12}$-biotin, (iii) $PEG_{24}$ and (iv) $PEG_{24}$-Tf.

A generalised schematic for VLP construction is shown in Figure 3.2. The previously used anti-*BCL2* siRNA will be used as the model drug cargo; conjugation to TR ('TR-BCL2') facilitates its encapsidation within MS2 VLPs during *in vitro* assembly, which can then be surface modified. Five different MS2 VLPs are used in this Chapter, including unmodified VLP, VLP-Tf, VLP-$PEG_{12}$-biotin, VLP-$PEG_{24}$ and VLP-$PEG_{24}$-Tf (Figure 3.2).

### 3.1.2 Aims

The aims of the work described in this chapter were to:

1. Synthesise RNA-encapsidated VLP, VLP-PEG and VLP-PEG-Tf.
2. Compare the uptake of VLP, VLP-PEG and VLP-PEG-Tf by HeLa cells.
3. Assess the cellular effects of siRNA delivery by VLP-PEG-Tf to HeLa cells.

## 3.2 Results and discussion

### 3.2.1 Purification of MS2 VLPs

The MS2 CP was previously recombinantly expressed in *E. coli* in the Stockley laboratory (Mastico et al., 1993). These CP readily assembled into capsids *in vivo*, typically packaging random *E. coli* nucleic acids. These structures are referred to as VLP(*E.coli*).

VLP(*E. coli*) was purified through two rounds of sucrose density gradient centrifugation (SDC), and analysed (Figure 3.3). SDS-PAGE indicated the presence of a large amount of *E. coli* protein contaminants in the unpurified sample, which was removed through SDC (Figure 3.3A). 2D densitometry analysis of the bands determined that a CP purity of ~90% and >99% was achieved after one or two rounds of SDC, respectively. Analysis on a native 2% (w/v) agarose gel revealed that SDC was also able to purify VLP(*E. coli*) from nucleic acid contaminants, most likely the *E. coli* genome (Figure 3.3B). The contaminants migrated much slower than the VLP(*E. coli*) band, which is consistent with VLP(*E. coli*) having a more compact structure compared to the large *E. coli* genome. Furthermore, the VLP(*E. coli*) bands were visualised by ethidium bromide staining, suggesting that nucleic acids were encapsidated within VLP(*E. coli*) – this is supported by the $A_{260}/A_{280}$ ratio of purified VLP(*E. coli*), typically ~1.7. Size exclusion chromatography of purified VLP(*E. coli*) revealed a major peak representing VLP(*E. coli*), and a negligible amount of smaller species that were likely dissociated CP or assembly intermediates (Figure 3.3C). The intact nature of VLP(*E. coli*) was confirmed by TEM, Figure 3.3C inset).

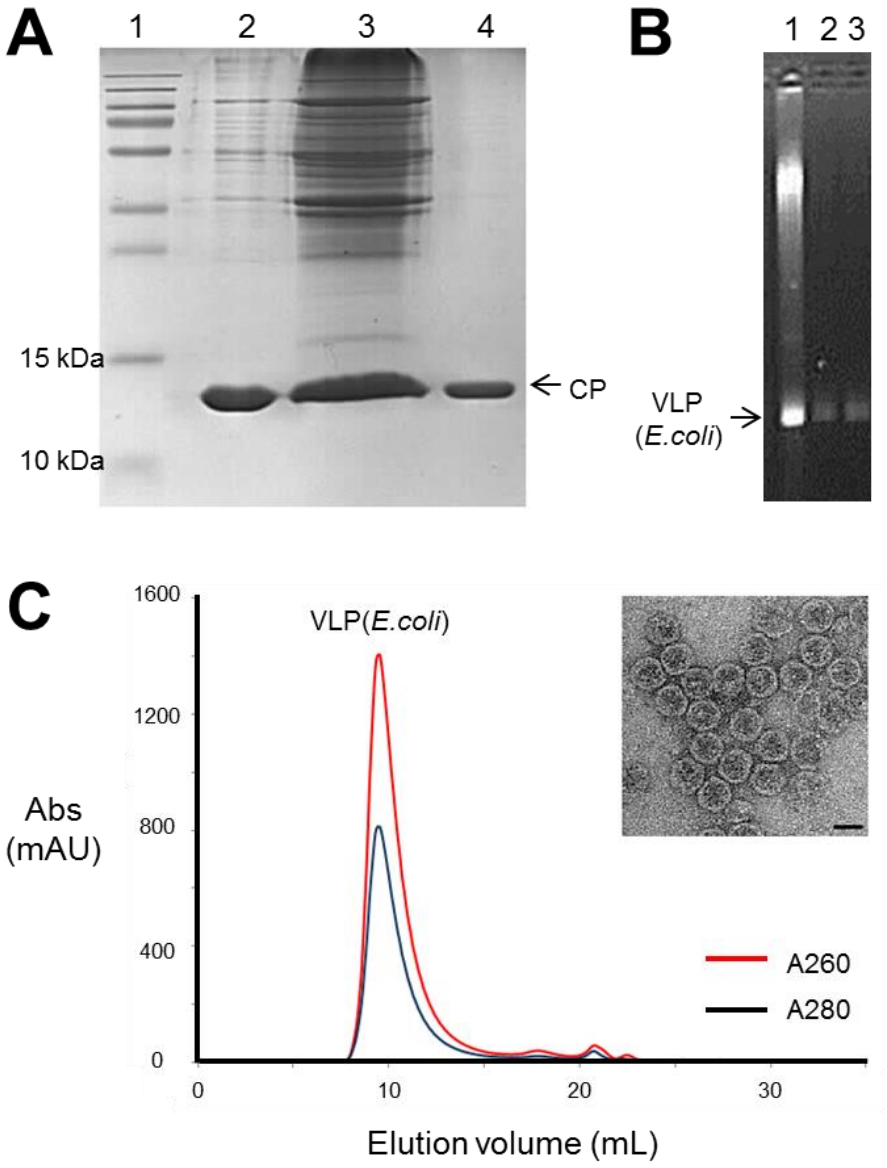


**Figure 3.3. Purification and analysis of VLP(*E. coli*).** After two rounds of purification by 15-45% (w/v) linear SDC, VLP(*E. coli*) was analysed by **(A)** SDS-PAGE. 1: Fermentas prestained ladder; 2: VLP(*E. coli*) after one round of SDC; 3: unpurified VLP(*E. coli*); 4: VLP(*E. coli*) after two rounds of SDC. Arrow indicates CP monomers. **(B)** Native 2% (w/v) agarose gel electrophoresis. 1: Unpurified VLP(*E. coli*); 2: VLP(*E. coli*) after one round of SDC; 3: VLP(*E. coli*) after two rounds of SDC. Arrow indicates VLP(*E. coli*). **(C)** Size exclusion chromatography. Absorbance traces at 260 nm (red) and 280 nm (black) are displayed. A TEM image of purified VLP(*E. coli*) is shown as an inset. Scale bar = 25 nm.

### 3.2.2 TR-siRNA design, synthesis and preparation

To be compatible with the MS2 VLP drug delivery system, the therapeutic siRNA must remain functional when attached to TR, and must not contain sequences complementary to TR, which might interfere with siRNA strand annealing as well as TR-mediated VLP assembly. Furthermore, it should also tolerate the terminal attachment of fluorescent dyes, which are required for quantifying siRNA packaging and cellular uptake. Two siRNAs have previously demonstrated to fulfill these requirements (Galaway, 2011, Galaway and Stockley, 2013): one targeted against the mRNA of the anti-apoptotic factor, BCL2; the other targeted against the mRNA of polo-like kinase 1 (PLK1). Both siRNAs were originally studied as aptamer-siRNA conjugates, and were shown to retain their ability to induce target knockdown and apoptosis in cells despite being coupled to a tumour-targeting RNA aptamer (McNamara et al., 2006). This prompted the use of these siRNAs as TR-siRNA conjugates in the MS2 VLP delivery system (Galaway, 2011).

Of the two siRNAs, the anti-*BCL2* siRNA showed better efficacy in HeLa cells (Galaway, 2011), and was chosen for the present study as the model therapeutic cargo. BCL2 is an anti-apoptotic factor, whose overexpression is associated with numerous human cancers and also their development of resistance to chemotherapeutics (Cory and Adams, 2002). The two strands of the siRNA (TR-BCL2, Figure 3.4B) were synthesised separately and then annealed, as shown previously (Galaway, 2011). The antisense strand is complementary to nucleotides 1208 to 1228 within the coding region of the BCL2 mRNA; the sense strand is synthesised with TR as a single chain, and is situated on the 3' end of TR. This siRNA could be considered a second

generation siRNA. It differs from a previous version only in the sense strand, in which a 3′ uracil overhang and two adenines between the siRNA and TR are incorporated; these modifications were shown to confer enhanced siRNA effects *in vitro* (Dassie et al., 2009, Galaway, 2011).

A control siRNA was also used to ensure that any cellular effects observed is siRNA sequence-dependent (Figure 3.4C). This siRNA has the same nucleotide composition as the BCL2 siRNA, but its sequence was scrambled using siRNA Wizard v3.1, and is not complementary to any known human mRNA. Cyanine 5 (Cy5) phosphoramidites (Figure 3.4D) were incorporated to the 5′ end of both strands of the TR-siRNAs during RNA synthesis to facilitate the quantification of siRNAs. In addition to the two TR-siRNAs, a sequence composed of only TR coupled to Cy5 (TR-Cy5, Figure 3.4A) was used to test for VLP assembly conditions and in cellular uptake experiments.

All RNAs were synthesised by Amy Barker using an ABI 394 DNA Synthesizer, prior to purification by reverse phase HPLC (Figure 3.5A). Typically three fractions were observed, containing unincorporated phosphoramidites (fraction 1), non-Cy5 coupled RNA (fraction 2) and Cy5 coupled RNA (fraction 3). The Cy5 phosphoramidite coupling efficiency ranged from ~40% to 70%.

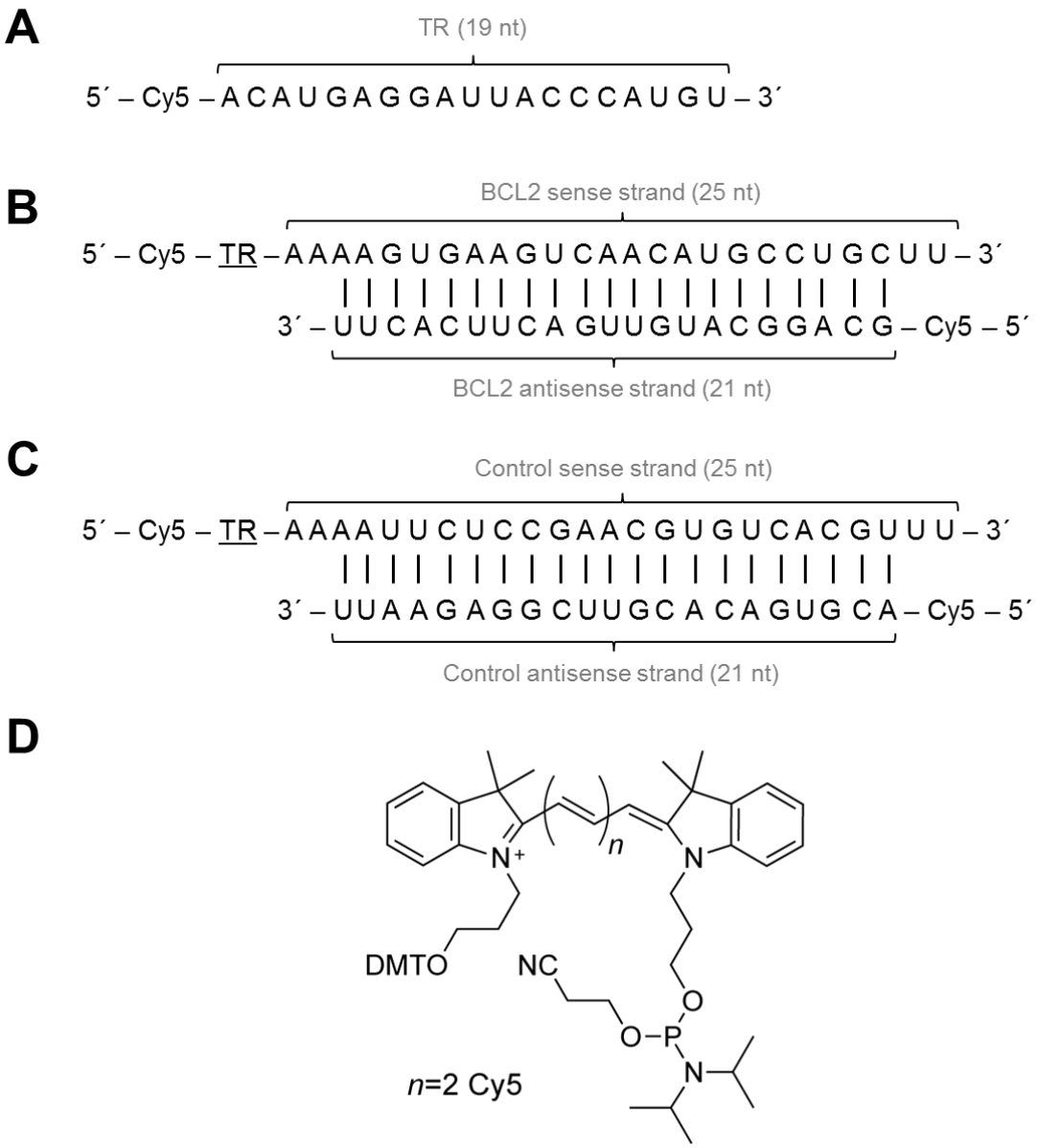


**Figure 3.4. Structures of the RNA sequences and fluorescent dye used.** The RNAs used include **(A)** TR, **(B)** TR-BCL2 and **(C)** TR-Control. TR is a known MS2 packaging signal. The TR-siRNAs, TR-BCL2 and TR-Control, are composed of two annealed strands, with the sense strand and TR as one chain. The TR-BCL2 antisense strand is complementary to BCL2 mRNA, whereas that of TR-Control has no complementary mRNA. **(D)** Cyanine 5 (Cy5) phosphoramidites were incorporated to the 5′ end of both strands of the TR-siRNAs during RNA synthesis.

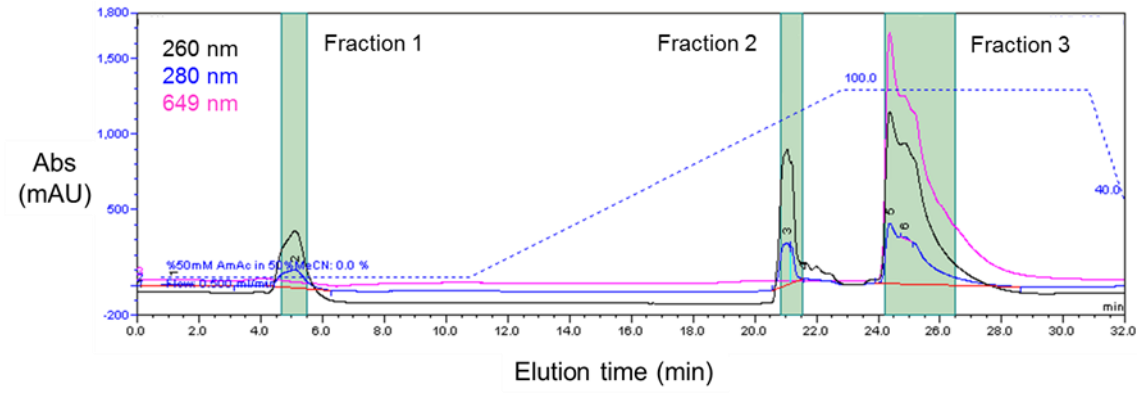


**Figure 3.5. Typical reverse-phase HPLC elution profile of synthesised RNAs.** Absorbance traces at 260 nm (black), 280 nm (blue) and 649 nm (magenta) are shown. The dotted blue line represents an increasing gradient of acetonitrile. Green shaded regions indicate fractions collected.

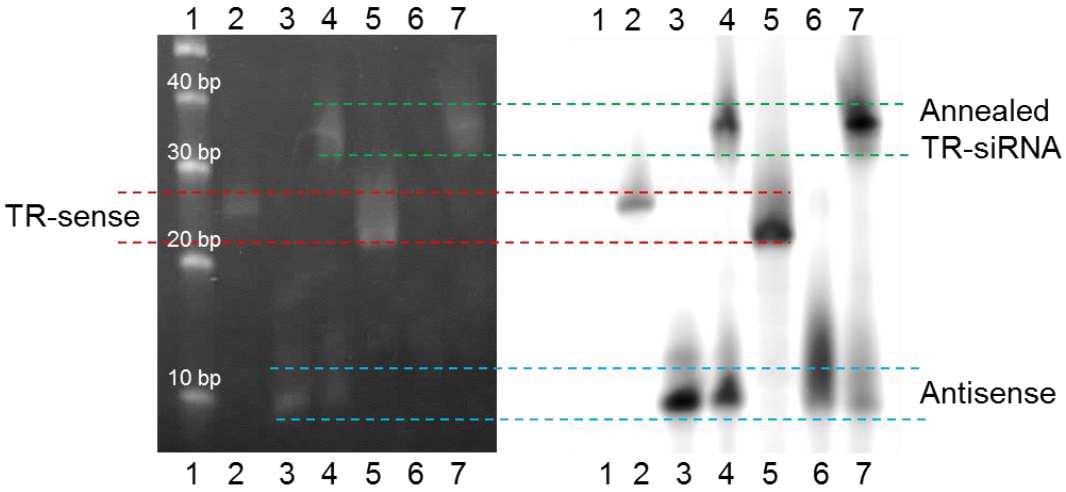


**Figure 3.6. Gel purification of annealed siRNAs.** Annealed TR-siRNAs were analysed on a native 15% (w/v) polyacrylamide gel, visualised by ethidium bromide staining (left) or Cy5 fluorescence scanning (right). 1: 10 bp DNA ladder; 2: TR-BCL2 sense; 3: BCL2 antisense; 4: TR-BCL2 annealed; 5: TR-Control sense; 6: Control antisense; 7: TR-Control annealed. Positions of bands representing annealed siRNAs, TR-sense or antisense strands are indicated.

The siRNAs were annealed as previously described (Galaway, 2011). Complementary TR-sense and antisense strands were mixed at a 1:1 molar ratio in DEPC-treated water, and briefly heated to 95$^{o}$C before it was cooled to room temperature. The products were analysed on a 15% (w/v) polyacrylamide gel (Figure 3.6). Three distinct bands were observed for each annealing reaction, representing the antisense strand, TR-sense strand, or annealed TR-siRNA. Bands corresponding to annealed TR-siRNAs (TR-BCL2 and TR-Control) were excised and extracted via electro-elution. The siRNAs were then concentrated by isopropanol precipitation, and resuspended in DEPC-treated water prior to use in VLP assembly.

### 3.2.3 VLP reassembly and cargo packaging

To adapt VLP(*E. coli*) for drug delivery, the encapsidated random nucleic acids must be replaced by TR-siRNAs. To achieve this, VLP(*E. coli*) was firstly dissociated into $CP_2$ by mixing with 66% (v/v) glacial acetic acid for 1 h at 4$^{o}$C. Following acid dissociation, a brief centrifugation step was sufficient to remove the encapsidated nucleic acids; the $CP_2$-containing supernatant was eluted into 20 mM acetic acid through a NAP-10 column. Fractions were collected and their $A_{260}/A_{280}$ ratios assessed; those with a ratio of <0.8 were designated as pure CP fractions and were used in subsequent reassembly experiments. The concentration of $CP_2$ was estimated using the $A_{280}$ and its molar extinction coefficient ($\varepsilon_{280nm}$ = 33,240 L.mol$^{-1}$.cm$^{-1}$). A typical yield of dissociated $CP_2$ from VLP(*E.coli*) was ~75%.

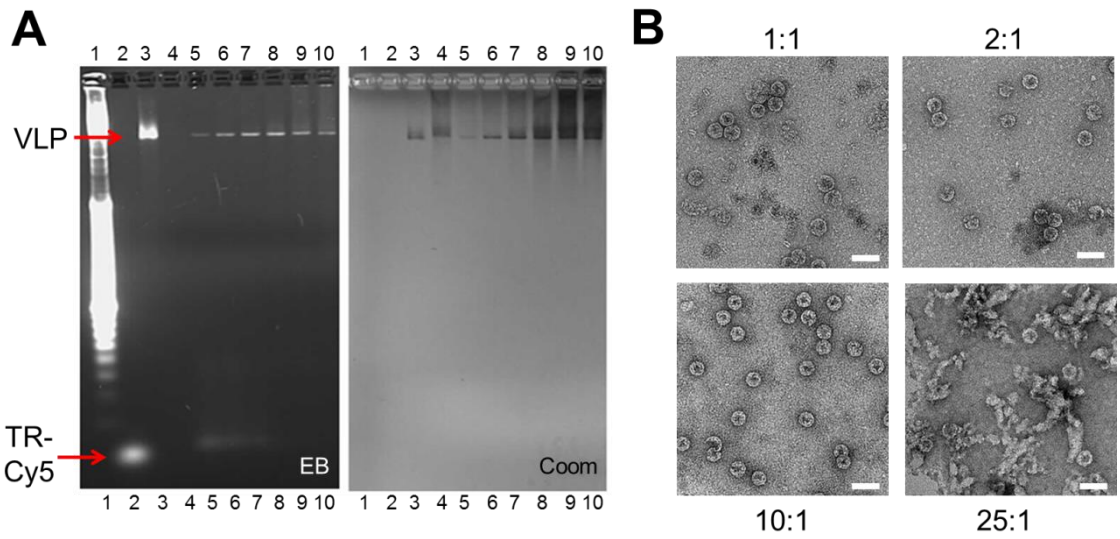


**Figure 3.7. Analysis of TR-Cy5 packaging and *in vitro* VLP assembly.** TR-Cy5 was mixed with dissociated $CP_2$ at various molar ratios at neutral pH. The reassemblies were subsequently analysed. **(A)** Native 2% (w/v) agarose gel electrophoresis. (1) HyperLadder I; (2) TR-Cy5; (3) VLP(*E.coli*); (4) $CP_2$-only control; and reassemblies with $CP_2$ : TR-Cy5 ratios of (5) 1:1; (6) 2:1; (7) 10:1; (8) 15:1; (9) 25:1 and (10) 50:1. The gel was visualised by ethidium bromide or Coomassie staining. **(B)** TEM. Scale bar = 50 nm.

Trial VLP reassembly experiments were carried out using TR-Cy5. $CP_2$ was mixed with TR-Cy5 in pH 7.3 HEPEs at room temperature for 5 h. Different $CP_2$ to TR molar ratios (1:1, 2:1, 10:1, 15:1, 25:1, 50:1) were tested, alongside a 10 µM $CP_2$-only control. The reassembly reactions were then analysed by native 2% (w/v) agarose gel electrophoresis (Figure 3.7A). For the $CP_2$-only control (lane 4), a band resembling VLP was observed with Coomassie staining, indicative of some TR-independent VLP formation – which has been previously reported (Wu et al., 1995). A smear was also observed above the band, suggesting that the reassembly efficiency was low and some aberrant or aggregated species were formed. Using its amino acid sequence, the isoelectric point of MS2 $CP_2$ was estimated to be slightly higher than the pH of the TBE

running buffer – thus, free $CP_2$ should run towards the cathode (seen on lanes 9 and 10), and hence could not account for the smear observed.

For the TR-mediated reassemblies, more intense VLP bands were observed with increasing $CP_2$ concentrations – up to the 10:1 molar ratio (lanes 5-8), with both ethidium bromide and Coomassie staining. As the ratio increased further to 15:1, 25:1 and 50:1, significant amounts of smear could be seen above the VLP bands, which were visualized by TEM as aggregate species (Figure 3.7B). These suggest that higher efficiency reassembly was achieved with greater $CP_2$ : TR ratios, up to 10:1, beyond which significant amounts of aberrant species were formed. This result was expected: at low $CP_2$ to TR molar ratios, $CP_2$ are saturated with TR and undergo conformational change to A/B-like dimers, and the availability of C/C-like dimers becomes limiting thus VLP formation is restricted (Stockley et al., 2007); at high $CP_2$ concentrations (>10 μM), VLPs can form independent of TR, as observed in the $CP_2$ only control, albeit is inefficient and results in high levels of aberrant species.

To achieve optimal reassembly and packaging efficiency, a compromise must be made between good TR-Cy5 incorporation and the avoidance of aberrant species. Whilst a $CP_2$ : TR-Cy5 molar ratio of 2:1 (lane 6) produced a relatively clean VLP band, free TR-Cy5 was still present indicating incomplete incorporation. For this reason, it appeared that a molar ratio of 10:1 is the best choice for cargo packaging and VLP assembly. This is consistent with previous results (Galaway, 2011). Additionally, the intact nature of VLP(TR-Cy5) formed from the reassembly reactions was confirmed by TEM (Figure 3.7B).

VLP(TR-Cy5) assembled using a 10:1 ratio were purified via linear 15-45%

(w/v) SDC, and concentrated using 100 kDa MWCO spin concentrators. The absorbance at 260 nm and 280 nm was measured, and used to estimate the concentration of $CP_2$ with the following equation:

$$\text{Concentration (mg/ml)} = 1.55 \times A_{280} - 0.76 \times A_{260}$$

Given 90 MS2 $CP_2$ assemble into one VLP, the concentration of VLP was derived. Furthermore, the absorbance at 649 nm was also measured to calculate the concentration of TR-Cy5 (Cy5 $\varepsilon_{649\ nm}$ = 250,000 $L.mol^{-1}.cm^{-1}$). Using these, the average number of TR-Cy5 packaged per VLP was calculated to be 9.9±1.6 from three repeats. The CP content in the purified VLP(TR-Cy5) was typically ~50% of the starting material.

### 3.2.4 Nuclease protection of packaged cargo

An ideal drug delivery system can protect its cargo from undesired interactions with cellular proteins, in particular endogenous proteases or nucleases, which can degrade the therapeutics into an inactive form. The *in vivo* instability of nucleic acid-based therapeutics, including siRNAs, has greatly hindered their clinical progress. The encapsidation of siRNAs within MS2 VLPs should solve this problem.

To assess the capacity of MS2 VLPs to protect its nucleic acid cargo from nuclease degradation, digest assays were carried out, in which TR-Cy5 – either free or packaged inside VLPs – were incubated with or without RNase A at 37$^{o}$C for 30 min, before the products were analysed on a native 2% (w/v) agarose gel (Figure 3.8). The bands corresponding to encapsidated TR-Cy5 did

not vary in intensity after either ethidium bromide or Coomassie staining (lanes 4 and 5), suggesting that encapsidated TR-Cy5 as well as the VLP particle remained stable after incubation with RNase A. However, the ethidium bromide signal of free TR-Cy5 disappeared upon RNase A treatment, suggesting complete degradation of the RNA (lanes 2 and 3). These results imply that encapsidation inside VLPs protected TR-Cy5 from RNase degradation.

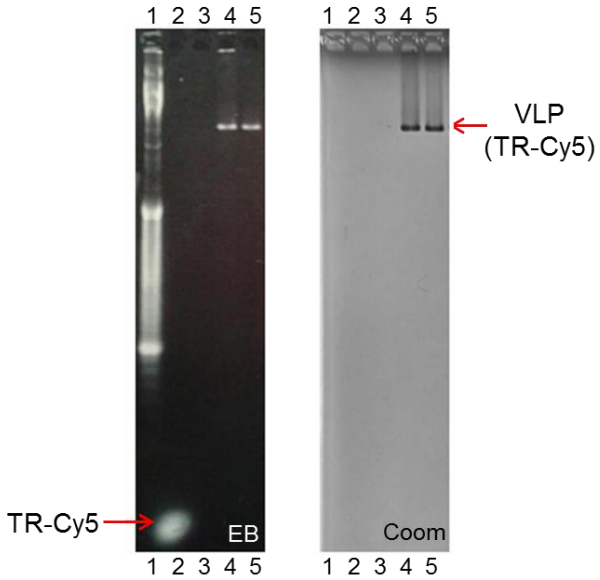


**Figure 3.8. RNA digest assay.** TR-Cy5, free or packaged inside VLP, was incubated with RNase A for 30 min at 37$^{o}$C. The reactions were analysed by 2% (w/v) agarose gel electrophoresis, visualised by ethidium bromide or Coomassie staining. 1: HyperLadder I; 2: TR-Cy5; 3: TR-Cy5 plus RNase A; 4: VLP(TR-Cy5); 5: VLP(TR-Cy5) plus RNase A.

### 3.2.5 Preparation and analysis of VLP-Tf

Human Tf is one of the most used targeting ligands in drug delivery (Daniels et al., 2012, Daniels et al., 2006a). Not only does it facilitate the cell entry of drug delivery systems through a natural pathway (Tf receptor-mediated endocytosis),

Tf also confers tumour-preferential targeting, as Tf receptors are known to be overexpressed on the surface of various cancer cells (Qian et al., 2002). In addition, it is biocompatible, non-immunogenic, and its mechanism of action is extremely well characterised (Daniels et al., 2006b).

Multivalent display of Tf on MS2 VLP was achieved by adapting a previously used protocol (Figure 3.9) (Wu et al., 1995, Galaway, 2011, Galaway and Stockley, 2013). Three surface accessible amines are present in each CP monomer: two presented by lysines at positions 106 and 113, and one by the N-terminus (Figure 1.12). This means that up to 540 copies of a ligand may be attached to the VLP surface for targeting – although this is significantly limited by factors such as the low efficiency of conjugative chemistry and steric constraints. Likewise, there are also amines on the surface of human Tf. The availability of these amines gives rise to the possibility of using NHS chemistry for conjugation.

VLP(TR-Cy5) was reacted with SATA to introduce thiol groups to the surface (Figure 3.9a, b); Tf was reacted with sulfo-SMCC, to introduce maleimide groups to its surface (Figure 3.9c). Both reactions were carried out at pH 8.3 – a compromise to ensure sufficient deprotonation of amines for the reaction to take place, whilst limiting the rate of hydrolysis of the NHS esters. These two reactions were separately eluted from NAP columns to remove excess crosslinking reagents, and mixed to allow the formation of amide bonds between the thiol and maleimide groups, resulting in VLP-Tf conjugates (Figure 3.9d).

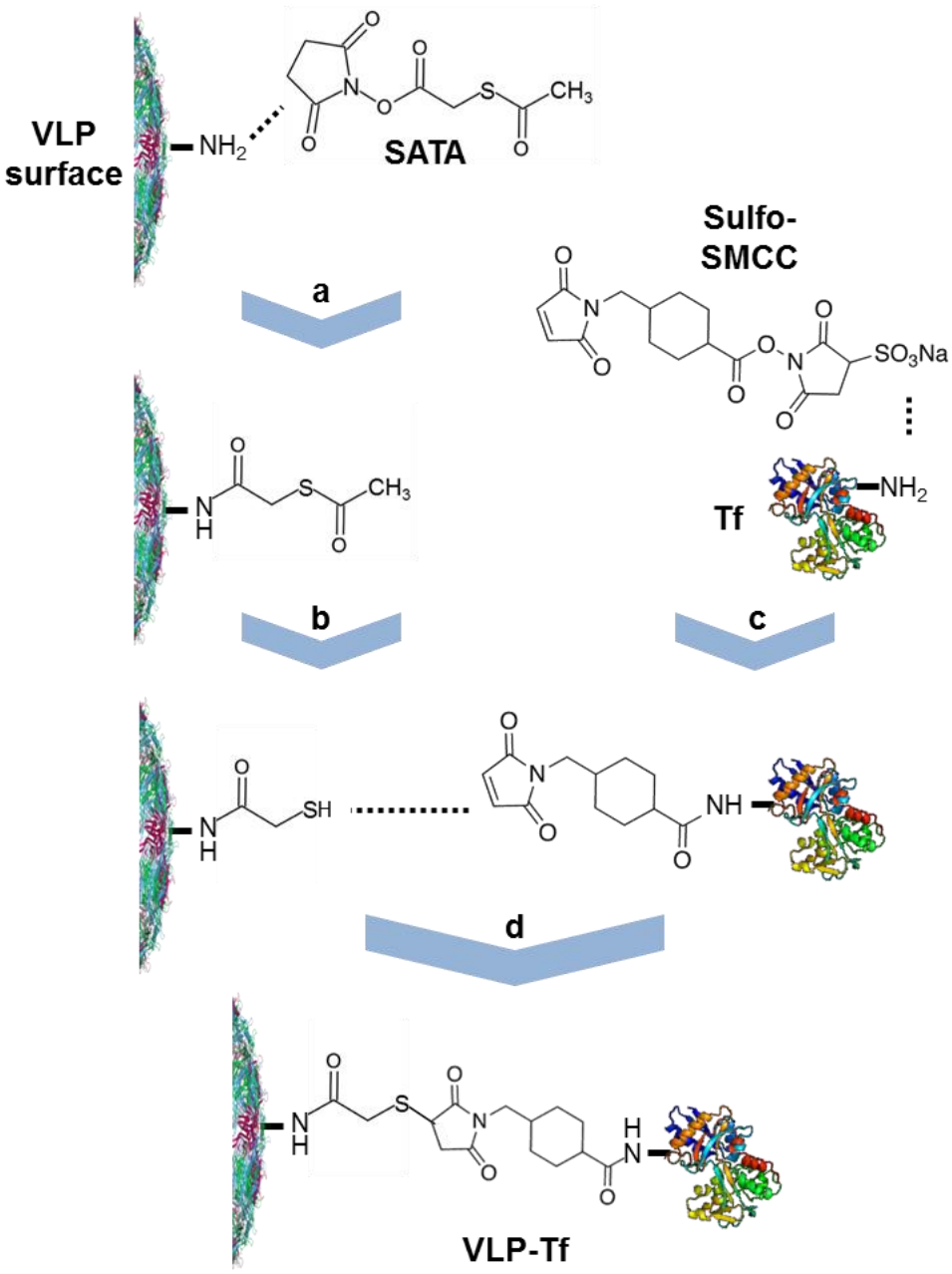


**Figure 3.9. Schematic depicting the conjugative chemistry used to synthesise VLP-Tf. (a)** Amines ($NH_2$) on the surface of MS2 VLPs are reacted with N-succinimidyl-S-acetylthioacetate (SATA), which incorporates a protected thiol group. **(b)** The thiol groups are deprotected by the addition of hydroxylamine hydrochloride. **(c)** $NH_2$ on the surface of Tf are reacted with sulfosuccinimidyl-4-(N-maleimidomethyl)cyclohexane-1-carboxylate (sulfo-SMCC), which incorporates a maleimide group. **(d)** The two reactions are purified separately through NAP columns, and then mixed to allow conjugation between the thiol and maleimide groups.

As before (Galaway, 2011), $Fe^{3+}$-binding sites within Tf were saturated by adding an iron(III) citrate buffer, the products were then analysed by size exclusion chromatography on a Superose 6 column (Figure 3.10A). $Fe^{3+}$-bound Tf, or holo-Tf, has a characteristic absorption peak at 465 nm, which arises as a result of the phenolate-to-iron charge transfer transition as iron binds to two tyrosine ligands (Patch and Carrano, 1981). The $A_{465}$ curve suggests the presence of holo-Tf in the first two peaks. Taking this into account, and using the $A_{260}$ and $A_{280}$ readings, the first two peaks observed in the chromatogram were designated, in order of elution: VLP-Tf conjugates (~7 mL) and free holo-Tf (~15 mL). VLP-Tf had a markedly reduced retention time compared to VLP (dotted curve, Figure 3.10A), as expected of a larger particle. The third peak (~20 mL) might have contained a mixture of excess crosslinking reagents and dissociated $CP_2$.

Using the $A_{260}$, $A_{280}$ and $A_{465}$ readings of the VLP-Tf containing peak, an average of 13.5±3.1 Tf per VLP was calculated from three repeats, which is similar to the previously obtained ratio of 15.2±2.3 (Galaway, 2011). The CP content in VLP-Tf was ~20% of the starting material used for conjugation, which is also comparable to previous results (Galaway, 2011).

TEM analysis of the VLP-Tf fraction revealed the presence of intact surface-modified VLPs; no aggregate species were observed (Figure 3.10B). Aggregates were previously encountered (Galaway, 2011), and were thought to be a result of the crosslinking of multiple VLPs via Tf: multivalently displayed maleimide groups on the surface of one molecule of Tf might react with thiols from multiple VLPs. The protocol was slightly modified in the present experiment, using less SATA : VLP, SMCC : Tf, and Tf : VLP molar ratios than

before in their respective reactions, and might be the reason for the reduced frequency of aggregate formation observed. Additional purification steps that were previously necessary to remove the aggregates are no longer required.

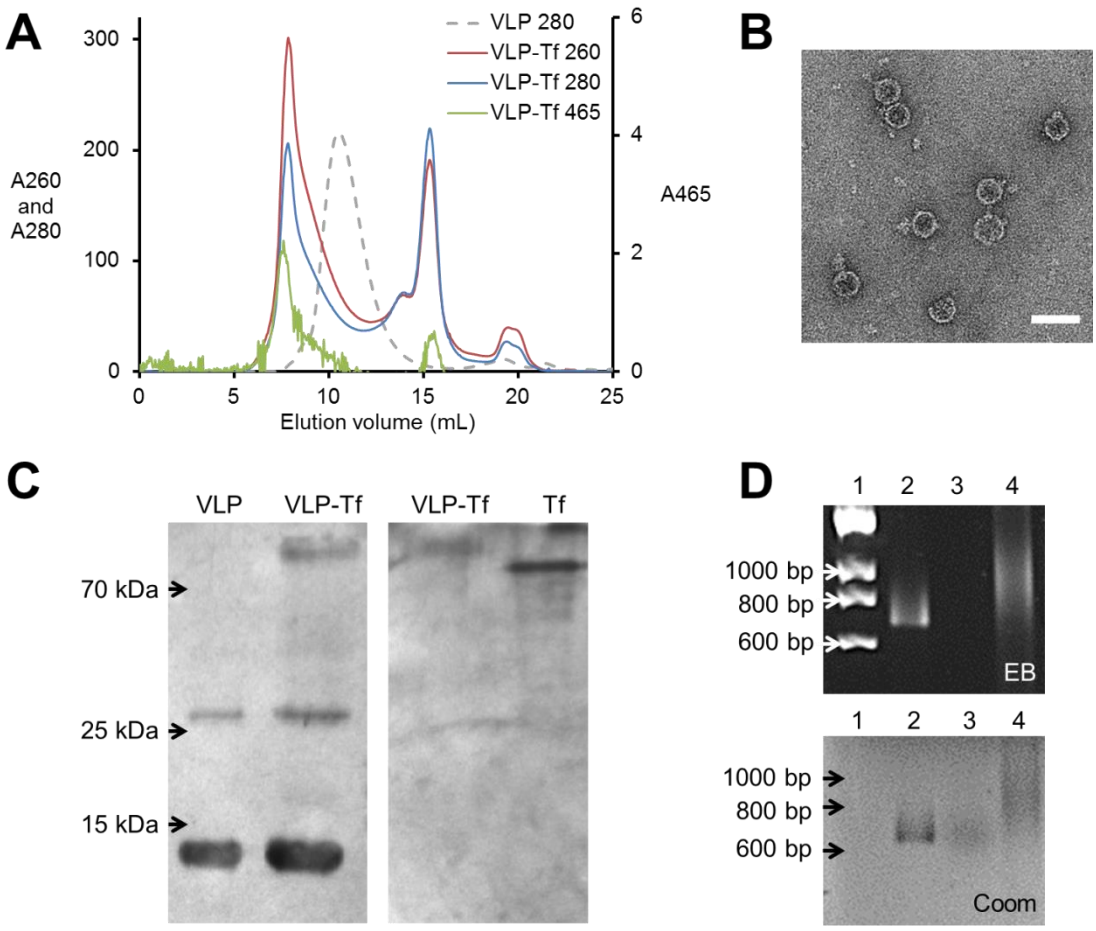


**Figure 3.10. Analysis of VLP-Tf. (A)** Superose 6 size exclusion chromatogram of VLP (dotted) and the product of the VLP-Tf conjugation reaction (solid). Absorbance measurements were taken at 260 nm, 280 nm and 465 nm for VLP-Tf, and at 280 nm for VLP. **(B)** TEM image of VLP-Tf. Scale bar = 50 nm. **(C)** Western blot analysis of VLP and VLP-Tf. Anti-MS2 CP antibodies (left) or anti-human Tf antibodies (right) were used as primary antibodies. **(D)** Native 2% (w/v) agarose. 1: HyperLadder I; 2: VLP; 3: VLP-SATA; 4: VLP-Tf. The gel was visualised by ethidium bromide or Coomassie staining.

Successful conjugation of Tf to VLP was confirmed by Western blotting (Figure 3.10C). A band was present in the VLP-Tf lane, which was higher than Tf (~77 kDa), and could be visualised with both anti-MS2 CP and anti-Tf primary antibodies, suggesting the co-presence and covalent attachment of CP and Tf. Native agarose gel electrophoresis was also used to analyse VLP-Tf (Figure 3.10D). The band representing VLP-SATA displayed a minor increase in electrophoretic mobility compared to VLP, possibly due to the removal of positive charges from the surface lysines. VLP-Tf had a lower electrophoretic mobility compared to both VLP and VLP-SATA, likely due to the increased size of the particle. Furthermore, the band resembling VLP-Tf was a smear, which suggests different levels of Tf conjugation for different VLPs. Due to the nature of the conjugation chemistry used, there was little control over some aspects of the conjugation, including the number of Tf per VLP and the orientation of Tf relative to the VLP surface. Therefore, it is likely that some level of heterogeneity was present in the resulting VLP-Tf population, which could be a limiting factor for its use as a drug delivery system.

### 3.2.6 Preparation of VLP-$PEG_{12}$-biotin and analysis of cellular uptake

To assess whether coating the VLP surface with PEG can reduce non-specific VLP uptake by cells, NHS-$PEG_{12}$-biotin was used to prepare VLP-$PEG_{12}$-biotin. The selection of NHS-$PEG_{12}$-biotin was due to its compatibility with the VLP surface amines and also its availability within the laboratory. VLP(TR-Cy5) was reacted with NHS-$PEG_{12}$-biotin in pH 8.3 HEPES at room temperature for 30 min, before the product was eluted through a NAP-5 column and concentrated using a 100 kDa MWCO spin concentrator.

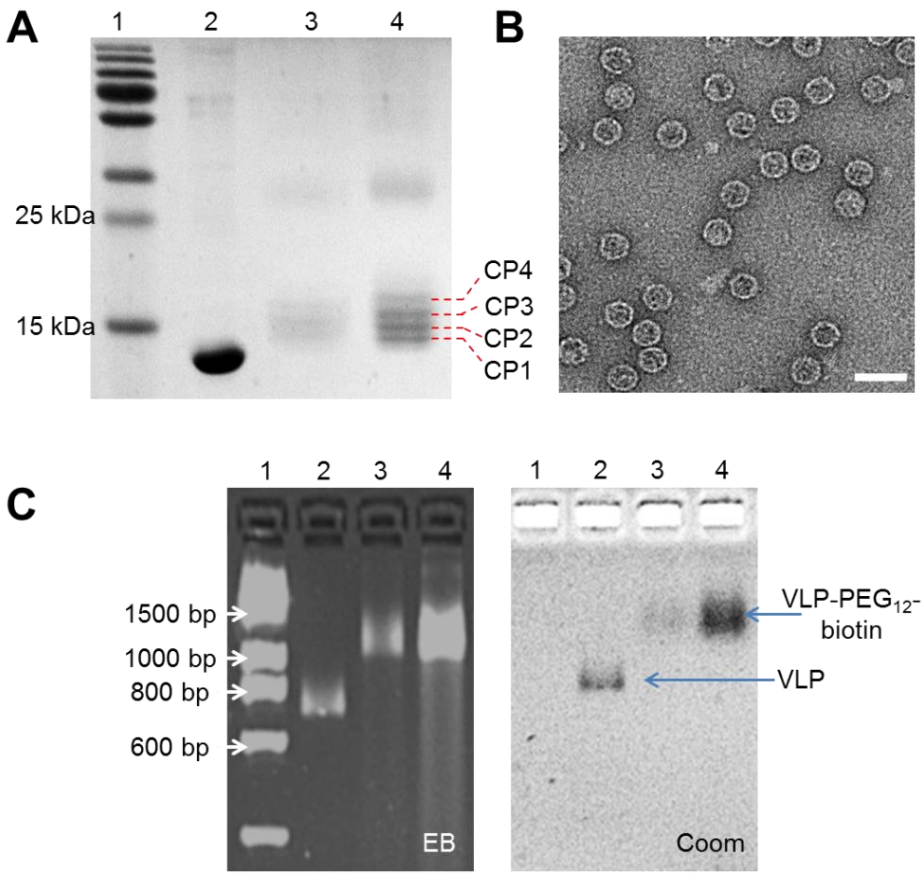


**Figure 3.11. Analysis of VLP-PEG$_{12}$-biotin.** VLP(TR-Cy5) was reacted with NHS-(PEG)$_{12}$-biotin at a PEG : surface amine ratio of 100 : 1. The product was purified through NAP-5 columns and then analysed. **(A)** SDS-PAGE. 1: Fermentas PageRuler prestained ladder; 2: VLP; 3: 1 µL VLP-PEG$_{12}$-biotin; 4: 5 µL VLP-PEG$_{12}$-biotin. The gel was visualised by silver nitrate staining. Putative bands resembling CP attached to one (CP1), two (CP2), three (CP3) or four (CP4) molecules of PEG$_{12}$-biotin are indicated on the right. **(B)** TEM. Scale bar = 50 nm. (C) Native 2% (w/v) agarose gel electrophoresis. 1: HyperLadder I; 2: VLP; 3: 1 µL VLP-PEG$_{12}$-biotin; 4: 5 µL VLP-PEG$_{12}$-biotin. The gel was visualised by ethidium bromide or Coomassie staining. Bands representing VLP and VLP-PEG$_{12}$-biotin are indicated on the right.

The product was analysed by SDS-PAGE (Figure 3.11A), which showed three high intensity bands just above where the unmodified CP monomer is expected (13.7 kDa, lane 2). Three possible sites for conjugation are present on each CP

monomer (Figure 1.12). The molecular weights of these species are consistent with them being CP conjugated to one, two, or three molecules of $PEG_{12}$-biotin. Low intensity bands were also observed above the three main bands – it is possible that a small fraction of VLPs were dissociated or partially assembled, exposing internal amines that would otherwise be inaccessible to the NHS ester, and thus enabling the conjugation of CP to more than three molecules of $PEG_{12}$-biotin. Another possibility is that the NHS terminus of some NHS-$PEG_{12}$-biotin entered VLPs via ~1.7 nm pores that are present on the VLP surface (Karin Valegård, 1990), gaining access to internal lysines for conjugation.

The intact nature of VLP-$PEG_{12}$-biotin was confirmed by TEM (Figure 3.11B), although it did not clearly show particles of an increased size or the presence of a PEG layer on the VLP surface. Analysis on a native agarose gel revealed that VLP-$PEG_{12}$-biotin had a notably lower electrophoretic mobility compared to VLP (Figure 3.11C), which is consistent with a larger particle.

The cellular uptake of VLP, VLP-Tf and VLP-$PEG_{12}$-biotin was then assessed. HeLa cells were harvested and pipetted into test tubes, to which 10 nM TR-Cy5 packaged inside VLP, VLP-Tf or VLP-$PEG_{12}$-biotin was added and incubated for up to 24 h. The cells were washed, fixed and resuspended in DPBS prior to flow cytometry analysis (Figures 3.12, 3.13). Two gates were set up, as previously described (Galaway, 2011). The first gate used the forward and side scatters to distinguish between cell and non-cell events. The second gate determined if a cell had taken up TR-Cy5: cells with Cy5 fluorescence greater than that of 99% of untreated cells were designated as positive for TR-Cy5 uptake, or ‘transfected’. This is demonstrated in the sample flow cytometry histograms in Figure 3.12.

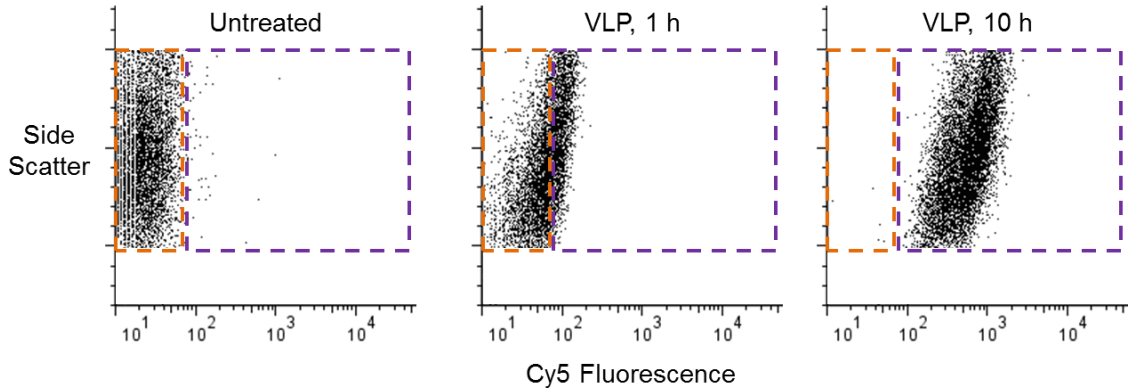


**Figure 3.12. Flow cytometry analysis of VLP uptake.** Sample flow cytometry histograms showing the effects of incubating HeLa cells with VLP(TR-Cy5) on their Cy5 fluorescence. Each dot represents an individual cell. Untreated cells are shown in the left-most histogram; these were used to draw gates to determine whether a cell was negative (orange box) or positive (purple box) for VLP(TR-Cy5) uptake.

Information extracted from the flow cytometry histograms, including the percentage cell uptake (Figure 3.13A) and the mean Cy5 fluorescence of cells (Figure 3.13B), are presented as scatter plots with respect to incubation time. The percentage uptake for both VLP and VLP-Tf increased with time (Figure 3.13A), although it saturated at 100% much quicker for VLP-Tf (~30 min) than for VLP (~180 min). This is consistent with previous reports (Galaway, 2011), and likely due to the faster uptake of VLP-Tf via Tf receptor-mediated endocytosis. VLP-$PEG_{12}$-biotin was still taken up by HeLa cells, but significantly slower than unmodified VLPs – only saturating in percentage uptake at ~350 min. Markedly different profiles were also observed for the mean Cy5 fluorescence of cells incubated with VLP and VLP-Tf over 24 h (Figure 3.13B). Although the two profiles shared similarly shaped curves – peaking at 10 h, the Cy5 fluorescence of VLP-Tf transfected cells was significantly greater than that

of VLP transfected cells at all time points. There was a reduction in mean Cy5 fluorescence after 10 h for all three transfections. This might be the result of a dilution of TR-Cy5 due to cell division.

An interesting observation was that, although the VLP and VLP-Tf curves almost converge at 960 min, a significant difference was seen again at 1440 min – as the mean Cy5 fluorescence of VLP transfected cells kept decreasing, but that of VLP-Tf transfected cells increased again. This might be due to the faster rate of uptake of VLP-Tf by newly divided HeLa cells compared to VLP, and also suggests that the concentration of TR-Cy5 used was not limiting in this time frame. Further, the mean Cy5 fluorescence of VLP-$PEG_{12}$-biotin transfected cells peaked at only 488.3±100.9, which was a ~2-fold reduction compared to VLP (Figure 3.13B). Again, a decrease in mean Cy5 fluorescence was observed after 10 h, suggesting dilution due to cell division. The reduced rate of VLP-$PEG_{12}$-biotin uptake suggests that PEGylation successfully mitigated non-specific VLP uptake by HeLa cells. The low level of uptake of VLP-$PEG_{12}$-biotin observed might be due to interactions between biotin and cell surface receptors.

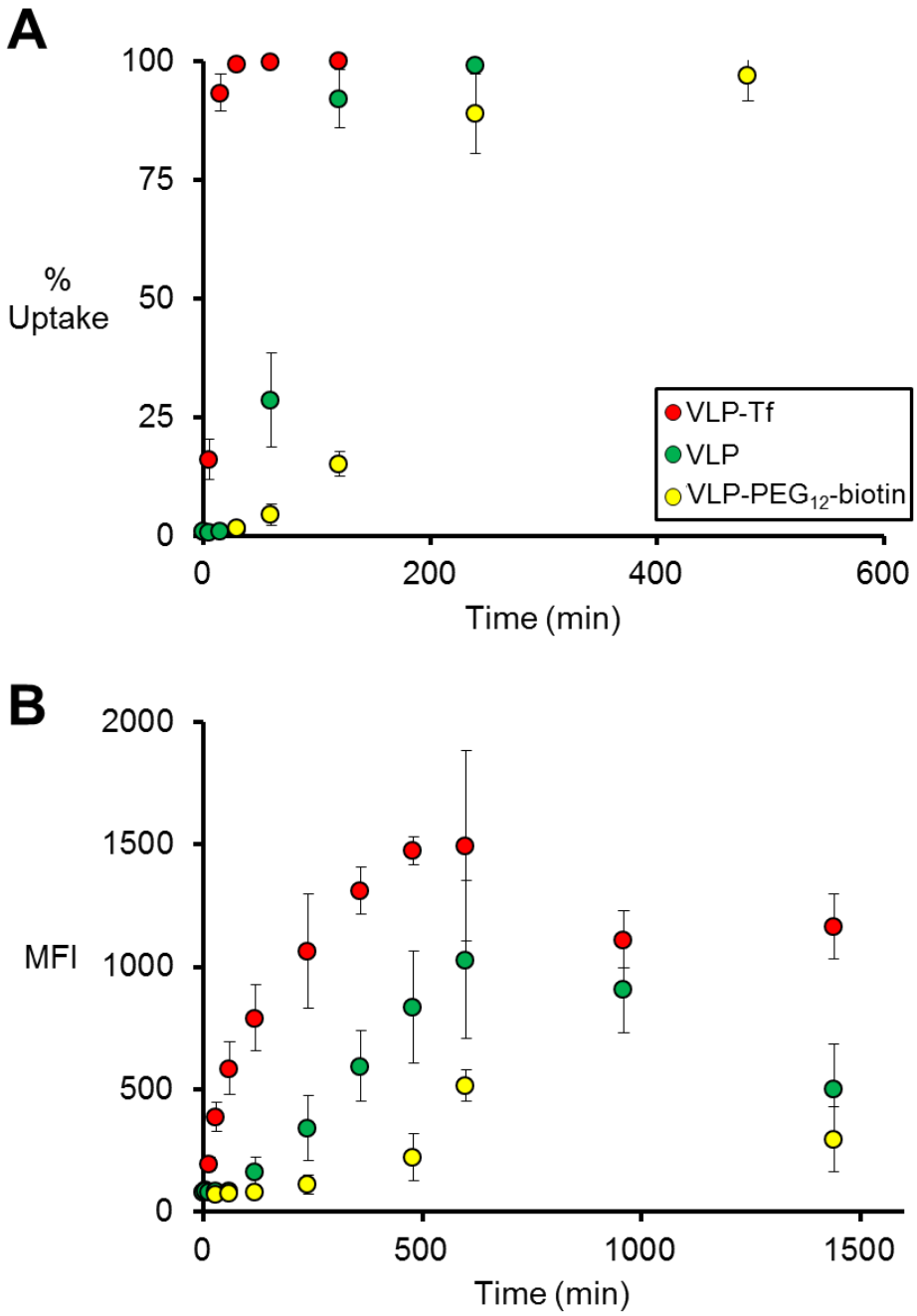


**Figure 3.13. Time-dependent cellular uptake of VLP, VLP-Tf and VLP-PEG$_{12}$-biotin.** Scatter plots showing the **(A)** percentage of HeLa cells positive for uptake, and **(B)** mean Cy5 fluorescence intensity (MFI) of HeLa cells after incubation with 10 nM TR-Cy5 packaged inside VLP, VLP-Tf or VLP-PEG$_{12}$-biotin for up to 24 h. Error bars indicate the standard deviation of three repeats.

### 3.2.7 Preparation and analysis of VLP-$PEG_{24}$-Tf

Although the surface attachment of $PEG_{12}$-biotin significantly mitigates non-specific uptake of VLPs, the main problem with its use is the difficulty of attaching targeting ligands to the PEG terminus via biotin. One possibility was to couple streptavidin to the targeting ligands, which could then be non-covalently attached to VLP-$PEG_{12}$-biotin via high affinity interactions between biotin and streptavidin. The use of the streptavidin-biotin system for conjugating two molecules has been utilised for a range of chemical and biological applications (Dundas et al., 2013). However, streptavidin is relatively large (~53 kDa), and its coupling to the targeting ligands would add unwanted complexity to the VLP delivery system. Furthermore, streptavidin is composed of four identical monomers and can bind to four molecules of biotin, this would likely result in the formation of large aggregates with the crosslinking of multiple VLPs.

The use of $SM(PEG)_{24}$ as a crosslinker between MS2 VLP and targeting ligands has previously been reported (Ashley et al., 2011). It is a hetero-bifunctional linker, ~9.5 nm in length, and facilitates amine-to-thiol conjugations with an NHS terminus and a maleimide terminus. The availability of amines of the MS2 VLP surface, and the possibility of modifying the Tf surface with the previously used SATA meant that $SM(PEG)_{24}$ should be suitable for their coupling. First, a range of $SM(PEG)_{24}$ to VLP surface amine molar ratios from 10 : 1 to 2,000 : 1 were tested to identify optimal conditions for PEGylation. VLP(TR-Cy5) was reacted with different amounts of $SM(PEG)_{24}$ in pH 8.3 HEPES at room temperature for 30 min; the product was eluted through a NAP-5 column and concentrated using a 100 kDa MWCO spin concentrator, before analysis (Figure 3.14).

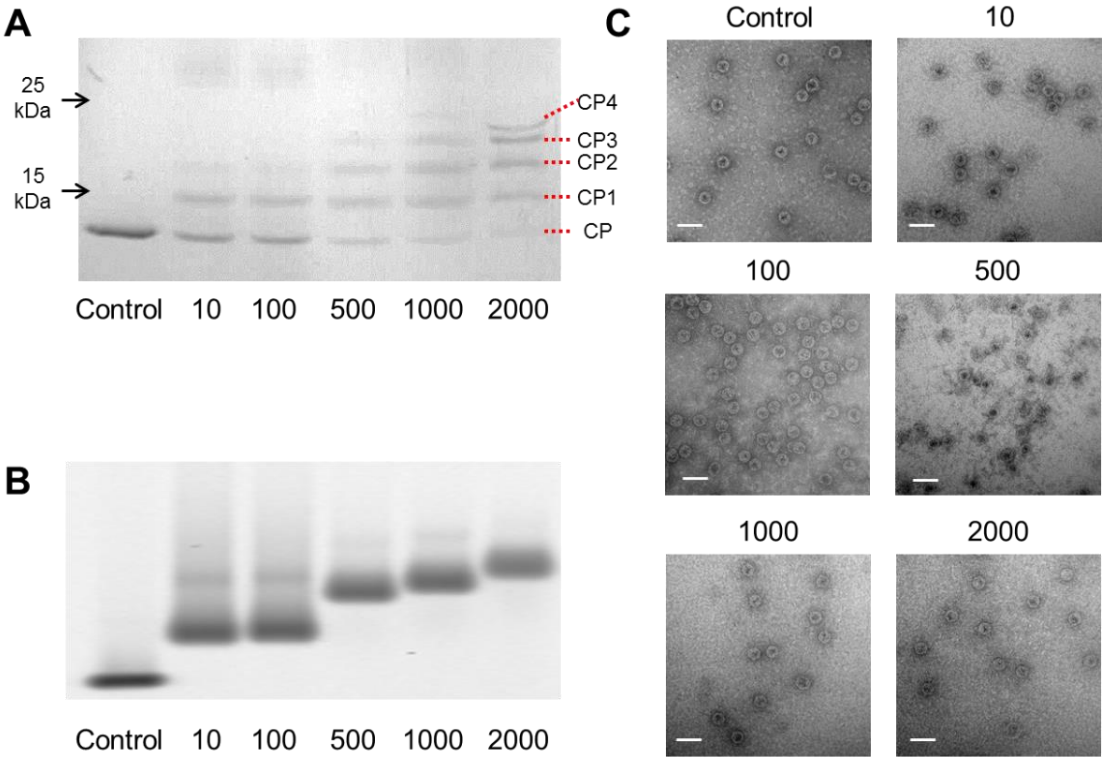


**Figure 3.14. Analysis of VLP-PEG$_{24}$.** VLP(TR-Cy5) was reacted with SM(PEG)$_{24}$ at various PEG : surface amine molar ratios, including 10:1, 100:1, 500:1, 1000:1 and 2000:1. The resulting particles were eluted through NAP-5 columns and then analysed. **(A)** SDS-PAGE visualised by Coomassie staining. Positions of 15 kDa and 25 kDa protein markers are indicated on the left. Putative bands resembling unmodified CP, and CP attached to one (CP1), two (CP2), three (CP3) or four (CP4) molecules of PEG$_{24}$ are indicated on the right. **(B)** Native 2% (w/v) agarose gel visualised by Cy5 fluorescence scanning. **(C)** TEM. Scale bar = 50 nm.

The successful coupling of SM(PEG)$_{24}$ to MS2 CP was confirmed by SDS-PAGE (Figure 3.14A), which showed bands above the unmodified CP band, with molecular weights corresponding to CP modified with one, two or three molecules of PEG$_{24}$. The distribution of intensity shifted towards the higher bands, indicating a greater extent of PEGylation, with greater SM(PEG)$_{24}$ to amine ratios. As observed previously with NHS-PEG$_{12}$-biotin (Figure 3.11A), a

fourth band was observed which was likely CP conjugated to four PEG molecules. This species only appeared at higher $SM(PEG)_{24}$ : amine ratios, at 1,000 : 1 and 2,000 :1, suggesting that high levels of PEGylation might destabilise VLPs to expose additional interior amines for conjugation. The products were also analysed by native agarose gel electrophoresis (Figure 3.14B), which showed that as the $SM(PEG)_{24}$ : amine ratio increased, the electrophoretic mobility of the products decreased, consistent with larger particles. The ratio of 500 : 1 seemed to be suitable – this was a good compromise between maximising the extent of VLP surface PEGylation and minimising the coupling of PEG to interior amines. Finally, TEM analysis of the products showed intact VLP particles and no evidence of aggregate formation, even at the higher $SM(PEG)_{24}$ : amine ratios used (Figure 3.14C).

A strategy for conjugating Tf to the VLP surface via $SM(PEG)_{24}$ was devised (Figure 3.15). VLP(TR-Cy5) was first reacted with $SM(PEG)_{24}$ – at a molar ratio of 500 PEG : 1 amine – in pH 8.3 HEPEs at room temperature for 30 min. Tf was reacted with the previously used SATA to introduce thiol groups to its surface (Figure 3.15B). As before, the thiols were deprotected via the addition of hydroxylamine hydrochloride. The two reactions were eluted through NAP-5 columns to remove excess reagents, and then pooled to allow maleimide and thiol groups to react, resulting in the production of VLP(TR-Cy5)-$PEG_{24}$-Tf.

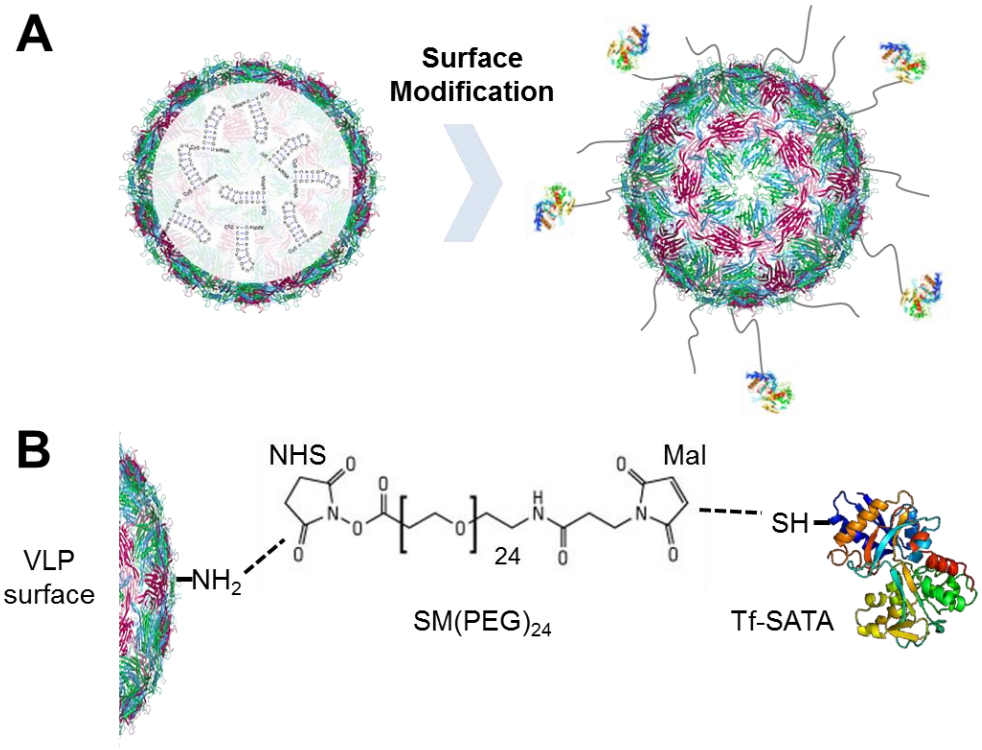


**Figure 3.15. Schematic depicting the preparation of VLP-PEG$_{24}$-Tf. (A)** Surface decoration of loaded VLPs with SM(PEG)$_{24}$ and the targeting ligand, Tf. **(B)** Conjugation chemistry used for VLP surface modification. SM(PEG)$_{24}$ is a hetero-bifunctional crosslinker, with an NHS terminus that reacts with VLP surface amines, and a maleimide terminus that reacts with SATA-modified Tf.

The product was incubated with β-mercaptoethanol overnight to quench unreacted maleimide groups. This was not done previously in the synthesis of VLP-Tf (Galaway and Stockley, 2013) – although maleimide groups readily hydrolyse (Hermanson, 2013), it is unknown whether hydrolysed maleimide groups can interact with the cell surface, thus they might have contributed to the non-specific uptake previously observed. The quenched product was purified by linear 15-45% (w/v) SDC, the fluorescent band resembling VLP(TR-Cy5)-PEG$_{24}$-Tf was collected and concentrated using 100 kDa MWCO spin concentrators, prior to analysis (Figure 3.16). The $A_{649}$ of the sample was

measured to calculate the concentration of Cy5 present, which was used to estimate the yield (~25% of starting material).

Size exclusion chromatography analysis revealed different elution volumes for VLP (11 mL), VLP-$PEG_{24}$ (10.5 mL) and VLP-$PEG_{24}$-Tf (10 mL) (Figure 3.16A), suggesting an increase in particle size with additional components. This was consistent with the linear 15-45% (w/v) sucrose gradients (Figure 3.16B), which showed that VLP-$PEG_{24}$-Tf migrated faster through the gradient relative to VLP-$PEG_{24}$, suggesting the presence of larger and denser particles. Additionally, Cy5 fluorescence could be seen at the top of the VLP-$PEG_{24}$-Tf gradient, suggesting the presence of free TR-Cy5. These might be the result of the destabilisation of some VLPs caused by the conjugation reactions.

Successful conjugation was confirmed by Western blotting (Figure 3.16C): a band was present in the VLP-$PEG_{24}$-Tf lane, which was larger than Tf and visualised by both anti-MS2 CP and anti-Tf primary antibodies, indicating the co-presence of CP and Tf. The bands were analysed by 2D densitometry, which estimated that 96.7±2.0% of CPs were conjugated to at least one molecule of $PEG_{24}$, and that 8.0±1.5% of CPs were conjugated to $PEG_{24}$ and Tf. Additionally, on average each VLP was coupled to 7.4±3.3 molecules of Tf. This was relatively low compared to the previously observed 13.5±3.1 Tf per VLP for VLP-Tf, even though the same Tf : VLP ratios were used in both conjugation reactions. The discrepancy might be due to the number estimated using Western blotting / 2D densitometry being an underestimate, as conjugation to $PEG_{24}$ and CP might affect the capacity of some Tf to bind antibodies, resulting in a lower intensity band.

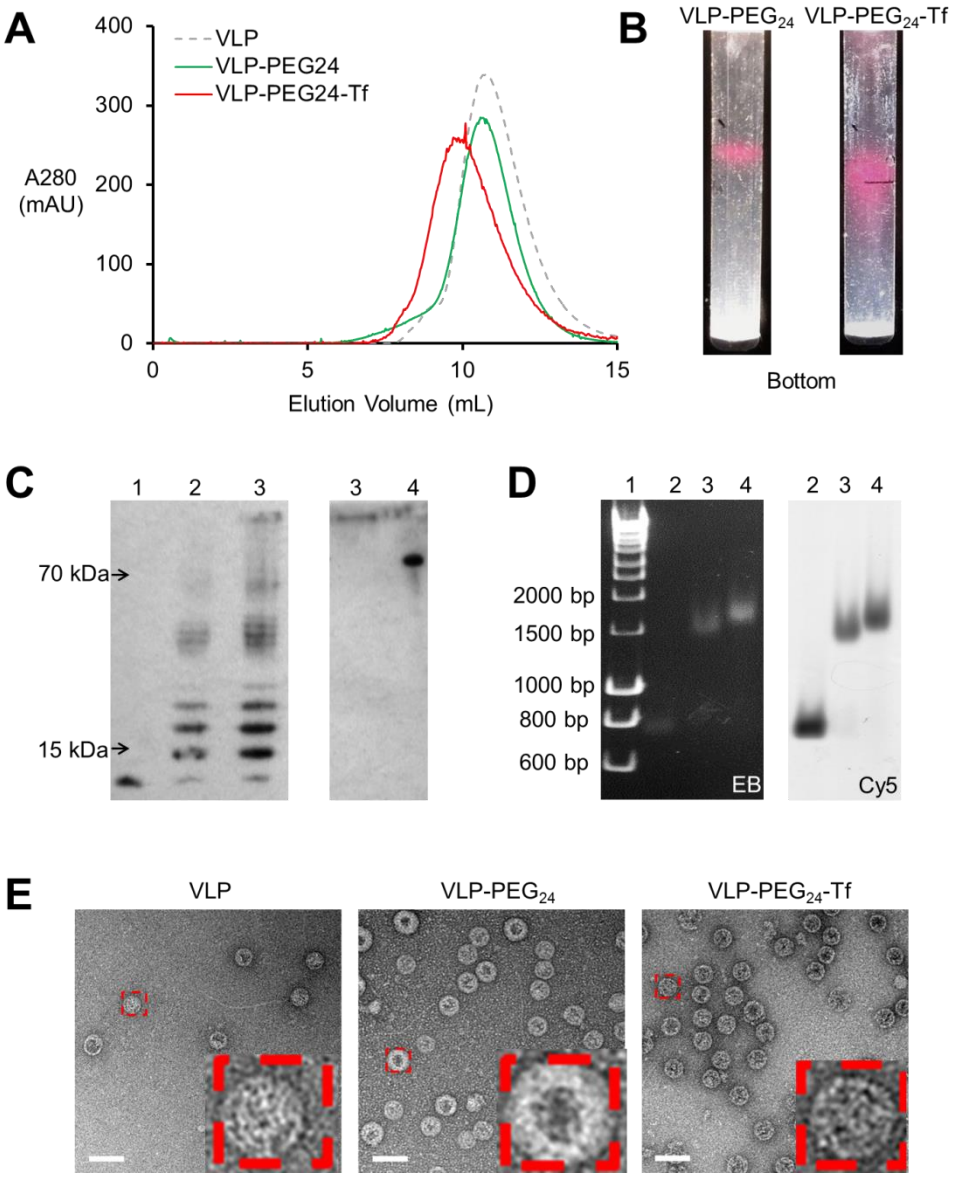


**Figure 3.16. Biochemical analysis of VLP-PEG$_{24}$-Tf. (A)** Superose 6 size exclusion chromatogram of VLP, VLP-PEG$_{24}$, and VLP-PEG$_{24}$-Tf; absorbance curves at 280 nm are displayed. **(B)** Linear 15-45% (w/v) sucrose gradients of VLP-PEG$_{24}$ (left) and VLP-PEG$_{24}$-Tf (right). Photos were taken at a fixed position in front of the gradients. **(C)** Western blot analysis. 1: VLP; 2: VLP-PEG$_{24}$; 3: VLP-PEG$_{24}$-Tf; 4: Tf. Anti-MS2 CP antibodies (left) or anti-human Tf antibodies (right) were used as primary antibodies. **(D)** Native 2% (w/v) gel electrophoretic analysis. 1: HyperLadder I; 2: VLP; 3: VLP-PEG$_{24}$; 4: VLP-PEG$_{24}$-Tf. The gel was visualised by ethidium bromide staining or Cy5 fluorescence scanning. **(E)** TEM images of VLP, VLP-PEG$_{24}$ and VLP-PEG$_{24}$-Tf. Scale bar = 50 nm. Red boxes of the same size are shown in each image, enclosing individual MS2 VLPs; these are scaled up in the bottom right corners for clarity.

Native 2% (w/v) agarose gel electrophoresis revealed a decrease in electrophoretic mobility as the $PEG_{24}$ and Tf layers were added (Figure 3.16D), indicating increased particle size after the respective conjugation reactions. Finally, TEM analysis showed the intact nature of the VLP-$PEG_{24}$-Tf products; no aggregate structures were observed (Figure 3.16E). Furthermore, a clear difference in size could be seen between VLP and VLP-$PEG_{24}$ / VLP-$PEG_{24}$-Tf.

### 3.2.8 Cellular uptake of VLP-$PEG_{24}$-Tf

The effects of adding Tf on the cell binding and internalisation of VLP-$PEG_{24}$-Tf were investigated. HeLa cells were grown on glass coverslips, and incubated with 100 nM TR-Cy5, packaged inside VLP, VLP-$PEG_{24}$ or VLP-$PEG_{24}$-Tf at 4$^{o}$C for 1 h, to enable cell surface binding but minimise receptor-mediated endocytosis (Klausner et al., 1983). The cells were washed with DPBS to remove unbound or weakly bound particles, and incubated at 37$^{o}$C for 1 h to allow internalisation of surface-bound particles. They were then washed and visualised by deconvolution microscopy (Figure 3.17A). Cy5 fluorescence was only observed in cells incubated with VLP-$PEG_{24}$-Tf, suggesting that Tf allowed tight binding of VLP-$PEG_{24}$-Tf to the cell surface via Tf receptors, which were not removed with DPBS wash steps and subsequently internalised at 37$^{o}$C. It is interesting that different levels of Cy5 fluorescence were observed in the cells visualised. This might reflect heterogeneity in the cell population in their surface Tf receptor expression. Contrastingly, no Cy5 fluorescence was observed for the VLP or VLP-$PEG_{24}$ incubations, suggesting that neither could bind to nor internalise into HeLa cells under the experimental conditions used.

Flow cytometry was also used to assess cellular uptake as before. However, cells were grown on 24 well plates (instead of test tubes), and then incubated with 10 nM TR-Cy5 packaged inside VLP, VLP-$PEG_{24}$, or VLP-$PEG_{24}$-Tf for 2 h or 18 h, before they were harvested and processed for flow cytometry analysis (Figure 3.17B). At 2 h, PEGylation resulted in a 4-fold reduction in the mean Cy5 fluorescence of transfected cells (25.7±8.3 AU for VLP-$PEG_{24}$; 109.0±33.7 AU for VLP); addition of the targeting ligand, Tf, resulted in a 9-fold increase in mean Cy5 fluorescence (222.3±19.2 AU). Further addition of 100 nM free Tf reduced mean Cy5 fluorescence 3-fold (71.7±11.4 AU), suggesting a Tf-dependent mechanism of cell entry via Tf receptor-mediated endocytosis. Intriguingly, this was still higher than the Cy5 fluorescence of VLP-$PEG_{24}$ – similar results were also previously observed with VLP-Tf (Galaway, 2011). Two possible reasons for this are: (i) Tf receptors were rapidly recycled to the cell surface (Ciechanover et al., 1983), and could not be fully saturated by the free Tf used, (ii) multivalent display of Tf on VLP-$PEG_{24}$-Tf favoured, to some extent, Tf receptor-binding and receptor mediated endocytosis over free Tf. Similar results were observed at the 18 h time point (Figure 3.17B): PEGylation significantly reduced the mean Cy5 fluorescence of transfected cells (251.0±76.4 AU for VLP-$PEG_{24;}$ 657.7±45.8 for VLP), whilst Tf-targeting led to notably enhanced uptake (1020.0±67.6 AU).

These results suggest that, although VLP could not tightly bind to nor quickly internalise into HeLa cells, at longer incubation times, they were still taken up non-specifically by cells. This is consistent with previous results (Figure 3.13). Importantly, this non-specific uptake could be significantly reduced by surface coating VLPs with $PEG_{24}$, likely due to the ability of PEG to mask VLP surface

epitopes that enable non-specific cell interactions. The further addition of a layer of targeting ligands, Tf, on the PEG termini led to significantly higher uptake, likely via Tf receptor-mediated endocytosis.

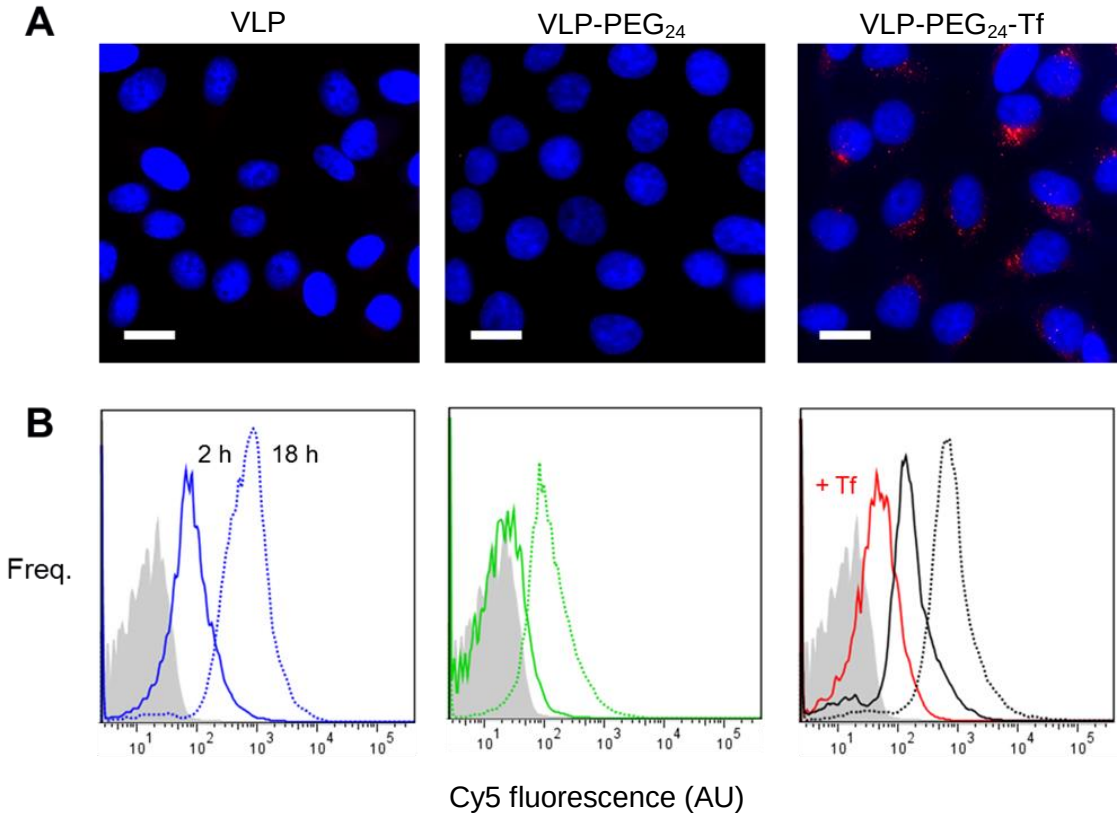


**Figure 3.17. Analysis of VLP-PEG$_{24}$-Tf binding and internalisation by HeLa cells. (A)** Cells were incubated with 100 nM TR-Cy5 packaged inside VLP, VLP-PEG$_{24}$ or VLP-PEG$_{24}$-Tf at 4$^{o}$C for 1 h. After washing with DPBS, cells were incubated at 37$^{o}$C for 1 h, and visualised by deconvolution microscopy. DAPI staining (nuclei) is depicted in blue; Cy5 fluorescence (siRNA) is depicted in red. Scale bar = 15 µm. **(B)** Flow cytometry analysis of cells incubated with 10 nM siRNA packaged inside VLP (blue), VLP-PEG$_{24}$ (green), VLP-PEG$_{24}$-Tf (black) or VLP-PEG$_{24}$-Tf plus 100 nM free Tf (red). 2 h and 18 h time points are represented by solid and dotted lines, respectively. Grey shaded curves depict untreated cells. Freq. = frequency; AU = arbitrary units.

### 3.2.9 Effects of siRNA delivery on BCL2 expression

The capacity of VLP-$PEG_{24}$-Tf to deliver siRNAs to HeLa cells was then investigated. TR-siRNA (either TR-BCL2 or TR-Control) encapsidated VLP-$PEG_{24}$-Tf was prepared using the same protocol as for TR-Cy5 encapsidated VLP-$PEG_{24}$-Tf, described above.

Firstly, the effect of siRNA delivery on cellular BCL2 protein expression was assessed, using intracellular antibody staining and flow cytometry. HeLa cells were incubated with TR-siRNA packaged inside various VLP formulations for up to 72 h, before they were fixed and washed with DPBS. Cells were incubated with FITC-conjugated anti-BCL2 antibodies in a permeabilisation buffer at $4^{o}C$ for 1 h, and then analysed by flow cytometry. The mean FITC fluorescence of untreated cells were assumed to represent 100% BCL2 expression, to which the fluorescence of siRNA treated cells were compared to calculate relative percentage BCL2 expressions. In addition, a FITC-conjugated isotype control antibody, which does not bind human BCL2, was used to stain untreated cells to determine non-specific background fluorescence, which was subtracted from the mean fluorescence of anti-BCL2 antibody stained cells for baseline correction.

HeLa cells were incubated with 10 nM TR-BCL2 packaged inside VLP-$PEG_{24}$-Tf for 0 h, 24 h, 48 h or 72 h, and assayed for BCL2 expression. Delivered siRNAs reduced BCL2 expression in a time-dependent manner (Figure 3.18A): 24 h incubation resulted in a slight decrease in BCL2 expression compared to the 0 h control (90.0±11.9%), whereas more significant reductions were observed at 48 h (53.6±6.8%) and 72 h (28.0±13.6%) time points. The relatively small effect at

24 h might allude to the time needed for VLP-$PEG_{24}$-Tf to be internalised into HeLa cells, for the acid-triggered dissociation of VLPs and, importantly, the endosomal escape of siRNA into the cytosol, before entry into the RNAi pathway. VLP-$PEG_{24}$-Tf delivered siRNAs also induced BCL2 knockdown in a concentration-dependent manner (Figure 3.18B): 69.8±10.5%, 53.6±6.8%, and 39.7±10.9% BCL2 expressions were observed following 48 h incubations with 5 nM, 10 nM and 25 nM siRNA, respectively.

Significant knockdown was observed with 10 nM siRNA and 48 h incubation time, which was chosen as the condition for assessing relative BCL2 expression following siRNA delivery by different VLP formulations (Figure 3.19C). TR-BCL2 delivered by VLP, VLP-$PEG_{24}$ and VLP-$PEG_{24}$-Tf reduced BCL2 expression in HeLa cells to 45.3±10.3%, 75.8±7.7% and 53.6±6.8%, respectively. This is consistent with the cellular uptake results, and suggests that the knockdown effects correlated positively with the uptake of siRNAs. Further addition of 100 nM free Tf to VLP-$PEG_{24}$-Tf increased BCL expression to 88.9±14.6%, suggesting that VLP-$PEG_{24}$-Tf delivered siRNAs via Tf receptor-mediated endocytosis. Lastly, negligible changes in BCL2 expression were observed when cells were incubated with TR-Control packaged inside VLP-$PEG_{24}$-Tf (97.2±9.1%). The control siRNA sequence is a scrambled version of the anti-*BCL2* siRNA sequence, and does not have complementarity to any known human mRNA. This result suggests that the observed knockdown of BCL2 were siRNA sequence-dependent.

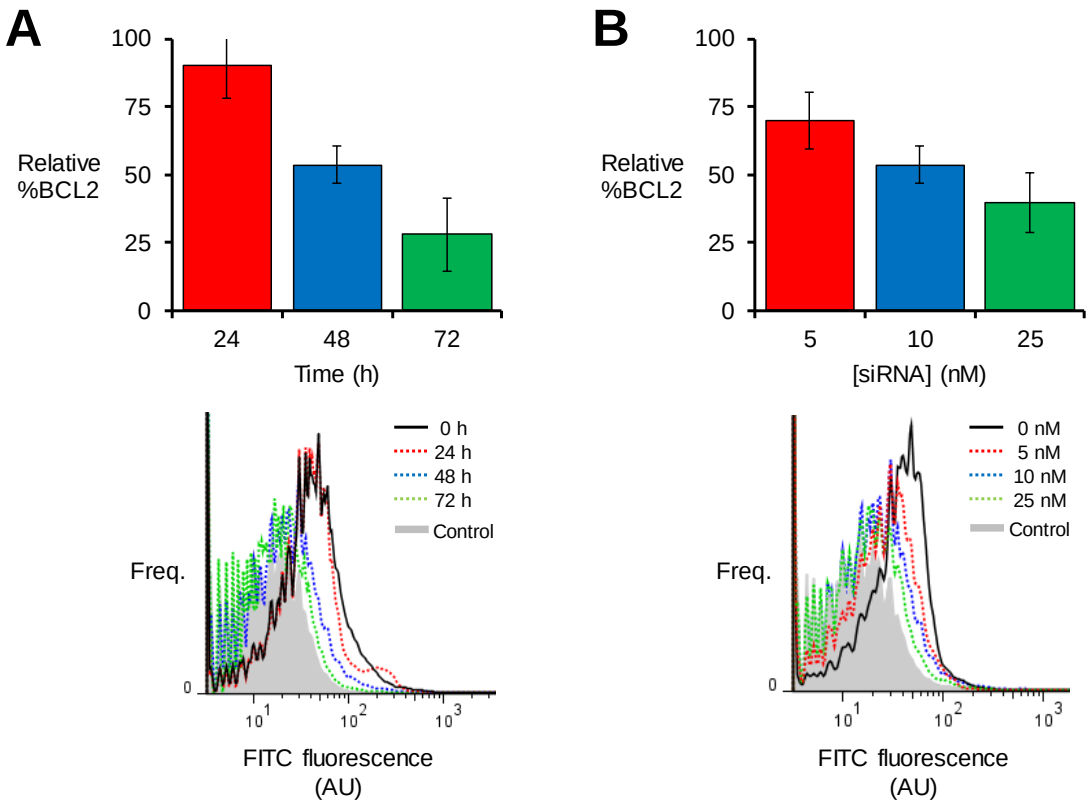


**Figure 3.18. Relative BCL2 expression in HeLa cells after siRNA delivery.** After treatment with either **(A)** 10 nM TR-BCL2 packaged inside VLP-PEG$_{24}$-Tf for 0, 24, 48 or 72 h, or **(B)** 0 nM, 5 nM, 10 nM or 25 nM TR-BCL2 siRNA packaged inside VLP-PEG$_{24}$-Tf for 48 h, cells were stained with FITC-conjugated anti-BCL2 antibodies, washed, and analysed by flow cytometry. The mean FITC fluorescence of untreated cells (0 h and 0 nM siRNA) were designated as 100% BCL2 expression, to which the FITC fluorescence of treated cells were compared to calculate relative percentage BCL2 expressions. Error bars indicate standard deviation of three repeats. Corresponding flow cytometry histograms are displayed under the bar charts. Black curves represent 0 h and 0 nM controls; grey shaded curves show the background fluorescence, determined by staining cells with a FITC-labelled isotype control antibody.

It is notable that, because RNAi occurs in the cytosol, the successful knockdown of BCL2 by delivered siRNAs could serve as indirect evidence that siRNAs were able to escape from VLP-PEG$_{24}$-Tf as well as the endosome to mediate their effect.

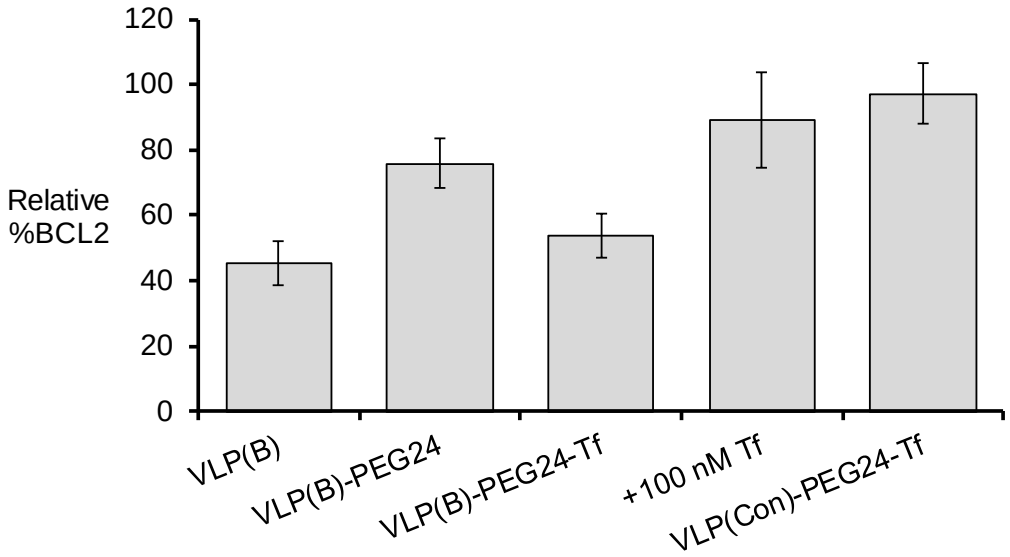


**Figure 3.19. Comparative BCL2 expression in HeLa cells after siRNA delivery.** HeLa cells were incubated with 10 nM TR-BCL2 packaged inside (from left) VLP, VLP-$PEG_{24}$, VLP-$PEG_{24}$-Tf, or VLP-$PEG_{24}$-Tf plus 100 nM free Tf, or with 10 nM TR-Control packaged inside VLP-$PEG_{24}$-Tf for 48 h, and then assayed for BCL2 expression. Error bars indicate standard deviation of three repeats.

### 3.2.10 Cytotoxic effects of siRNA delivery

To assess the cytotoxic effects of TR-BCL2 delivery by VLP-$PEG_{24}$-Tf, a flow cytometry assay was used, based on established protocols (Galaway, 2011). HeLa cells were incubated with various treatments on 24 well plates. After harvesting with TrypLE, cells were washed, resuspended into annexin binding buffer and then stained with FITC-conjugated annexin V and propidium iodide, before flow cytometry analysis. Annexin V binds with high affinity to the apoptotic marker, phosphatidylserine; propidium iodide intercalates with nucleic acids but is only taken up by cells undergoing late stage apoptosis or necrosis, due to the loss of membrane integrity.

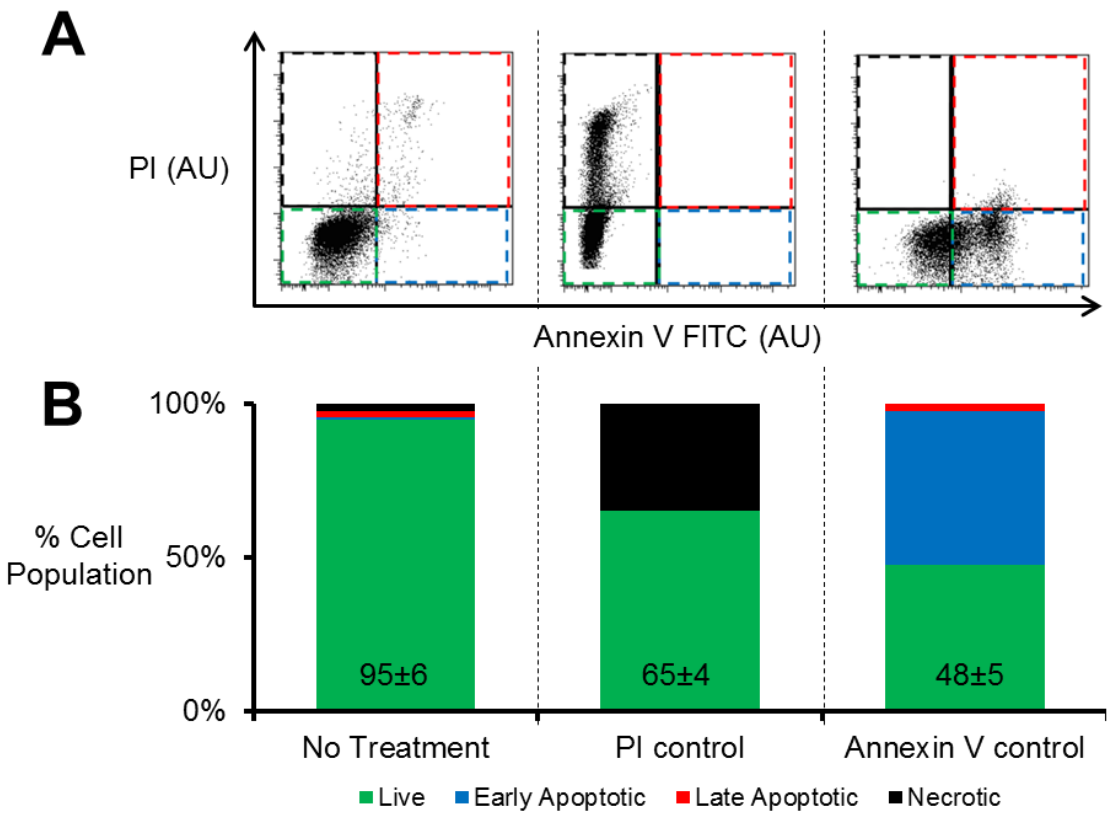


**Figure 3.20. Flow cytometry analysis of cell toxicity.** As a necrotic control, HeLa cells were exposed to UV radiation for 2 h, and stained with propidium iodide (PI). As an apoptotic control, HeLa cells were incubated with 50 µM cisplatin for 24 h, and stained with annexin V-FITC. **(A)** Flow cytometry histograms of (un)treated cells. Gates were drawn using untreated cells, stained with both PI and annexin V-FITC, which resembles a quadrant. Cells negative for PI and FITC fluorescence were designated live (green box); cells positive for FITC fluorescence only were designated early apoptotic (blue box); cells positive for PI and FITC fluorescence were designated late apoptotic (red box); and cells positive for PI fluorescence only were designated necrotic (black box). **(B)** Bar charts displaying the relative percentage of cell populations that were live (green), early apoptotic (blue), late apoptotic (red), or necrotic (black). The percentages shown represent the average of three repeats. Numbers indicate mean percentage cell viability ± SD.

Initial controls were set up as follows. Untreated cells were stained with annexin V-FITC and propidium iodide, and analysed by flow cytometry. A scatter plot of

propidium iodide fluorescence against FITC fluorescence is shown (Figure 3.20A); this was used to establish gates to determine if cells were positive for staining by the two fluorescent dyes relative to untreated cells. The gates resemble a quadrant, which divide the cells, based on their fluorescence emissions, into live, early apoptotic, late apoptotic and necrotic populations. Cells negative for both annexin V and propidium iodide staining were designated live (green); those positive for annexin V staining only were designated early apoptotic (blue); those positive for propidium iodide staining only were designated necrotic (black); and those positive for both annexin V and propidium iodide staining were designated late apoptotic (red). Each cell population was then presented as a percentage of the total cell population, shown in Figure 3.20B. As expected, the majority of untreated HeLa cells were viable (95±6%); a small population of cells were positive for FITC or propidium iodide staining, thus showing evidence of background cytotoxicity. It is unclear whether these cells were naturally present in the cell population or a result of the conditions used in the assay.

As a necrotic control, HeLa cells were exposed to UV radiation for 2 h and stained with propidium iodide. As an apoptotic control, cells were treated with 50 μM cisplatin for 24 h, and stained with annexin V-FITC. The percentage of live cells after these treatments decreased to 65±4% and 48±5%, respectively, with cells taking up propidium iodide or binding annexin V-FITC (Figure 3.20B). The conditions used in these controls did not completely eliminate the live cell populations. A smear was observed for both treatments, possibly suggesting heterogeneity within the cell population in their sensitivity to the treatments or to the assay used. Comparison between untreated cells stained with both annexin

V-FITC and propidium iodide with UV-exposed cells only stained with propidium iodide shows that there was background binding of annexin V-FITC by untreated live cells (Figure 3.20A). A smaller background uptake of propidium iodide by untreated cells was also observed by comparing the untreated and apoptotic controls (Figure 3.20A).

BCL2 is an anti-apoptotic factor, thus its siRNA-mediated knockdown should trigger apoptosis in cells. Although apoptotic cells can progress to necrosis (Kravchenko-Balasha et al., 2009), the apoptotic state should still be detectable under the experimental conditions, as siRNA effects take 24-72 h. It has been reported that cells can persist in an apoptotic state with a duration that largely correlates with BCL2 protein levels in the cell, and that a longer duration increases the chance of cells escaping apoptosis (Skommer et al., 2010).

HeLa cells were incubated with 10 nM TR-BCL2 packaged inside VLP-$PEG_{24}$-Tf for 0 h, 24 h, 48 h or 72 h, stained with annexin V-FITC and propidium iodide, and analysed by flow cytometry (Figure 3.21A). Significant toxicity was observed at 48 h and 72 h, with 39±9% and 26±4% of the cell population remaining viable, respectively. Little change in percentage cell viability was observed at 24 h (86±6%) compared to the 0 h control (88±5%). These results indicate a correlation between BCL2 expression and cytotoxicity: at 24 h, TR-BCL2 delivered by VLP-$PEG_{24}$-Tf only reduced BCL2 protein expression by ~10%, whereas more significant knockdown occurred after 48 h (~46%) and 72 h (~70%). There was a diminishing return on the cytotoxic effects of siRNA delivery as the incubation time increased, which might be caused by the dilution of siRNAs from cell division (HeLa cells have a doubling time of ~24 h). Other

factors also cannot be ruled out, such as heterogeneity within the cell population – some cells might be more sensitive to BCL2 knockdown than others, and the development of resistance to the treatment in a subset of cells.

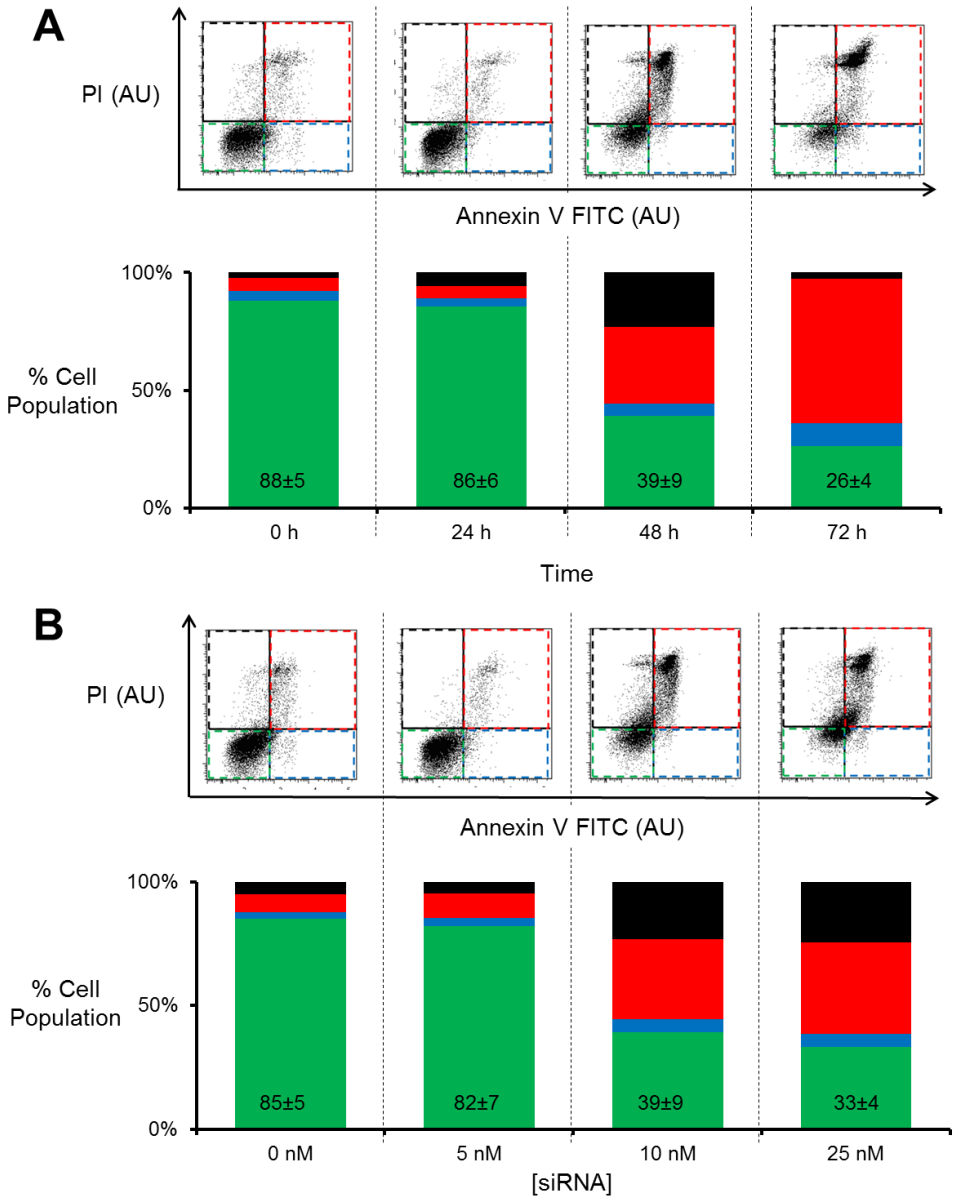


**Figure 3.21. Time- and concentration-dependent toxicity of siRNA delivery. (A)** HeLa cells were incubated with 10 nM TR-BCL2 packaged inside VLP-$PEG_{24}$-Tf for 0, 24, 48 or 72 h, and assessed for toxicity. **(B)** HeLa cells were incubated with 0, 5, 10 or 25 nM TR-BCL2 packaged inside VLP-$PEG_{24}$-Tf for 48 h, and assessed for toxicity. The percentages shown represent the average of three repeats. Numbers indicate mean percentage cell viability ± SD.

Distinct populations of cells were observed after the 48 and 72 h treatments, with the majority of cells designated as live (negative for annexin V-FITC and propidium iodide) or late apoptotic (positive for both dyes). A large portion of necrotic cells was only observed at 48 h (23±7%), which interestingly disappeared at 72 h (3±1%). It is possible that a subset of cells progressed quickly through necrosis, resulting in cell swelling and membrane rupture, and thus was not counted at 72 h.

The siRNA concentration dependence of cytotoxicity was also investigated: HeLa cells were incubated with 0 nM, 5 nM, 10 nM or 25 nM TR-BCL2 packaged inside VLP-$PEG_{24}$-Tf for 48 h. Delivered siRNA reduced cell viability in a concentration-dependent manner – with 85±5%, 82±7%, 39±9% and 33±4% of cells remaining viable following incubation with 0 nM, 5 nM, 10 nM and 25 nM siRNA, respectively (Figure 3.21B). Although there seems to be a correlation between BCL2 knockdown and cytotoxicity, this is not a simple linear relationship. For instance, a knockdown of BCL2 by ~30% at 5 nM siRNA only reduced percentage cell viability by ~3%, whilst BCL2 knockdown by ~46% at 10 nM reduced percentage viability by ~46%. It is possible that apoptosis is triggered in cells only at a given threshold of BCL2 expression. An increase of siRNA concentration from 10 nM to 25 nM produced a small change in percentage cell viability compared to from 5 nM to 10 nM siRNA. This might be due to the saturation of RNAi components in the cell: the intracellular siRNA concentration resulting from a 10 nM transfection might be close to saturating limiting components, such as the Argonaute-2 protein (Diederichs et al., 2008, Grimm et al., 2010), thus further increases in siRNA concentration will see diminishing returns on its cytotoxic effects.

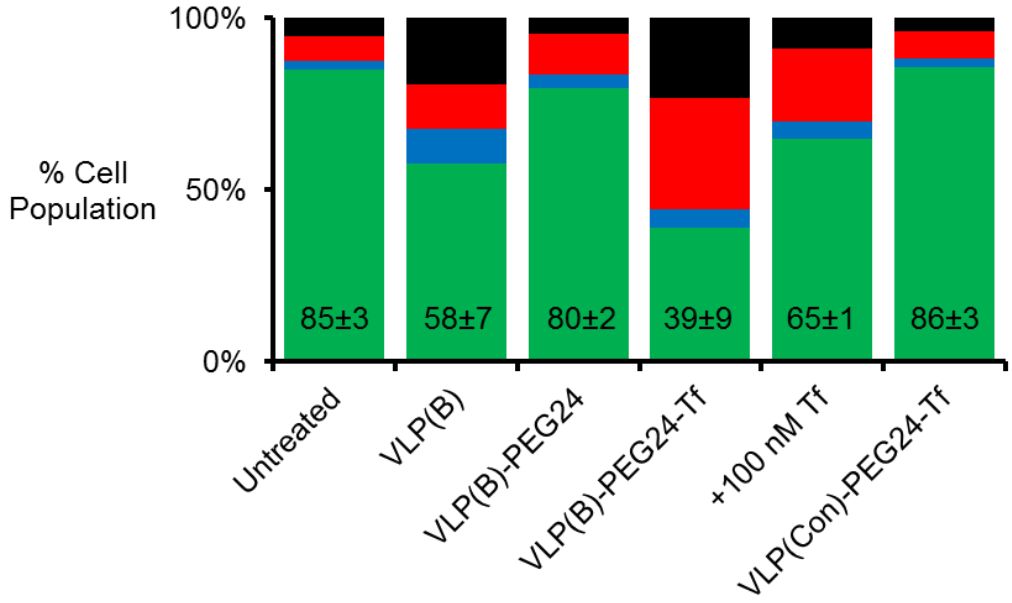


**Figure 3.22. Comparative toxicity of siRNA delivery.** HeLa cells were (from left) untreated, incubated with 10 nM TR-BCL2 siRNA delivered by VLP, VLP-$PEG_{24}$, VLP-$PEG_{24}$-Tf, or VLP-$PEG_{24}$-Tf plus 100 nM free Tf, or 10 nM TR-Control delivered by VLP-$PEG_{24}$-Tf for 48 h, and then assayed for cytotoxicity. The percentages shown represent the average of three repeats. Numbers indicate mean percentage cell viability ± SD.

As before, 10 nM siRNA and 48 h were selected as the condition for comparing the cytotoxic effects of siRNA delivery by various VLP formulations (Figure 3.22). Background toxicity unrelated to siRNA treatments was again observed, with 84.8±2.8% of untreated cells designated as live. In comparison, treatment with TR-BCL packaged inside VLP, VLP-$PEG_{24}$ and VLP-$PEG_{24}$-Tf reduced the percentage cell viability to 58±7%, 80±2% and 39±9%, respectively. This is consistent with the BCL2 expression data (Figure 3.18), and correlates the observed cytotoxicity with siRNA-mediated BCL2 knockdown. The lack of cytotoxic effect of siRNA delivery by VLP-$PEG_{24}$ was surprising, as it was observed to reduce BCL2 expression by ~25% (Figure 3.19). One possible explanation is that apoptosis is triggered below a given threshold of BCL2

expression, which was not achieved by the effects of VLP-$PEG_{24}$ mediated siRNA delivery. Interestingly, TR-BCL2 delivery by VLP-$PEG_{24}$-Tf was notably more effective at inducing cytotoxicity within cells compared to delivery by VLP, despite producing comparable BCL knockdowns (Figure 3.19). One possible explanation for this is that VLP-$PEG_{24}$-Tf particles triggered off-target toxicity that was unrelated to BCL2 knockdown.

Further addition of 100 nM free Tf to VLP-$PEG_{24}$-Tf increased the percentage cell viability to 65±1%, which supports a Tf receptor-dependent mechanism for the cellular uptake of VLP-$PEG_{24}$-Tf. Interestingly, this is somewhat contradictory to the previous assumption that a threshold of BCL2 knockdown was required for triggering cell death, as free Tf inhibition only produced an ~11% reduction in BCL2 expression. One possibility is that the apoptosis observed here was, at least in part, caused by the uptake of large amounts of free holo-Tf. The cytotoxic potential of iron overload and the subsequent production of reactive oxygen species in cells have been documented (Allameha et al., 2008, Dixon and Stockwell, 2014).

Finally, the delivery of TR-Control by VLP-$PEG_{24}$-Tf produced no change in percentage cell viability (86±3%). This suggests that the cellular uptake of VLP-$PEG_{24}$-Tf particles did not produce off-target toxicities, and that the cytotoxicity observed when TR-BCL2 was delivered by VLP-$PEG_{24}$-Tf can be largely attributed to the siRNA-mediated knockdown of BCL2. It has been reported that off-target toxicity can also result from robust RNAi expression in mammalian cells, as limiting components like exportin-5 and Argonaute proteins become saturated and natural miRNAs are outcompeted (Grimm, 2011, Grimm et al.,

2006). The lack of cytotoxic effect of the control siRNA rules out this possibility, at least for the siRNA concentration used.

## 3.3 Summary of Chapter 3

1. Previous protocols (Galaway, 2011) were adapted to construct TR-Cy5 encapsidated VLP and VLP-Tf. The resulting particles packaged on average ~10 molecules of TR-Cy5 each, and protected them from nuclease degradation. For VLP-Tf, a Tf valency of ~14 was achieved, which was comparable to previous results (Galaway, 2011). Notably fewer aggregates were formed than before, eliminating the necessity of additional purification steps. TR-Cy5 encapsidated VLP-$PEG_{24}$ and VLP-$PEG_{24}$-Tf were also synthesised using the hetero-bifunctional crosslinker, $SM(PEG)_{24}$, and amine-to-maleimide conjugation chemistry. Extensive PEGylation of the VLP surface was achieved (~97% of CPs); each VLP-$PEG_{24}$-Tf particle displayed on average ~7 molecules of Tf on the termini of $PEG_{24}$.

2. Consistent with previous results (Galaway, 2011), Tf targeting resulted in significantly higher uptake of VLP-Tf by HeLa cells compared to VLP, whilst some level of non-specific VLP uptake was still observed. PEGylation of the VLP surface (VLP-$PEG_{24}$) was able to significantly mitigate non-specific uptake by HeLa cells, likely by masking viral epitopes. Further addition of Tf (VLP-$PEG_{24}$-Tf) led to markedly increased uptake, likely via Tf receptor-mediated endocytosis.

3. TR-BCL2 encapsidated VLP-$PEG_{24}$-Tf were constructed. VLP-$PEG_{24}$-Tf successfully delivered the siRNA to HeLa cells. Significant cellular responses, including ~50% BCL2 protein knockdown and a ~45% decrease in cell viability, were achieved at just 10 nM TR-BCL2 concentrations. The uptake of VLP-$PEG_{24}$-Tf did not trigger any off-target toxicity in cells.

**This page is intentionally blank**

# Chapter 4

RNA aptamers as a novel tumour-targeting VLP ligand

# 4.1 Introduction

### 4.1.1 Nucleic acid aptamers

A major development in nucleic acid research came in the early 1980s, with the discovery of RNAs with catalytic activities, termed ribozymes (Kruger et al., 1982, Guerriertakada et al., 1983). This ground-breaking finding not only shattered the long-held paradigm that only proteins could catalyse chemical reactions, but also the belief that nucleic acids were mere passive carriers of genetic information. Based on this idea that RNAs can fold into complex, three dimensional structures which enable specific interactions with biomolecules and confer functions, it was hypothesised that RNA ligands could be isolated against specific targets by *in vitro* selection from a library of random nucleotide sequences.

Three laboratories independently provided proof-of-principle for this in 1990. The Gold laboratory coined the term to a selection method 'Systematic Evolution of Ligands by Exponential Enrichment', or SELEX, and used it to select for high affinity RNA ligands against the bacteriophage T4 DNA polymerase (Tuerk and Gold, 1990). The Szostak laboratory used a similar protocol to select RNA ligands against poly-thymine oligonucleotides and organic dyes that mimicked metabolic co-factors (Ellington, 1990), and subsequently coined the resulting ligands 'aptamers', derived from the Latin word apto, meaning 'to fit'. In addition, the Joyce laboratory developed an *in vitro* selection method to identify RNA ligands capable of efficiently cleaving ssDNA (Robertson and Joyce, 1990).

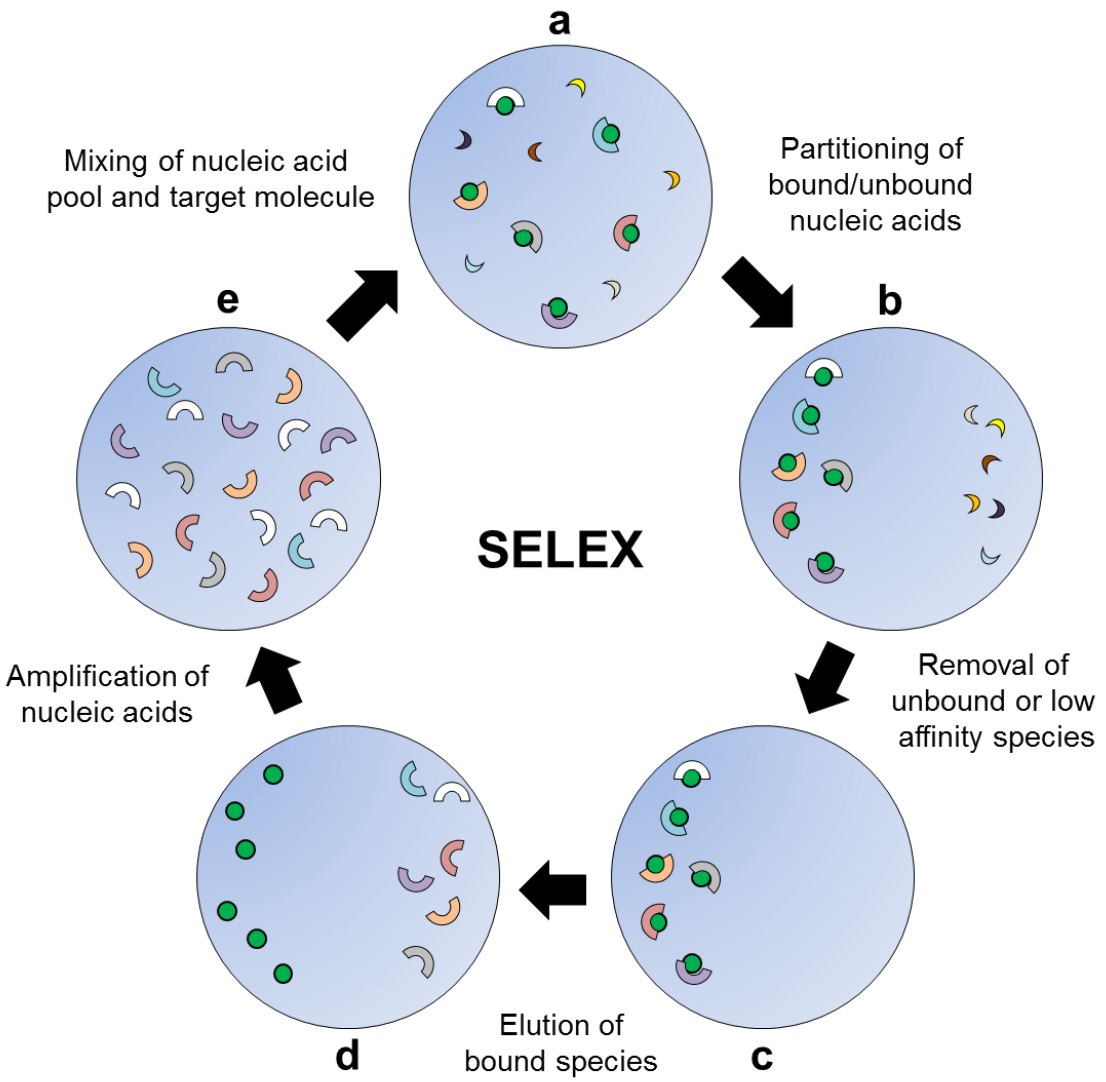


**Figure 4.1.** ***In vitro*** **nucleic acid aptamer selection via SELEX. (a)** A large random oligonucleotide library is incubated with the target molecule. The library consists of sequences with a randomised region, flanked by constant 5' and 3' ends which serve as primer-binding regions. **(b)** Nucleic acids bound to the target molecule are partitioned from those not bound. **(c)** Nucleic acids which are unbound to the target molecules are removed. **(d)** Nucleic acids which are bound to the target molecules are eluted. **(e)** Bound nucleic acids are then amplified by (RT)PCR and used as the starting nucleic acid pool in subsequent cycles. Through successive rounds of SELEX, higher affinity aptamers are selected as they outcompete low affinity species for target binding and amplification – this is akin to Darwinian evolution. Typically 10 to 20 cycles are performed, before the resulting aptamers are characterised.

The process of SELEX is illustrated in Figure 4.1. The starting point of SELEX is a synthetic library of oligonucleotides, containing sequences with a randomised region flanked by constant 5' and 3' regions for primer binding. The random region is typically 20-80 (n) nt in length, with the number of possible sequences being $4^n$. The pool of oligonucleotides is incubated with a target molecule for binding, before unbound or weakly bound species are removed through partitioning (e.g. affinity chromatography) and wash steps. Species which are bound are eluted and then amplified by (RT-)PCR to create an enriched pool for subsequent rounds of selection. To select for the tightest binders, the stringency of selection conditions is increased with successive SELEX rounds. This can be achieved by varying the conditions for the binding and washing steps, and by decreasing the concentration of target molecules used. Typically, 10 to 20 rounds of SELEX are carried out before the final enriched aptamer pool is cloned, sequenced and characterised.

Aptamer sequences identified from SELEX can fold into unique higher order structures – with a combination of bulges, hairpins, quadruplexes, pseudoknots, stems or loops (Patel et al., 1997) – through intramolecular base-pairing. These structures enable specific binding to target molecules through a series of intermolecular interactions, including hydrogen bonding, electrostatic interactions as well as van der Waal forces. Aptamers typically display high affinity for their targets, with dissociation constants ($K_d$) ranging from mM to pM values, which rival the affinities between antibodies and their corresponding antigens. Although analogous in function, aptamers offer numerous advantages over antibodies as targeting agents (Bunka and Stockley, 2006), including (i) they can be isolated *in vitro*, (ii) they can bind to a wider range of target

molecules including nucleic acids, proteins, peptides, organics, metal ions or even toxic species, (iii) they are amenable to large-scale chemical synthesis with minimal batch-to-batch variations, (iv) they elicit little or no immunogenicity *in vivo*, (v) their smaller size enables binding to epitopes which might be inaccessible to antibodies, and (vi) they are tolerant of chemical modifications that can enhance their stability or binding.

The original SELEX reports used RNA libraries. Subsequent work revealed that DNA libraries could also be used to isolate DNA aptamers against specific target molecules, such as human thrombin (Bock et al., 1992). DNA aptamers are functionally similar to their RNA counterparts, although RNA aptamers require the extra steps of (reverse) transcription during SELEX.

The process of SELEX has constantly evolved since its first reported use, due to rapid technological advances. One key development came in 2001, when Cox and coworkers demonstrated the automation of SELEX using Biomek 2000 liquid-handling robots, which significantly reduced the duration of selection from six weeks to just three days (Cox and Ellington, 2001). The efficiency of the partitioning steps has also been improved with advances in techniques such as surface plasmon resonance (Misono and Kumar, 2005) and capillary electrophoresis (Mendonsa and Bowser, 2004). The nuclease resistance of aptamers can be significantly improved by the incorporation of 2'-modified pyrimidines (Beigelman et al., 1995), or by the use of unnatural L-ribose nucleotides to synthesise Spiegelmers (Klussmann et al., 1996). In addition to modified sugar groups, the use of modified bases for SELEX has been demonstrated by Somalogic (Ochsner et al., 2014, Ostroff et al., 2010) – resulting aptamers have extremely high affinity to their targets, with $K_d$ typically

in the low nM range. Furthermore, advances in next-generation sequencing and computer programming have enabled more efficient, high-throughput aptamer characterisation (Cho et al., 2010, Lu et al., 2014).

Hundreds of nucleic acid aptamers have now been isolated against a myriad of targets – including small molecules (Niazi et al., 2008), peptides (Vater et al., 2003), proteins (Svobodova et al., 2013), bacteria (Duan et al., 2013), viruses (Wang et al., 2013) and even whole cells (Shangguan et al., 2006). These aptamers are catalogued online in the Aptamer Database (http://aptamer.icmb.utexas.edu/), and have been adapted to a range of applications, such as biotechnological, therapeutic, diagnostic and bio-sensing.

### 4.1.2 Therapeutic applications of nucleic acid aptamers

Nucleic acid aptamers have attracted major clinical interest due to their ability to tightly and specifically bind to target molecules. Development began as early as 1994, when Jellinek and coworkers reported the use of an *n=30* random RNA library to select aptamers against the 165 isoform of vascular endothelial growth factor ($VEGF_{165}$) (Jellinek et al., 1994). $VEGF_{165}$ is a signalling protein that stimulates angiogenesis, and is implicated in the formation of abnormal blood vessels that impair the retina in age-related macular degeneration. Following 13 rounds of SELEX, six structural families of sequences were obtained; each containing conserved sequences that shared a defined secondary structure. Importantly, the aptamers effectively blocked the interaction between $VEGF_{165}$ and the VEGF receptor on cells, with a $K_d$ of ~30 nM.

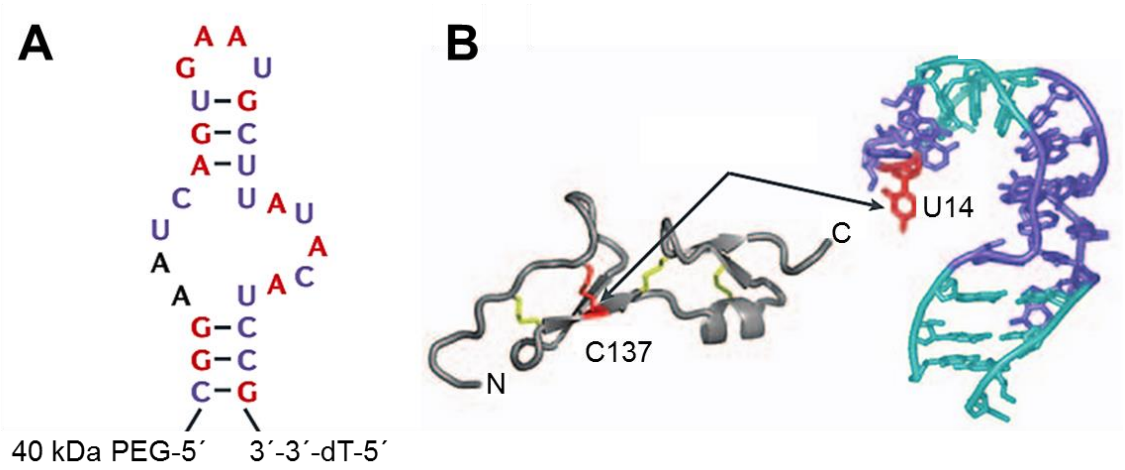


**Figure 4.2. Structure and binding mechanism of pegaptanib. (A)** Predicted secondary structure of pegaptanib. Highlighted in black are unmodified nucleotides; in red are 2′-OMe purines; in blue are 2′-F pyrimidines. A 40 kDa PEG is conjugated to the 5′ end of the aptamer. An inverted deoxythymidine cap is attached at the 3′ end. **(B)** Binding of pegaptanib (right) to the heparin-binding domain of $VEGF_{165}$ (left). Disulfide bonds in the heparin-binding domain are highlighted in yellow. Helical stems in the aptamer are highlighted in teal. Shown in red is nucleotide U-14 on the aptamer, which interacts with cysteine-137 of $VEGF_{165}$. Adapted from Ng et al. (2006).

The instability of RNA and their susceptibility to nuclease degradation hindered the clinical progress of these $VEGF_{165}$-targeting aptamers. This prompted the same group to introduce chemical modifications, by using SELEX libraries containing 2′-modified sequences for selection against $VEGF_{165}$ (Ruckman et al., 1998). After 10 rounds of selection, 46 aptamer sequences were identified, which were characterised into 3 structural families and all displayed high affinity binding to $VEGF_{165}$ ($K_d$~5 nM). The consensus sequence from each family was truncated, yielding three minimal sequences 23-29 nt in length, which retained their $VEGF_{165}$ binding. The capacity of these aptamers to inhibit the activity of VEGF was then investigated in guinea pig models (Ruckman et al., 1998).

Intradermal injection of one of the aptamers, t44-OMe, inhibited the vascular permeability response to VEGF by up to ~58%. Additionally, coupling of the t44-OMe aptamer to a 40 kDa PEG was shown to dramatically prolong its plasma half-life, from a few minutes to 9 h in rhesus monkeys (Tucker et al., 1999). This PEG-aptamer conjugate was named pegaptanib (Figure 4.2).

| Aptamer | Target | Therapeutic application | Development |
|---|---|---|---|
| AS1411 | Nucleolin | Renal cell carcinoma/NSCLC | Phase III |
| ARC1779 | von Willebrand factor | von Willebrand's disease | Phase III |
| ARC1905 | Complement component 5 | Neovascular AMD | Phase I |
| Macugen | VEGF | AMD, DME, PDR | Approved |
| NOX-A12 | Stromal cell-derived factor 1 | CLL, MM, glioblastoma | Phase II |
| NOX-E36 | CCL2 | Type II diabetes mellitus | Phase II |
| RB006 | Factor IXa | Coronary artery disease | Phase II |

**Table 4.1. Selected examples of DNA and RNA aptamers in clinical development.** NSCLC = non-small cell lung carcinoma; AMD = age-related macular degeneration; VEGF = vascular endothelial growth factor; DME = diabetic macular edema; PDR = proliferative diabetic retinopathy; CLL = chronic lymphocytic leukaemia; MM = multiple myeloma; CCL2 = chemokine (C-C motif) ligand 2.

Pegaptanib entered clinical trials for treating wet age-related macular degeneration in 1998 (Trujillo et al., 2007). Following intraocular administration of the drug, a high response rate was achieved, with 80% of patients experiencing improved vision after 3 months of treatment. Moreover, the doses used were well tolerated and no significant off-target effects were observed

even at 3 mg/eye doses. In 2004, pegaptanib became the first nucleic acid aptamer to be FDA approved, and was trademarked as Macugen. Although to date, pegaptanib remains the only FDA approved aptamer drug, many more candidates are beginning to emerge from the clinical pipelines, for treating a variety of diseases. Selected examples are highlighted in Table 4.1; many more exist (Keefe, 2010).

As well as direct therapeutics, nucleic acid aptamers have also been developed as targeting ligands against cancer cell surface markers. In 2002, Lupold and coworkers performed SELEX against the extracellular portion of prostate surface membrane antigen (PSMA) (Lupold, 2002). PSMA is a membrane protein that catalyses the hydrolysis of N-acetylaspartylglutamate. Although low levels of PSMA are found in the salivary glands, small intestine and brain, it is predominantly a prostate-specific protein, and is highly overexpressed on prostate cancer cells (O'Keefe et al., 2004, Israeli et al., 1994). Six rounds of selection from a 40mer RNA library of ~$6x10^{14}$ random sequences led to the identification of two unique sequences, named A9 and A10 (Lupold, 2002). Both aptamers inhibited the enzyme activity of PSMA with low nM $K_i$s; though non-competitive inhibition was observed with A9, and competitive inhibition with A10. The different modes of inhibition suggested that A9 and A10 bound to distinct epitopes on the extracellular portion of PSMA. Furthermore, systematic 3'-truncation of the A10 aptamer produced a smaller version which displayed comparable affinity, and bound specifically to $PSMA_{+ve}$ LNCaP prostate cancer cells, but not to $PSMA_{-ve}$ PC-3 cells.

The A10 aptamer was subsequently utilised by McNamara and coworkers, who coupled it to two therapeutic siRNAs, targeted against *BCL2* and *PLK1*

(McNamara et al., 2006). Aptamer targeting specifically delivered the siRNAs to $PSMA_{+ve}$ LNCaP cells, which induced significant knockdown of the target mRNA and protein, as well as apoptosis at sub nM doses. These effects were not observed in the $PSMA_{-ve}$ PC-3 cell line. In addition, it was shown that the cellular uptake of aptamer-siRNA conjugates did not trigger a substantial type I interferon response, suggesting the absence of any non-specific inflammatory response. This work was previously mentioned in Chapter 3: the fact that the siRNAs remained functional despite being coupled to another oligonucleotide prompted their use as model drug cargos for the MS2 VLP delivery system (Galaway, 2011).

The A10-PLK1 siRNA sequence was then optimised by adding 2-nucleotide overhangs at the 3' end, and tested in athymic mice bearing tumours derived from $PSMA_{+ve}$ 22RV1 or $PSMA_{-ve}$ PC3 cells (Dassie et al., 2009). Following systemic administration, significant tumour regression was observed in mice with 22RV1-derived tumours, but not those bearing PC3-derived tumours. Addition of the 3'-overhang enhanced RISC loading of the guide strand. Furthermore, the addition of a ~20kDa PEG to the 5' end of the PLK1 passenger strand enhanced the circulating half-life of the aptamer-siRNA conjugate from 35 min to >30 h, and also induced tumour progression at lower doses.

More recently, computer modelling was used to rationally truncate A9 (70mer) to A9L (41mer) (Figure 4.3), which demonstrated comparable PSMA binding ($K_d$~5 nM) as well as specific uptake by PSMA expressing cells (Rockey et al., 2011). The yield of chemically synthesised RNA decreases significantly with increasing nucleotide length, as the efficiency of each coupling step is typically

~98% (Caruthers, 2011). For this reason, sequence truncation greatly facilitates the large-scale chemical synthesis of aptamers: the expected yield of a 41mer ($0.98^{40}$=45%) is almost double that of a 71mer ($0.98^{69}$=25%).

Since the original work on aptamers A9 and A10, many more aptamers have been identified which target overexpressed cancer cell surface markers such as Tf receptor (Chen et al., 2008), epidermal growth factor receptor (Mi et al., 2010), and protein tyrosine kinase-7 (Huang et al., 2009).

### 4.1.3 MS2 VLPs and nucleic acid aptamers as targeting ligands

The MS2 VLP drug delivery system is highly modular in that a variety of targeting ligands and drug cargos can be combined, to potentially treat a diverse range of cancers. Coupled with a flexible targeting ligand, such as nucleic acid aptamers that can be selected against any target, MS2 VLPs could be a powerful platform for targeted drug delivery. For a model targeting aptamer, A9L seems suitable as it is relatively short (41 nt) and is amenable to chemical synthesis, and it has been well characterised. Furthermore, the relevant prostate cancer cell lines ($PSMA_{+ve}$ LNCaP and $PSMA_{-ve}$ PC-3) are relatively simple to maintain. The use of two cell lines would provide the benefit of an extra negative control, which was lacking in the previous experiments (Galaway, 2011) and in Chapter 3.

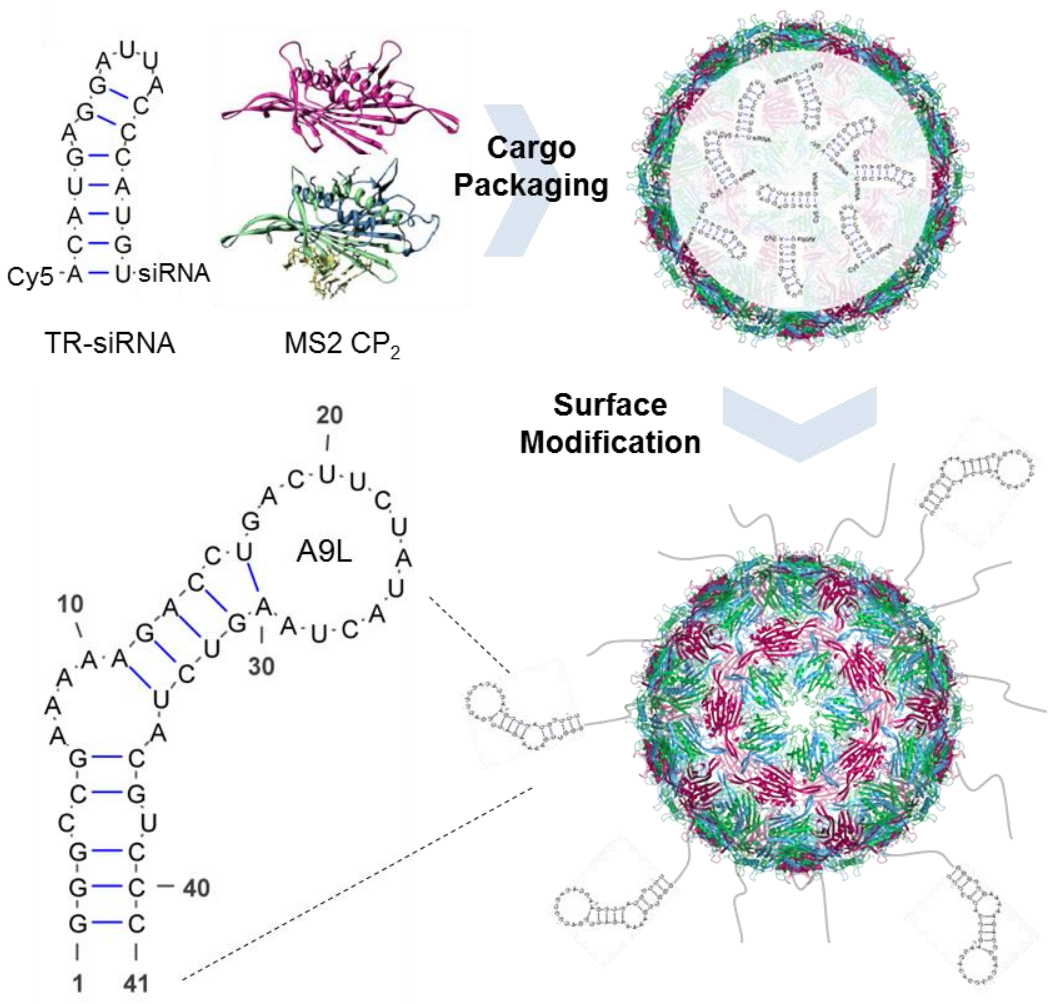


**Figure 4.3. Schematic showing the synthesis of siRNA encapsidated, PEG-aptamer modified VLP.** Cargo packaging is achieved by mixing TR-siRNA with dissociated MS2 $CP_2$ at roughly neutral pH. Packaged VLPs can be surface modified with $PEG_{24}$, as described in Chapter 3, and with the RNA aptamer A9L as a tumour-targeting ligand. The sequence and predicted secondary structure of A9L is shown. The resulting particles are denoted as VLP-$PEG_{24}$-A9L.

It is notable that aptamer targeting had been previously attempted by Galaway (Galaway, 2011). Aptamer A10-3.2, a truncated version of A10, was directly conjugated to the surface of MS2 VLPs using thiol-to-amine conjugation chemistry. However, when tested *in vitro* on LNCaP and PC-3 cells, aptamer-mediated specific targeting was not observed. Two likely explanations include:

(1) aptamer conjugation was not sufficient to cover viral epitopes that enabled high levels of non-specific uptake, and (2) steric effects of the direct conjugation of aptamers to a rigid surface prevented the correct folding of aptamers, or interfered with their PSMA binding. The addition of $PEG_{24}$ as an intermediary layer (as shown in Chapter 3) between MS2 VLPs and the targeting aptamer should solve these problems. A schematic of the preparation of VLP-$PEG_{24}$-Apt is shown in Figure 4.3.

### 4.1.4 Aims

The aims of the work described in this chapter were to:

1. Conjugate aptamer A9L to the surface of VLP-$PEG_{24}$.
2. Assess the stability and immunogenicity of VLP-$PEG_{24}$-A9L.
3. Evaluate VLP-$PEG_{24}$-A9L binding and uptake in LNCaP and PC-3 prostate cancer cell lines, and assess the cellular effects of TR-BCL2 delivery by VLP-$PEG_{24}$-A9L.

## 4.2 Results and discussion

### 4.2.1 Preparation and analysis of VLP-PEG$_{24}$-A9L

The protocol for synthesising VLP-PEG$_{24}$-Tf in Chapter 3 was adapted for the preparation of VLP-PEG$_{24}$-A9L (Figure 4.4). The 41 nt RNA aptamer, A9L, was synthesised by DNA Technology using 3'-Thiol-Modifier C3 Controlled Pore Glass columns, and purified by reverse-phase high-performance liquid chromatography. The resulting aptamer contained a protected disulfide linker at the 3' end, which could be reduced to a thiol group and thus was compatible with the amine-to-thiol conjugation chemistry used (Figure 4.4B). One advantage of using aptamers over Tf as a targeting ligand, from a conjugation perspective, is that the 1:1 thiol to aptamer ratio results in aptamers being presented in a defined orientation, with the regions responsible for PSMA recognition and binding fully exposed to the exterior. This level of control was not possible for Tf, as the introduction of thiol groups by SATA utilised NHS chemistry to randomly incorporate them to exposed amines on Tf.

Although a fluorescent dye would facilitate aptamer quantification as well as the assessment of cellular binding and uptake, it was not incorporated because (i) it would reduce the efficiency of RNA synthesis, significantly raising its cost, and more importantly (ii) it might affect aptamer folding and its ability to bind PSMA. Therefore, a second RNA oligonucleotide, U6-FAM, was synthesised to test for conjugation conditions. U6-FAM is a short oligonucleotide composed of 6 uridines, a 3'-thiol modification, and a 5'-fluorescein modification to facilitate quantification.

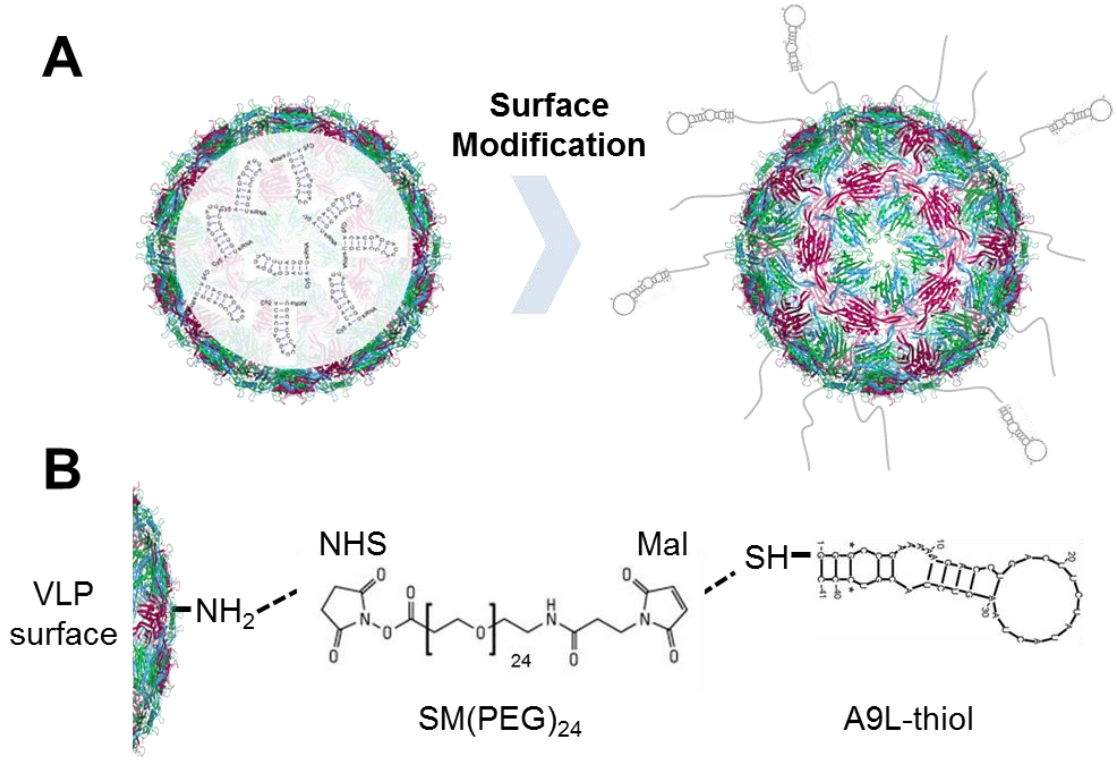


**Figure 4.4. Schematic depicting the preparation of VLP-PEG$_{24}$-A9L. (A)** Surface decoration of VLP with SM(PEG)$_{24}$ and subsequently the 41 nt RNA aptamer, A9L. **(B)** Conjugation chemistry used for VLP surface modification. SM(PEG)$_{24}$ is a hetero-bifunctional crosslinker, with an NHS terminus that can react with VLP surface amines, and a maleimide terminus that can react with thiol-modified A9L.

To expose terminal thiol groups for conjugation, U6-FAM was reduced via incubation with TCEP. TR-Cy5 encapsidated VLPs were reacted with SM(PEG)$_{24}$ as previously described. The two reaction mixtures were separately eluted through NAP-5 columns to remove excess reagents; the fractions containing U6-FAM or VLP-PEG$_{24}$ were pooled, and then mixed to allow conjugation to take place. A molar ratio of 75 U6-FAM to 1 VLP was used. The final reaction mixture was incubated with excess β-mercaptoethanol overnight to quench unreacted maleimide groups, and eluted through a NAP-25 column before it was concentrated using a 100 kDa MWCO spin concentrator.

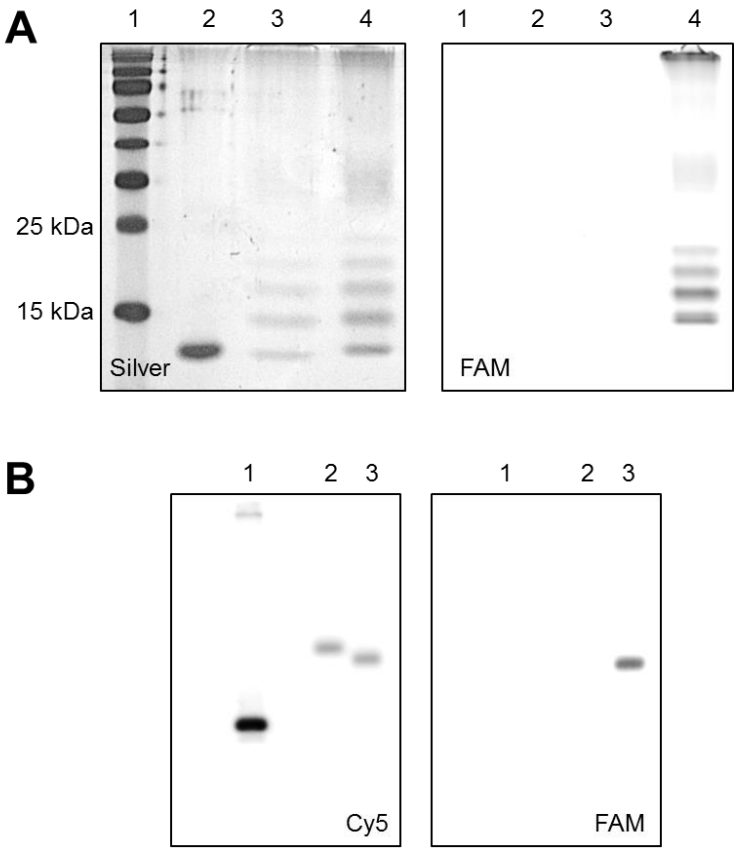


**Figure 4.5. Analysis of VLP-PEG$_{24}$-U6-FAM. (A)** SDS-PAGE. 1: Fermentas Prestained Ladder; 2: VLP; 3: VLP-PEG$_{24}$; 4: VLP-PEG$_{24}$-U6-FAM. The gel was visualised by silver staining (left) or FAM fluorescence scanning (right). **(B)** Native 2% (w/v) agarose gel electrophoresis. 1: VLP; 2: VLP-PEG$_{24}$; 3: VLP-PEG$_{24}$-U6-FAM. The gel was visualised via Cy5 or FAM fluorescence scanning.

The products were firstly analysed by UV-visible spectroscopy. The absorbance at 649 nm was measured to calculate the concentration of Cy5 in solution (Cy5 $\varepsilon_{649\ nm}$ = 250,000 L.mol$^{-1}$.cm$^{-1}$). From this, the concentration of MS2 VLPs was estimated using the previously observed ratio from Chapter 3 (~10 TR-Cy5 to 1 VLP). The absorbance at 495 nm was also measured to calculate the concentration of U6-FAM present in solution (FAM $\varepsilon_{495\ nm}$ = 75,000 L.mol$^{-1}$.cm$^{-1}$).

Using these, an average U6-FAM to VLP ratio of 15.7±2.1 was calculated from three repeats.

SDS-PAGE analysis revealed bands which were only visualised by fluorescein fluorescence scanning for the putative VLP-$PEG_{24}$-U6-FAM lane, but not for the VLP or VLP-$PEG_{24}$ lanes (Figure 4.5A). This confirms the successful conjugation of U6-FAM to PEGylated MS2 CP. Analysis by native 2% (w/v) agarose gel electrophoresis revealed that, whilst the VLP-$PEG_{24}$ displayed a lower electrophoretic mobility relative to VLP, reflecting their larger particle size, addition of U6-FAM increased the mobility (Figure 4.5B). This might be due to the conjugated RNA imparting more negative charge, which outweighed the effects of their relatively small mass contribution on the electrophoretic mobility of the particle. Hence, VLP-$PEG_{24}$-U6-FAM migrated further towards the positive anode. Moreover, FAM fluorescence was only observed for the VLP-$PEG_{24}$-U6-FAM band, and not for the VLP or VLP-$PEG_{24}$ bands, confirming the successful conjugation of U6-FAM.

The same protocol was used to synthesise VLP-$PEG_{24}$-A9L, again, using an aptamer to VLP ratio of 75 to 1. VLP-$PEG_{24}$-A9L was eluted through a NAP-25 column, and then concentrated using a 100 kDa MWCO spin concentrator. The $A_{649nm}$ of the sample was measured to calculate the concentration of Cy5 present, which was used to estimate the yield (~40% of the starting material). Analysis on a native 2% (w/v) agarose gel revealed the previously observed characteristic shift in electrophoretic mobility towards the anode for VLP-$PEG_{24}$-A9L, relative to VLP-$PEG_{24}$, which suggests successful conjugation (Figure 4.6A). TEM analysis of VLP-$PEG_{24}$-A9L did not clearly show evidence of larger

particles (Figure 4.6B). However, it did show that the VLP particles remained intact after the conjugation reactions. No aggregate structures were observed.

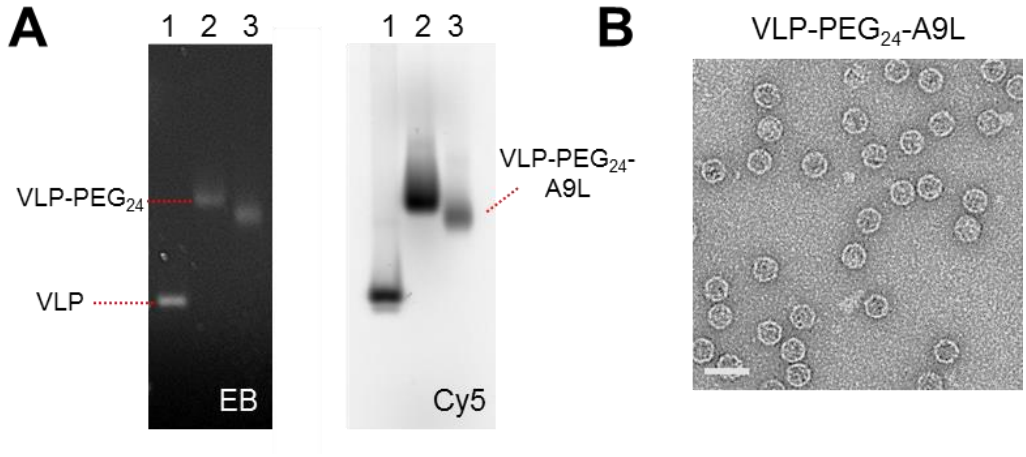


**Figure 4.6. Analysis of VLP-PEG$_{24}$-A9L.** The same protocol for the preparation of VLP-PEG$_{24}$-U6-FAM was used for synthesising VLP-PEG$_{24}$-A9L, which was then analysed. **(A)** Native 2% (w/v) agarose gel electrophoresis. 1: HyperLadder I; 2: VLP; 3: VLP-PEG$_{24}$; 4: VLP-PEG$_{24}$-A9L. The gel was visualised by ethidium bromide scanning or Cy5 fluorescence scanning. **(B)** TEM analysis of VLP-PEG$_{24}$-A9L. Scale bar = 50 nm.

### 4.2.2 Stability of VLP-PEG$_{24}$-A9L

Various modifications are typically made to RNA aptamers to stabilise them against hydrolysis and nuclease degradation, such as 2'-OH substitutions and phosphodiester backbone modifications (Shigdar et al., 2013). However, the A9L aptamer used here did not contain any stabilising modifications. To assess the stability of VLP-PEG$_{24}$-A9L in cell medium, the nanoparticles were incubated in either the PC-3 medium (Ham's F-12k with 7% (v/v) FBS) or the

LNCaP medium (RPMI-1640 with 10% (v/v) FBS) at 37°C for up to 48 h, before they were concentrated through 100 kDa MWCO spin concentrators.

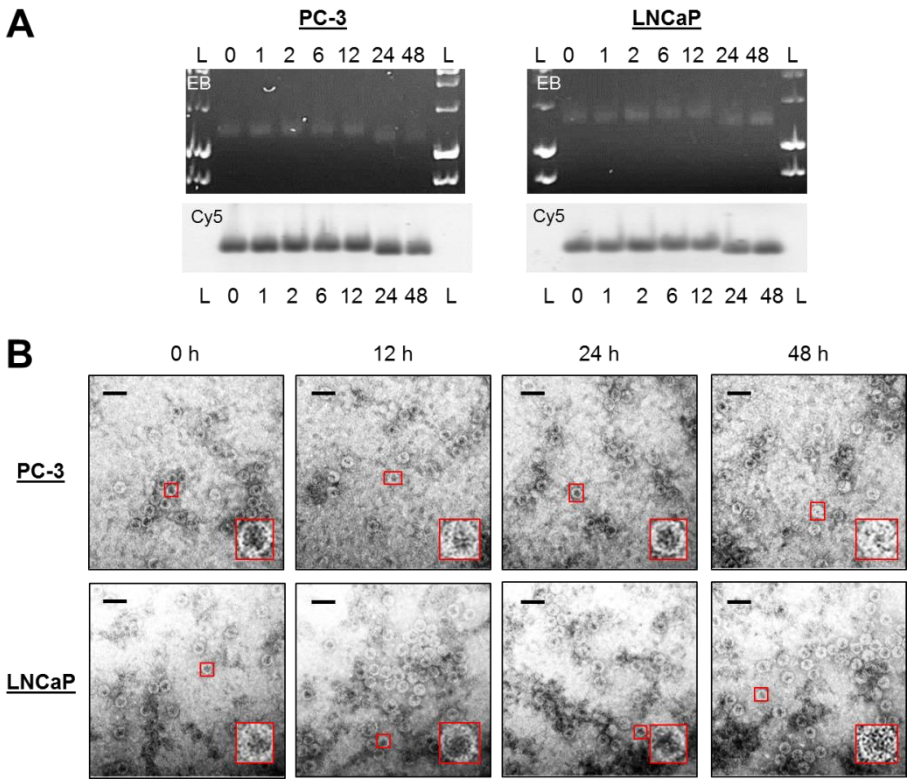


**Figure 4.7. Stability analysis of VLP-PEG$_{24}$-A9L in cell media.** VLP-PEG$_{24}$-A9L was incubated in either the PC-3 or LNCaP cell medium at 37°C for 0 h, 1 h, 2 h, 6 h, 12 h, 24 h or 48 h, and spin concentrated into HEPES before analysis. **(A)** Native 2% (w/v) agarose gel electrophoresis. L = HyperLadder I. The gel was visualised by ethidium bromide staining or Cy5 fluorescence. **(B)** TEM analysis. Scale bar = 50 nm. Selected individual particles were scaled up in size and shown in red boxes (bottom right) for clarity.

The products were analysed on a native 2% (w/v) agarose gel (Figure 4.7A). Increasing the incubation time did not produce changes in the VLP-PEG$_{24}$-A9L bands in either cell medium, which remained constant in electrophoretic mobility as well as intensity. This suggests that, under the conditions used for growing

PC-3 and LNCaP cells, (i) A9L remain stable, (ii) VLP-PEG$_{24}$-A9L particles remain intact, and (iii) there is no non-specific binding to components in the cell media. TEM analysis also revealed intact particles, indicating that VLP-PEG$_{24}$-A9L was not destabilised under the cell growth conditions (Figure 4.7B). The poor quality of the TEM images might be due to the presence of components of the cell media, which could not be removed via 100 kDa MWCO spin concentrators.

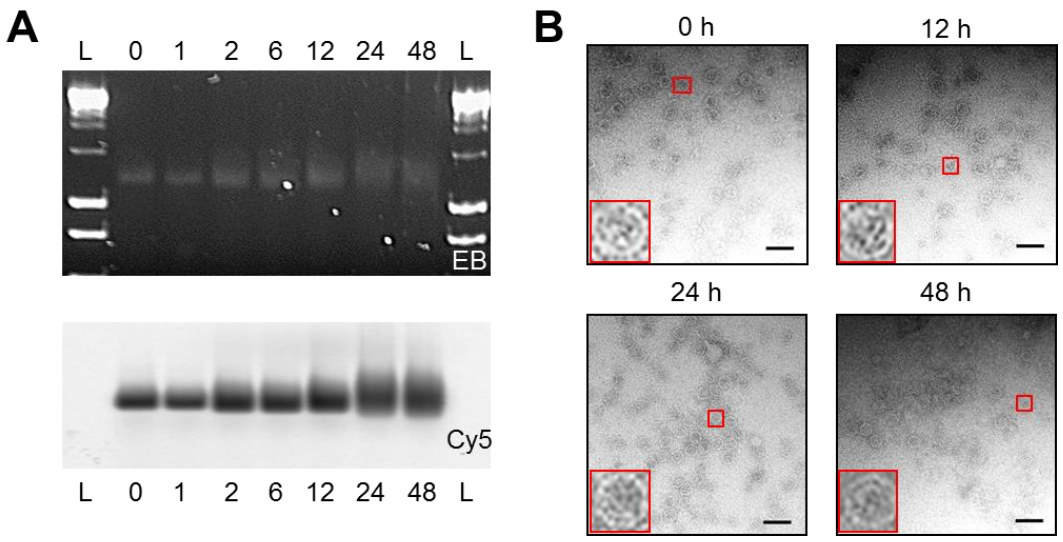


**Figure 4.8. Stability analysis of VLP-PEG$_{24}$-A9L in human serum.** VLP-PEG$_{24}$-A9L was incubated in human serum at 37$^{o}$C for 0 h, 1 h, 2 h, 6 h, 12 h, 24 h or 48 h, and spin concentrated into HEPES before analysis. **(A)** Native 2% (w/v) agarose gel electrophoresis. L = HyperLadder I. The gel was visualised by ethidium bromide staining or Cy5 fluorescence. **(B)** TEM analysis. Scale bar = 50 nm. Selected individual particles were scaled up in size and shown in red boxes (bottom left) for clarity.

The same assay was then carried out using human serum instead of cell medium, to investigate the stability of VLP-PEG$_{24}$-A9L under conditions more similar to those found *in vivo*. After incubation at 37$^{o}$C for up to 48 h, VLP-

$PEG_{24}$-A9L was concentrated using 100 kDa MWCO spin concentrators, and analysed on a native 2% (w/v) agarose gel (Figure 4.8A). Bands representing VLP-$PEG_{24}$-A9L remained relatively unchanged in intensity with increasing incubation times, suggesting that the VLP-$PEG_{24}$-A9L particles remained stable (Figure 4.8A). This was supported by TEM images showing the presence of intact VLP particles, indicating that prolonged exposure to human serum did not disrupt particle stability (Figure 4.8B). However, the bands appeared more diffuse with increasing incubation times, resembling smears with slightly lower electrophoretic mobility most notably at 24 h and 48 h (Figure 4.8A). Given the relative electrophoretic mobility observed for VLP-$PEG_{24}$ and VLP-$PEG_{24}$-A9L (Figure 4.6A), this result suggests that some A9L on VLP-$PEG_{24}$-A9L became degraded after prolonged incubation in human serum. One possibility is that the RNA aptamers were degraded by nucleases present in the serum used.

Altogether, these results indicate that both VLP-$PEG_{24}$-A9L particles and A9L remained stable after prolonged incubation at 37$^{o}$C with cell media, and thus should be compatible with the *in vitro* experiments used in Chapter 3 to investigate cellular uptake, BCL2 knockdown and cytotoxicity. However, the unmodified RNA aptamers on VLP-$PEG_{24}$-A9L appeared to degrade when incubated in human serum in a time-dependent manner, therefore future *in vivo* testing of RNA aptamer targeted VLPs should utilise chemically modified aptamers, which can better tolerate such conditions.

### 4.2.3 Antibody binding of VLP-PEG$_{24}$-A9L

As shown in the previous Chapter, PEGylation significantly mitigates the non-specific uptake of VLPs by cells, which was assumed to be due to the masking of viral epitopes on the VLP surface that interact with cells. To assess this idea, an experiment was carried out to compare the antibody-binding capacity of VLP-PEG$_{24}$-A9L to that of unmodified VLPs. An ideal drug delivery system should elicit minimal immunogenicity when administered *in vivo*, thus this assay could provide a good indication of the likely immunogenicity of aptamer targeted, PEGylated MS2 VLPs.

VLP and VLP-PEG$_{24}$-A9L were mixed with increasing quantities of rabbit polyclonal anti-MS2 CP antibodies that were previously raised in the Stockley laboratory. The mixtures were left at room temperature for 30 min to allow antibody binding, and then analysed on a native 2% (w/v) agarose gel (Figure 4.9A). TR-Cy5 encapsidated VLP and VLP-PEG$_{24}$-A9L were used, thus bands on the gel could be visualised by Cy5 fluorescence scanning. The intensities of the bands were quantitated by 2D densitometry, and compared to calculate the relative % bound VLP or VLP-PEG$_{24}$-A9L; bands representing VLP and VLP-PEG$_{24}$-A9L in the absence of antibodies were assumed to be 0% bound (Figure 4.9B).

The addition of 1 µL and 5 µL anti-MS2 antibodies resulted in the binding of 58.3±3.6% and 86.7±8.1% of VLP, respectively. The diminishing intensity of the VLP band coincided with the increasing intensity of a band at the top of the gel, which likely represented complexes of VLPs bound to multiple anti-MS2 antibodies that were too large to migrate through the gel. In comparison, only

7.9±3.1% and 43.9±10.8% of VLP-$PEG_{24}$-A9L became bound with the addition of 1 µL and 5 µL antibodies, respectively, indicating a 7-fold and 2-fold reduction in antibody binding compared to VLP. This suggests that PEGylation masked VLP surface epitopes and mitigated their recognition and binding by anti-MS2 antibodies.

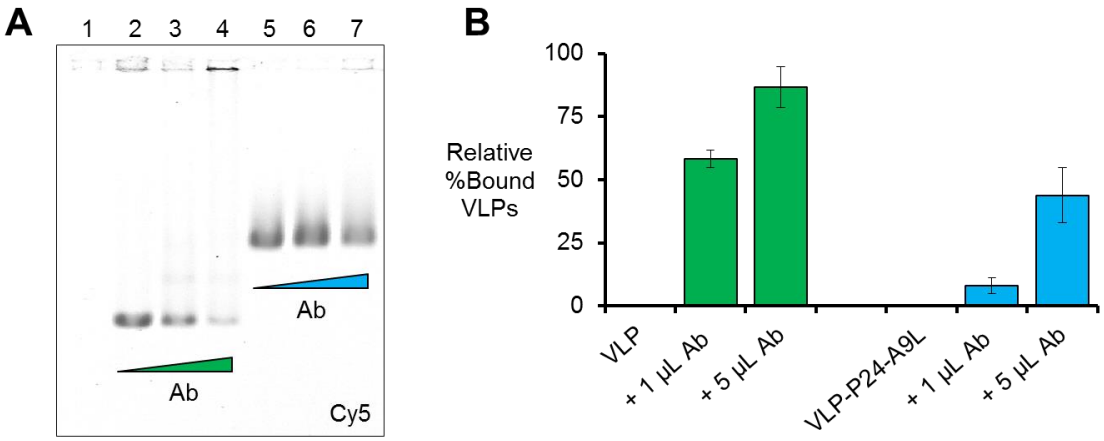


**Figure 4.9. Antibody binding analysis of VLP-$PEG_{24}$-A9L.** VLP or VLP-$PEG_{24}$-A9L was mixed with 0, 1 or 5 µL rabbit polyclonal anti-MS2 CP antibodies at room temperature for 30 min, and then analysed. **(A)** Native 2% (w/v) agarose gel electrophoresis. 1: HyperLadder I; 2: VLP; 3: VLP with 1 µL antibody; 4: VLP with 5 µL antibody; 5: VLP-$PEG_{24}$-A9L; 6: VLP-$PEG_{24}$-A9L with 1 µL antibody; 7: VLP-$PEG_{24}$-A9L with 5 µL antibody. The gel was visualised by Cy5 fluorescence scanning. **(B)** 2D densitometry analysis of the bands. The intensities of the bands were compared to calculate relative % bound VLP or VLP-$PEG_{24}$-A9L. Error bars indicate the standard deviation of three repeats.

It is unclear why some level of antibody binding was still observed for VLP-$PEG_{24}$-A9L at higher antibody concentrations. From the SDS-PAGE analysis of PEGylated VLP (Figure 3.16, Figure 4.5), it appears that a small portion of MS2 CP was not conjugated to $PEG_{24}$ at the VLP to $SM(PEG)_{24}$ molar ratios used. It

is therefore likely that certain regions on some particles were insufficiently covered by PEG, to prevent antibodies binding. Another possibility is that, due to the polyclonal nature of the anti-MS2 antibodies used, some non-specific antibodies might have been present, which bound to other parts of VLP-$PEG_{24}$-A9L, such as quenched maleimide groups or A9L. Obviously the immune system is highly complex, which is not reflected in the simple *in vitro* antibody binding assay. Therefore, *in vivo* work must be carried out to accurately assess the true immunogenicity of MS2 VLPs. There are currently few reports of the *in vivo* testing of MS2 VLPs – the Wang laboratory systemically administered non-PEGylated MS2 VLPs to mice, to deliver nucleic acid-based cargos, such as miRNAs and mRNA vaccines (Li et al., 2013, Pan et al., 2012b, Pan et al., 2012a). No significant immune responses were observed in those studies.

### 4.2.4 Cellular binding and uptake of VLP-$PEG_{24}$-A9L

Two prostate cancer cell lines were used to assess VLP-$PEG_{24}$-A9L uptake, including PC-3 and LNCaP. PC-3 cells differ from LNCaP cells in their high metastatic potential and, importantly, in their lack of PSMA expression (Kaighn et al., 1979, Carter et al., 1996). Since aptamer A9L targets PSMA, PC-3 can serve as the negative cell line and LNCaP as the positive cell line.

To confirm the relative PSMA expression levels, PC-3 and LNCaP cell lysates were analysed by Western blotting (Figure 4.10A). When probed with anti-PSMA antibodies, a ~100 kDa band was observed for the LNCaP cell lysate but not for the PC-3 cell lysate, indicating their differential PSMA expression. As a control, anti-GADPH antibodies were also used, which produced a ~37 kDa

band for both LNCaP and PC-3 cell lysates. This was expected, as GADPH is a housekeeping protein.

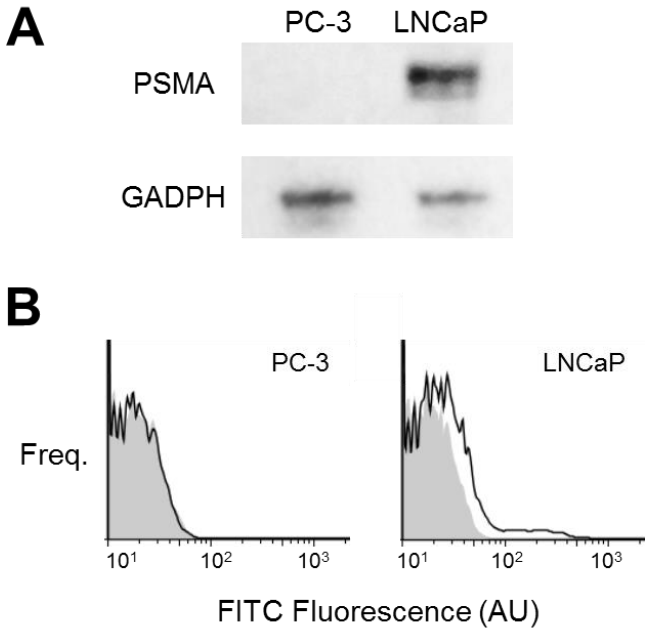


**Figure 4.10. Analysis of the PC-3 and LNCaP prostate cancer cell lines. (A)** Western blots of PC-3 and LNCaP cell lysates, using either anti-PSMA or anti-GADPH antibodies as the primary antibody. **(B)** Flow cytometry analysis of PC-3 and LNCaP cells stained with primary anti-PSMA antibodies and secondary FITC-labelled antibodies (black curves). Grey shaded curves represent cells incubated with the secondary FITC-labelled antibodies only.

The surface display of PSMA in each cell line was also assessed using an adapted protocol (McNamara et al., 2006). PC-3 and LNCaP cells were incubated with an anti-PSMA rabbit antibody for 1 h, washed, then incubated with a FITC-labelled anti-rabbit IgG antibody for 30 min. Cells were washed again and analysed by flow cytometry (Figure 4.10B). In addition, cells stained with only FITC-labelled anti-rabbit IgG antibodies were used to determine the

non-specific background fluorescence, shown as grey shaded curves in the flow cytometry histograms (Figure 4.10B). An increase in FITC fluorescence was only observed for LNCaP cells incubated with both antibodies, whereas the fluorescence of PC-3 cells did not change with respect to the control. These results suggest that PSMA is expressed in LNCaP, but not in PC-3 cells, and also that PSMA is present on the LNCaP cell surface. Therefore, these two cell lines should be suitable for investigating PSMA-targeted drug delivery.

Next, the cell binding capacity of VLP-$PEG_{24}$-A9L was evaluated using an established protocol (McNamara et al., 2006). PC-3 and LNCaP cells were harvested and incubated in FIX at room temperature for 10 min. Fixed cells were then washed in DPBS, and incubated in a binding buffer containing 25 nM TR-Cy5 packaged inside various VLP formulations for 1 h. The binding buffer also contained 0.01% (w/v) BSA to minimise any non-specific interactions. The cells were washed and analysed by flow cytometry (Figure 4.11). Compared to untreated cells, a small increase in Cy5 fluorescence was observed for both PC-3 and LNCaP cells incubated with VLP-$PEG_{24}$, which indicates low levels of non-specific cell binding. Incubation with VLP-$PEG_{24}$-A9L led to a notable increase in the Cy5 fluorescence of LNCaP, but not PC-3 cells. In contrast, the addition of 100 nM free A9L reduced the Cy5 fluorescence of LNCaP cells to a level comparable to VLP-$PEG_{24}$, suggesting that A9L was mediating cell binding by VLP-$PEG_{24}$-A9L.

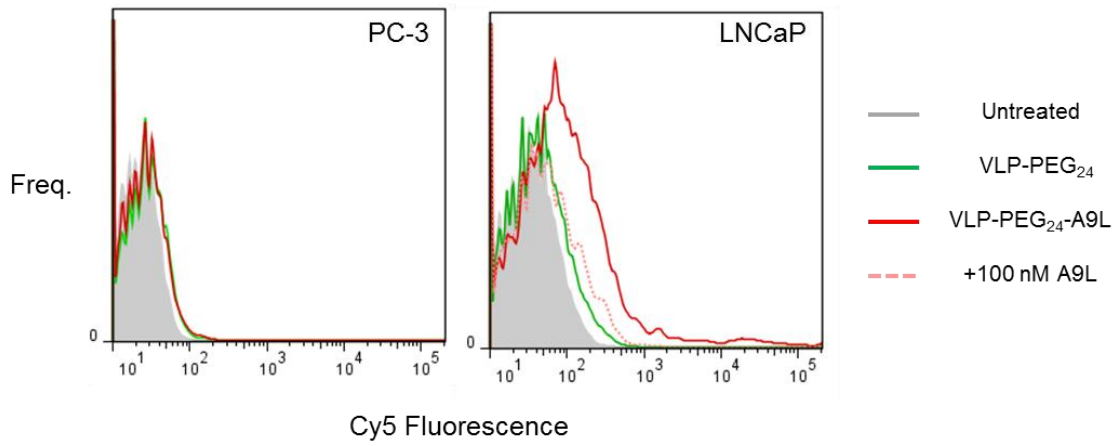


**Figure 4.11. Cell binding analysis of VLP-PEG$_{24}$-A9L.** Flow cytometry histograms of PC-3 and LNCaP cells incubated with 25 nM TR-Cy5 packaged inside VLP-PEG$_{24}$, VLP-PEG$_{24}$-A9L, or VLP-PEG$_{24}$-A9L in the presence of 100 nM free A9L for 1 h. Grey shaded curves represent untreated cells.

The cellular uptake of VLP-PEG$_{24}$-A9L was also evaluated. PC-3 and LNCaP cells were grown on 24 well plates, and incubated with 10 nM TR-Cy5 packaged inside VLP-PEG$_{24}$, VLP-PEG$_{24}$-A9L or VLP-PEG$_{24}$-A9L in the presence of 100 nM free A9L, for 2 h or 18 h, before they were processed for flow cytometry analysis (Figure 4.12). At 2 h, a significant increase in mean Cy5 fluorescence was observed for LNCaP cells incubated with VLP-PEG$_{24}$-A9L (90.4±12.5 AU); other treatments did not affect the Cy5 fluorescence of cells relative to untreated cells, for both cell lines (Figure 4.12A). At 18 h (Figure 4.12B), incubation with VLP-PEG$_{24}$ led to an increase in the mean Cy5 fluorescence of LNCaP cells (225.3±34.1 AU) compared to untreated cells (5.0±1.0 AU), which is indicative of some level of non-specific uptake of VLP-PEG$_{24}$. A ~5-fold increase in mean Cy5 fluorescence was observed when LNCaP cells were incubated with VLP-PEG$_{24}$-A9L (1087.7±118.0 AU), whilst further addition of 100 nM free A9L led to a ~3-fold decrease in fluorescence

(386.7±77.1 AU). For PC-3 cells, an increase in mean Cy5 fluorescence was observed (~500 AU), which was comparable for all three treatments, thus it likely indicates non-specific uptake.

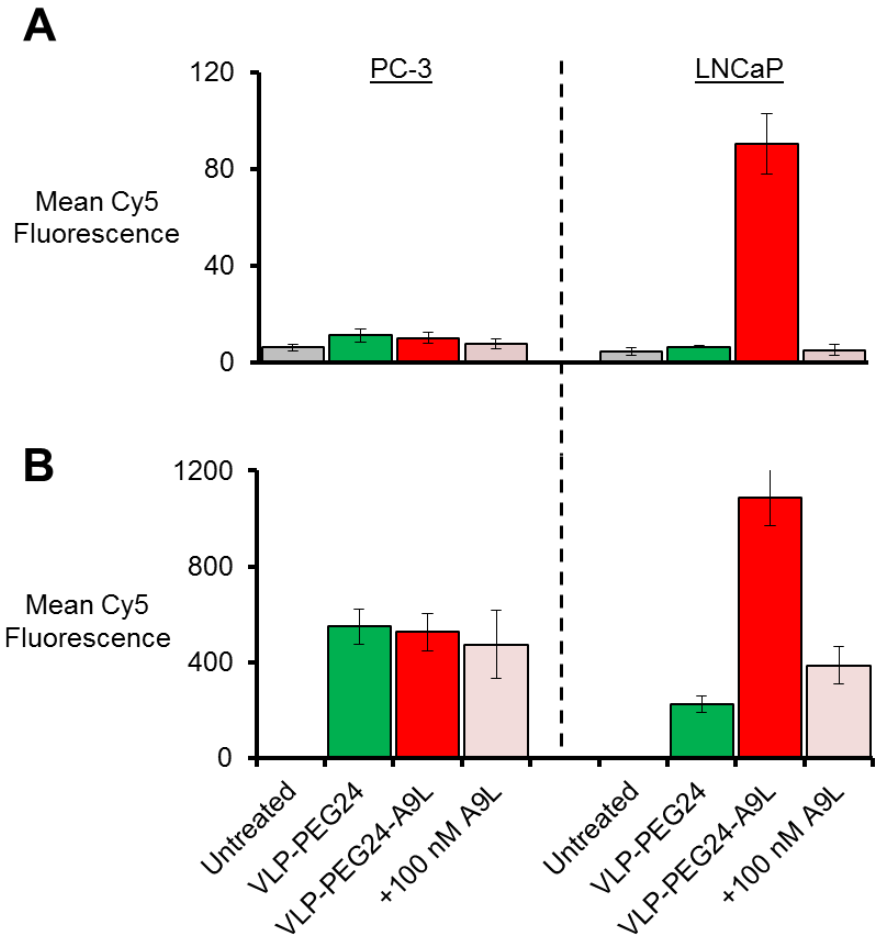


**Figure 4.12. Cellular uptake analysis of VLP-PEG$_{24}$-A9L.** PC-3 and LNCaP cells were either untreated, or incubated with 10 nM TR-Cy5 packaged inside VLP-PEG$_{24}$, VLP-PEG$_{24}$-A9L, or VLP-PEG$_{24}$-A9L in the presence of 100 nM free A9L for **(A)** 2 h or **(B)** 18 h. Cells were analysed by flow cytometry and the mean Cy5 fluorescence of cells were measured. Error bars indicate the standard deviation of three repeats.

Altogether, these results suggest that (i) A9L targeting is specific to LNCaP, and not PC-3 cells, (ii) there is some level of non-specific uptake for both cell lines

with longer incubations, and (iii) the A9L targeted uptake by LNCaP cells and the non-specific uptake by both cell lines likely utilise different pathways for cell entry, with the former occurring at a markedly faster rate.

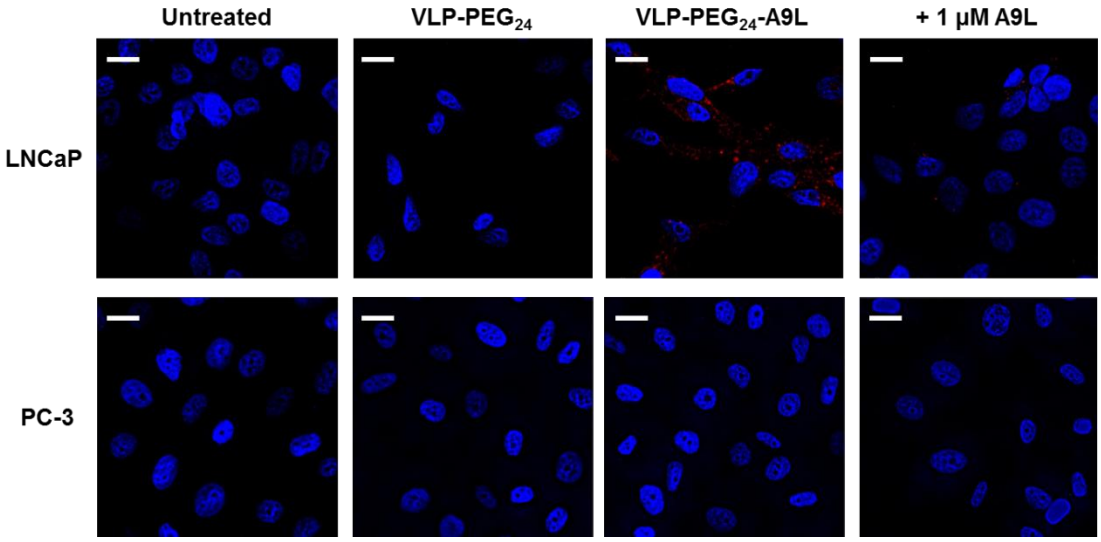


**Figure 4.13. Analysis of VLP-PEG$_{24}$-A9L binding and internalisation.** Deconvolution microscopy images of LNCaP and PC-3 cells either untreated, or incubated with 100 nM TR-Cy5 packaged inside VLP-PEG$_{24}$, VLP-PEG$_{24}$-A9L or VLP-PEG$_{24}$-A9L in the presence of 1 µM free A9L. DAPI staining (nuclei) is depicted in blue; Cy5 fluorescence (siRNA) is depicted in red. Scale bar = 20 µM.

The effects of A9L targeting on the cell binding and internalisation of VLP-PEG$_{24}$-A9L were further investigated. LNCaP and PC-3 cells were grown on glass coverslips, and incubated with 100 nM TR-Cy5 packaged inside VLP-PEG$_{24}$, VLP-PEG$_{24}$-A9L or VLP-PEG$_{24}$-A9L in the presence of 1 µM A9L at 4$^{o}$C for 1 h. The cells were washed with DPBS to remove unbound particles from the cell surface, and incubated at 37$^{o}$C for 1 h to enable internalization of surface-bound particles. They were then washed and visualized by

deconvolution microscopy (Figure 4.13). High Cy5 fluorescence was observed in LNCaP cells incubated with VLP-$PEG_{24}$-A9L, suggesting that A9L enabled tight binding of VLP-$PEG_{24}$-A9L to the LNCaP cell surface via PSMA, which were not removed in the wash steps and subsequently internalised at 37$^{o}$C. Addition of excess free A9L aptamers led to a significant decrease in Cy5 fluorescence, suggesting that free aptamers competed with those present on VLP-$PEG_{24}$-A9L for PSMA binding on the LNCaP cell surface, thus reducing VLP-$PEG_{24}$-A9L uptake. In comparison, no Cy5 fluorescence was observed for PC-3 cells, or for LNCaP cells incubated with VLP-$PEG_{24}$, indicating the lack of non-specific cell binding and uptake.

### 4.2.5 Effects of siRNA delivery on BCL2 expression

To investigate the effect of siRNA delivery by VLP-$PEG_{24}$-A9L on cellular BCL2 expression, intracellular antibody staining was used, as described in Chapter 3. Cells were stained with FITC-labelled anti-BCL2 antibodies and analysed by flow cytometry. The mean FITC fluorescence of untreated cells were assumed to represent 100% BCL2 protein production, to which that of treated cells were compared to calculate relative % BCL2 expression.

LNCaP and PC-3 cells were incubated with 10 nM TR-BCL2 packaged inside VLP-$PEG_{24}$-A9L for 0 h, 24 h, 48 h or 72 h, and assayed for relative BCL2 expression (Figure 4.14). For LNCaP cells, whilst 24 h incubation led to a small reduction in BCL2 expression relative to the 0 h control (89.4±10.1%), more significant reductions were observed at 48 h (49.9±6.8%) and 72 h (14.7±9.0%). This result is reminiscent of that observed for HeLa cells in Chapter 3 (Figure

3.18), in which BCL2 expression was relatively unchanged until the 48 h time point. The delay between the start of incubation and the significant BCL2 knockdown seen at 48 h possibly reflects the cumulative time required for the VLP-$PEG_{24}$-A9L to be taken up, the release of siRNA from the endosome, and their entry into the RNAi pathway. In contrast, negligible changes in BCL2 expression were observed for PC-3 cells at 24 h (94.4±9.6%) and 48 h (100.3±15.0%), whilst 72 h incubation produced a noticeable decrease in BCL2 expression (75.0±8.9%). This ~25.0% BCL2 knockdown might be a result of the non-specific uptake previously observed in PC-3 cells (Figure 4.12). The lack of effect at earlier time points indicates that the level of non-specific uptake was not sufficient to induce BCL2 knockdown at 24 h and 48 h. Another possibility is that non-specific uptake by PC-3 cells occurred via a distinct pathway to that utilised by A9L targeted uptake by LNCaP cells, which resulted in much smaller quantities of siRNAs in the cytoplasm.

The siRNA concentration dependence of BCL2 knockdown was also investigated. LNCaP and PC-3 cells were incubated with 0 nM, 5 nM, 10 nM or 25 nM TR-BCL2 packaged inside VLP-$PEG_{24}$-A9L for 48 h, before their relative BCL2 expressions were measured (Figure 4.15). The level of BCL2 knockdown correlated positively with the concentration of TR-BCL2 used, as the BCL2 expression decreased to 80.2±13.2%, 49.9±6.8% or 34.2±10.6% following incubation with 5 nM, 10 nM or 25 nM siRNA, respectively. For PC-3 cells, a relatively small reduction in BCL2 expression was observed with 25 nM siRNA (86.8±17.3%), whilst 5 nM and 10 nM did not produce a noticeable change compared to untreated cells.

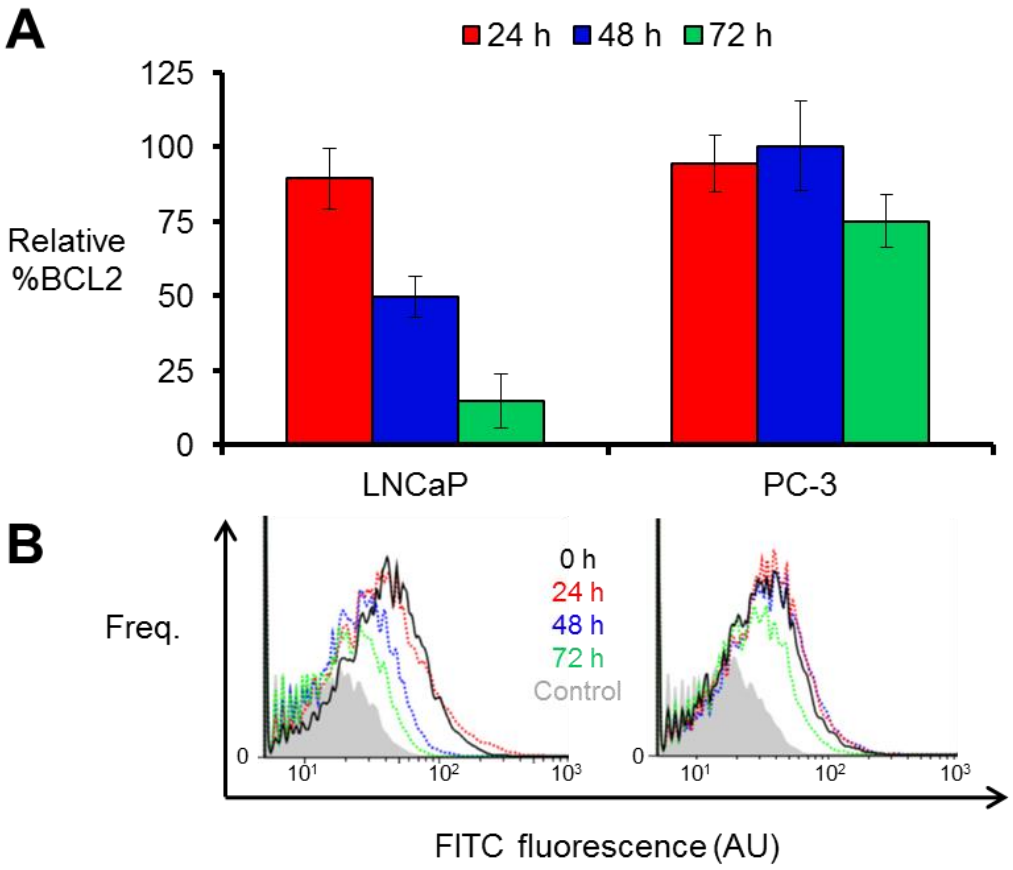


**Figure 4.14. Time-dependent BCL2 knockdown after siRNA delivery.** After treatment with 10 nM TR-BCL2 packaged inside VLP-PEG$_{24}$-A9L for 0 h, 24 h, 48 h or 72 h, LNCaP and PC-3 cells were stained with FITC-conjugated anti-BCL2 antibodies, washed, and analysed by flow cytometry. The mean FITC fluorescence of untreated cells (0 h) was designated as 100% BCL2 expression, to which the FITC fluorescence of treated cells were compared to calculate relative % BCL2 expressions. **(A)** Bar chart showing relative % BCL2 expressions after siRNA delivery. Error bars indicate standard deviation of three repeats. **(B)** Flow cytometry histograms showing the FITC fluorescence of antibody stained cells. Curves in the histograms are colour-coded to match the corresponding bar charts above. Black curves represent 0 h controls; grey shaded curves show the background fluorescence, determined by staining cells with a FITC-labelled isotype control antibody.

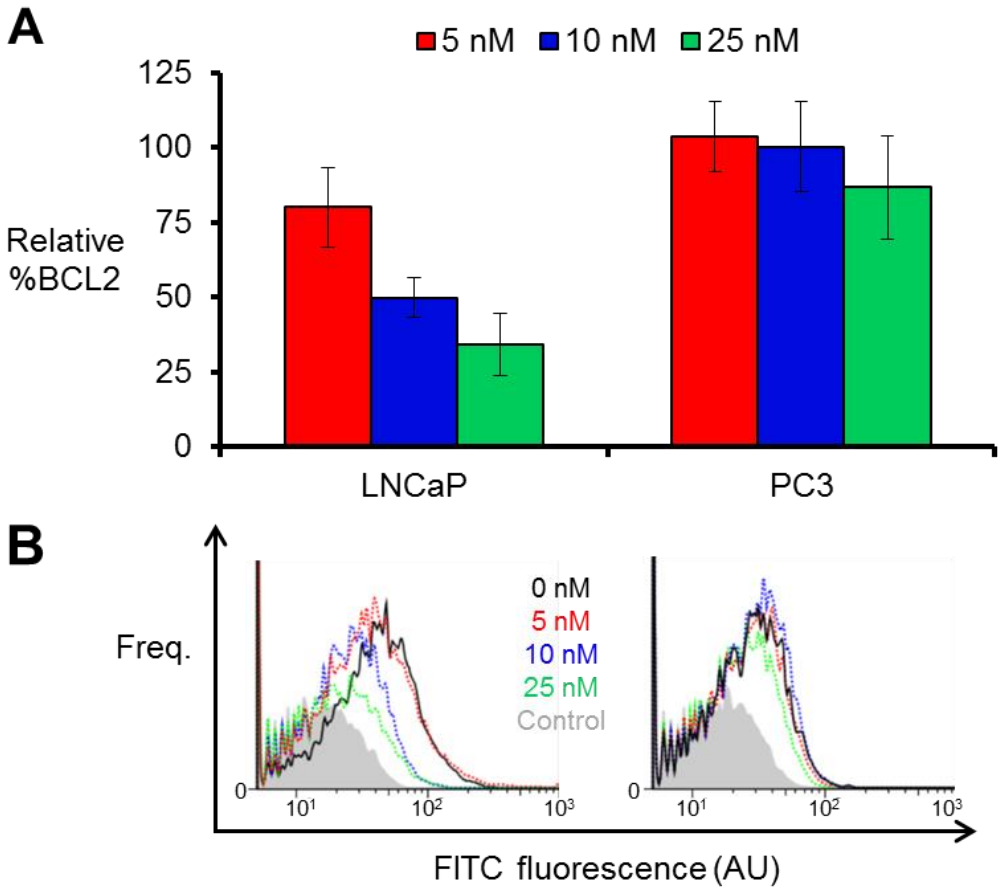


**Figure 4.15. Concentration-dependent BCL2 knockdown after siRNA delivery.** After treatment with 0 nM, 5 nM, 10 nM or 25 nM TR-BCL2 packaged inside VLP-$PEG_{24}$-A9L for 48 h, LNCaP and PC-3 cells were analysed for relative BCL2 expression. **(A)** Bar chart showing relative % BCL2 expressions after siRNA delivery. Error bars indicate standard deviation of three repeats. **(B)** Flow cytometry histograms showing the FITC fluorescence of antibody stained cells. Curves in the histograms are colour-coded to match the corresponding bar charts above. Black curves represent 0 h controls; grey shaded curves show the background fluorescence, determined by staining cells with a FITC-labelled isotype control antibody.

LNCaP and PC-3 cells were then incubated with 10 nM TR-siRNA packaged inside various VLP formulations for 48 h, and assayed for relative BCL2 expression (Figure 4.16). For LNCaP cells, TR-BCL2 delivered by VLP-$PEG_{24}$ and VLP-$PEG_{24}$-A9L led to BCL2 expressions of 94.2±11.9% and 49.9±6.8%,

respectively. This is consistent with the cellular uptake data: the relatively low level of non-specific uptake of VLP-$PEG_{24}$ had a minimal impact on BCL2 expression in LNCaP cells, whilst the much higher uptake of VLP-$PEG_{24}$-A9L produced a significant knockdown in BCL2 expression. Further addition of 100 nM free A9L to VLP-$PEG_{24}$-A9L increased the BCL2 expression to 82.1±6.8%, confirming that A9L mediates VLP-$PEG_{24}$-A9L uptake by LNCaP cells.

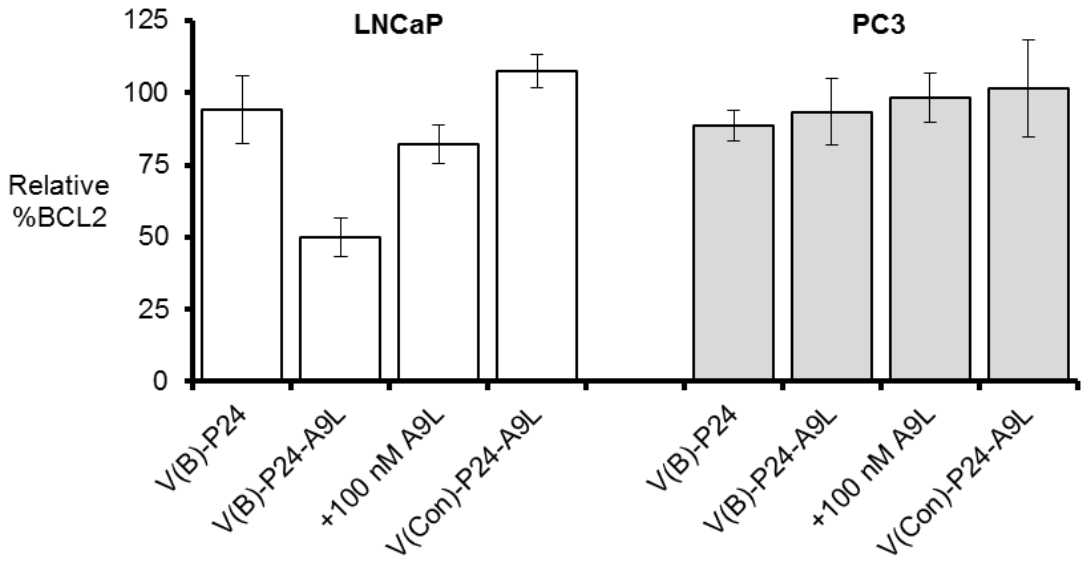


**Figure 4.16. Comparative cellular BCL2 expression after siRNA delivery.** LNCaP and PC-3 cells were incubated with 10 nM TR-BCL2 packaged inside (from left) VLP-$PEG_{24}$, VLP-$PEG_{24}$-A9L, or VLP-$PEG_{24}$-A9L plus 100 nM free Tf, or with 10 nM TR-Control packaged inside VLP-$PEG_{24}$-A9L for 48 h, and then assayed for BCL2 expression. Error bars indicate standard deviation of three repeats.

Interestingly, this level of BCL2 expression was lower than that observed for VLP-$PEG_{24}$ treated cells (94.2±11.9%) – similar findings were reported for HeLa cells incubated with VLP-$PEG_{24}$-Tf and free Tf (Figure 3.19). This indicates that the presence of 100 nM free A9L was insufficient to fully inhibit the uptake and

effects of A9L targeted siRNA delivery. Possible explanations include: (i) the multivalent display of A9L to some extent favoured the binding and uptake of VLP-$PEG_{24}$-A9L, due to increased avidity to PSMA on LNCaP cells, (ii) PSMA could not be fully saturated by the free A9L due to its recycling to the cell surface, and (iii) there was a low level of non-specific uptake of VLP-$PEG_{24}$-A9L which occurred independently of A9L targeting. Furthermore, TR-Control delivery by VLP-$PEG_{24}$-A9L did not produce a significant change in BCL2 expression (107.3±5.7%), indicating that the observed knockdown was siRNA sequence-dependent, and not associated with the uptake of VLP-$PEG_{24}$-A9L or TR-conjugated dsRNAs. For PC-3 cells, none of the treatments produced a notable change in BCL2 expression relative to the untreated control. This suggests that, despite the previously observed non-specific uptake by PC-3 cells, the cytoplasmic siRNA concentrations resulting from these transfections were insufficient to induce significant BCL2 knockdown.

### 4.2.6 Cytotoxic effects of siRNA delivery

The cytotoxicity assay described in Chapter 3 was used to assess whether siRNA delivery by VLP-$PEG_{24}$-A9L could induce toxicity in LNCaP and PC-3 cells. As a control, LNCaP and PC-3 cells were treated with varying concentrations of free cisplatin for 24 h (Skjoth and Issinger, 2006), and stained with annexin V-FITC and propidium iodide, before they were analysed by flow cytometry (Figure 4.17, Figure 4.18).

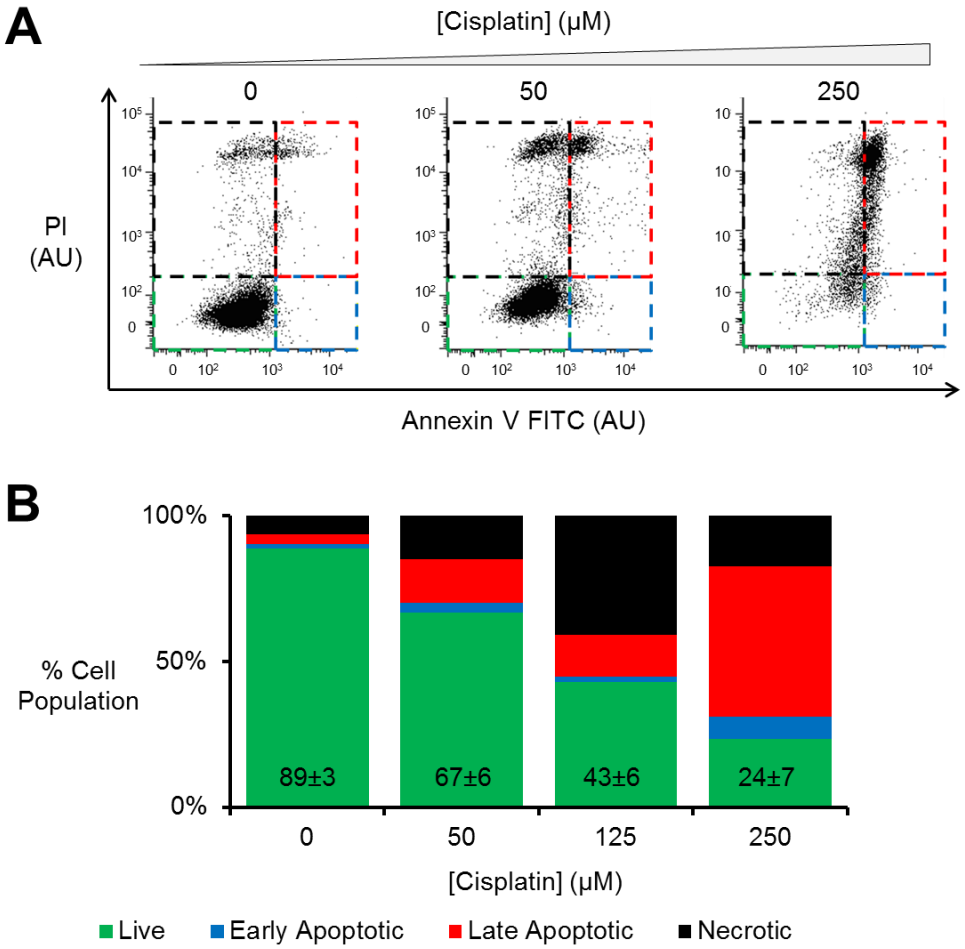


**Figure 4.17. Flow cytometry analysis of cell toxicity in LNCaP cells.** LNCaP cells were incubated with 0 μM, 50 μM, 125 μM or 250 μM cisplatin for 24 h, and assayed for toxicity. **(A)** Sample flow cytometry histograms showing the 0 μM, 50 μM and 250 μM treatments. **(B)** Bar charts displaying relative % cell populations that were live (green), early apoptotic (blue), late apoptotic (red), or necrotic (black). The percentages shown represent the average of three repeats. Numbers indicate mean percentage cell viability ± SD.

LNCaP cells exhibited higher annexin V-FITC binding as well as propidium iodide uptake with increasing cisplatin concentrations, indicative of increased cytotoxicity (Figure 4.17). As described previously, flow cytometry histograms were divided into quadrants to determine relative populations of cells that were live, early apoptotic, late apoptotic or necrotic (Figure 4.17A). These were then

represented as a percentage of the total cell population in stacked bar charts (Figure 4.17B). Untreated LNCaP cells largely remained viable (88.6±3.4%); the small population of dead cells might be a result of the conditions used for incubation, or possibly artefacts produced by the assay. However, significant reductions in % cell viability were observed as the cisplatin concentration increased to 50 µM (67±6%), 125 µM (43±6%) and 500 µM (24±7%).

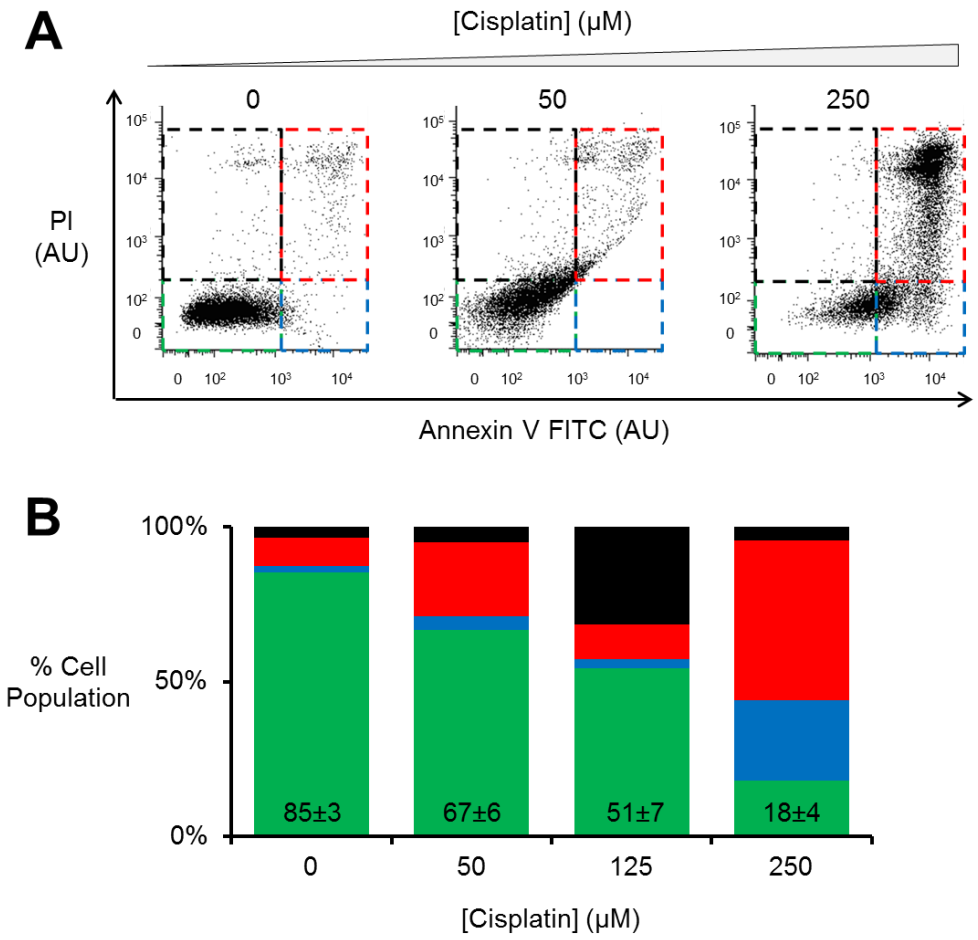


**Figure 4.18. Flow cytometry analysis of cell toxicity in PC-3 cells.** PC-3 cells were incubated with 0 µM, 50 µM, 125 µM or 250 µM cisplatin for 24 h, and assayed for toxicity. **(A)** Sample flow cytometry histograms showing the 0 µM, 50 µM and 250 µM treatments. **(B)** Bar charts displaying relative % cell populations that are live (green), early apoptotic (blue), late apoptotic (red), or necrotic (black). The percentages shown represent the average of three repeats. Numbers indicate mean percentage cell viability ± SD.

One interesting observation is that the non-viable cell populations consisted mainly of late apoptotic or necrotic cells at all cisplatin concentrations. This might be due to LNCaP cells progressing quickly from early to late apoptosis, thus very few early apoptotic cells were detected by the assay after 24 h incubation. Furthermore, a relatively large necrotic population was observed at 125 µM cisplatin (34±6%), which interestingly diminished at 250 µM (17±4%). One possibility is that higher cisplatin concentrations caused some cells to rapidly progress through necrosis, undergoing cell swelling and membrane rupture, and thus were not counted at 250 µM.

Likewise, the % cell viability of PC-3 cells also decreased in a cisplatin concentration-dependent manner (Figure 4.18). These results suggest that both LNCaP and PC-3 cells are responsive to a conventional chemotherapeutic, and that the cytotoxicity assay is compatible with these cells.

LNCaP and PC-3 cells were incubated with 10 nM TR-BCL2 packaged inside VLP-$PEG_{24}$-A9L for 0 h, 24 h, 48 h or 72 h, stained with annexin V-FITC and propidium iodide, and then analysed by flow cytometry (Figure 4.19A). For LNCaP cells, a small decrease in % cell viability was observed at 24 h (75±10%) compared to the 0 h control (89±1%), whilst more significant reductions were observed for the 48 h (35±3%) and 72 h (13±6%) time points. This suggests that TR-BCL2 delivery by VLP-$PEG_{24}$-A9L induced cytotoxicity in LNCaP cells in a time-dependent manner, and that there is a strong correlation between cytotoxicity and BCL2 expression.

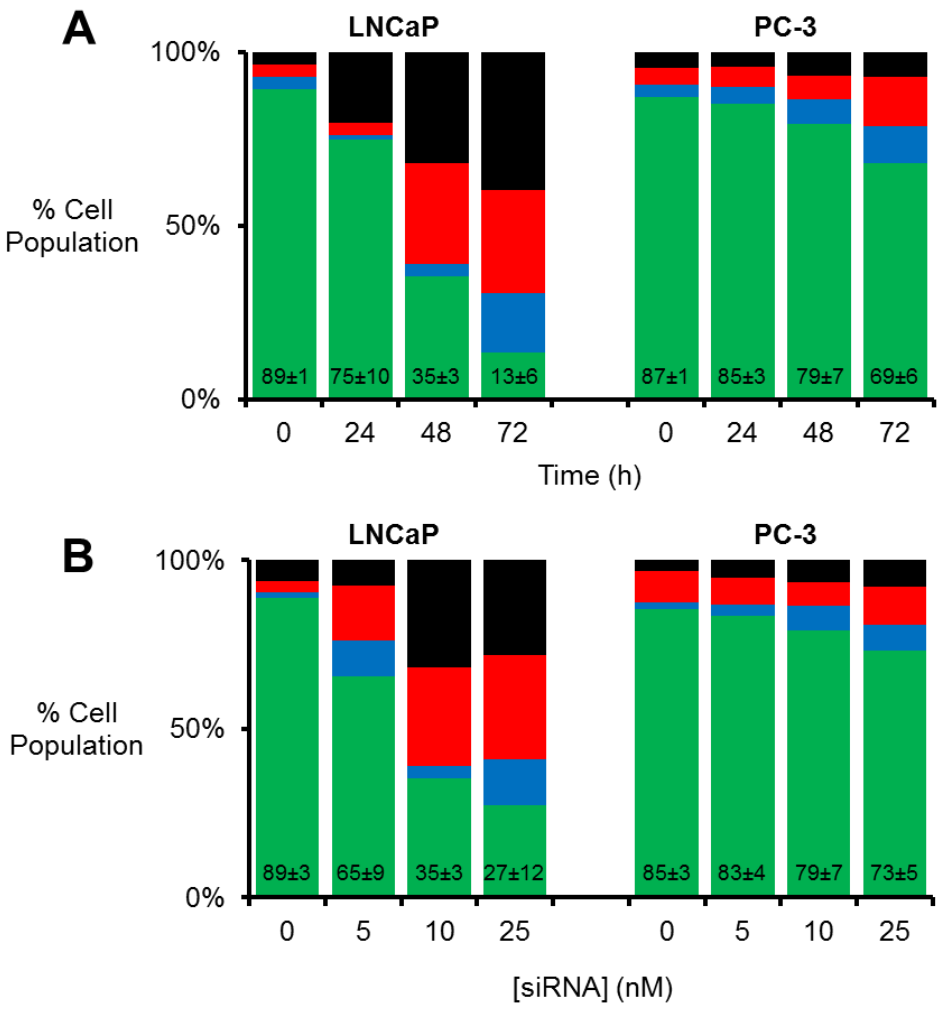


**Figure 4.19. Time- and concentration-dependent toxicity of siRNA delivery. (A)** LNCaP and PC-3 cells were incubated with 10 nM TR-BCL2 packaged inside VLP-$PEG_{24}$-A9L for 0 h, 24 h, 48 h or 72 h, and assessed for toxicity. **(B)** LNCaP and PC-3 cells were incubated with 0 nM, 5 nM, 10 nM or 25 nM TR-BCL2 packaged inside VLP-$PEG_{24}$-A9L for 48 h, and assessed for toxicity. The percentages shown represent the average of three repeats. Numbers indicate mean percentage cell viability ± SD.

It was described in Chapter 3 that increasing the incubation time up to 72 h produced notable diminishing returns on the cytotoxicity of treated HeLa cells (Figure 3.21A). However, this diminishing return effect appeared to be much less pronounced in LNCaP cells. This might be due to different rates of cell division, as LNCaP cells have a doubling time of ~60 h compared to the ~24 h

of HeLa cells. Since cell division is associated with the dilution of internalised TR-BCL2, a larger dilution effect was expected in the rapidly dividing HeLa cells, hence a greater proportion of HeLa cells were expected to remain viable after prolonged treatments compared to LNCaP cells.

Time-dependent cytotoxicity was also observed in PC-3 cells, although the effects were much less significant, with 69±6% of cells still remaining viable after 72 h incubation, compared to the 87±1% of untreated cells (Figure 4.19A). This mild increase in cytotoxicity correlates with BCL2 expression, as a ~25% BCL2 knockdown was observed for PC-3 cells at the same time point (Figure 4.14).

The cytotoxic effect of siRNA delivery at different siRNA concentrations was also investigated. LNCaP and PC-3 cells were incubated with 0 nM, 5 nM, 10 nM or 25 nM TR-BCL2 packaged inside VLP-$PEG_{24}$-A9L for 48 h, before they were assayed for cytotoxicity. For LNCaP cells, higher levels of cytotoxicity was observed with increasing siRNA concentrations – with 89±3%, 65±9%, 35±3% and 27±12% of cells remaining viable after incubation with 0 nM, 5 nM, 10 nM and 25 nM siRNA, respectively (Figure 4.19B). The % cell viability seems to correlate positively with the BCL2 expression of LNCaP cells treated under the same conditions (Figure 4.15). Interestingly, increasing the siRNA concentration from 10 nM to 25 nM produced a relatively small change in % cell viability compared to that from 5 nM to 10 nM siRNA (Figure 4.19B). It is possible that the intracellular siRNA concentration resulting from a 10 nM transfection was close to saturating certain RNAi components in the cell, thus further increasing the siRNA concentration would yield significant diminishing returns on its cytotoxic effects. For PC-3 cells, a similar pattern of concentration-dependent

cytotoxicity was observed, albeit the effects were relatively insignificant with 73±5% of cells still remaining viable after incubation with 25 nM siRNA, compared to the 85±3% of untreated cells (Figure 4.19B). The low level of cytotoxicity observed might be due to the non-specific uptake of VLP-$PEG_{24}$-A9L by some PC-3 cells.

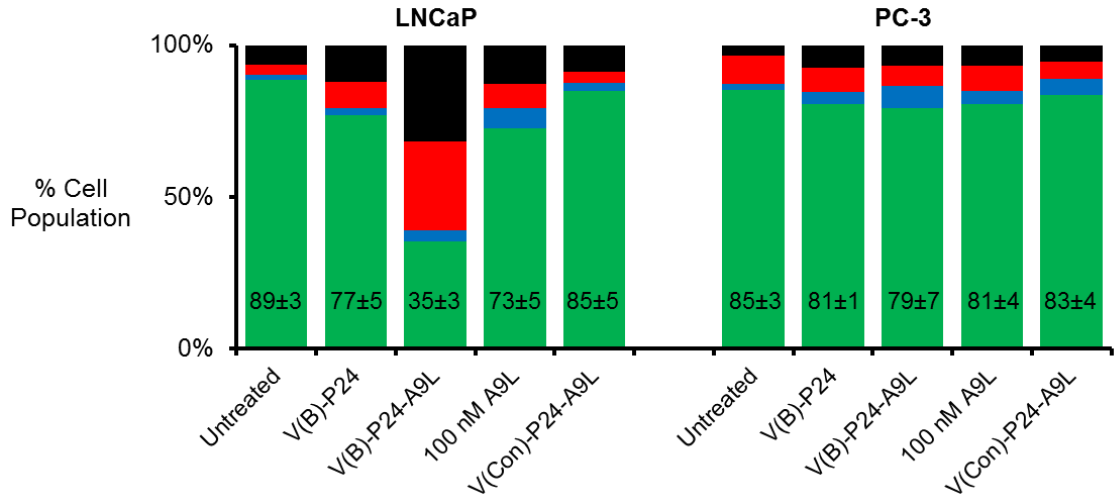


**Figure 4.20. Comparative toxicity of siRNA delivery.** LNCaP and PC-3 cells were (from left) untreated, incubated with 10 nM TR-BCL2 siRNA packaged inside VLP-$PEG_{24}$, VLP-$PEG_{24}$-A9L, or VLP- $PEG_{24}$-A9L plus 100 nM free A9L, or 10 nM TR-Control packaged inside VLP-$PEG_{24}$-A9L for 48 h, and then assayed for cytotoxicity. The percentages shown represent the average of three repeats. Numbers indicate mean percentage cell viability ± SD.

LNCaP and PC-3 cells were then incubated with 10 nM TR-siRNA packaged inside various VLP formulations for 48 h, and assayed for cytotoxicity (Figure 4.20). For LNCaP cells, a small background level of toxicity was observed, with 89±3% of untreated cells remaining live. Comparatively, TR-BCL2 delivery by VLP-$PEG_{24}$ and VLP-$PEG_{24}$-A9L reduced the % cell viability to 77±5% and 35±3%, respectively. The increased cytotoxicity of VLP-$PEG_{24}$ treated cells was unexpected, as TR-BCL2 delivery by VLP-$PEG_{24}$ produced a fairly negligible

effect on BCL2 expression (94±12%, Figure 4.16). It is possible that uptake of small amounts of VLP-$PEG_{24}$ (Figure 4.12B) led to off-target toxicities in some LNCaP cells. Further addition of 100 nM free A9L to VLP-$PEG_{24}$-A9L increased the % cell viability to 73±5%, which is comparable to that observed for VLP-$PEG_{24}$ treated cells. This implies that A9L targeted VLP-$PEG_{24}$-A9L for uptake by LNCaP cells, and they were outcompeted by the presence of excess free A9L. Delivery of TR-Control by VLP-$PEG_{24}$-A9L did not produce a significant change in % cell viability relative to untreated cells (85±5%). This suggests that the uptake of TR-siRNA encapsidated VLP-$PEG_{24}$-A9L by LNCaP cells did not trigger off-target toxicities, and that the cytotoxicity observed for TR-BCL2 delivery by VLP-$PEG_{24}$-A9L could be largely attributed to siRNA-mediated BCL2 knockdown.

In contrast, negligible effects were observed in PC-3 cells with all treatments (Figure 4.20). The biggest effect was observed with TR-BCL2 delivery by VLP-$PEG_{24}$-A9L, with 79±7% of cells remaining viable, compared to the 85±3% for untreated PC-3 cells. Altogether, these results suggest that VLP-$PEG_{24}$-A9L delivered the TR-BCL2 cargo specifically to LNCaP cells via A9L-mediated targeting of PSMA, which subsequently induced cytotoxicity in these cells.

### 4.2.7 Liposomal siRNA delivery to PC-3 cells

To ensure the lack of cellular effect seen for PC-3 cells was due to aptamer-specific targeting, and not their insensitivity to the BCL2 siRNA, HiPerFect Transfection Reagent was used to package TR-BCL2 for delivery to PC-3 cells. HiPerFect contains a mixture of cationic and neutral lipids, which can interact

electrostatically with polyanionic molecules, such as siRNA, to form lipoplexes with the siRNA packaged inside. These lipid particles can deliver packaged siRNAs to cells indiscriminately.

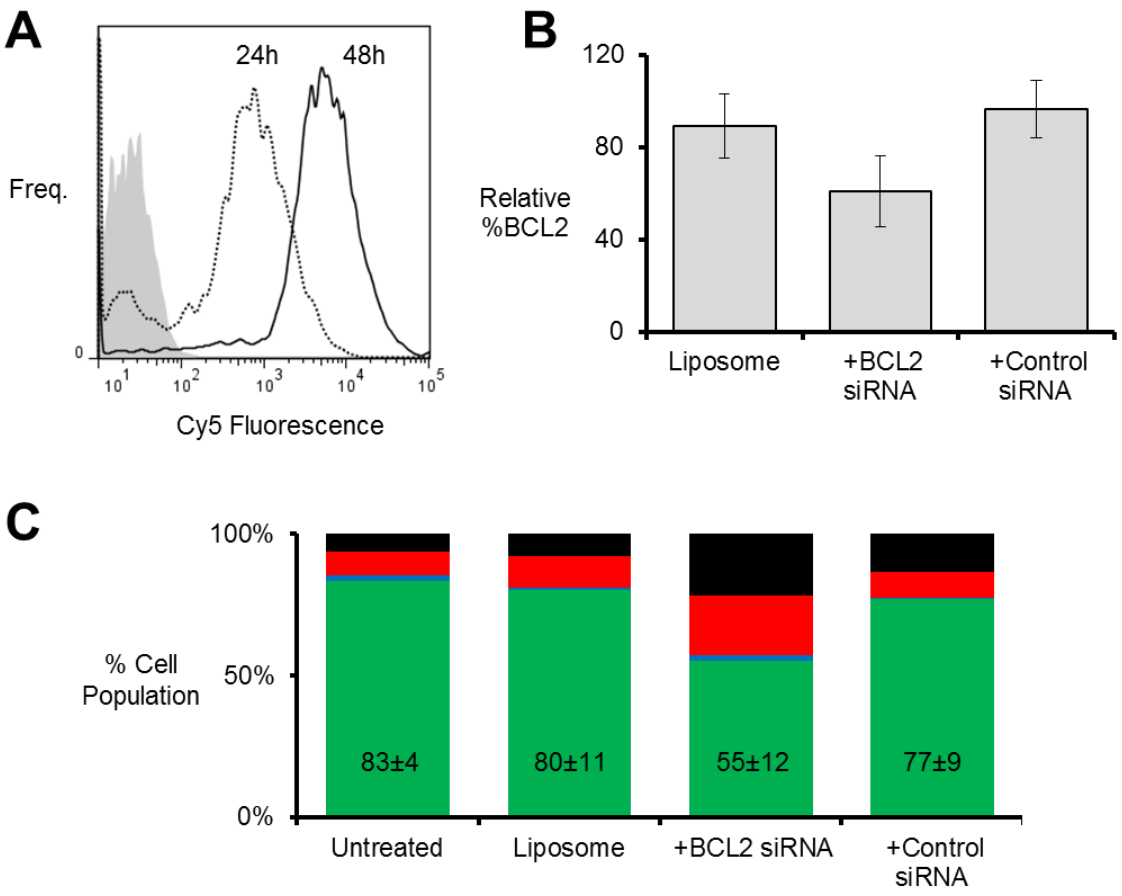


**Figure 4.21. Analysis of liposomal siRNA delivery to PC-3 cells. (A)** Flow cytometry histogram showing PC-3 cells either untreated (grey), or incubated with 10 nM TR-Cy5 packaged inside liposomes for 24 h (dotted) or 48 h (solid). **(B)** Relative % BCL2 expression of PC-3 cells after various treatments at 48 h. Error bars indicate the standard deviation of three repeats. **(C)** Relative populations of PC-3 cells that were live (green), early apoptotic (blue), late apoptotic (red) or necrotic (black) after various treatments at 48 h. The percentages shown represent the average of three repeats. Numbers indicate mean percentage cell viability ± SD.

Firstly, the uptake of liposomes by PC-3 cells was investigated. PC-3 cells were grown on 24 well plates, incubated with 10 nM TR-Cy5 packaged inside HiPerFect for 24 h or 48 h, and processed for flow cytometry analysis (Figure 4.21A). The mean Cy5 fluorescence of PC-3 cells increased significantly at 24 h (651.3±48.9 AU) and 48 h (4037.1±572.3 AU) incubations, which indicates the accumulation of TR-Cy5 inside cells with time. The curves in the histogram suggest that, whilst a distinct, small portion of cells remained untransfected at 24 h, the vast majority of cells were transfected by 48 h (Figure 4.21A). The untransfected population might reflect newly divided cells that did not take up any liposomal TR-Cy5.

Next, relative cellular BCL2 expressions were assessed using the previously used protocol. PC-3 cells were grown on 24 well plates, and were either untreated, or incubated with various HiPerFect treatments for 48 h, before they were processed for intracellular antibody staining and flow cytometry analysis (Figure 4.21B). A HiPerFect (liposome) only control produced a small change in % BCL expression (90±14%) compared to untreated cells; likewise, negligible change was observed after liposomal delivery of TR-Control (97±13%). However, liposomal delivery of TR-BCL2 resulted in a noticeable reduction in BCL2 expression (61±15%), somewhat comparable to that observed in LNCaP cells after TR-BCL2 delivery by VLP-$PEG_{24}$-A9L. This suggests that liposomes were able to deliver siRNAs to the cytoplasm of PC-3 cells, and trigger siRNA-mediated knockdown of BCL2.

Finally, the cytotoxic effects of siRNA delivery were analysed (Figure 4.21C). As above, PC-3 cells were grown on 24 well plates, and were untreated, or

incubated with various HiPerFect treatments for 48 h, before they were assayed for cytotoxicity. Some background cell death was observed, as 83±4% of untreated cells remained viable. The % cell viability was relatively unaffected with the addition of liposome (80±11%), or with the liposomal delivery of TR-Control (77±9%). However, a significant reduction in % cell viability was observed with the liposomal delivery of TR-BCL2 (55±12%). This is consistent with the relative BCL2 expression data (Figure 4.21B), and indicates a positive correlation between BCL2 knockdown and cytotoxicity. The lack of toxicity observed for the liposome only control, and for the liposomal delivery of TR-Control suggests that the treatments did not produce any off-target toxicities.

## 4.3 Summary of Chapter 4

1. A thiol-modified, fluorescently labelled RNA ligand, U6-FAM, was attached to VLPs via $SM(PEG)_{24}$ using amine-to-thiol conjugation. Each VLP-$PEG_{24}$-U6-FAM particle displayed on average ~16 molecules of U6-FAM. The same protocol was then used to conjugate an RNA aptamer, A9L, to VLPs via $SM(PEG)_{24}$, resulting in VLP-$PEG_{24}$-A9L. A9L binds specifically to PSMA, a tumour marker that is prevalently and highly expressed on the surface of prostate cancer cells.

2. Both VLP-$PEG_{24}$-A9L particles and their displayed A9L remained stable in cell media. There was evidence of A9L degradation in human serum, prompting the use of chemically modified RNA aptamers for future *in vivo* experiments. VLP-$PEG_{24}$-A9L displayed markedly reduced binding by anti-MS2

antibodies compared to unmodified VLP, confirming the immuno-masking effect of PEGylation. However, PEGylation could not completely block antibody binding at higher antibody concentrations; *in vivo* tests will be necessary to assess the true immunogenicity of PEGylated VLPs.

3. A9L specifically targeted VLP-$PEG_{24}$-A9L to $PSMA_{+ve}$ LNCaP cells, but not $PSMA_{-ve}$ PC-3 cells, for binding and uptake. TR-BCL2 delivery by VLP-$PEG_{24}$-A9L produced significant responses in LNCaP cells, including ~50% BCL2 knockdown and a ~53% decrease in cell viability, at just 10 nM siRNA concentration. Further addition of free A9L significantly reduced the uptake of siRNA delivered by VLP-$PEG_{24}$-A9L, as well as its cellular effects. As for VLP-$PEG_{24}$-Tf, the uptake of VLP-$PEG_{24}$-A9L did not produce any off-target toxicity in cells. PC-3 cells were responsive to TR-BCL2 when delivered by a commercially available liposome.

# Chapter 5

Aptamer-targeted cellular delivery of doxorubicin

# 5.1 Introduction

### 5.1.1 Anthracyclines in chemotherapy

Since the first report of their isolation from *Streptomyces peucetius* in the 1960s (Dimarco et al., 1964), the anthracyclines have proven to be one of the most effective anti-cancer therapeutics and have significantly improved cancer survival statistics. The anti-tumour activity of anthracyclines has been attributed to several mechanisms (Binaschi et al., 2001), including:

- Inhibition of nucleic acid synthesis by intercalating between base pairs of DNA/RNA strands (Pratt and Ruddon, 1979),
- Generation of free oxygen radicals resulting in DNA damage or lipid peroxidation (Vasquez-Vivar et al., 1997),
- Inhibition of topoisomerase II triggering DNA damage and apoptosis (Jensen et al., 1993), and
- Eviction of key histones implicated in DNA repair from the chromatin (Pang et al., 2013).

Doxorubicin (Dox) and daunorubicin were among the first identified anthracyclines, both of which still remain prevalently used in the treatment of a range of haematological and solid cancers (Weiss, 1992). They are similar in structure, with an aglyconic group resembling a tetracyclic ring, attached to a daunosamine sugar, with the distinction being that the side chain terminates with either a primary alcohol or a methyl group for Dox and daunorubicin, respectively (Figure 5.1). Though subtle, this distinction seems to have a notable impact on their anti-tumour activities: Dox shows a broad spectrum of

activity against various solid tumours, whereas daunorubicin is more effective against acute leukemias (Martindale, 1996).

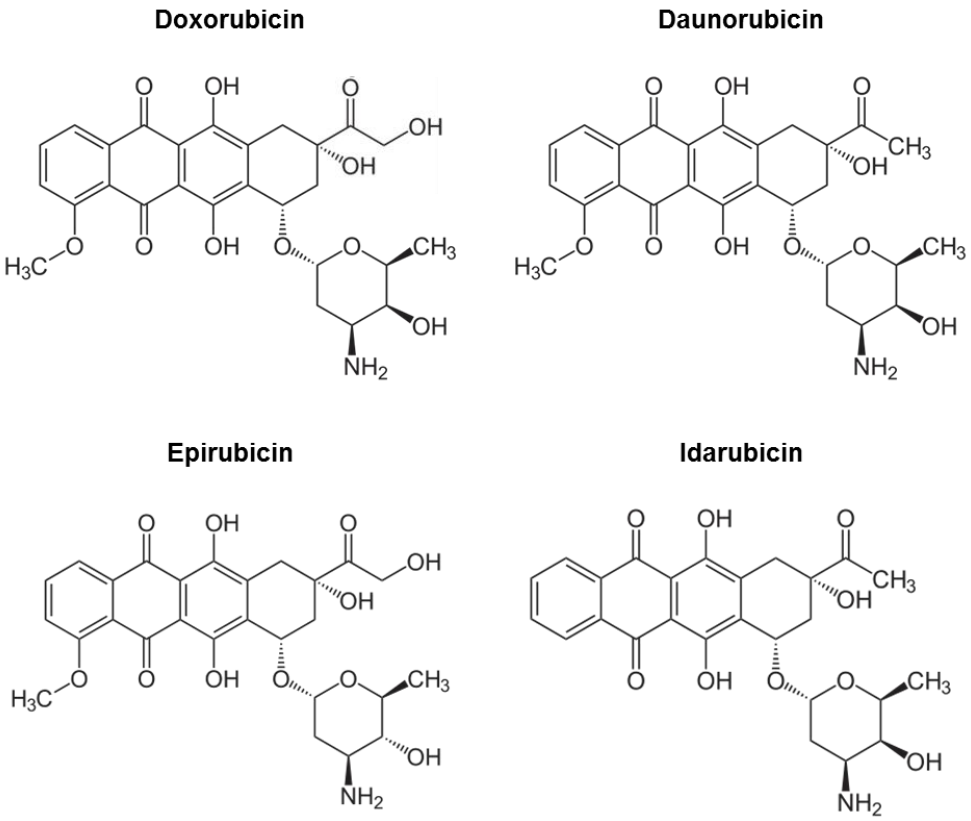


**Figure 5.1. Chemical structures of anthracyclines.** Shown are the four most commonly used anthracyclines in the clinic. Epirubicin was structurally derived from Dox, resulting from an axial-to-equatorial epimerisation of the hydroxyl on the daunosamine sugar. Idarubicin was structurally derived from daunorubicin, via removal of a 4-methoxy group.

Whilst the anthracyclines have undoubtedly played a significant part in the treatment of cancers, they have some notable drawbacks. Firstly, non-specific uptake of Dox or daunorubicin can induce toxicity in healthy cells and lead to adverse effects. One major side effect is cumulative dose-dependent cardiotoxicity, which can lead to severe cases of chronic cardiomyopathy and congestive heart failure in patients (Volkova and Russell, 2011). Another

problem is the development of multiple drug resistance, with as many as ~70% of patients experiencing a relapse despite having complete remission after initial anthracycline treatment (Ma and Mumper, 2013). The mode of resistance typically involves overexpression of drug efflux proteins, such as P-glycoprotein and breast cancer resistance protein (Chien and Moasser, 2008).

These problems have prompted the development of second generation anthracyclines, derived from modifying the structures of Dox and daunorubicin (Weiss, 1992). Two commonly used anthracycline derivatives in the clinic include epirubicin and idarubicin. Epirubicin is derived via an axial-to-equatorial epimerisation of the hydroxyl group on the daunosamine sugar of Dox (Figure 5.1). This epimerisation opens an unique glucuronidation metabolic pathway that is not available to Dox, which enhances the plasma clearance of epirubicin, and has been shown to reduce cardiotoxic effects compared to Dox (Robert, 1993). Idarubicin is derived via removal of a 4-methoxy group from one of the tetracyclic rings on daunorubicin (Figure 5.1). This modification has been demonstrated to significantly enhance the lipophilicity of the drug, resulting in faster cellular uptake, higher DNA-binding capacity and improved cytotoxicity compared to daunoribicin (Binaschi et al., 2001, Minotti et al., 2004). Additionally, idarubicin is more effective in some multidrug resistant tumour cell lines compared to daunorubicin (Jonsson-Videsater et al., 2003, Toffoli et al., 1994), and has a wider spectrum of activity in cancers such as non-Hodgkin's lymphoma, multiple myeloma and breast cancer (Borchmann et al., 1997). Many other anthracycline derivatives have also been developed, though only a few have been clinically approved for treating cancers (Minotti et al., 2004), with only modest improvements with respect to drug resistance and cardiotoxicity.

### 5.1.2 Dox delivery

Aside screening for anthracycline derivatives, another approach to improve the pharmacological properties of anthracyclines has been to utilise drug delivery systems (Table 5.1). One of the earliest examples of an anthracycline delivery system is Doxil, which received FDA approval in 1995 for treating AIDS-related Kaposi's sarcoma, and later for treating multiple myeloma, and advanced breast and ovarian cancers (Barenholz, 2012). Doxil is a PEGylated liposomal formulation of Dox, composed of PEG-coupled distearoyl phosphatidylethanolamine, hydrogenated soy phosphatidylcholine and cholesterol. With an average diameter of ~90 nm, Doxil nanoparticles benefit fully from EPR (Matsumura and Maeda, 1986). In addition, surface coating with PEG minimises the detection of liposomes by the mononuclear phagocytic system (Vail et al., 2004). As a result, Doxil displays significantly longer plasma retention, a lower volume of distribution, as well as reduced cardiotoxicity compared to free Dox (Batist, 2007).

Polymer conjugates have also been utilised to deliver Dox to cancer cells. The first polymer-drug conjugate to enter clinical trials was AD-70, a ~70 kDa dextran polymer coupled to Dox via the formation of a Schiff base (Figure 5.2). In a phase I clinical trial, AD-70 resulted in significantly higher off-target toxicities compared to free Dox, which was attributed to dextran uptake by the mononuclear phagocytic system (Danhauser-Riedl et al., 1993), and therefore did not advance further.

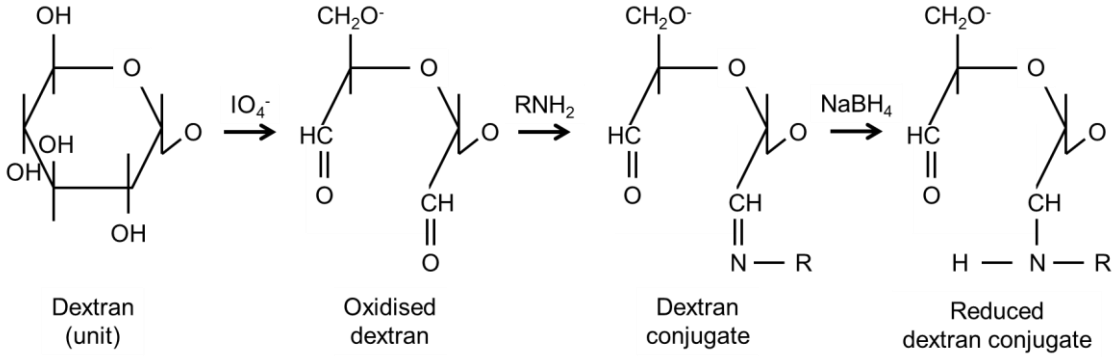


**Figure 5.2. Preparation of dextran-drug conjugates via Schiff base formation.** Periodate ($IO_4^-$) oxidation of dextran yields aldehyde groups, which react with amine-containing drugs (R) to form a Schiff base. The Schiff base can then be reduced with sodium borohydride ($NaBH_4$) to produce a stable dextran-drug conjugate.

A more successful polymer conjugate currently undergoing clinical evaluation is PK1, a synthetic polymer composed of HPMA conjugated to Dox (Figure 5.3). Similar to PEG, HPMA is a highly soluble, non-toxic, and non-immunogenic polymer, and is commonly used as a carrier for low molecular weight drugs such as Dox. HPMA is conjugated to Dox via a tetrapeptide (GFLG) linker, which is stable in blood but readily degraded by lysosomal enzymes to facilitate drug release upon endocytosis. PK1 demonstrated promising results in a phase I study, producing partial and minor responses in some patients with anthracycline-resistant breast cancer, NSCLC, and colorectal cancer (Vasey et al., 1999). Importantly, the maximum tolerated dose of PK1 was ~5 times that of free Dox, and no cardiotoxicity was observed. In a subsequent phase II trial, partial response was again observed in patients with breast cancer and NSCLC, but not colorectal cancer (Seymour et al., 2009). PK1 seemed to be well tolerated even at higher doses, without any signs of immunogenicity or HPMA-associated toxicity. A similar polymer, PK2 (Figure 5.3), has also shown

promise in clinical trials. The difference between PK2 and PK1 is the addition of a galactosamine, which targets the liver-specific asialoglycoprotein receptor. In a phase I study, PK2 demonstrated notable anti-tumour activity in hepatocellular carcinoma patients (Seymour et al., 2002). Importantly, ~17% of the administered drug localised to the liver after 24 h (Seymour et al., 2002), which is 12-50 times higher than free Dox (Duncan et al., 2005). PK1 and PK2 are currently undergoing phase III and phase II clinical trials, respectively.

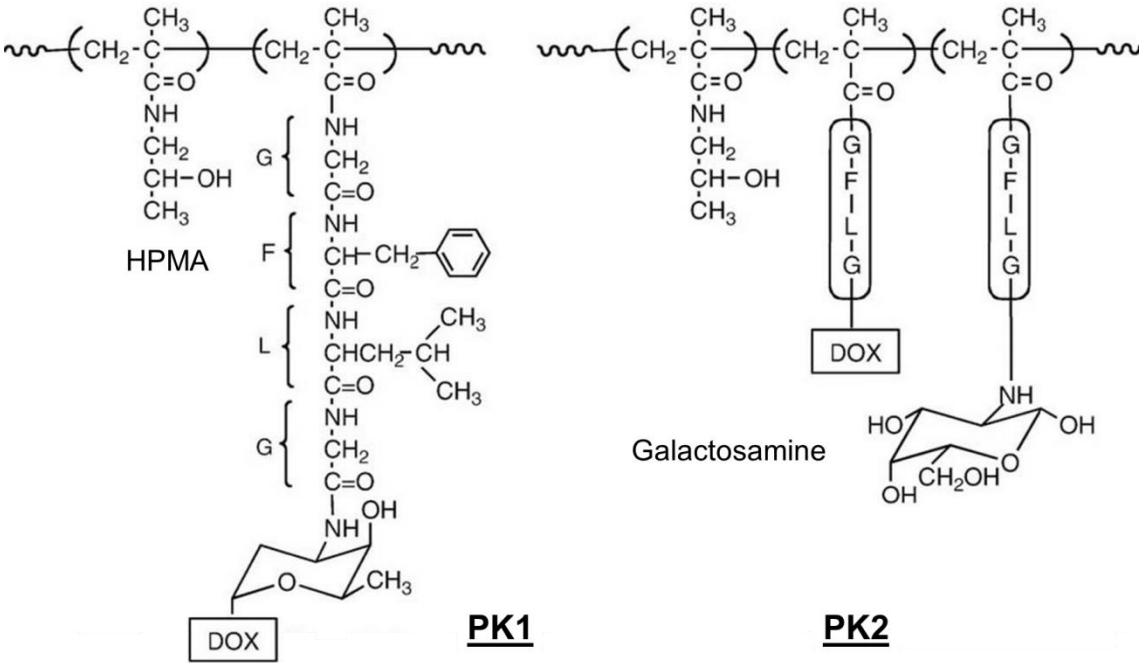


**Figure 5.3. Compositions of the HPMA-Dox conjugates, PK1 and PK2.** PK1 (left) is a synthetic polymer containing of N-(2-hydroxypropyl)methacrylamide (HPMA), conjugated to Dox via a Gly-Phe-Leu-Gly (GFLG) tetrapeptide linker. PK2 (right) has additional side chains that terminate with an N-acylated galactosamine. Synthesis of PK1/2 involves the copolymerisation of HPMA with N-methacryloylated GFLG tetrapeptides, which contain *p*-nitrophenyl esters. Subsequent addition of amine-containing moieties, such as Dox and galactosamine, results in their stable conjugation, with nitrophenol as the leaving group. Adapted from Kopecek and Kopeckova (2010).

Many other types of delivery systems have also been tested for delivering Dox, including micelles, carbon nanotubes, cyclodextrin polymers, as well as gold, silica and magnetic nanoparticles (Matyszewska, 2014). These have demonstrated improved pharmacological profiles compared to free Dox. For instance, some are able to circumvent multidrug resistance in cancers (Ma and Mumper, 2013), whilst some display improved pharmacokinetics or reduced cardiotoxicity (Zhang et al., 2013, Matsumura et al., 2004).

| Name | Description | Indication | Development | Ref |
|---|---|---|---|---|
| Doxil | PEGylated liposome | Ovarian and breast cancers, MM, ARKS | Approved | (James et al., 1994) |
| Livatag | PIHCA nanoparticles | Advanced HCC | Phase III | (Merle et al., 2006) |
| NK911 | PEGylated micelle | Metastatic pancreatic cancer | Phase III | (Matsumura et al., 2004) |
| PK1 | HPMA conjugate | Breast cancer, NSCLC | Phase III | (Seymour et al., 2009) |
| PK2 | HPMA conjugate + galactosamine | HCC | Phase II | (Seymour et al., 2002) |
| SP1049C | PEGylated micelle | Upper GI cancer | Phase II | (Valle et al., 2011) |

**Table 5.1. Selected examples of Dox delivery systems in clinical use or under development.** MM = multiple myeloma; ARKS = AIDS-related Kaposi's sarcoma; PIHCA = polyisohexylcyanoaerylate; HCC = hepatocellular carcinoma; NSCLC = non-small cell lung carcinoma; HPMA = N-(2-Hydroxypropyl)methacrylamide; GI = gastrointestinal.

### 5.1.3 Targeted Dox delivery by MS2 VLPs

Of the large number of Dox delivery systems already approved or in clinical trials, the majority depend on passive targeting to reach tumour tissues, but lack an active tumour-targeting mechanism. The aforementioned HPMA-Dox conjugate, PK2, is one of the only examples of tumour-targeted Dox delivery undergoing clinical evaluation. PK2 utilises galactosamine to target the liver-specific asialoglycoprotein receptor, and aims to treat patients with hepatocellular carcinoma (HCC). However, these receptors are abundantly expressed on healthy hepatocytes, and there is evidence to suggest HCC cells have a significantly lower surface expression of the receptor (Hyodo et al., 1993). Thus it is unsurprising that only a small fraction (<20%) of the administered PK2 which localised to the liver accumulated in cancer cells (Seymour et al., 2002).

It might be beneficial to target tumour markers which are overexpressed on the surface of cancer cells, to facilitate preferential binding and uptake by them. VLP-$PEG_{24}$-A9L has already demonstrated tumour-targeted siRNA delivery to prostate cancer cells, and can be tested for Dox delivery using the same cell lines. If successful, Dox will be added to the growing repertoire of cargos that can be delivered by MS2 VLPs (Brown et al., 2002, Wu et al., 2005, Ashley et al., 2011, Pan et al., 2012a, Pan et al., 2012b, Galaway and Stockley, 2013, Li et al., 2013), which would underline their versatility as a drug delivery system. Further, Dox has numerous advantages as a model drug cargo, including (i) it is a well-characterised, established cancer therapeutic, (ii) it is relatively cheap and commercially available, (iii) the presence of an amine group on its daunosamine sugar supports NHS chemistry if modifications are required, and

(iv) its affinity for nucleic acids might provide a simple method for packaging inside RNA encapsidated VLPs.

### 5.1.4 Aims

The aims of the work described in this chapter were to:

1. Stably package Dox inside VLP-$PEG_{24}$-A9L.
2. Assess the capacity of VLP-$PEG_{24}$-A9L to deliver Dox to LNCaP and PC-3 cells, and also the cytotoxic effects of Dox delivery.

## 5.2 Results and discussion

### 5.2.1 Preparation of Dox encapsidated VLP-PEG$_{24}$-A9L

In Chapters 3 and 4, cargo packaging was achieved by mixing TR-siRNA with dissociated $CP_2$ at near neutral pH, resulting in VLP assembly with the siRNA encapsidated inside. In addition to siRNAs, which can be synthesised as an extension of TR, other non-nucleic acid based cargos have also been packaged this way, including ricin A chain (Wu et al., 1995), cisplatin and PEGylated quantum dots (Ashley et al., 2011). These cargos contain amine groups, and were covalently conjugated to thiol-modified TR using amine-to-thiol crosslinkers, before mixing with $CP_2$ for VLP assembly and packaging. The presence of an amine on the daunosamine sugar of Dox makes it compatible with this packaging strategy. However, one concern was that the covalent attachment of TR to Dox might disrupt its capacity to intercalate with DNA and, consequently, reduce its cytotoxic effects in cancer cells.

An alternative method for packaging Dox is to soak it into assembled, RNA-encapsidated VLPs. MS2 VLPs contain pores, ~1.7 nm in diameter (Karin Valegård, 1990), which permit access for small molecules to the VLP interior (Wu et al., 2005). Once inside, the high affinity interaction between Dox and the encapsidated RNA should keep them stably retained (Subramanian et al., 2012). This soaking method has been used to package a variety of therapeutic and imaging agents, which have an affinity to nucleic acids, inside CPMV VLPs (Yildiz et al., 2013).

A construction scheme of Dox encapsidated VLP-$PEG_{24}$-A9L is shown in Figure 5.4. TR-Cy5 is firstly mixed with dissociated $CP_2$ at neutral pH to trigger *in vitro* assembly, resulting in VLP(TR-Cy5). VLP(TR-Cy5) is then mixed with Dox, which should permeate through the pores into the VLP interior, where it will be retained due to its high affinity interaction with encapsidated RNA. VLP(TR-Cy5/Dox) is then surface decorated with $SM(PEG)_{24}$ and A9L, as described previously, prior to cellular delivery experiments.

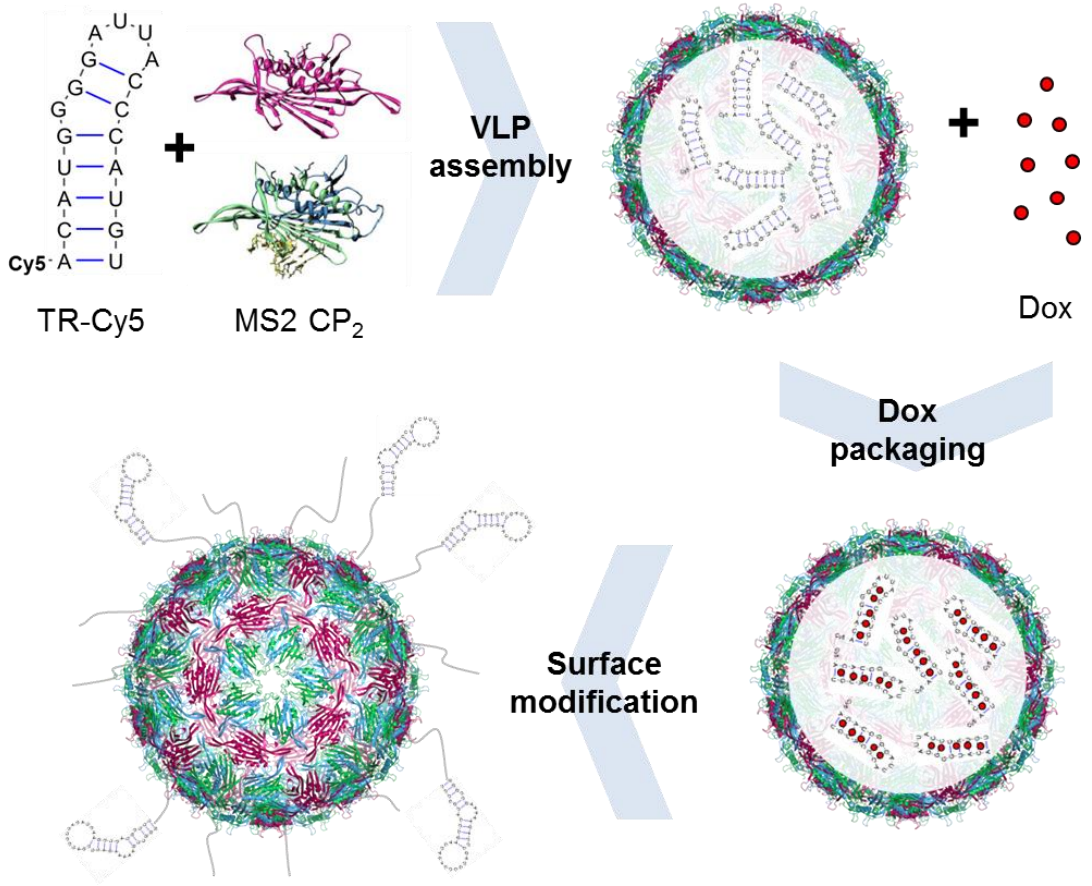


**Figure 5.4. Strategy for synthesising Dox encapsidated VLP-$PEG_{24}$-A9L.** TR-Cy5 is mixed with MS2 $CP_2$ at neutral pH to trigger VLP assembly, as described previously. VLP(TR-Cy5) is incubated with Dox, which can enter the VLP interior via pores on the VLP surface, and should become stably encapsidated. VLP(TR-Cy5/Dox) can then be surface decorated with $SM(PEG)_{24}$ and A9L. The figure is not drawn to scale.

Free Dox was firstly analysed by UV-visible spectroscopy (Figure 5.5A). The wavelength of maximum absorption was determined to be 486 nm. Next, a calibration graph was constructed by measuring the $A_{486nm}$ of different concentrations of Dox. From this, a molar extinction coefficient of 9080 $M^{-1}.cm^{-1}$ was obtained (Figure 5.5B), which is similar to values quoted in previous literature (Samra et al., 2013), and was used in subsequent experiments for the quantification of Dox.

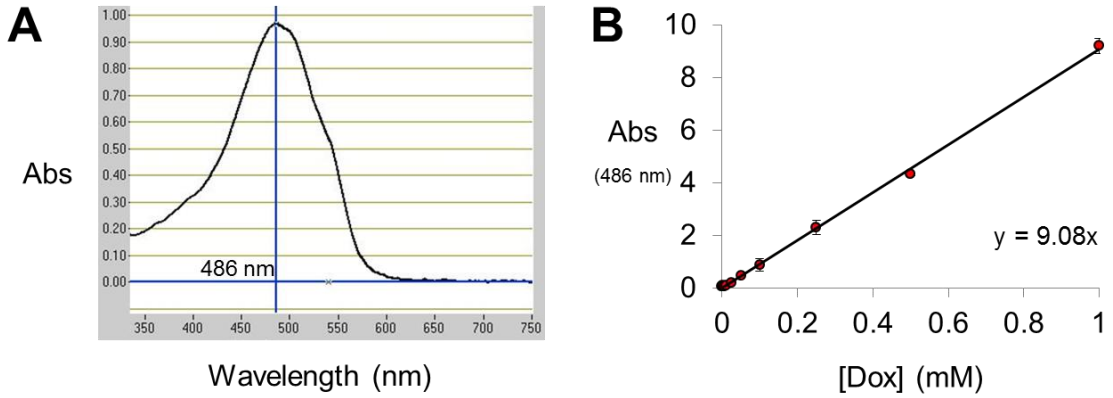


**Figure 5.5. Spectroscopic analysis of free Dox. (A)** UV-visible absorption profile of Dox. **(B)** Calibration graph showing the absorbance (at $\lambda_{max}$) of varying concentrations of Dox. The equation for the line of best fit is shown. The gradient of the slope was used as the molar extinction coefficient of Dox (9080 $M^{-1}.cm^{-1}$).

Trial Dox packaging experiments were set up to identify optimal conditions. A fixed concentration of VLP(TR-Cy5) was mixed with various concentrations of Dox in 10 µL pH 8.3 HEPES at room temperature for 1 h. The starting Dox:VLP molar ratio ranged from 54:1 to 3456:1. In addition, two controls were set up, containing either Dox only or VLP(TR-Cy5) only. The mixtures were centrifuged in 100 kDa MWCO spin concentrators three times to remove free Dox. The retentates were analysed by UV-visible spectroscopy: the $A_{649nm}$ was used to

estimate the concentration of VLP(TR-Cy5) present, and the $A_{486nm}$ was used to estimate the concentration of Dox present. Any Dox present in the retentate was assumed to be packaged within VLP(TR-Cy5).

The Dox packaging efficiencies are shown in Figure 5.6. The average number of Dox packaged per VLP increased with the starting Dox:VLP molar ratio, saturating at 111.0±10.5 with a starting molar ratio of 1728:1. Further increasing the starting Dox:VLP molar ratio to 3456:1 produced a negligible change in the number of Dox packaged (113.7±18.7). No absorbance at 486 nm was detected for the Dox only and VLP(TR-Cy5) only controls, indicating that free Dox was fully removed by the 100 kDa MWCO filter, and that VLP(TR-Cy5) does not contribute to $A_{486nm}$. From these results, a starting Dox:VLP molar ratio of 1728:1 appeared to be optimal for maximum Dox loading.

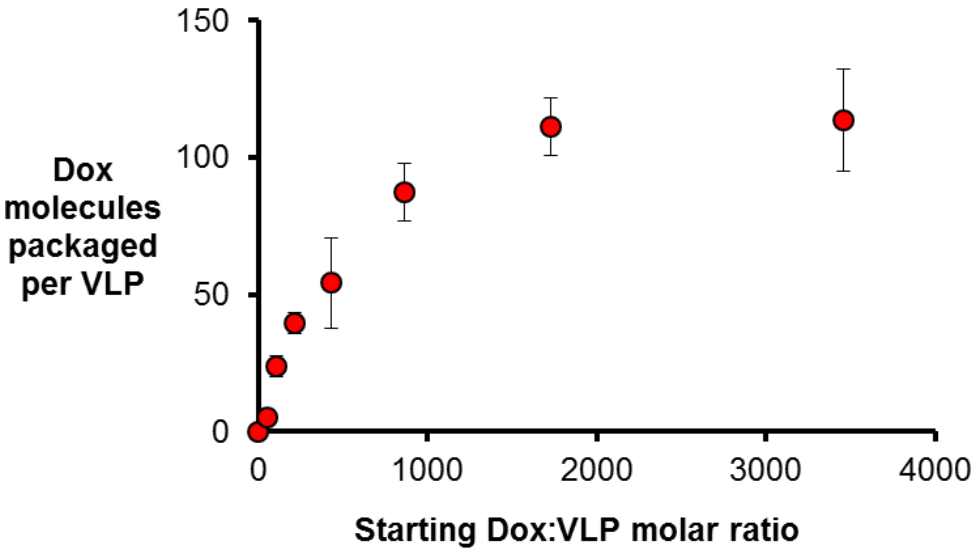


**Figure 5.6. Dox packaging inside VLP(TR-Cy5).** Scatter plot displaying the average number of Dox molecules packaged per VLP with different starting Dox:VLP molar ratios.

The Dox packaging experiment was scaled up, in which Dox was mixed with VLP(TR-Cy5) at a molar ratio of 1728:1 in 100 µL pH 8.3 HEPES. The resulting VLP(TR-Cy5/Dox) was eluted through a NAP-5 column, and concentrated into pH 8.3 HEPES using a 100 kDa MWCO spin concentrator. VLP(TR-Cy5/Dox) was then surface decorated with $SM(PEG)_{24}$ to make VLP(TR-Cy5/Dox)-$PEG_{24}$, or $SM(PEG)_{24}$ and A9L to make VLP(TR-Cy5/Dox)-$PEG_{24}$-A9L (as described in Chapter 4). The resulting particles were analysed (Figure 5.7). Native 2% (w/v) agarose gel electrophoresis showed the expected shifts in electrophoretic mobility when VLP(TR-Cy5/Dox) was decorated with $SM(PEG)_{24}$, or $SM(PEG)_{24}$ and A9L (Figure 5.7A), as observed previously (Figure 4.6). TEM analysis confirmed the intact nature of the particles (Figure 5.7B). They were also analysed by UV-visible spectroscopy to determine the $A_{486nm}$ and $A_{649nm}$, using which Dox:VLP molar ratios of 110.0±4.6 (for VLP(TR-Cy5/Dox)-$PEG_{24}$) and 105.3±6.2 (VLP(TR-Cy5/Dox)-$PEG_{24}$-A9L) were estimated. This indicates that there was negligible loss, or 'leakage' of Dox, during VLP surface modification.

Finally, a month-old stock of VLP(TR-Cy5/Dox)-$PEG_{24}$-A9L – stored in DPBS at $4^oC$ – was concentrated three times through a 100 kDa MWCO spin concentrator. The $A_{486nm}$ and $A_{649nm}$ of the retentate were measured, using which a Dox:VLP molar ratio of 96.8 was estimated. This signifies >90% retention of Dox, and indicates that Dox can remain stably encapsidated inside VLP(TR-Cy5/Dox)-$PEG_{24}$-A9L for at least one month when stored at $4^oC$.

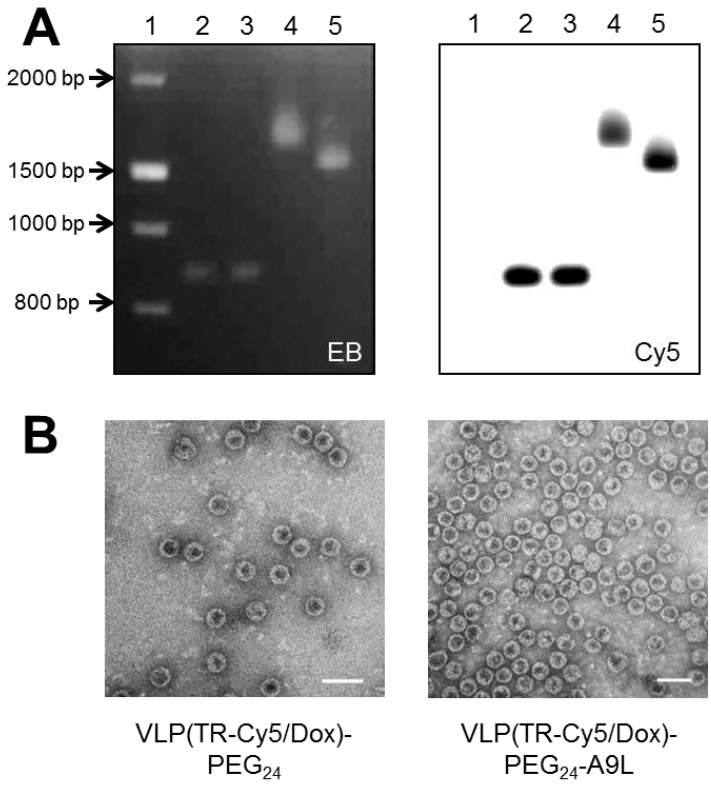


**Figure 5.7. Analysis of VLP(TR-Cy5/Dox)-$PEG_{24}$-A9L.** VLP(TR-Cy5/Dox) was prepared as described above. Following elution through a NAP-5 column and concentration using a 100 kDa MWCO spin concentrator, the surface of VLP(TR-Cy5/Dox) was decorated with $SM(PEG)_{24}$ to make VLP(TR-Cy5/Dox)-$PEG_{24}$, or $SM(PEG)_{24}$ and A9L to make VLP(TR-Cy5/Dox)-$PEG_{24}$-A9L. The resulting particles were analysed. **(A)** Native 2% (w/v) agarose gel electrophoresis. 1: HyperLadder I; 2: VLP(TR-Cy5); 3: VLP(TR-Cy5/Dox); 4: VLP(TR-Cy5/Dox)-$PEG_{24}$; 5: VLP(TR-Cy5/Dox)-$PEG_{24}$-A9L. The gel was visualised by ethidium bromide scanning or Cy5 fluorescence scanning. **(B)** TEM analysis of VLP(TR-Cy5/Dox)-$PEG_{24}$ and VLP(TR-Cy5/Dox)-$PEG_{24}$-A9L. Scale bar = 50 nm.

### 5.2.2 Cellular effects of Dox delivery

The emission spectra of all fluorescent dyes previously used in the cell assays, including Cy5 (TR-Cy5), FITC (annexin V-FITC) and PI, are shown in Figure 5.8. These show that the dyes have minimal spectral overlap, and thus are compatible with one another. However, Dox has an emission spectrum which

ranges from 565 nm to 630 nm, peaking at ~580 nm (Dai et al., 2008) – this significantly overlaps with the emission spectrum of PI, therefore an alternative viability dye was required. One potential candidate, DAPI, utilises the same mechanism as PI – whilst impermeable to the membranes of healthy cells, it is readily taken up by cells undergoing late apoptosis or necrosis due to compromised membrane integrity (Hornicek et al., 1986). Importantly, the emission spectrum of DAPI lies closer to the UV region (Figure 5.8), and exhibits little overlap with that of Dox, therefore DAPI should be a suitable substitution for PI.

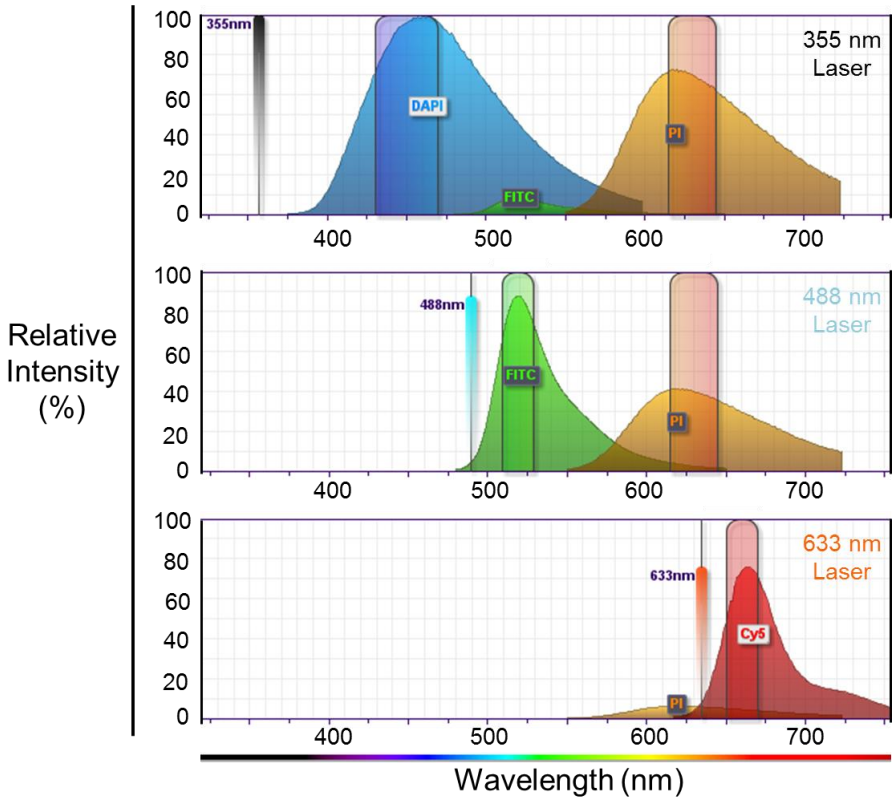


**Figure 5.8. Emission spectra of fluorescent dyes used.** Displayed are the emission spectra of DAPI, FITC, PI and Cy5 when excited with 355 nm, 488 nm or 633 nm lasers. Highlighted in boxes are the range of filters used to detect specific fluorescent signals, which include 450/40 for DAPI, 525/10 for FITC, 630 for PI and 660/20 for Cy5. The spectra were made using the BD Fluorescence Spectrum Viewer.

Free Dox can enter cells via passive diffusion (Skovsgaard and Nissen, 1982), and induce cytotoxicity via the multiple mechanisms previously discussed. Initial experiments were set up to assess these cytotoxic effects, and also to test the use of DAPI as a viability dye. LNCaP cells were incubated with 0 nM, 200 nM or 2000 nM Dox for 24 h on 24 well plates, and were either stained with annexin V-FITC and DAPI or left unstained, before they were analysed by flow cytometry for cytotoxicity (Figure 5.9).

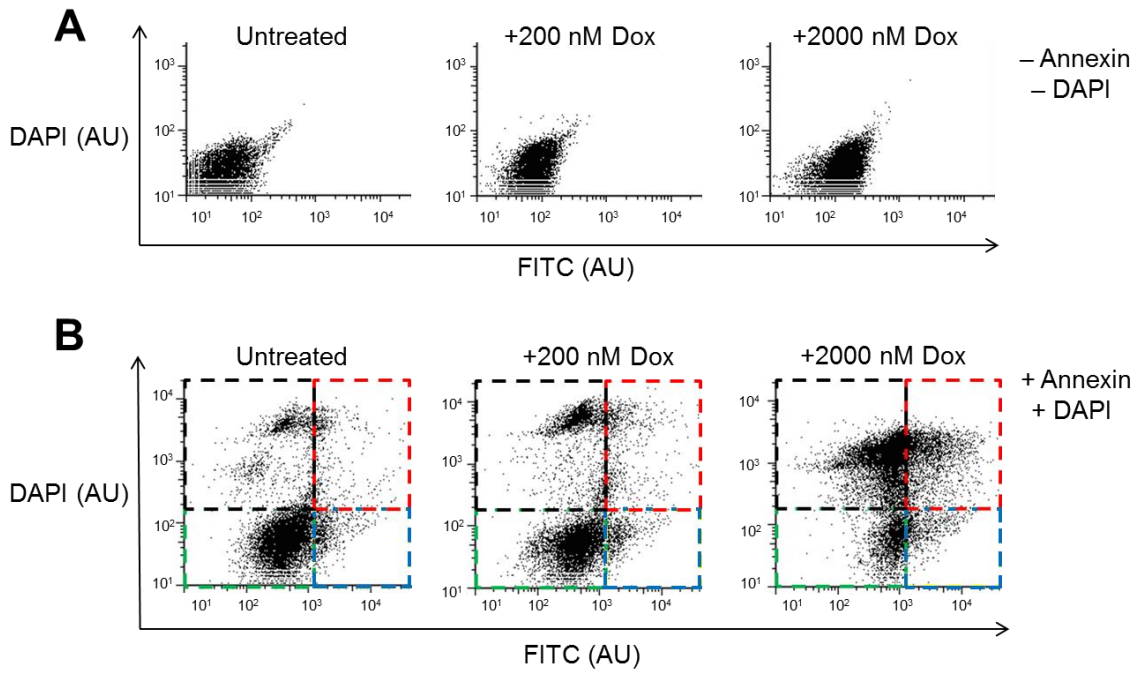


**Figure 5.9. Control cytotoxicity assay using Dox treated LNCaP cells.** LNCaP cells were incubated with different concentrations of free Dox for 24 h, and were either **(A)** unstained or **(B)** stained with annexin V-FITC and DAPI, prior to flow cytometry analysis. The histograms were divided into quadrants, based on the DAPI and FITC fluorescence emission of cells, to distinguish between cells that were live (green), early apoptotic (blue), late apoptotic (red) and necrotic (black).

For the unstained cells, increasing Dox concentrations did not affect the DAPI fluorescence, however, a small increase in FITC fluorescence was observed (Figure 5.9A), consistent with minor spectral overlap between Dox and FITC. For the stained cells, increasing Dox concentrations resulted in a significant increase in both the cell binding of annexin V-FITC and uptake of DAPI, suggesting that free Dox induced cytotoxicity in LNCaP cells in a concentration-dependent manner (Figure 5.9B). As before, the flow cytometry histograms were divided into quadrants, and cells were designated as live (green), early apoptotic (blue), late apoptotic (red) or necrotic (black) based on their FITC and DAPI fluorescence emission. These results indicate that DAPI is a suitable dye for identifying cells that are late apoptotic or necrotic, and that LNCaP cells are responsive to Dox.

LNCaP and PC-3 cells were incubated with various concentrations (0 nM to 10000 nM) of free Dox for 24 h, and assayed for cytotoxicity (Figures 5.10, 5.11). For LNCaP cells, a background level of toxicity was observed, with 80±7% of untreated cells remaining live (Figure 5.10B). Increasing Dox concentrations correlated positively with cytotoxicity, as the percentage cell viability decreased to as low as 7±3% and 8±3%, at 5000 nM and 10000 nM Dox, respectively (Figure 5.10B). To estimate the $LC_{50}$, the percentage viability of Dox treated cells were normalised to the live population of untreated cells, assuming that to represent 100% viability (Figure 5.10C, primary axis). From this, the $LC_{50}$ of free Dox in LNCaP cells was estimated to be ~780 nM. Furthermore, the Dox fluorescence emission of LNCaP cells also increased in a Dox concentration-dependent manner (Figure 5.10C, secondary axis), which is indicative of increased cellular uptake of Dox.

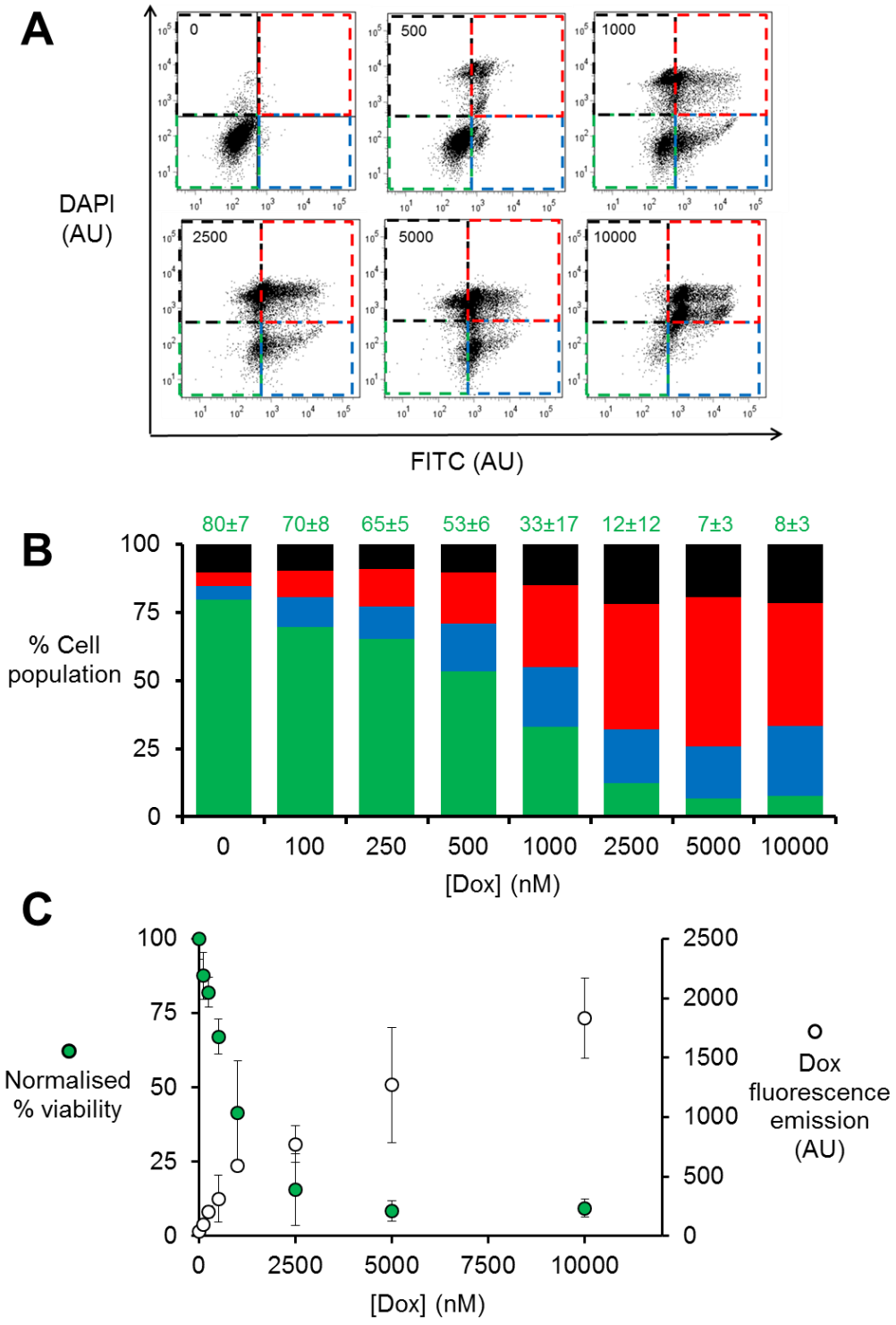


**Figure 5.10. Cytotoxicity in Dox-treated LNCaP cells.** LNCaP cells were incubated with different concentrations of free Dox for 24 h, and assayed for cytotoxicity. **(A)** Representative flow cytometry histograms at selected Dox concentrations. Quadrants were drawn to distinguish between cell populations, as described. **(B)** Stacked bar chart showing the percentage of cells that were live (green), early apoptotic (blue), late apoptotic (red) or necrotic (black) after treatment. Numbers in green indicate mean percentage cell viability ± SD. **(C)** Scatter plot

showing the normalised percentage viability of Dox treated cells with respect to Dox concentration (primary axis, green). These were calculated on the basis that the live population of untreated cells represent 100% cell viability. The Dox fluorescence emission of cells is also shown (secondary axis, white). Data in **(B)** and **(C)** represent the averaged result of three repeats.

In contrast, the Dox gradient did not produce a significant cytotoxic response in PC-3 cells (Figure 5.11B). The percentage cell viability remained relatively unchanged from the 0 nM control (80±1%) up to 2500 nM (78±6%), although low levels of toxicity was observed at the highest Dox concentrations used. Several mechanisms by which cancer cells develop anthracycline resistance have been reported, including (i) drug efflux through the overexpression of transporters such as P-glycoprotein (Chien and Moasser, 2008), (ii) loss of function of the DNA mismatch repair pathway (Fedier et al., 2001), (iii) alterations in the intracellular distribution of the drug (Coley et al., 1993), and (iv) downregulation or mutation of topoisomerase II (Deffie et al., 1992). The exact mechanism of Dox resistance in the PC-3 cells is unknown, although it appears to be unrelated to drug efflux, as the Dox fluorescence emission increased with higher Dox concentrations, indicating intracellular accumulation (Figure 5.11C). It was concluded that PC-3 was unsuitable for use as the negative control cell line, and another cell line, which is sensitive to Dox and does not express PSMA, was needed to confirm the effects of specific targeting by VLP(TR-Cy5/Dox)-$PEG_{24}$-A9L.

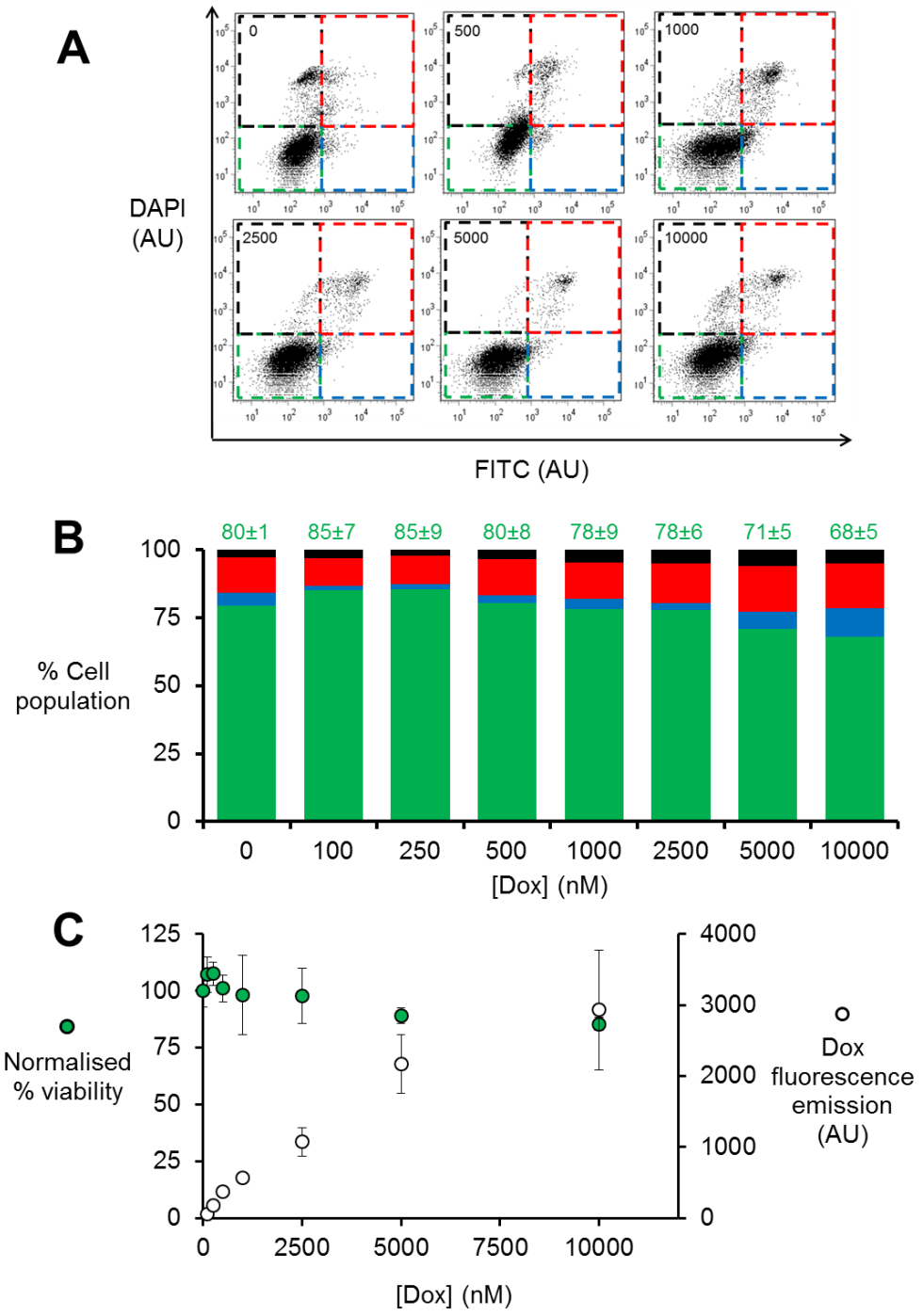


**Figure 5.11. Cytotoxicity in Dox-treated PC-3 cells.** PC-3 cells were incubated with different concentrations of free Dox for 24 h, and assayed for cytotoxicity. **(A)** Representative flow cytometry histograms at selected Dox concentrations. **(B)** Stacked bar chart showing the percentage of cells that were live (green), early apoptotic (blue), late apoptotic (red) or necrotic (black) after treatment. Numbers in green indicate mean percentage cell viability ± SD. **(C)** Scatter plot showing the normalised percentage viability of Dox treated cells with respect to Dox

concentration (primary axis, green). The Dox fluorescence emission of cells is also shown (secondary axis, white). Data in **(B)** and **(C)** represent the averaged result of three repeats.

HeLa cells do not express PSMA and might be suitable as the $PSMA_{-ve}$ control. To test this, HeLa cells were incubated with up to 10000 nM Dox for 24 h, before they were analysed for cytotoxicity (Figure 5.12). Higher levels of toxicity (Figure 5.12B) and Dox fluorescence emission (Figure 5.12C, secondary axis) were observed with increasing Dox concentrations. Again, the percentage viability was normalised to the live population of untreated HeLa cells (Figure 5.12C, primary axis), from which an $LC_{50}$ of ~2900 nM was obtained. This is ~4-fold higher than the $LC_{50}$ of Dox in LNCaP cells, and might reflect some level of Dox resistance in HeLa cells.

Another possible reason for the discrepancy in the $LC_{50}$ of Dox in LNCaP and HeLa cells is their different rates of division, as LNCaP cells have a doubling time of ~60 h compared to the ~24 h of HeLa cells. The faster rate of division of HeLa cells might result in an increased dilution of intracellular Dox, thereby increasing the concentration of Dox required to produce the same level of toxicity as in LNCaP cells. However, this seems unlikely as the Dox fluorescence emission was considerably higher in HeLa cells (Figure 5.12C) than in LNCaP cells (Figure 5.10C) at most Dox concentrations, which is the opposite as would be expected if there was an increased dilution effect in HeLa cells. Overall, HeLa cells were responsive to the cytotoxic effects of Dox, and were thus deemed suitable as the $PSMA_{-ve}$ control for testing Dox delivery by VLP(TR-Cy5/Dox)-$PEG_{24}$-A9L.

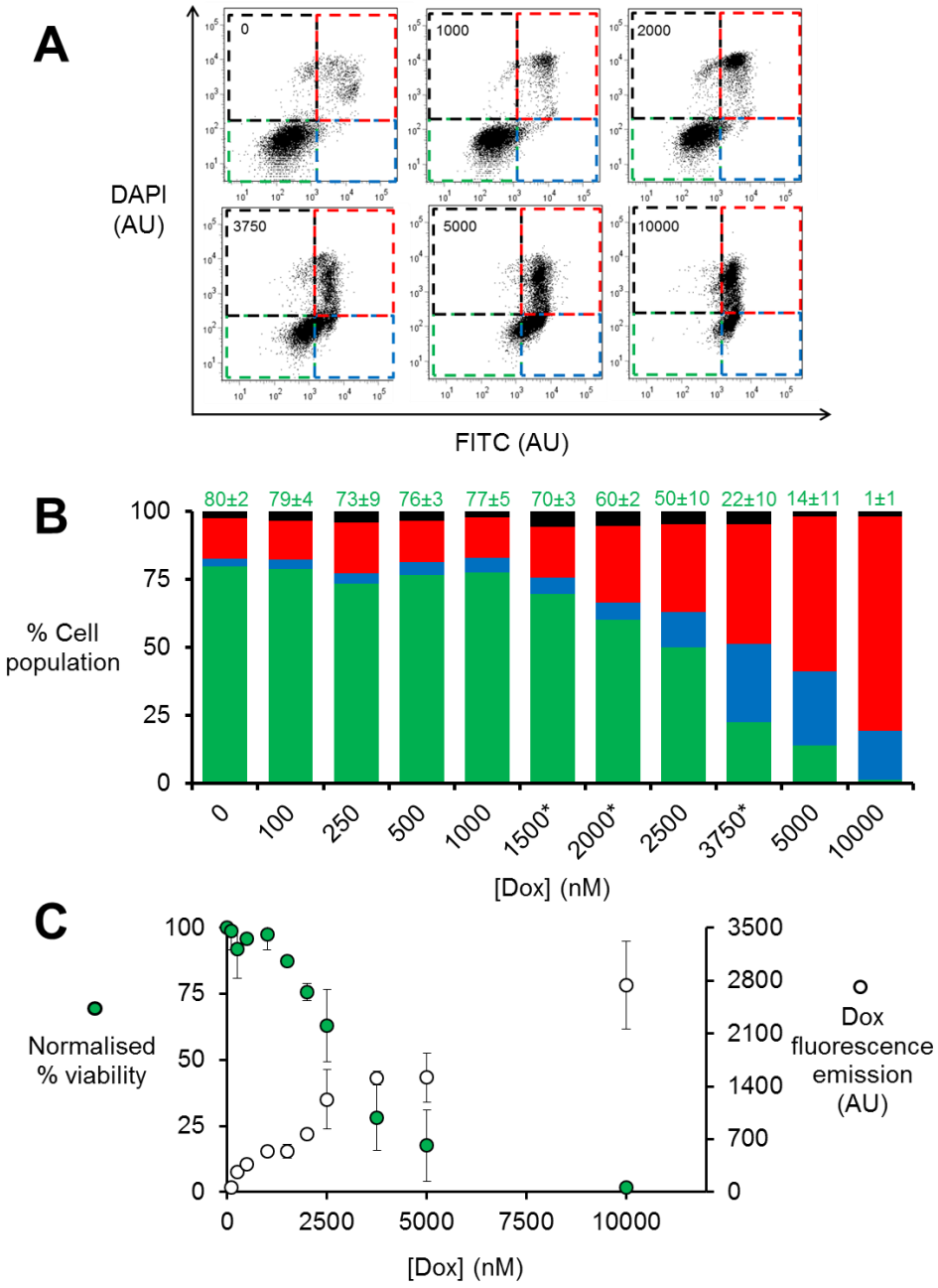


**Figure 5.12. Cytotoxicity in Dox-treated HeLa cells.** HeLa cells were incubated with different concentrations of free Dox for 24 h, and assayed for cytotoxicity. **(A)** Representative flow cytometry histograms at selected Dox concentrations. **(B)** Stacked bar chart showing the percentage of cells that were live (green), early apoptotic (blue), late apoptotic (red) or necrotic (black) after treatment. Additional Dox concentrations tested are indicated by an asterisk. Numbers in green indicate mean percentage cell viability ± SD. **(C)** Scatter plot showing the normalised percentage viability of Dox treated cells with respect to Dox concentration (primary

axis, green). The Dox fluorescence emission of cells is also shown (secondary axis, white). Data in **(B)** and **(C)** represent the averaged result of three repeats.

Next, the cytotoxic effect of Dox delivery by VLP(TR-Cy5/Dox)-$PEG_{24}$-A9L was investigated. LNCaP and HeLa cells were incubated with a concentration of Dox equal to their respective $LC_{50}$'s (780 nM for LNCaP, 2900 nM for HeLa), either as free drug or after packaging into various VLP formulations for 24 h, before they were analysed for cytotoxicity (Figures 5.13, 5.14). For LNCaP cells, incubation with 780 nM free Dox resulted in a normalised percentage viability of 60±13% (Figure 5.13B), which is close to the expected 50%. Dox delivery by VLP(TR-Cy5/Dox)-$PEG_{24}$ and VLP(TR-Cy5/Dox)-$PEG_{24}$-A9L resulted in percentage viabilities of 90±13% and 57±6%, respectively, whilst further addition of 100 nM free A9L increased the percentage viability back to 89±4%. Dox delivery by VLP(TR-Cy5/Dox)-$PEG_{24}$-A9L resulted in a moderate increase in Dox fluorescence emission (451±83 AU) compared to free Dox (384±72 AU), indicating higher Dox uptake by LNCaP cells (Figure 5.13C). Furthermore, there is a strong correlation between the percentage viability (Figure 5.13B) and Dox fluorescence emission (Figure 5.13C), suggesting that greater Dox uptake leads to higher levels of cytotoxicity.

For HeLa cells, incubation with 2900 nM free Dox resulted in a normalised percentage cell viability of 48±12% (Figure 5.14B), which is expected of the $LC_{50}$. In contrast, incubation with 2900 nM Dox packaged inside VLP(TR-Cy5/Dox)-$PEG_{24}$-A9L did not produce a significant change in percentage viability (87±9%) relative to untreated cells. Again, the level of cytotoxicity correlated positively with the Dox fluorescence emission (Figure 5.14C).

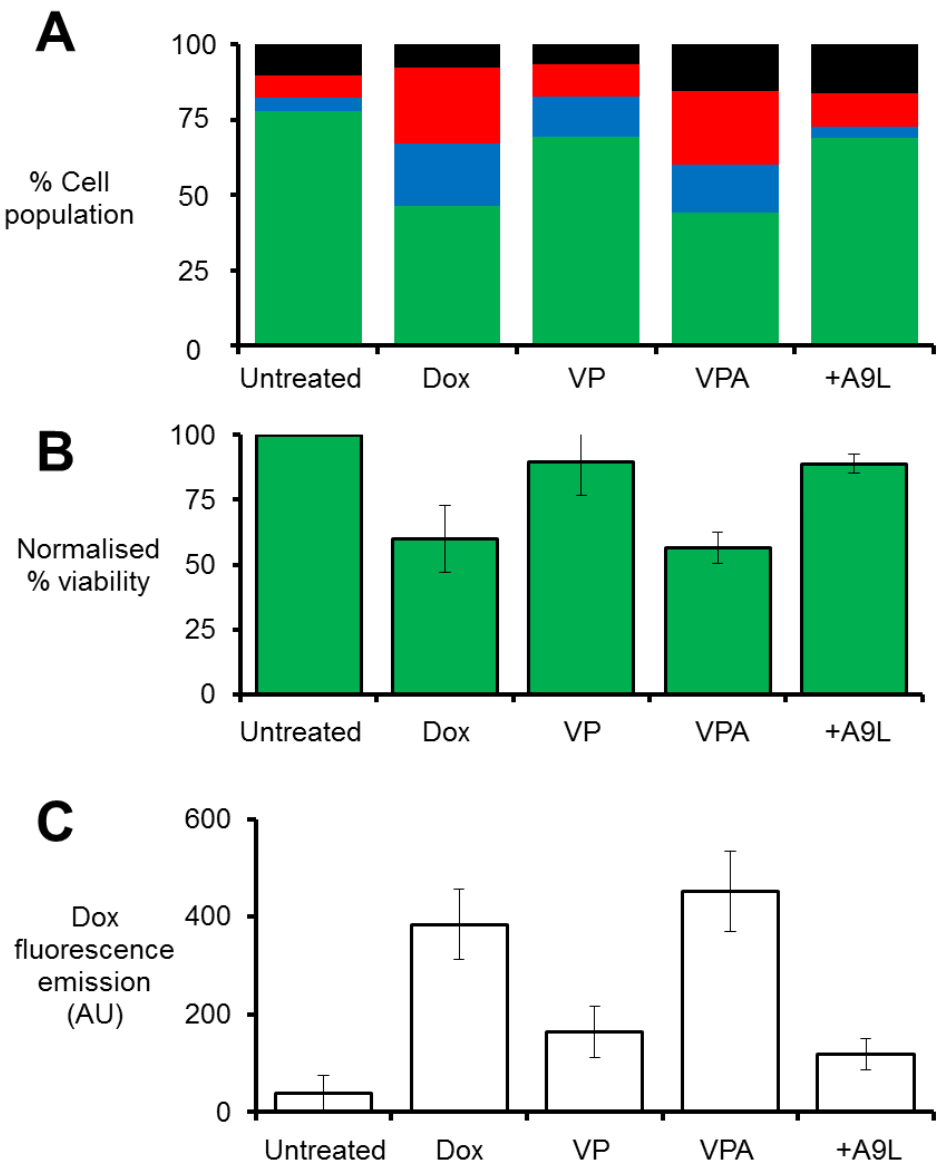


**Figure 5.13. Comparative cytotoxic effects of Dox delivery in LNCaP cells.** LNCaP cells were (from left) either untreated, or incubated with 780 nM Dox, or 780 nM Dox packaged inside VLP-PEG$_{24}$ (VP), VLP-PEG$_{24}$-A9L (VPA) or VLP-PEG$_{24}$-A9L in the presence of 100 nM free A9L (+A9L) for 24 h, and assayed for cytotoxicity. All data shown represent the averaged result from three repeats. **(A)** Stacked bar chart showing the percentage of cells that were live (green), early apoptotic (blue), late apoptotic (red) or necrotic (black) after treatment. **(B)** Bar chart showing the normalised percentage viability of cells after various treatments. These were calculated on the basis that the live population of untreated cells represent 100% cell viability. **(C)** Bar chart showing the Dox fluorescence emission of cells after various treatments.

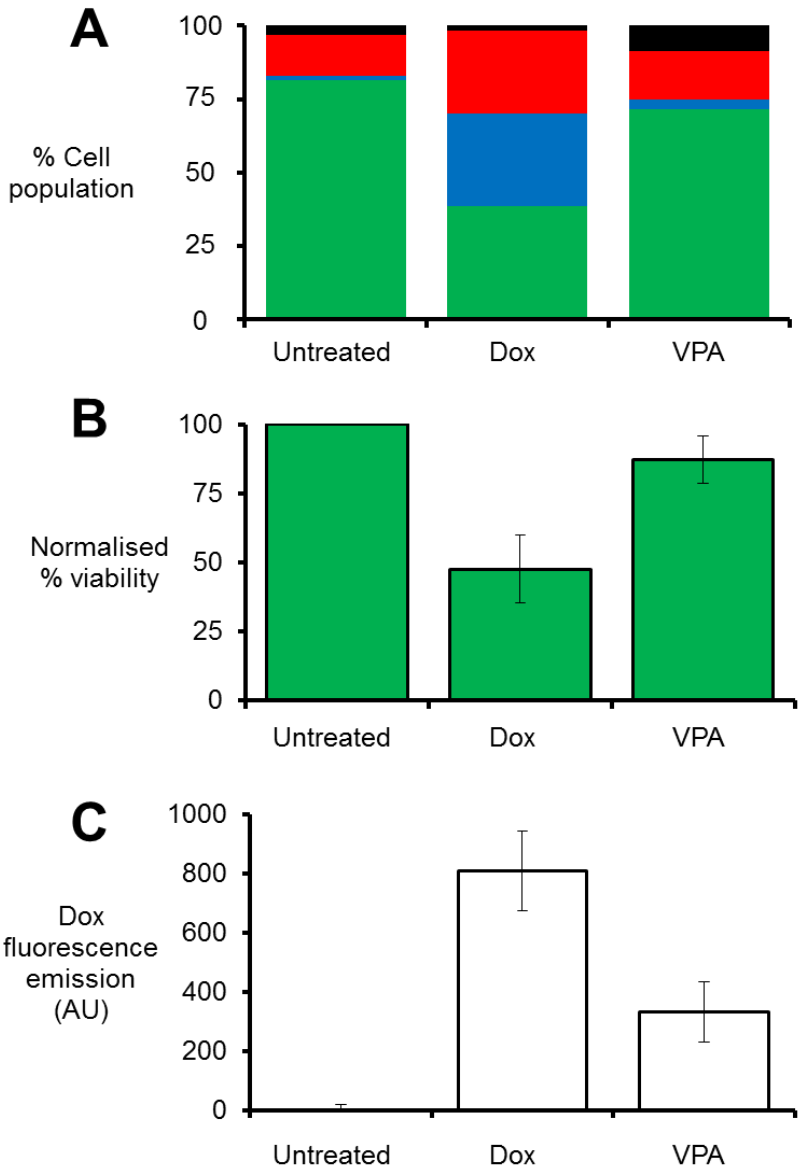


**Figure 5.14. Comparative cytotoxic effects of Dox delivery in HeLa cells.** HeLa cells were (from left) either untreated, or incubated with 2900 nM Dox, or 2900 nM Dox packaged inside VLP-$PEG_{24}$-A9L (VPA) for 24 h, and assayed for cytotoxicity. All data shown represent the averaged result from three repeats. **(A)** Stacked bar chart showing the percentage of cells that were live (green), early apoptotic (blue), late apoptotic (red) or necrotic (black) after treatment. **(B)** Bar chart showing the normalised percentage viability of cells after various treatments. These were calculated on the basis that the live population of untreated cells represent 100% cell viability. **(C)** Bar chart showing the Dox fluorescence emission of cells after various treatments.

Overall, these results indicate that delivery by VLP(TR-Cy5/Dox)-$PEG_{24}$-A9L did not significantly improve the degree of uptake or level of cytotoxicity of Dox compared to free Dox. Their comparable cytotoxicity in LNCaP cells indicates that intercalation of Dox into TR-Cy5 was no barrier to their release inside the cell. The uptake of VLP(TR-Cy5/Dox)-$PEG_{24}$-A9L was specific to LNCaP cells, and could be largely inhibited by the addition of free A9L, suggesting A9L-mediated targeting of PSMA on the surface of LNCaP cells. Importantly, only low levels of uptake of VLP(TR-Cy5/Dox)-$PEG_{24}$-A9L and cytotoxicity were observed in HeLa cells, compared to free Dox. The ability to promote uptake by targeted cells whilst reducing uptake by non-targeted cells can significantly improve the efficacy of anti-cancer drugs, as well as reduce their side effects *in vivo*.

Two further experiments were carried out to augment the data described above, but these were unsuccessful. The first involved the testing of two additional cell lines, $PSMA_{+ve}$ 22RV1 (Regino et al., 2009) and $PSMA_{-ve}$ PNT1A (Lang et al., 2002), for Dox delivery by VLP(TR-Cy5/Dox)-$PEG_{24}$-A9L. However, neither cell line responded to free Dox over a large concentration gradient up to 10000 nM (Figure 5.15A). As for PC-3 cells, internalisation of Dox was evident for both 22RV1 and PNT1A cells (Figure 5.15B), thus their mechanism of resistance to Dox could not be attributed to drug efflux. Due to their insensitivity to Dox, it was decided that 22RV1 and PNT1A were unsuitable for further assays.

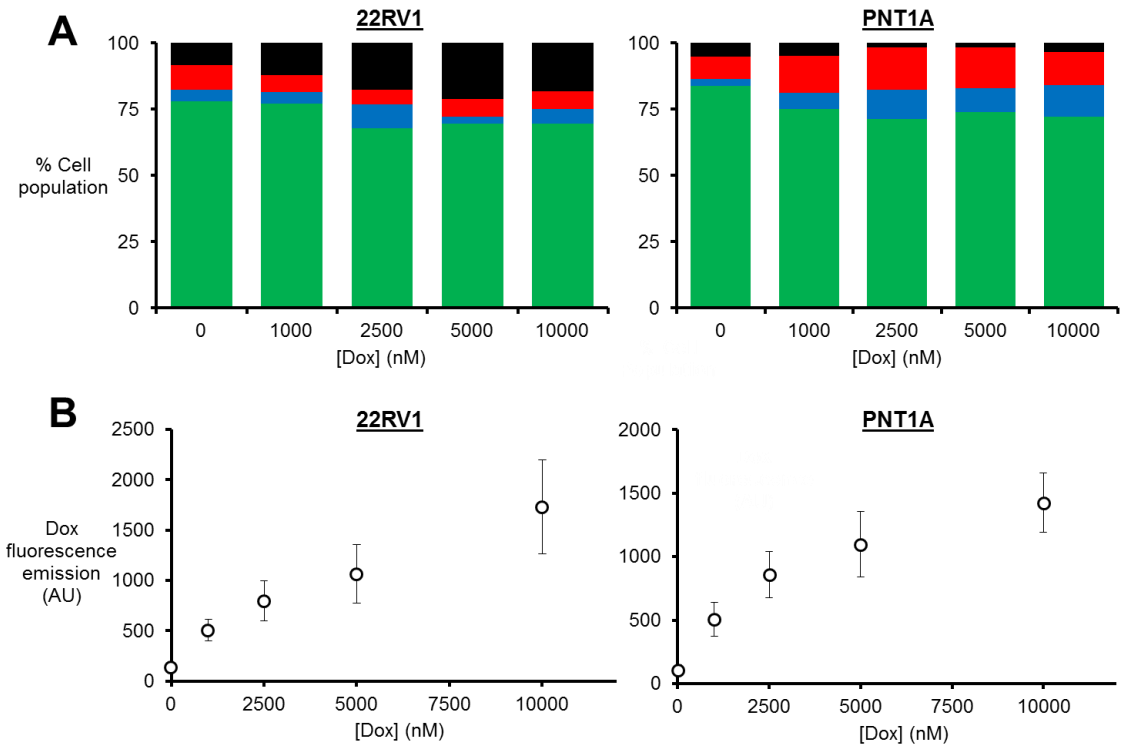


**Figure 5.15. Cytotoxicity in Dox-treated 22RV1 and PNT1A cells.** 22RV1 (left) and PNT1A (right) cells were incubated with different concentrations of free Dox for 24 h, and assayed for cytotoxicity. All data shown represent the averaged result from three repeats. **(A)** Stacked bar chart showing the percentage of cells that were live (green), early apoptotic (blue), late apoptotic (red) or necrotic (black) after treatment. **(B)** Scatter plot showing the Dox fluorescence emission of cells with respect to Dox concentration.

The second experiment was inspired by a recent paper (Ashley et al., 2011), describing the specific delivery of a diverse range of imaging and therapeutic cargoes by MS2 VLPs. One of the cargoes used was a chemotherapeutic cocktail of Dox, cisplatin, and 5-fluorouracil, which induced significant cytotoxicity in Dox-resistant Hep3B cells. If Dox resistance could be built up in LNCaP and HeLa cells, the hypothesis that delivery by VLP(TR-Cy5/Dox)-$PEG_{24}$-A9L can overcome resistance could be tested. The same protocol for building cellular resistance to Dox was used, which entailed incubating LNCaP

and HeLa cells with increasing concentrations (25 to 250 nM) of free Dox at 24 h intervals, interspersed with 48 h recovery periods, over a period of 3 weeks (Ashley et al., 2011). The resulting cells were incubated with different concentrations (0-10000 nM) of Dox for 24 h, before analysis by flow cytometry (Figures 5.16, 5.17). As before, the percentage viability was normalised to the live population of untreated cells (Figures 5.16B and 5.17B, primary axes), from which an $LC_{50}$ of ~680 nM was estimated for LNCaP cells, and ~2500 nM for HeLa cells. These are comparable to the previous values of ~780 nM (LNCaP) and ~2900 nM (HeLa), suggesting that the experiment failed to increase Dox resistance in these cells. Furthermore, the Dox fluorescence emission of LNCaP and HeLa cells after incubation were comparable to previous results (Figures 5.16B and 5.17B, secondary axes), suggesting that the level of Dox uptake also remained unchanged.

Modifications to the protocol were also made, including extending the Dox gradient from 25 to 250 nM to up to 25 nM to the $LC_{50}$ (780 nM for LNCaP, 2900 nM for HeLa). However, for both cell lines, the majority of cells (~95%) did not survive after incubation with higher Dox concentrations, whilst the remaining cell population ceased further growth and cell division during the subsequent recovery phase. This might reflect a cumulative dose-dependent or time-dependent effect of Dox, which was not observed in the previous 24 h cytotoxicity assays. It is unclear why Dox resistance could not be built up this way in LNCaP and HeLa cells, as previously shown for Hep3B cells (Ashley et al., 2011). Further modifications to the protocol might be needed, for example changes in the duration of Dox incubation and recovery periods, and adjustments to the Dox gradients used.

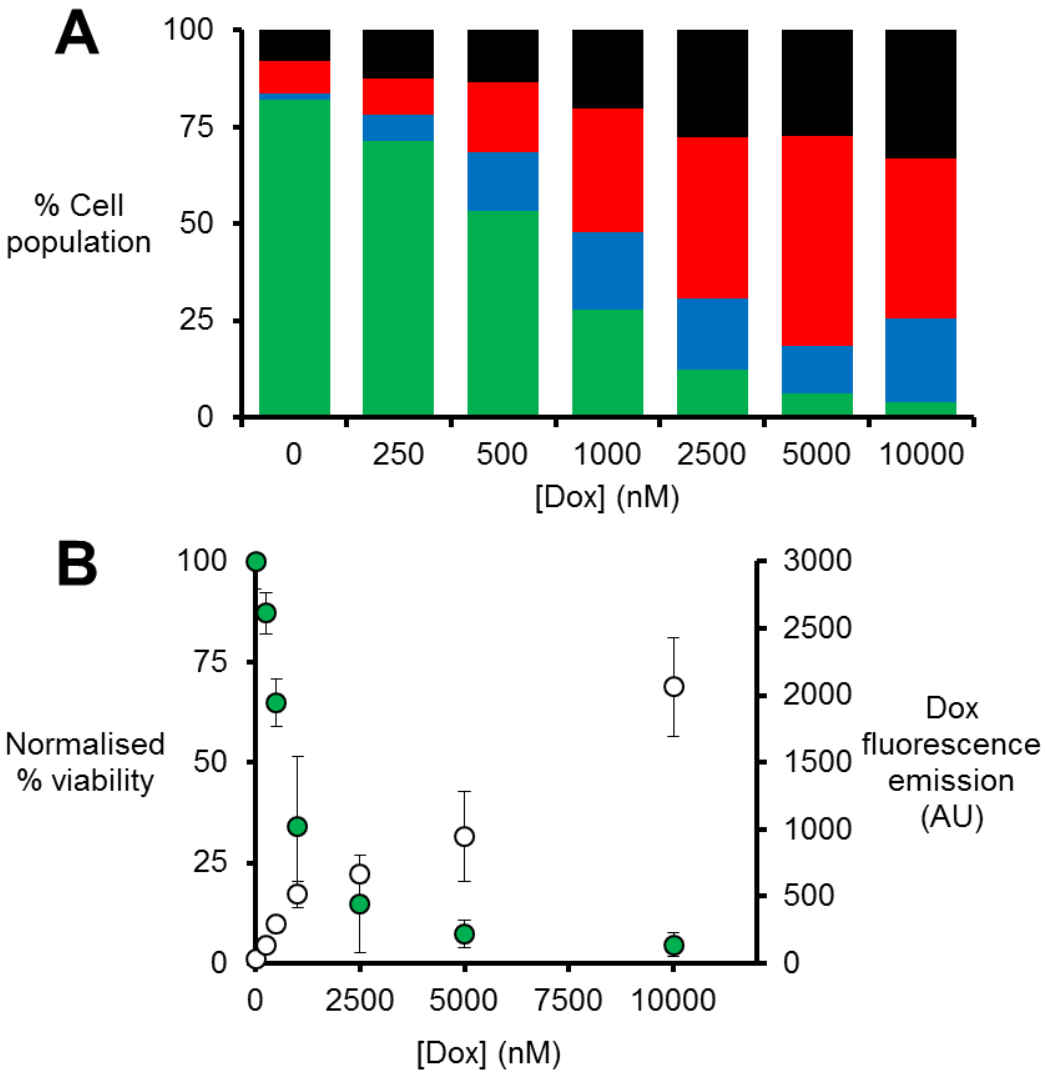


**Figure 5.16. Cytotoxicity of free Dox in 'Dox-resistant' LNCaP cells.** To build Dox resistance, LNCaP cells were incubated with an increasing concentration (25 to 250 nM) of Dox at 24 h intervals, interspersed by 48 h recovery periods, over 3 weeks (as previously described (Ashley et al., 2011)). The resulting cells were then incubated with up to 10000 nM Dox for 24 h, before they were analysed by flow cytometry. All data shown represent the averaged result from three repeats. **(A)** Stacked bar chart showing the percentage of cells that were live (green), early apoptotic (blue), late apoptotic (red) or necrotic (black) after treatment. The percentages shown represent the average of three repeats. **(B)** Scatter plot showing the normalised percentage viability of Dox treated cells with respect to Dox concentration (primary axis, green). The Dox fluorescence emission of cells is also shown (secondary axis, white).

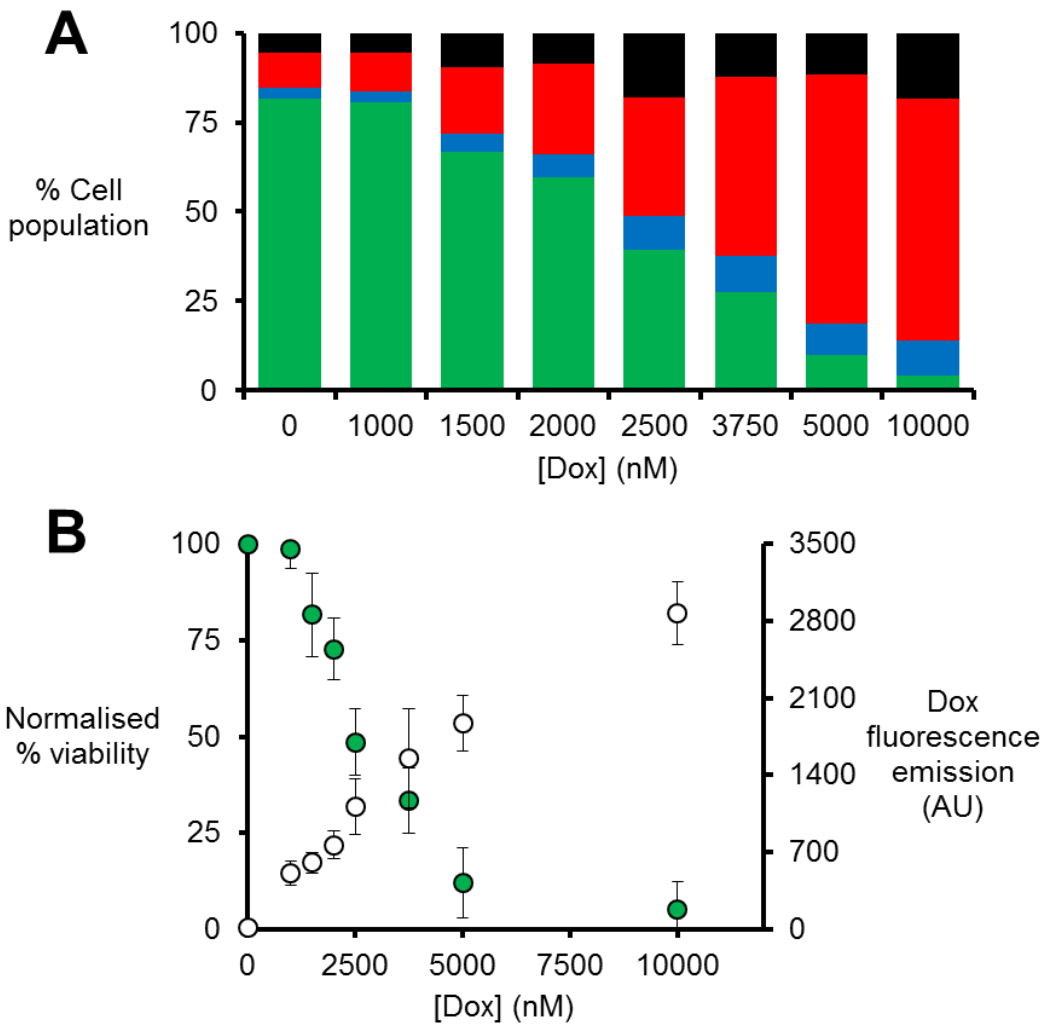


**Figure 5.17. Cytotoxicity of free Dox in 'Dox-resistant' HeLa cells.** To build Dox resistance, HeLa cells were incubated with an increasing concentration (25 to 250 nM) of Dox at 24 h intervals, interspersed by 48 h recovery periods, over 3 weeks (as previously described (Ashley et al., 2011)). The resulting cells were then incubated with up to 10000 nM Dox for 24 h, before they were analysed by flow cytometry. All data shown represent the averaged result from three repeats. **(A)** Stacked bar chart showing the percentage of cells that were live (green), early apoptotic (blue), late apoptotic (red) or necrotic (black) after treatment. The percentages shown represent the average of three repeats. **(B)** Scatter plot showing the normalised percentage viability of Dox treated cells with respect to Dox concentration (primary axis, green). The Dox fluorescence emission of cells is also shown (secondary axis, white).

## 5.3 Summary of Chapter 5

1. Dox was soaked into pre-assembled VLP(TR-Cy5) via pores present on the capsid surface, and became encapsidated inside via interactions with TR-Cy5. The resulting VLP(TR-Cy5/Dox) particles contained on average ~111 molecules of Dox each, and were surface decorated with $SM(PEG)_{24}$ and A9L (as described in Chapter 4), to produce VLP(TR-Cy5/Dox)-$PEG_{24}$-A9L. There appeared to be minimal Dox escape from VLPs during the surface modification and subsequent purification process.

2. Whilst toxicity was observed in LNCaP cells after incubation with free Dox, no effect was observed in PC-3 cells – even at extremely high Dox concentrations. This prompted the use of HeLa as the $PSMA_{-ve}$ control cell line.

   VLP(TR-Cy5/Dox)-$PEG_{24}$-A9L delivered Dox specifically to LNCaP cells via A9L targeting, and induced comparable cytotoxicity to free Dox at $LC_{50}$. Further addition of free A9L strongly inhibited the uptake and cytotoxic effects of VLP(TR-Cy5/Dox)-$PEG_{24}$-A9L. Negligible uptake and cytotoxicity were observed in HeLa cells.

3. Two additional prostate cancer cell lines, ($PSMA_{+ve}$) 22RV1 and ($PSMA_{-ve}$) PNT1A, were also tested. However, neither cell lines responded to high concentrations of free Dox, and thus could not be used. Furthermore, attempts at building Dox resistance in LNCaP and HeLa cells were made using protocols described in (Ashley et al., 2011), but were unsuccessful.

**This page is intentionally blank**

# Chapter 6

Conclusions and future perspectives

## 6.1 Conclusions

The general aim of this project was to further develop the MS2 VLP-based drug delivery system first pioneered in the Stockley laboratory in 1995 (Wu et al., 1995). Specific goals were to: (i) mitigate non-specific cellular uptake of VLPs, (ii) test a relatively novel class of targeting ligands, nucleic acid aptamers, to facilitate tumour-specific uptake, and (iii) incorporate various drug cargos inside VLPs for delivery.

**Chapter 3** addressed the issue of non-specific cellular uptake of VLPs that was previously observed (Wu et al., 1995, Brown et al., 2002, Wu et al., 2005, Galaway, 2011). Using established protocols (Galaway, 2011), TR-conjugated cargos were packaged inside VLPs during *in vitro* assembly, using a TR:$CP_2$ molar ratio of 10:1. On average ~10 molecules of TR-X were packaged inside each VLP. VLP-$PEG_{24}$ and VLP-$PEG_{24}$-Tf were then synthesised using the hetero-bifunctional crosslinker, $SM(PEG)_{24}$, which contains an NHS terminus that conjugates to VLP surface amines, and a maleimide terminus that conjugates to thiol-modified Tf. Significant PEGylation of the VLP surface was achieved (~97% of CPs), and each VLP-$PEG_{24}$-Tf particle displayed on average ~7 molecules of Tf. PEGylation (VLP-$PEG_{24}$) led to a ~4-fold decrease in the uptake of VLPs by HeLa cells at 2 h; further addition of Tf (VLP-$PEG_{24}$-Tf) increased uptake ~9-fold, likely due to Tf receptor-mediated endocytosis. Next, VLPs were used to deliver an established siRNA (Galaway, 2011, Dassie et al., 2009) targeted against mRNA of the anti-apoptotic factor, BCL2, to HeLa cells. TR-BCL2 delivery by VLP-$PEG_{24}$-Tf resulted in ~50% BCL2 protein knockdown and a ~45% decrease in cell viability. Negligible cellular effects were observed

when TR-BCL2 was delivered by VLP-$PEG_{24}$, or when a control siRNA was delivered by VLP-$PEG_{24}$-Tf, indicating the absence of off-target toxicity.

**Chapter 4** explored the use of RNA aptamers as the tumour-targeting ligand. The model aptamer was A9L, which specifically targets the prostate cancer marker, PSMA, and enables uptake by PSMA expressing cell lines (Rockey et al., 2011). Thiol-modified A9L aptamers were conjugated to VLPs via $SM(PEG)_{24}$, using the same chemistry as that used for Tf in Chapter 3. An average ligand density of ~16 per VLP was estimated using a shorter, fluorescently labelled RNA oligo, U6-FAM. After prolonged incubation in cell media, VLP-$PEG_{24}$-A9L particles remained intact and their displayed A9L remained stable. However, there was evidence of A9L degradation after VLP-$PEG_{24}$-A9L was incubated in human serum, signifying the importance of using more stable, chemically modified RNA (Wang et al., 2011), or DNA aptamers for future *in vivo* studies. PEGylation significantly reduced VLP binding by antibodies, likely by masking viral epitopes. However, the true immunogenicity of PEGylated VLPs can only be accurately assessed *in vivo*. To date, there are only a few reports on the *in vivo* testing of MS2 VLPs (Li et al., 2013, Pan et al., 2012a, Pan et al., 2012b), originating from the Wang laboratory. No significant immune response or off-target toxicity was observed in mice after systemic administration of non-PEGylated MS2 VLPs decorated with cell-penetrating Tat peptides, which is highly encouraging. VLP-$PEG_{24}$-A9L delivered TR-BCL2 specifically to $PSMA_{+ve}$ LNCaP cells via A9L targeting, triggering significant BCL2 knockdown and cytotoxicity at low nM siRNA concentrations. Negligible effects were observed in $PSMA_{-ve}$ PC-3 cells, suggesting the effects of A9L targeting were specific.

Finally, **Chapter 5** assessed the use of the anthracycline, Dox, as an alternative drug cargo for the MS2 VLP delivery system. Dox was soaked into pre-assembled VLP(TR-Cy5) via pores present on the capsid surface, and became stably encapsidated inside via interactions with TR-Cy5. The resulting VLP(TR-Cy5/Dox) particles contained on average ~111 molecules of Dox each, and were surface decorated with $SM(PEG)_{24}$ and A9L (as described in Chapter 4), to produce VLP(TR-Cy5/Dox)-$PEG_{24}$-A9L. Free Dox induced toxicity in LNCaP cells, but not in PC-3 cells – even at extremely high concentrations. The mechanism of resistance was not associated with drug efflux. This prompted the use of HeLa as the $PSMA_{-ve}$ control cell line. VLP(TR-Cy5/Dox)-$PEG_{24}$-A9L delivered Dox specifically to LNCaP cells via A9L targeting, and induced comparable cytotoxicity to free Dox at $LC_{50}$. Negligible uptake and cytotoxicity were observed in HeLa cells. Two additional prostate cancer cell lines, ($PSMA_{+ve}$) 22RV1 and ($PSMA_{-ve}$) PNT1A, were tested, but neither responded to free Dox, and thus could not be used. Furthermore, attempts at building Dox resistance in LNCaP and HeLa cells were made using protocols described in (33), but were unsuccessful.

## 6.2 Future perspectives

One advantage of MS2 VLPs over some other drug delivery systems, such as liposomes and cyclodextrin polymers, is the consistency of capsids with fixed physical properties. However, after surface decoration with ligands, some level of heterogeneity was present in the resulting particles, as evidenced by agarose gels and TEM images (Figure 3.10). This can be attributed to the nature of the

ligand and the conjugation chemistry used. Tf displays numerous surface amines (Galaway, 2011), which were derivitised with SATA or SMCC to install appropriate chemical groups for conjugation to VLPs or VLP-$PEG_{24}$. As a result, there was little control over the position and orientation of Tf displayed. One strategy to improve this is to target specific sites on Tf for modification, for example, at the terminal sialic acids, which are situated in a distal position from the Tf receptor-binding site (Banerjee et al., 2010). The resulting VLP-$PEG_{24}$-Tf should then display Tf in a defined orientation that is optimal for Tf receptor binding. It is notable that this did not affect VLP-$PEG_{24}$-A9L, because A9L was synthesised with a thiol modification at a single defined location (at the 3' end). Furthermore, there are now potentially better crosslinking chemistries available, such as the highly efficient copper-catalysed azide-alkyne cycloaddition click reaction (Kolb et al., 2001). They should be tested to compare the conjugation efficiency with currently used NHS-amine/maleimide-thiol chemistries. A more efficient crosslinking strategy can potentially reduce heterogeneity in ligand-modified VLPs, and also allow more control over the number of the ligands displayed.

Whilst the size and zeta potential of unmodified VLPs are established in literature (Pang et al., 2009, Strauss and Sinsheimer, 1963), those of modified VLPs have not been well defined. Subtle changes in these properties can significantly affect the pharmacokinetics and biodistribution of the drug delivery system, hence one focus for future work should be to characterise the physical properties of modified VLPs. Also needed is better characterisation of the mechanism of cell entry of VLPs. The receptor-mediated endocytosis of Tf- and A9L-targeted VLPs is presumed from previous studies of the targeting ligands

(Rockey et al., 2011, Daniels et al., 2006a). To confirm this, fluorescence colocalisation microscopy can be carried out, using Cy5-labelled cargo and a fluorescently-labelled endocytosis marker (such as Tf, early endosome antigen 1, Rab6 or lysosomal-associated membrane protein 1). Time-lapse fluorescence microscopy might also reveal any limiting steps in the endocytosis pathway, for example, one common limiting step is the endosomal escape of drugs (Varkouhi et al., 2011). If this is the case for MS2 VLPs, proton sponges can be incorporated to facilitate endosomal escape and improve drug efficacy (Behr, 1997, Ashley et al., 2011, Varkouhi et al., 2011). Another possible limiting step is the release of drugs from VLPs. Although VLPs should disassemble in the acidified environment of the endosome (Anobom et al., 2003), PEGylation of the surface might make VLPs more stable, thus reducing drug release and efficacy. For this reason, a less stable MS2 capsid mutant (Caldeira and Peabody, 2011) might be better suited for PEGylation and drug delivery, and could be tested.

MS2 VLPs have proven to be a highly modular, flexible drug delivery system, capable of displaying numerous ligands on its surface, as well as packaging a diverse range of cargos for delivery (Galaway and Stockley, 2013, Li et al., 2013, Pan et al., 2012a, Pan et al., 2012b, Ashley et al., 2011, Wu et al., 2005, Brown et al., 2002, Wu et al., 1995, Stephanopoulos et al., 2010). Many more ligands and drugs remain to be tested. Effective high-throughput screening systems (Galaway, 2011) will be needed to identify the best combinations of cargos and ligands, which can subsequently be tested *in vivo* for efficacy and safety. It is important to note that whilst adding extra components to a drug delivery system might impart additional functionalities, it also means extra

synthetic steps and concomitant cost of production, as well as more convoluted behavior *in vivo* (Cheng et al., 2012). It will therefore be important to critically assess and weigh the cost and clinical benefits of adding them.

MS2 VLPs can incorporate multiple drug cargos to deliver them simultaneously to cancer cells. So far, various anti-cyclin siRNAs, and a chemotherapeutic cocktail containing Dox, cisplatin and 5-fluorouracil, have been delivered *in vitro*, achieving cytotoxicity at sub pM drug concentrations (Ashley et al., 2011). Various other combinations of drugs can be tested. Some of these, despite showing good synergy, are limited *in vivo* by having inherently different pharmacokinetics and biodistribution, and thus could benefit from simultaneous delivery (Kummar et al., 2010, Peters et al., 2000). Hence, it is likely that drug delivery systems such as MS2 VLPs will play an important future role in deterring the development of cancer drug resistance.

Finally, in this project, the effects of MS2 VLP-mediated drug delivery were investigated *in vitro* using monolayer cell lines, which are often considered to be an oversimplified representation of cancer (Maitland et al., 2010). Therefore, one focus for future work should be to investigate its efficacy in more sophisticated cancer models, such as 2D bilayers (Swift et al., 2013) and 3D multicellular spheroids (Kurioka, 2011, Hirschhaeuser et al., 2010), which can better recapitulate various aspects of cancer *in vivo*, such as tissue structure as well as complex cell-cell and cell-matrix interactions found in 3D microenvironments. Once the ideal model disease, drug cargo and targeting ligand are established from these *in vitro* models, MS2 VLPs can then be tested *in vivo* using mice models, primate models and, ultimately, in human patients.

## 6.3 Closing remarks

MS2 VLPs continue to show great potential as an effective, robust drug delivery system. This project highlighted the versatility of VLPs for displaying useful ligands for immunomasking and tumour-targeting, as well as packaging various drug cargos, and demonstrated their ability to specifically deliver cytotoxic drugs to targeted cancer cells. It seems likely that flexible drug delivery systems like MS2 VLPs – alongside our accumulating knowledge on the molecular mechanisms of cancer (Weber, 2007), with increasingly sophisticated sequencing and disease screening technologies (Shendure and Ji, 2008), coupled to the emergence of a plethora of novel tumour-targeting ligands (Zhong et al., 2014) – will help to pave the way to making personalised medicine a practical reality.

# References

ABUCHOWSKI, A., MCCOY, J. R., PALCZUK, N. C., VAN ES, T. & DAVIS, F. F. 1977a. Effect of covalent attachment of polyethylene glycol on immunogenicity and circulating life of bovine liver catalase. *Journal of Biological Chemistry,* 252**,** 3582-3586.

ABUCHOWSKI, A., VAN ES, T., PALCZUK, N. C. & DAVIS, F. F. 1977b. Alteration of immunological properties of bovine serum albumin by covalent attachment of polyethylene glycol. *Journal of Biological Chemistry,* 252**,** 3578-3581.

ALCONCEL, S. N. S., BAAS, A. S. & MAYNARD, H. D. 2011. FDA-approved poly(ethylene glycol)-protein conjugate drugs. *Polymer Chemistry,* 2**,** 1442-1448.

ALIABADI, H. M. & LAVASANIFAR, A. 2006. Polymeric micelles for drug delivery. *Expert Opinion on Drug Delivery,* 3**,** 139-162.

ALLAMEHA, A., AMINI-HARANDI, A., OSATI-ASHTIANI, F. & O'BRIEN, P. J. 2008. Iron overload induced apoptotic cell death in isolated rat hepatocytes mediated by reactive oxygen species. *Iranian Journal of Pharmaceutical Research,* 7**,** 115-121.

ALLEN, C., MAYSINGER, D. & EISENBERG, A. 1999. Nano-engineering block copolymer aggregates for drug delivery. *Colloids and Surfaces B-Biointerfaces,* 16**,** 3-27.

ALLEN, T. M. & CLELAND, L. G. 1980. Serum-induced leakage of liposome contents. *Biochimica et Biophysica Acta,* 597**,** 418-426.

ALLEN, T. M. & CULLIS, P. R. 2004. Drug delivery systems: entering the mainstream. *Science,* 303**,** 1818-1822.

ALLEN, T. M. & CULLIS, P. R. 2013. Liposomal drug delivery systems: from concept to clinical applications. *Advanced Drug Delivery Reviews,* 65**,** 36-48.

ANOBOM, C. D., ALBUQUERQUE, S. C., ALBERNAZ, F. P., OLIVEIRA, A. C., SILVA, J. L., PEABODY, D. S., VALENTE, A. P. & ALMEIDA, F. C. 2003. Structural studies of MS2 bacteriophage virus particle disassembly by nuclear magnetic resonance relaxation measurements. *Biophysical Journal,* 84**,** 3894-3903.

ARMSTRONG, G. L., CONN, L. A. & PINNER, R. W. 1999. Trends in infectious disease mortality in the United States during the 20th century. *Journal of the American Medical Association,* 281**,** 61-66.

ARRONDEAU, J., GAN, H. K., RAZAK, A. R., PAOLETTI, X. & LE TOURNEAU, C. 2010. Development of anti-cancer drugs. *Discovery Medicine,* 10**,** 355-362.

ASHLEY, C. E., CARNES, E. C., PHILLIPS, G. K., DURFEE, P. N., BULEY, M. D., LINO, C. A., PADILLA, D. P., PHILLIPS, B., CARTER, M. B., WILLMAN, C. L., BRINKER, C. J., CALDEIRA JDO, C., CHACKERIAN, B., WHARTON, W. & PEABODY, D. S. 2011. Cell-specific delivery of diverse cargos by bacteriophage MS2 virus-like particles. *ACS Nano,* 5**,** 5729-5745.

BAKER, B. E., KESTLER, D. P. & ICHIKI, A. T. 2006. Effects of siRNAs in combination with Gleevec on K-562 cell proliferation and Bcr-Abl expression. *Journal of Biomedical Science,* 13**,** 499-507.

BALIS, M. E., BROWN, G. B., ELION, G. B., HITCHINGS, G. H. & VANDERWERFF, H. 1951. On the interconversion of purines by Lactobacillus casei. *Journal of Biological Chemistry,* 188**,** 217-219.

BALTIMORE, D. 1970. Viral RNA-dependent DNA polymerase: RNA-dependent DNA polymerase in virions of RNA tumour viruses. *Nature,* 226**,** 1209-1211.

BANERJEE, D., LIU, A. P., VOSS, N. R., SCHMID, S. L. & FINN, M. G. 2010. Multivalent display and receptor-mediated endocytosis of transferrin on virus-like particles. *ChemBioChem,* 11**,** 1273-1279.

BANGHAM, A. D., STANDISH, M. M. & WATKINS, J. C. 1965. Diffusion of univalent ions across the lamellae of swollen phospholipids. *Journal of Molecular Biology,* 13**,** 238-252.

BAREFORD, L. M. & SWAAN, P. W. 2007. Endocytic mechanisms for targeted drug delivery. *Advanced Drug Delivery Reviews,* 59**,** 748-758.

BARENHOLZ, Y. 2012. Doxil(R)--the first FDA-approved nano-drug: lessons learned. *Journal of Controlled Release,* 160**,** 117-134.

BARRATT, G. 2003. Colloidal drug carriers: achievements and perspectives. *Cellular and Molecular Life Sciences,* 60**,** 21-37.

BARTLETT, D. W. & DAVIS, M. E. 2007. Physicochemical and biological characterization of targeted, nucleic acid-containing nanoparticles. *Bioconjugate Chemistry,* 18**,** 456-468.

BATIST, G. 2007. Cardiac safety of liposomal anthracyclines. *Cardiovascular Toxicology,* 7**,** 72-74.

BATIST, G., RAMAKRISHNAN, G., RAO, C. S., CHANDRASEKHARAN, A., GUTHEIL, J., GUTHRIE, T., SHAH, P., KHOJASTEH, A., NAIR, M. K., HOELZER, K., TKACZUK, K., PARK, Y. C. & LEE, L. W. 2001. Reduced cardiotoxicity and preserved antitumor efficacy of liposome-encapsulated doxorubicin and cyclophosphamide compared with conventional doxorubicin and cyclophosphamide in a randomized, multicenter trial of metastatic breast cancer. *Journal of Clinical Oncology,* 19**,** 1444-1454.

BAULCOMBE, D. C. 1996. RNA as a target and an initiator of post-transcriptional gene silencing in transgenic plants. *Plant Molecular Biology,* 32**,** 79-88.

BEHR, J. P. 1997. The proton sponge - a trick to enter cells the viruses did not exploit. *Chimia,* 51**,** 34-36.

BEIGELMAN, L., MCSWIGGEN, J. A., DRAPER, K. G., GONZALEZ, C., JENSEN, K., KARPEISKY, A. M., MODAK, A. S., MATULICADAMIC, J., DIRENZO, A. B., HAEBERLI, P., SWEEDLER, D., TRACZ, D., GRIMM, S., WINCOTT, F. E., THACKRAY, V. G. & USMAN, N. 1995. Chemical modification of hammerhead ribozymes - catalytic activity and nuclease resistance. *Journal of Biological Chemistry,* 270**,** 25702-25708.

BELLOCQ, N. C., DAVIS, M. E., ENGLER, H., JENSEN, G. S., LIU, A., MACHEMER, T., MANEVAL, D. C., QUIJANO, E., PUN, S. H., SCHLUEP, T. & WEN, S. 2003. Transferrin-targeted, cyclodextrin polycation-based gene vector for systemic delivery. *Mol. Ther.,* 7**,** S290.

BERNARDS, R. 2006. The Nobel Prize in Physiology or Medicine for 2006 for the discovery of RNA interference. *Nederlands Tijdschrift voor Geneeskunde,* 150**,** 2849-2853.

BIESELE, J. J., BERGER, R. E., WILSON, A. Y., HITCHINGS, G. H. & ELION, G. B. 1951. Studies on 2,6-diaminopurine and related substances in cultures of embryonic and sarcomatous rodent tissues. *Cancer,* 4**,** 186-197.

BINASCHI, M., BIGIONI, M., CIPOLLONE, A., ROSSI, C., GOSO, C., MAGGI, C. A., CAPRANICO, G. & ANIMATI, F. 2001. Anthracyclines: selected new developments. *Current Medicinal Chemistry - Anti-Cancer Agents,* 1**,** 113-130.

BJORGE, J. D., PANG, A. S., FUNNELL, M., CHEN, K. Y., DIAZ, R., MAGLIOCCO, A. M. & FUJITA, D. J. 2011. Simultaneous siRNA targeting of Src and downstream signaling molecules inhibit tumor formation and metastasis of a human model breast cancer cell line. *PLoS One,* 6**,** e19309.

BLADE, J., SONNEVELD, P., SAN MIGUEL, J. F., SUTHERLAND, H. J., HAJEK, R., NAGLER, A., SPENCER, A., ROBAK, T., LANTZ, K. C., ZHUANG, S. H., HAROUSSEAU, J. L., ORLOWSKI, R. Z. & INVESTIGATORS, D.-M.-S. 2011. Efficacy and safety of pegylated liposomal Doxorubicin in combination with bortezomib for multiple myeloma: effects of adverse prognostic factors on outcome. *Clinical Lymphoma Myeloma and Leukemia,* 11**,** 44-49.

BOCK, L. C., GRIFFIN, L. C., LATHAM, J. A., VERMAAS, E. H. & TOOLE, J. J. 1992. Selection of single-stranded DNA molecules that bind and inhibit human thrombin. *Nature,* 355**,** 564-566.

BOEHM, J. S., ZHAO, J. J., YAO, J., KIM, S. Y., FIRESTEIN, R., DUNN, I. F., SJOSTROM, S. K., GARRAWAY, L. A., WEREMOWICZ, S., RICHARDSON, A. L., GREULICH, H., STEWART, C. J., MULVEY, L. A., SHEN, R. R., AMBROGIO, L., HIROZANE-KISHIKAWA, T., HILL, D. E., VIDAL, M., MEYERSON, M., GRENIER, J. K., HINKLE, G., ROOT, D. E., ROBERTS, T. M., LANDER, E. S., POLYAK, K. & HAHN, W. C. 2007. Integrative genomic approaches identify IKBKE as a breast cancer oncogene. *Cell,* 129**,** 1065-1079.

BONDAR, O. V., SAIFULLINA, D. V., SHAKHMAEVA, I. I., MAVLYUTOVA, I. I. & ABDULLIN, T. I. 2012. Monitoring of the zeta potential of human cells upon reduction in their viability and interaction with polymers. *Acta Naturae,* 4**,** 78-81.

BORCHMANN, P., HUBEL, K., SCHNELL, R. & ENGERT, A. 1997. Idarubicin: a brief overview on pharmacology and clinical use. *International Journal of Clinical Pharmacology and Therapeutics,* 35**,** 80-83.

BORODAVKA, A., TUMA, R. & STOCKLEY, P. G. 2012. Evidence that viral RNAs have evolved for efficient, two-stage packaging. *Proceedings of the National Academy of Sciences of the United States of America,* 109**,** 15769-15774.

BOUCHIE, A. 2012. Companies in footrace to deliver RNAi. *Nature Biotechnology,* 30**,** 1154-1157.

BRADBURY, P. A. & SHEPHERD, F. A. 2008. Immunotherapy for lung cancer. *Journal of Thoracic Oncology,* 3**,** S164-170.

BROWN, W. L., MASTICO, R. A., WU, M., HEAL, K. G., ADAMS, C. J., MURRAY, J. B., SIMPSON, J. C., LORD, J. M., TAYLOR-ROBINSON, A. W. & STOCKLEY, P. G. 2002. RNA bacteriophage capsid-mediated drug delivery and epitope presentation. *Intervirology,* 45**,** 371-380.

BRUMMELKAMP, T. R., BERNARDS, R. & AGAMI, R. 2002. Stable suppression of tumorigenicity by virus-mediated RNA interference. *Cancer Cell,* 2**,** 243-247.

BUNKA, D. H., LANE, S. W., LANE, C. L., DYKEMAN, E. C., FORD, R. J., BARKER, A. M., TWAROCK, R., PHILLIPS, S. E. & STOCKLEY, P. G. 2011. Degenerate RNA packaging signals in the genome of Satellite Tobacco Necrosis Virus: implications for the assembly of a T=1 capsid. *Journal of Molecular Biology,* 413**,** 51-65.

BUNKA, D. H. & STOCKLEY, P. G. 2006. Aptamers come of age - at last. *Nature Reviews Microbiology,* 4**,** 588-596.

BUNKA, D. H. J. & STOCKLEY, P. G. 2012. CHAPTER 6 Therapeutic applications of nucleic acid aptamer conjugates. *DNA Conjugates and Sensors.* The Royal Society of Chemistry.

BURCHENAL, J. H., BENDICH, A. & ET AL. 1949. Preliminary studies on the effect of 2,6-diaminopurine on transplanted mouse leukemia. *Cancer,* 2**,** 119.

BURCHENAL, J. H., KARNOFSKY, D. A., KINGSLEY-PILLERS, E. M., SOUTHAM, C. M., MYERS, W. P., ESCHER, G. C., CRAVER, L. F., DARGEON, H. W. & RHOADS, C. P. 1951. The effects of the folic acid

antagonists and 2,6-diaminopurine on neoplastic disease, with special reference to acute leukemia. *Cancer,* 4**,** 549-569.

BURCHENAL, J. H., MURPHY, M. L., ELLISON, R. R., SYKES, M. P., TAN, T. C., LEONE, L. A., KARNOFSKY, D. A., CRAVER, L. F., DARGEON, H. W. & RHOADS, C. P. 1953. Clinical evaluation of a new antimetabolite, 6-mercaptopurine, in the treatment of leukemia and allied diseases. *Blood,* 8**,** 965-999.

BURNETT, J. C., ROSSI, J. J. & TIEMANN, K. 2011. Current progress of siRNA/shRNA therapeutics in clinical trials. *Biotechnology Journal,* 6**,** 1130-1146.

BYRD, J. C., WASELENKO, J. K., MANEATIS, T. J., MURPHY, T., WARD, F. T., MONAHAN, B. P., SIPE, M. A., DONEGAN, S. & WHITE, C. A. 1999. Rituximab therapy in hematologic malignancy patients with circulating blood tumor cells: Association with increased infusion-related side effects and rapid blood tumor clearance. *Journal of Clinical Oncology,* 17**,** 791-795.

CALDEIRA, J. C. & PEABODY, D. S. 2011. Thermal stability of RNA phage virus-like particles displaying foreign peptides. *Journal of Nanobiotechnology,* 9**,** 22.

CAMPOS, S. K. & BARRY, M. A. 2007. Current advances and future challenges in Adenoviral vector biology and targeting. *Current Gene Therapy,* 7**,** 189-204.

CAPDEVILLE, R., BUCHDUNGER, E., ZIMMERMANN, J. & MATTER, A. 2002. Glivec (STI571, imatinib), a rationally developed, targeted anticancer drug. *Nature Reviews Drug Discovery,* 1**,** 493-502.

CARTER, P. 2001. Improving the efficacy of antibody-based cancer therapies. *Nature Reviews Cancer,* 1**,** 118-129.

CARTER, R. E., FELDMAN, A. R. & COYLE, J. T. 1996. Prostate-specific membrane antigen is a hydrolase with substrate and pharmacologic characteristics of a neuropeptidase. *Proceedings of the National Academy of Sciences of the United States of America,* 93**,** 749-753.

CARTHEW, R. W. 2006. Gene regulation by microRNAs. *Current Opinion in Genetics & Development,* 16**,** 203-208.

CARUTHERS, M. H. 2011. A brief review of DNA and RNA chemical synthesis. *Biochemical Society Transactions,* 39**,** 575-580.

CASTANOTTO, D. & ROSSI, J. J. 2009. The promises and pitfalls of RNA-interference-based therapeutics. *Nature,* 457**,** 426-433.

CERQUEIRA, N. M., FERNANDES, P. A. & RAMOS, M. J. 2007. Ribonucleotide reductase: a critical enzyme for cancer chemotherapy and antiviral agents. *Recent Patents on Anti-Cancer Drug Discovery,* 2**,** 11-29.

CHARI, R. V., MILLER, M. L. & WIDDISON, W. C. 2014. Antibody-drug conjugates: an emerging concept in cancer therapy. *Angewandte Chemie International Edition,* 53**,** 3796-3827.

CHAUDRY, M. A., SALES, K., RUF, P., LINDHOFER, H. & WINSLET, M. C. 2007. EpCAM an immunotherapeutic target for gastrointestinal malignancy: current experience and future challenges. *British Journal of Cancer,* 96**,** 1013-1019.

CHEN, C. H., DELLAMAGGIORE, K. R., OUELLETTE, C. P., SEDANO, C. D., LIZADJOHRY, M., CHERNIS, G. A., GONZALES, M., BALTASAR, F. E., FAN, A. L., MYEROWITZ, R. & NEUFELD, E. F. 2008. Aptamer-based endocytosis of a lysosomal enzyme. *Proceedings of the National Academy of Sciences of the United States of America,* 105**,** 15908-15913.

CHENG, Z., AL ZAKI, A., HUI, J. Z., MUZYKANTOV, V. R. & TSOURKAS, A. 2012. Multifunctional nanoparticles: cost versus benefit of adding targeting and imaging capabilities. *Science,* 338**,** 903-910.

CHIEN, A. J. & MOASSER, M. M. 2008. Cellular mechanisms of resistance to anthracyclines and taxanes in cancer: intrinsic and acquired. *Seminars in Oncology,* 35**,** S1-S14; quiz S39.

CHO, M., XIAO, Y., NIE, J., STEWART, R., CSORDAS, A. T., OH, S. S., THOMSON, J. A. & SOH, H. T. 2010. Quantitative selection of DNA aptamers through microfluidic selection and high-throughput sequencing. *Proceedings of the National Academy of Sciences of the United States of America,* 107**,** 15373-15378.

CHOI, H. S., LIU, W., MISRA, P., TANAKA, E., ZIMMER, J. P., ITTY IPE, B., BAWENDI, M. G. & FRANGIONI, J. V. 2007. Renal clearance of quantum dots. *Nature Biotechnology,* 25**,** 1165-1170.

CIARDIELLO, F. & TORTORA, G. 2008. Drug therapy: EGFR antagonists in cancer treatment. *New England Journal of Medicine,* 358**,** 1160-1174.

CIECHANOVER, A., SCHWARTZ, A. L., DAUTRY-VARSAT, A. & LODISH, H. F. 1983. Kinetics of internalization and recycling of transferrin and the transferrin receptor in a human hepatoma cell line. Effect of lysosomotropic agents. *Journal of Biological Chemistry,* 258**,** 9681-9689.

COLEY, H. M., AMOS, W. B., TWENTYMAN, P. R. & WORKMAN, P. 1993. Examination by laser scanning confocal fluorescence imaging microscopy of the subcellular localization of anthracyclines in parent and multidrug-resistant cell lines. *British Journal of Cancer,* 67**,** 1316-1323.

CORY, S. & ADAMS, J. M. 2002. The Bcl2 family: regulators of the cellular life-or-death switch. *Nature Reviews Cancer,* 2**,** 647-656.

COX, J. C. & ELLINGTON, A. D. 2001. Automated selection of anti-protein aptamers. *Bioorganic & Medicinal Chemistry,* 9**,** 2525-2531.

CROOKE, S. T. & BRADNER, W. T. 1976. Mitomycin C: a review. *Cancer Treatment Reviews,* 3**,** 121-139.

CULLIS, P. R. 1976. Lateral diffusion rates of phosphatidylcholine in vesicle membranes: effects of cholesterol and hydrocarbon phase transitions. *FEBS Letters,* 70**,** 223-228.

CUTTS, J. H., BEER, C. T. & NOBLE, R. L. 1960. Biological properties of Vincaleukoblastine, an alkaloid in Vinca rosea Linn, with reference to its antitumor action. *Cancer Research,* 20**,** 1023-1031.

DAI, X., YUE, Z., ECCLESTON, M. E., SWARTLING, J., SLATER, N. K. & KAMINSKI, C. F. 2008. Fluorescence intensity and lifetime imaging of free and micellar-encapsulated doxorubicin in living cells. *Nanomedicine (Lond),* 4**,** 49-56.

DALBY, B., CATES, S., HARRIS, A., OHKI, E. C., TILKINS, M. L., PRICE, P. J. & CICCARONE, V. C. 2004. Advanced transfection with Lipofectamine 2000 reagent: primary neurons, siRNA, and high-throughput applications. *Methods,* 33**,** 95-103.

DANHAUSER-RIEDL, S., HAUSMANN, E., SCHICK, H. D., BENDER, R., DIETZFELBINGER, H., RASTETTER, J. & HANAUSKE, A. R. 1993. Phase I clinical and pharmacokinetic trial of dextran conjugated doxorubicin (AD-70, DOX-OXD). *Investigational New Drugs,* 11**,** 187-195.

DANIELS, T. R., BERNABEU, E., RODRIGUEZ, J. A., PATEL, S., KOZMAN, M., CHIAPPETTA, D. A., HOLLER, E., LJUBIMOVA, J. Y., HELGUERA, G. & PENICHET, M. L. 2012. The transferrin receptor and the targeted delivery of therapeutic agents against cancer. *Biochimica et Biophysica Acta,* 1820**,** 291-317.

DANIELS, T. R., DELGADO, T., HELGUERA, G. & PENICHET, M. L. 2006a. The transferrin receptor part II: Targeted delivery of therapeutic agents into cancer cells. *Clinical Immunology,* 121**,** 159-176.

DANIELS, T. R., DELGADO, T., RODRIGUEZ, J. A., HELGUERA, G. & PENICHET, M. L. 2006b. The transferrin receptor part I: Biology and targeting with cytotoxic antibodies for the treatment of cancer. *Clinical Immunology,* 121**,** 144-158.

DASSIE, J. P., LIU, X. Y., THOMAS, G. S., WHITAKER, R. M., THIEL, K. W., STOCKDALE, K. R., MEYERHOLZ, D. K., MCCAFFREY, A. P., MCNAMARA, J. O., 2ND & GIANGRANDE, P. H. 2009. Systemic administration of optimized aptamer-siRNA chimeras promotes regression of PSMA-expressing tumors. *Nature Biotechnology,* 27**,** 839-849.

DAVIS, M. E. 2009. The first targeted delivery of siRNA in humans via a self-assembling, cyclodextrin polymer-based nanoparticle: from concept to clinic. *Mol Pharm,* 6**,** 659-668.

DAVIS, M. E. & BREWSTER, M. E. 2004. Cyclodextrin-based pharmaceutics: past, present and future. *Nature Reviews Drug Discovery,* 3**,** 1023-1035.

DAVIS, M. E., ZUCKERMAN, J. E., CHOI, C. H., SELIGSON, D., TOLCHER, A., ALABI, C. A., YEN, Y., HEIDEL, J. D. & RIBAS, A. 2010. Evidence of RNAi in humans from systemically administered siRNA via targeted nanoparticles. *Nature,* 464**,** 1067-1070.

DEFFIE, A. M., MCPHERSON, J. P., GUPTA, R. S., HEDLEY, D. W. & GOLDENBERG, G. J. 1992. Multifactorial resistance to antineoplastic agents in drug resistant P388 murine leukemia, chinese hamster ovary, and human Hela cells, with emphasis on the role of DNA topoisomerase II. *Biochemistry and Cell Biology,* 70**,** 354-364.

DEININGER, M. W. N., GOLDMAN, J. M. & MELO, J. V. 2000. The molecular biology of chronic myeloid leukemia. *Blood,* 96**,** 3343-3356.

DERRY, W. B., WILSON, L. & JORDAN, M. A. 1995. Substoichiometric binding of taxol suppresses microtubule dynamics. *Biochemistry,* 34**,** 2203-2211.

DESTITO, G., YEH, R., RAE, C. S., FINN, M. G. & MANCHESTER, M. 2007. Folic acid-mediated targeting of cowpea mosaic virus particles to tumor cells. *Chemistry & Biology,* 14**,** 1152-1162.

DICKO, A., MAYER, L. D. & TARDI, P. G. 2010. Use of nanoscale delivery systems to maintain synergistic drug ratios in vivo. *Expert Opinion on Drug Delivery,* 7**,** 1329-1341.

DIEDERICHS, S., JUNG, S., ROTHENBERG, S. M., SMOLEN, G. A., MLODY, B. G. & HABER, D. A. 2008. Coexpression of Argonaute-2 enhances RNA interference toward perfect match binding sites. *Proceedings of the National Academy of Sciences of the United States of America,* 105**,** 9284-9289.

DIGIUSTO, D. L., KRISHNAN, A., LI, L., LI, H., LI, S., RAO, A., MI, S., YAM, P., STINSON, S., KALOS, M., ALVARNAS, J., LACEY, S. F., YEE, J. K., LI, M., COUTURE, L., HSU, D., FORMAN, S. J., ROSSI, J. J. & ZAIA, J. A. 2010. RNA-based gene therapy for HIV with lentiviral vector-modified CD34(+) cells in patients undergoing transplantation for AIDS-related lymphoma. *Science Translational Medicine,* 2**,** 36ra43.

DIMARCO, A., GAETANI, M., OREZZI, P., SCARPINATO, B. M., SILVESTRINI, R., SOLDATI, M., DASDIA, T. & VALENTINI, L. 1964. 'Daunomycin', a new antibiotic of the rhodomycin group. *Nature,* 201**,** 706-707.

DIXON, S. J. & STOCKWELL, B. R. 2014. The role of iron and reactive oxygen species in cell death. *Nature Chemical Biology,* 10**,** 9-17.

DOMAGK, G. 1935. A new class of disinfectants. *Deutsche Medizinische Wochenschrift,* 61**,** 829-832.

DOMAGK, G. 1947. Nobel Lecture.

DRUKER, B. J. 2008. Translation of the Philadelphia chromosome into therapy for CML. *Blood,* 112**,** 4808-4817.

DRUKER, B. J., TALPAZ, M., RESTA, D. J., PENG, B., BUCHDUNGER, E., FORD, J. M., LYDON, N. B., KANTARJIAN, H., CAPDEVILLE, R., OHNO-JONES, S. & SAWYERS, C. L. 2001. Efficacy and safety of a specific inhibitor of the BCR-ABL tyrosine kinase in chronic myeloid leukemia. *New England Journal of Medicine,* 344**,** 1031-1037.

DUAN, N., WU, S. J., CHEN, X. J., HUANG, Y. K., XIA, Y., MA, X. Y. & WANG, Z. P. 2013. Selection and characterization of aptamers against Salmonella typhimurium using whole-bacterium systemic evolution of ligands by exponential enrichment (SELEX). *Journal of Agricultural and Food Chemistry,* 61**,** 3229-3234.

DUNCAN, R., VICENT, M. J., GRECO, F. & NICHOLSON, R. I. 2005. Polymer-drug conjugates: towards a novel approach for the treatment of endrocine-related cancer. *Endocrine-Related Cancer,* 12 Suppl 1**,** S189-199.

DUNDAS, C. M., DEMONTE, D. & PARK, S. 2013. Streptavidin-biotin technology: improvements and innovations in chemical and biological applications. *Applied Microbiology and Biotechnology,* 97**,** 9343-9353.

EHRLICH, P. 1878. Beiträge zur Theorie und Praxis der histologischen Färbung. *Thesis, University of Leipzig*.

EHRLICH, P. 1909. *Über den jetzigen stand der karzinomforschung*.

EHRLICH, P. 1910. Die behandlung der syphilis mit dem Ehrlichschen präparat 606. *Deutsche medizinische Wochenschrift***,** 1893–1896.

EHRLICH, P. 1911. Aus theorie und praxis der chemotherapie. *Folia Serologica,* 7**,** 697-714.

EHRLICH, P. & SHIGA, K. 1904. Farbentherapeutische versuche bei Trypanosomenerkrankung. *Berliner klinische Wochenschrift,* 41**,** 329-332.

ELION, G. B., BUCKLEY, S. M., STOCK, C. C. & HITCHINGS, G. H. 1951. Effect of some substituted 2,6-diaminopurines on the growth of sarcoma 180. *Cancer Research,* 11**,** 246-246.

ELION, G. B. & HITCHINGS, G. H. 1955. The synthesis of 6-thioguanine. *Journal of the American Chemical Society,* 77**,** 1676-1676.

ELION, G. B., VANDERWERFF, H., HITCHINGS, G. H., BALIS, M. E., LEVIN, D. H. & BROWN, G. B. 1953. Purine metabolism of a diaminopurine-resistant strain of Lactobacillus Casei. *Journal of Biological Chemistry,* 200**,** 7-16.

ELLINGTON, A. D., SZOSTAK, J. W. 1990. In vitro selection of RNA molecules that bind specific ligands. *Nature,* 346**,** 818 - 822

ESQUELA-KERSCHER, A. & SLACK, F. J. 2006. Oncomirs - microRNAs with a role in cancer. *Nature Reviews Cancer,* 6**,** 259-269.

FANTINI, M., GIANNI, L., SANTELMO, C., DRUDI, F., CASTELLANI, C., AFFATATO, A., NICOLINI, M. & RAVAIOLI, A. 2011. Lipoplatin treatment in lung and breast cancer. *Chemotherapy Research and Practice,* 2011**,** 125192.

FARBER, S., DIAMOND, L. K., MERCER, R. D., SYLVESTER, R. F. & WOLFF, J. A. 1948. Temporary remissions in acute leukemia in children produced

by folic acid antagonist, 4-aminopteroyl-glutamic acid (aminopterin). *New England Journal of Medicine,* 238**,** 787-793.

FASOL, U., FROST, A., BUCHERT, M., ARENDS, J., FIEDLER, U., SCHARR, D., SCHEUENPFLUG, J. & MROSS, K. 2012. Vascular and pharmacokinetic effects of EndoTAG-1 in patients with advanced cancer and liver metastasis. *Annals of Oncology,* 23**,** 1030-1036.

FEDIER, A., SCHWARZ, V. A., WALT, H., CARPINI, R. D., HALLER, U. & FINK, D. 2001. Resistance to topoisomerase poisons due to loss of DNA mismatch repair. *International Journal of Cancer,* 93**,** 571-576.

FIERS, W., CONTRERAS, R., DUERINCK, F., HAEGEMAN, G., ISERENTANT, D., MERREGAERT, J., MIN JOU, W., MOLEMANS, F., RAEYMAEKERS, A., VAN DEN BERGHE, A., VOLCKAERT, G. & YSEBAERT, M. 1976. Complete nucleotide sequence of bacteriophage MS2 RNA: primary and secondary structure of the replicase gene. *Nature,* 260**,** 500-507.

FIRE, A., XU, S. Q., MONTGOMERY, M. K., KOSTAS, S. A., DRIVER, S. E. & MELLO, C. C. 1998. Potent and specific genetic interference by double-stranded RNA in Caenorhabditis elegans. *Nature,* 391**,** 806-811.

FLEMING, A. 1929. On the antibacterial action of cultures of a penicillium, with special reference to their use in the isolation of B. Influenzae. *British Journal of Experimental Pathology,* 10**,** 226-236.

FLEMING, A. 1945. Nobel lecture, December 11.

GABIZON, A. & PAPAHADJOPOULOS, D. 1988. Liposome formulations with prolonged circulation time in blood and enhanced uptake by tumors. *Proceedings of the National Academy of Sciences of the United States of America,* 85**,** 6949-6953.

GABIZON, A., SHMEEDA, H. & BARENHOLZ, Y. 2003. Pharmacokinetics of pegylated liposomal doxorubicin: review of animal and human studies. *Clinical Pharmacokinetics,* 42**,** 419-36.

GALAWAY, F. 2011. An evaluation of viral nanoparticles for siRNA delivery. *PhD Thesis*.

GALAWAY, F. A. & STOCKLEY, P. G. 2013. MS2 viruslike particles: a robust, semisynthetic targeted drug delivery platform. *Mol Pharm,* 10**,** 59-68.

GALIZIA, G., LIETO, E., DE VITA, F., ORDITURA, M., CASTELLANO, P., TROIANI, T., IMPERATORE, V. & CIARDIELLO, F. 2007. Cetuximab, a chimeric human mouse anti-epidermal growth factor receptor monoclonal antibody, in the treatment of human colorectal cancer. *Oncogene,* 26**,** 3654-3660.

GAMBACORTI-PASSERINI, C. B., GUNBY, R. H., PIAZZA, R., GALIETTA, A., ROSTAGNO, R. & SCAPOZZA, L. 2003. Molecular mechanisms of resistance to imatinib in Philadelphia-chromosome-positive leukaemias. *Lancet Oncology,* 4**,** 75-85.

GANTA, S., DEVALAPALLY, H., SHAHIWALA, A. & AMIJI, M. 2008. A review of stimuli-responsive nanocarriers for drug and gene delivery. *Journal of Controlled Release,* 126**,** 187-204.

GAO, X. & HUANG, L. 1995. Cationic liposome-mediated gene transfer. *Gene Therapy,* 2**,** 710-722.

GILMAN, A. 1963. The initial clinical trial of nitrogen mustard. *American Journal of Surgery,* 105**,** 574-578.

GILMAN, A. & PHILIPS, F. S. 1946. The biological actions and therapeutic applications of the B-chloroethyl amines and sulfides. *Science,* 103**,** 409-436.

GOLDACRE, R. J., LOVELESS, A. & ROSS, W. C. 1949. Mode of production of chromosome abnormalities by the nitrogen mustards; the possible role of cross-linking. *Nature,* 163**,** 667-669.

GONG, J., CHEN, M. W., ZHENG, Y., WANG, S. P. & WANG, Y. T. 2012. Polymeric micelles drug delivery system in oncology. *Journal of Controlled Release,* 159**,** 312-323.

GOTO, H., MURAMOTO, Y., NODA, T. & KAWAOKA, Y. 2013. The genome-packaging signal of the influenza A virus genome comprises a genome incorporation signal and a genome-bundling signal. *Journal of Virology,* 87**,** 11316-11322.

GRIMM, D. 2011. The dose can make the poison: lessons learned from adverse in vivo toxicities caused by RNAi overexpression. *Silence,* 2**,** 8.

GRIMM, D., STREETZ, K. L., JOPLING, C. L., STORM, T. A., PANDEY, K., DAVIS, C. R., MARION, P., SALAZAR, F. & KAY, M. A. 2006. Fatality in mice due to oversaturation of cellular microRNA/short hairpin RNA pathways. *Nature,* 441**,** 537-541.

GRIMM, D., WANG, L., LEE, J. S., SCHURMANN, N., GU, S., BORNER, K., STORM, T. A. & KAY, M. A. 2010. Argonaute proteins are key determinants of RNAi efficacy, toxicity, and persistence in the adult mouse liver. *Journal of Clinical Investigation,* 120**,** 3106-3119.

GROVES, W. E., DAVIS, F. C. & SELLS, B. H. 1968. Spectrophotometric determination of microgram quantities of protein without nucleic acid interference. *Analytical Biochemistry,* 22**,** 195-210.

GUERRIERTAKADA, C., GARDINER, K., MARSH, T., PACE, N. & ALTMAN, S. 1983. The RNA moiety of ribonuclease P is the catalytic subunit of the enzyme. *Cell,* 35**,** 849-857.

HAHN, W. C. & WEINBERG, R. A. 2002. Modelling the molecular circuitry of cancer. *Nature Reviews Cancer,* 2**,** 331-341.

HAMIDI, M., AZADI, A. & RAFIEI, P. 2008. Hydrogel nanoparticles in drug delivery. *Advanced Drug Delivery Reviews,* 60**,** 1638-1649.

HANAHAN, D. & WEINBERG, R. A. 2000. The hallmarks of cancer. *Cell,* 100**,** 57-70.

HARTMAN, Z. C., APPLEDORN, D. M. & AMALFITANO, A. 2008. Adenovirus vector induced innate immune responses: impact upon efficacy and toxicity in gene therapy and vaccine applications. *Virus Research,* 132**,** 1-14.

HEIDEL, J. D. & SCHLUEP, T. 2012. Cyclodextrin-containing polymers: versatile platforms of drug delivery materials. *Journal of Drug Delivery,* 2012**,** 262731.

HEIDEL, J. D., YU, Z., LIU, J. Y., RELE, S. M., LIANG, Y., ZEIDAN, R. K., KORNBRUST, D. J. & DAVIS, M. E. 2007. Administration in non-human primates of escalating intravenous doses of targeted nanoparticles containing ribonucleotide reductase subunit M2 siRNA. *Proceedings of the National Academy of Sciences of the United States of America,* 104**,** 5715-5721.

HEILBRONN, R. & WEGER, S. 2010. Viral vectors for gene transfer: current status of gene therapeutics. *Handbook of Experimental Pharmacology***,** 143-170.

HERMANSON, G. T. 2013. Bioconjugate techniques, 3rd Edition. *Bioconjugate Techniques, 3rd Edition***,** 1-1146.

HIRSCHHAEUSER, F., MENNE, H., DITTFELD, C., WEST, J., MUELLER-KLIESER, W. & KUNZ-SCHUGHART, L. A. 2010. Multicellular tumor

spheroids: An underestimated tool is catching up again. *Journal of Biotechnology,* 148**,** 3-15.

HITCHINGS, G. H., JR. 1989. Nobel lecture in physiology or medicine--1988. Selective inhibitors of dihydrofolate reductase. *In Vitro Cellular & Developmental Biology,* 25**,** 303-310.

HOLOHAN, C., VAN SCHAEYBROECK, S., LONGLEY, D. B. & JOHNSTON, P. G. 2013. Cancer drug resistance: an evolving paradigm. *Nature Reviews Cancer,* 13**,** 714-726.

HONG, Y., MACNAB, S., LAMBERT, L. A., TURNER, A. J., WHITEHOUSE, A. & USMANI, B. A. 2011. Herpesvirus saimiri-based endothelin-converting enzyme-1 shRNA expression decreases prostate cancer cell invasion and migration. *International Journal of Cancer,* 129**,** 586-598.

HORNICEK, F. J., MALININ, G. I., THORNTHWAITE, J. T. & MALININ, T. I. 1986. Flow cytometry of blastogenesis and the concomitant viability assay of lymphocytes stained with 4', 6 diamidino-2-phenylindole. *Basic and Applied Histochemistry,* 30**,** 453-461.

HU-LIESKOVAN, S., HEIDEL, J. D., BARTLETT, D. W., DAVIS, M. E. & TRICHE, T. J. 2005. Sequence-specific knockdown of EWS-FLI1 by targeted, nonviral delivery of small interfering RNA inhibits tumor growth in a murine model of metastatic Ewing's sarcoma. *Cancer Research,* 65**,** 8984-8992.

HUANG, Y. F., SHANGGUAN, D. H., LIU, H. P., PHILLIPS, J. A., ZHANG, X. L., CHEN, Y. & TAN, W. H. 2009. Molecular assembly of an aptamer-drug conjugate for targeted drug delivery to tumor cells. *ChemBioChem,* 10**,** 862-868.

HUDZIAK, R. M., LEWIS, G. D., WINGET, M., FENDLY, B. M., SHEPARD, H. M. & ULLRICH, A. 1989. P185her2 monoclonal antibody has

antiproliferative effects in vitro and sensitizes human breast tumor cells to tumor necrosis factor. *Molecular and Cellular Biology,* 9**,** 1165-1172.

HYODO, I., MIZUNO, M., YAMADA, G. & TSUJI, T. 1993. Distribution of asialoglycoprotein receptor in human hepatocellular carcinoma. *Liver,* 13**,** 80-85.

ISLAM, A. & YASIN, T. 2012. Controlled delivery of drug from pH sensitive chitosan/poly (vinyl alcohol) blend. *Carbohydrate Polymers,* 88**,** 1055-1060.

ISRAELI, R. S., POWELL, C. T., CORR, J. G., FAIR, W. R. & HESTON, W. D. 1994. Expression of the prostate-specific membrane antigen. *Cancer Research,* 54**,** 1807-1811.

JAMES, N. D., COKER, R. J., TOMLINSON, D., HARRIS, J. R., GOMPELS, M., PINCHING, A. J. & STEWART, J. S. 1994. Liposomal doxorubicin (Doxil): an effective new treatment for Kaposi's sarcoma in AIDS. *Clinical Oncology,* 6**,** 294-296.

JELLINEK, D., GREEN, L. S., BELL, C. & JANJIC, N. 1994. Inhibition of receptor binding by high-affinity RNA ligands to vascular endothelial growth factor. *Biochemistry,* 33**,** 10450-10456.

JENSEN, P. B., SORENSEN, B. S., SEHESTED, M., DEMANT, E. J. F., KJELDSEN, E., FRICHE, E. & HANSEN, H. H. 1993. Different modes of anthracycline interaction with topoisomerase II separate structures critical for DNA cleavage, and for overcoming topoisomerase II-related drug resistance. *Biochemical Pharmacology,* 45**,** 2025-2035.

JOHNSON, I. S., WRIGHT, H. F. & SVOBODA, G. H. 1959. Experimental basis for clinical evaluation of anti-tumor principles derived from Vinca rosea Linn. *Journal of Laboratory and Clinical Medicine,* 54**,** 830-830.

JOLIVET, J., COWAN, K. H., CURT, G. A., CLENDENINN, N. J. & CHABNER, B. A. 1983. The pharmacology and clinical use of methotrexate. *New England Journal of Medicine,* 309**,** 1094-1104.

JONSSON-VIDESATER, K., ANDERSSON, G., BERGH, J. & PAUL, C. 2003. Doxorubicin-resistant, MRP1-expressing U-1285 cells are sensitive to idarubicin. *Therapeutic Drug Monitoring,* 25**,** 331-339.

JORDAN, M. A., MARGOLIS, R. L., HIMES, R. H. & WILSON, L. 1986. Identification of a distinct class of vinblastine binding-sites on microtubules. *Journal of Molecular Biology,* 187**,** 61-73.

JORDAN, M. A., THROWER, D. & WILSON, L. 1991. Mechanism of Inhibition of Cell-Proliferation by Vinca Alkaloids. *Cancer Research,* 51**,** 2212-2222.

JORDAN, M. A., WENDELL, K., GARDINER, S., DERRY, W. B., COPP, H. & WILSON, L. 1996. Mitotic block induced in HeLa cells by low concentrations of paclitaxel (Taxol) results in abnormal mitotic exit and apoptotic cell death. *Cancer Research,* 56**,** 816-825.

JORDAN, M. A. & WILSON, L. 2004. Microtubules as a target for anticancer drugs. *Nature Reviews Cancer,* 4**,** 253-265.

KAIGHN, M. E., NARAYAN, K. S., OHNUKI, Y., LECHNER, J. F. & JONES, L. W. 1979. Establishment and characterization of a human prostatic carcinoma cell line (PC-3). *Investigative Urology,* 17**,** 16-23.

KARIN VALEGÅRD, L. L., KERSTIN FRIDBORG, TORSTEN UNGE 1990. The three-dimensional structure of the bacterial virus MS2. *Nature,* 345**,** 36-41.

KASTELEIN, R. A., REMAUT, E., FIERS, W. & VAN DUIN, J. 1982. Lysis gene expression of RNA phage MS2 depends on a frameshift during translation of the overlapping coat protein gene. *Nature,* 295**,** 35-41.

KEEFE, A. D., PAI, S., ELLINGTON, A. 2010. Aptamers as therapeutics. *Nature Reviews Drug Discovery,* 9**,** 537-550.

KESHARWANI, P., JAIN, K. & JAIN, N. K. 2014. Dendrimer as nanocarrier for drug delivery. *Progress in Polymer Science,* 39**,** 268-307.

KIM, D. W., KIM, S. Y., KIM, H. K., KIM, S. W., SHIN, S. W., KIM, J. S., PARK, K., LEE, M. Y. & HEO, D. S. 2007. Multicenter phase II trial of Genexol-PM, a novel Cremophor-free, polymeric micelle formulation of paclitaxel, with cisplatin in patients with advanced non-small-cell lung cancer. *Annals of Oncology,* 18**,** 2009-2014.

KIM, H. K., DAVAA, E., MYUNG, C. S. & PARK, J. S. 2010. Enhanced siRNA delivery using cationic liposomes with new polyarginine-conjugated PEG-lipid. *International Journal of Pharmaceutics,* 392**,** 141-147.

KIM, H. R., KIM, I. K., BAE, K. H., LEE, S. H., LEE, Y. & PARK, T. G. 2008. Cationic solid lipid nanoparticles reconstituted from low density lipoprotein components for delivery of siRNA. *Mol Pharm,* 5**,** 622-631.

KIM, S. C., KIM, D. W., SHIM, Y. H., BANG, J. S., OH, H. S., WAN KIM, S. & SEO, M. H. 2001. In vivo evaluation of polymeric micellar paclitaxel formulation: toxicity and efficacy. *Journal of Controlled Release,* 72**,** 191-202.

KIM, T. Y., KIM, D. W., CHUNG, J. Y., SHIN, S. G., KIM, S. C., HEO, D. S., KIM, N. K. & BANG, Y. J. 2004. Phase I and pharmacokinetic study of Genexol-PM, a cremophor-free, polymeric micelle-formulated paclitaxel, in patients with advanced malignancies. *Clinical Cancer Research,* 10**,** 3708-3716.

KLAUSNER, R. D., VAN RENSWOUDE, J., ASHWELL, G., KEMPF, C., SCHECHTER, A. N., DEAN, A. & BRIDGES, K. R. 1983. Receptor-mediated endocytosis of transferrin in K562 cells. *Journal of Biological Chemistry,* 258**,** 4715-4724.

KLUSSMANN, S., NOLTE, A., BALD, R., ERDMANN, V. A. & FURSTE, J. P. 1996. Mirror-image RNA that binds D-adenosine. *Nature Biotechnology,* 14**,** 1112-1115.

KNOP, K., HOOGENBOOM, R., FISCHER, D. & SCHUBERT, U. S. 2010. Poly(ethylene glycol) in drug delivery: Pros and cons as well as potential alternatives. *Angewandte Chemie International Edition,* 49**,** 6288-6308.

KOHLER, G. & MILSTEIN, C. 1975. Continuous cultures of fused cells secreting antibody of predefined specificity. *Nature,* 256**,** 495-497.

KOHN, K. W., HARTLEY, J. A. & MATTES, W. B. 1987. Mechanisms of DNA-sequence selective alkylation of guanine-N7 positions by nitrogen mustards. *Nucleic Acids Research,* 15**,** 10531-10549.

KOLA, I. & LANDIS, J. 2004. Can the pharmaceutical industry reduce attrition rates? *Nature Reviews Drug Discovery,* 3**,** 711-715.

KOLB, H. C., FINN, M. G. & SHARPLESS, K. B. 2001. Click chemistry: Diverse chemical function from a few good reactions. *Angewandte Chemie International Edition,* 40**,** 2004-2021.

KOLCH, W. & PITT, A. 2010. Functional proteomics to dissect tyrosine kinase signalling pathways in cancer. *Nature Reviews Cancer,* 10**,** 618-629.

KOPECEK, J. & KOPECKOVA, P. 2010. HPMA copolymers: origins, early developments, present, and future. *Advanced Drug Delivery Reviews,* 62**,** 122-149.

KOZAK, M. & NATHANS, D. 1971. Fate of maturation protein during infection by coliphage MS2. *Nature: New Biology* 234**,** 209-211.

KRAHN, P. M., O'CALLAGHAN, R. J. & PARANCHYCH, W. 1972. Stages in phage R17 infection. VI. Injection of A protein and RNA into the host cell. *Virology,* 47**,** 628-637.

KRAVCHENKO-BALASHA, N., MIZRACHY-SCHWARTZ, S., KLEIN, S. & LEVITZKI, A. 2009. Shift from apoptotic to necrotic cell death during human papillomavirus-induced transformation of keratinocytes. *Journal of Biological Chemistry,* 284**,** 11717-11727.

KRUGER, K., GRABOWSKI, P. J., ZAUG, A. J., SANDS, J., GOTTSCHLING, D. E. & CECH, T. R. 1982. Self-splicing RNA: autoexcision and autocyclization of the ribosomal RNA intervening sequence of Tetrahymena. *Cell,* 31**,** 147-157.

KUMMAR, S., CHEN, H. X., WRIGHT, J., HOLBECK, S., MILLIN, M. D., TOMASZEWSKI, J., ZWEIBEL, J., COLLINS, J. & DOROSHOW, J. H. 2010. Utilizing targeted cancer therapeutic agents in combination: novel approaches and urgent requirements. *Nature Reviews Drug Discovery,* 9**,** 843-856.

KURIOKA, D., TAKAGI, A., YONEDA, M., HIROKAWA, Y., SHIRAISHI, T. 2011. Multicellular spheroid culture models: Applications in prostate cancer research and therapeutics. *Journal of Cancer Science & Therapy,* 3**,** 60-65.

KWON, G. S. & FORREST, M. L. 2006. Amphiphilic block copolymer micelles for nanoscale drug delivery. *Drug Development Research,* 67**,** 15-22.

KWON, G. S. & KATAOKA, K. 1995. Block-copolymer micelles as long-circulating drug vehicles. *Advanced Drug Delivery Reviews,* 16**,** 295-309.

LANG, S. H., HYDE, C., REID, I. N., HITCHCOCK, I. S., HART, C. A., BRYDEN, A. A., VILLETTE, J. M., STOWER, M. J. & MAITLAND, N. J. 2002. Enhanced expression of vimentin in motile prostate cell lines and in poorly differentiated and metastatic prostate carcinoma. *Prostate,* 52**,** 253-263.

LAOUINI, A., JAAFAR-MAALEJ, C., LIMAYEM-BLOUZA, I., SFAR, S., CHARCOSSET, C. & FESSI, H. 2012. Preparation, characterization and

applications of liposomes: State of the art. *Journal of Colloid Science and Biotechnology,* 1**,** 147-168.

LATTERICH, M. (ed.) 2008. *RNAi,* New York: Taylor & Francis Group.

LI, J., SUN, Y., JIA, T., ZHANG, R., ZHANG, K. & WANG, L. 2013. Messenger RNA vaccine based on recombinant MS2 virus-like particles against prostate cancer. *International Journal of Cancer,* 134**,** 1683-1694.

LI, M. C., HERTZ, R. & BERGENSTAL, D. M. 1958. Therapy of choriocarcinoma and related trophoblastic tumors with folic acid and purine antagonists. *New England Journal of Medicine,* 259**,** 66-74.

LI, R. H., YERGANIAN, G., DUESBERG, P., KRAEMER, A., WILLER, A., RAUSCH, C. & HEHLMANN, R. 1997. Aneuploidy correlated 100% with chemical transformation of Chinese hamster cells. *Proceedings of the National Academy of Sciences of the United States of America,* 94**,** 14506-14511.

LIU, L. & GUO, Q. X. 2002. The driving forces in the inclusion complexation of cyclodextrins. *Journal of Inclusion Phenomena and Macrocyclic Chemistry,* 42**,** 1-14.

LIU, Q. & MURUVE, D. A. 2003. Molecular basis of the inflammatory response to adenovirus vectors. *Gene Therapy,* 10**,** 935-940.

LIU, R., LI, D., HE, B., XU, X. H., SHENG, M. M., LAI, Y. S., WANG, G. & GU, Z. W. 2011. Anti-tumor drug delivery of pH-sensitive poly(ethylene glycol)-poly(L-histidine-)-poly(L-lactide) nanoparticles. *Journal of Controlled Release,* 152**,** 49-56.

LO, A., LIN, C. T. & WU, H. C. 2008. Hepatocellular carcinoma cell-specific peptide ligand for targeted drug delivery. *Molecular cancer therapeutics,* 7**,** 579-589.

LU, E., ELIZONDO-RIOJAS, M. A., CHANG, J. T. & VOLK, D. E. 2014. Aptaligner: Automated software for aligning pseudorandom DNA X-aptamers from next-generation sequencing data. *Biochemistry,* 53**,** 3523-3525.

LUND, E. & DAHLBERG, J. E. 2006. Substrate selectivity of exportin 5 and Dicer in the biogenesis of microRNAs. *Cold Spring Harbor Symposia on Quantitative Biology,* 71**,** 59-66.

LUO, J., SOLIMINI, N. L. & ELLEDGE, S. J. 2009. Principles of cancer therapy: oncogene and non-oncogene addiction. *Cell,* 136**,** 823-837.

LUPOLD, S. E., HICKE, B. J., LIN, Y., COFFEY, D. S. 2002. Identification and characterization of nuclease-stabilized RNA molecules that bind human prostate cancer cells via the prostate-specific membrane antigen. *Cancer Research,* 62**,** 4029-4033.

LYNCH, T. J., BELL, D. W., SORDELLA, R., GURUBHAGAVATULA, S., OKIMOTO, R. A., BRANNIGAN, B. W., HARRIS, P. L., HASERLAT, S. M., SUPKO, J. G., HALUSKA, F. G., LOUIS, D. N., CHRISTIANI, D. C., SETTLEMAN, J. & HABER, D. A. 2004. Activating mutations in the epidermal growth factor receptor underlying responsiveness of non-small-cell lung cancer to gefitinib. *New England Journal of Medicine,* 350**,** 2129-2139.

MA, P. & MUMPER, R. J. 2013. Anthracycline nano-delivery systems to overcome multiple drug resistance: A comprehensive review. *Nano Today,* 8**,** 313-331.

MACFARLANE, L. A. & MURPHY, P. R. 2010. MicroRNA: Biogenesis, function and role in cancer. *Current Genomics,* 11**,** 537-561.

MAIER, M. A., JAYARAMAN, M., MATSUDA, S., LIU, J., BARROS, S., QUERBES, W., TAM, Y. K., ANSELL, S. M., KUMAR, V., QIN, J., ZHANG, X., WANG, Q., PANESAR, S., HUTABARAT, R., CARIOTO, M.,

HETTINGER, J., KANDASAMY, P., BUTLER, D., RAJEEV, K. G., PANG, B., CHARISSE, K., FITZGERALD, K., MUI, B. L., DU, X., CULLIS, P., MADDEN, T. D., HOPE, M. J., MANOHARAN, M. & AKINC, A. 2013. Biodegradable lipids enabling rapidly eliminated lipid nanoparticles for systemic delivery of RNAi therapeutics. *Mol Ther,* 21**,** 1570-1578.

MAITLAND, N., CHAMBERS, K., GEORGOPOULOS, L., SIMPSON-HOLLEY, M., LEADLEY, R., EVANS, H., ESSAND, M., DANIELSSON, A., VAN WEERDEN, W., DE RIDDER, C., KRAAIJ, R., BANGMA, C. H. & CONSORTIUM, G. F. 2010. Gene transfer vectors targeted to human prostate cancer: do we need better preclinical testing systems? *Human Gene Therapy,* 21**,** 815-827.

MALONEY, D. G., GRILLO-LOPEZ, A. J., WHITE, C. A., BODKIN, D., SCHILDER, R. J., NEIDHART, J. A., JANAKIRAMAN, N., FOON, K. A., LILES, T. M., DALLAIRE, B. K., WEY, K., ROYSTON, I., DAVIS, T. & LEVY, R. 1997. IDEC-C2B8 (Rituximab) anti-CD20 monoclonal antibody therapy in patients with relapsed low-grade non-Hodgkin's lymphoma. *Blood,* 90**,** 2188-2195.

MARSHALL, E. 1999. Gene therapy death prompts review of adenovirus vector. *Science,* 286**,** 2244-2245.

MARTINDALE, W. 1996. *The extra pharmacopoeia, 31st edition*, London: Royal Pharmaceutical Society of Great Britain.

MASAKI, T., SHIRATORI, Y., RENGIFO, W., IGARASHI, K., YAMAGATA, M., KUROKOHCHI, K., UCHIDA, N., MIYAUCHI, Y., YOSHIJI, H., WATANABE, S., OMATA, M. & KURIYAMA, S. 2003. Cyclins and cyclin-dependent kinases: comparative study of hepatocellular carcinoma versus cirrhosis. *Hepatology,* 37**,** 534-543.

MASTA, A., GRAY, P. J. & PHILLIPS, D. R. 1995. Nitrogen-mustard inhibits transcription and translation in a cell-free system. *Nucleic Acids Research,* 23**,** 3508-3515.

MASTICO, R. A., TALBOT, S. J. & STOCKLEY, P. G. 1993. Multiple presentation of foreign peptides on the surface of an RNA-free spherical bacteriophage capsid. *Journal of General Virology,* 74 ( Pt 4)**,** 541-548.

MATSUMURA, Y., HAMAGUCHI, T., URA, T., MURO, K., YAMADA, Y., SHIMADA, Y., SHIRAO, K., OKUSAKA, T., UENO, H., IKEDA, M. & WATANABE, N. 2004. Phase I clinical trial and pharmacokinetic evaluation of NK911, a micelle-encapsulated doxorubicin. *British Journal of Cancer,* 91**,** 1775-1781.

MATSUMURA, Y. & MAEDA, H. 1986. A new concept for macromolecular cherapeutics in cancer chemotherapy: Mechanism of tumoritropic accumulation of proteins and the antitumor agent Smancs1. *Cancer Research,* 46**,** 6387-6392.

MATYSZEWSKA, D. 2014. Drug delivery systems in the transport of doxorubicin. *Surface Innovations,* 2**,** 201-210.

MCDONAGH, C. F., HUHALOV, A., HARMS, B. D., ADAMS, S., PARAGAS, V., OYAMA, S., ZHANG, B., LUUS, L., OVERLAND, R., NGUYEN, S., GU, J. M., KOHLI, N., WALLACE, M., FELDHAUS, M. J., KUDLA, A. J., SCHOEBERL, B. & NIELSEN, U. B. 2012. Antitumor activity of a novel bispecific antibody that targets the ErbB2/ErbB3 oncogenic unit and inhibits heregulin-induced activation of ErbB3. *Molecular Cancer Therapeutics,* 11**,** 582-593.

MCLAUGHLIN, P., GRILLO-LOPEZ, A. J., LINK, B. K., LEVY, R., CZUCZMAN, M. S., WILLIAMS, M. E., HEYMAN, M. R., BENCE-BRUCKLER, I., WHITE, C. A., CABANILLAS, F., JAIN, V., HO, A. D., LISTER, J., WEY, K., SHEN, D. & DALLAIRE, B. K. 1998. Rituximab chimeric anti-CD20 monoclonal antibody therapy for relapsed indolent lymphoma: half of

patients respond to a four-dose treatment program. *Journal of Clinical Oncology,* 16**,** 2825-2833.

MCMENAMIN, M. M., BYRNES, A. P., CHARLTON, H. M., COFFIN, R. S., LATCHMAN, D. S. & WOOD, M. J. 1998. A gamma34.5 mutant of herpes simplex 1 causes severe inflammation in the brain. *Neuroscience,* 83**,** 1225-1237.

MCNAMARA, J. O., 2ND, ANDRECHEK, E. R., WANG, Y., VILES, K. D., REMPEL, R. E., GILBOA, E., SULLENGER, B. A. & GIANGRANDE, P. H. 2006. Cell type-specific delivery of siRNAs with aptamer-siRNA chimeras. *Nature Biotechnology,* 24**,** 1005-1015.

MENDONSA, S. D. & BOWSER, M. T. 2004. In vitro selection of high-affinity DNA ligands for human IgE using capillary electrophoresis. *Analytical Chemistry,* 76**,** 5387-5392.

MERLE, P., AHMED, S., HABERSETZER, F., ABERGEL, A., TAIEB, J., BONYHAY, L., COSTANTINI, D., DUFOUR-LAMARTINIE, J. & TREPO, C. 2006. Phase 1 study of intra-arterial hepatic (IAH) delivery of Doxorubicin-Transdrug (R) (DT) for patients with advanced hepatocellular carcinoma (HCC). *Liver International,* 26**,** 61-62.

MI, J., LIU, Y. M., RABBANI, Z. N., YANG, Z. G., URBAN, J. H., SULLENGER, B. A. & CLARY, B. M. 2010. In vivo selection of tumor-targeting RNA motifs. *Nature Chemical Biology,* 6**,** 22-24.

MINOTTI, G., MENNA, P., SALVATORELLI, E., CAIRO, G. & GIANNI, L. 2004. Anthracyclines: molecular advances and pharmacologic developments in antitumor activity and cardiotoxicity. *Pharmacological Reviews,* 56**,** 185-229.

MISONO, T. S. & KUMAR, P. K. R. 2005. Selection of RNA aptamers against human influenza virus hemagglutinin using surface plasmon resonance. *Analytical Biochemistry,* 342**,** 312-317.

MOZAFARI, M. R. 2005. Liposomes: an overview of manufacturing techniques. *Cellular and Molecular Biology Letters,* 10**,** 711-719.

NAKANISHI, T., FUKUSHIMA, S., OKAMOTO, K., SUZUKI, M., MATSUMURA, Y., YOKOYAMA, M., OKANO, T., SAKURAI, Y. & KATAOKA, K. 2001. Development of the polymer micelle carrier system for doxorubicin. *Journal of Controlled Release,* 74**,** 295-302.

NEEDHAM, D., ANYARAMBHATLA, G., KONG, G. & DEWHIRST, M. W. 2000. A new temperature-sensitive liposome for use with mild hyperthermia: Characterization and testing in a human tumor xenograft model. *Cancer Research,* 60**,** 1197-1201.

NG, E. W. M., SHIMA, D. T., CALIAS, P., CUNNINGHAM, E. T., GUYER, D. R. & ADAMIS, A. P. 2006. Pegaptanib, a targeted anti-VEGF aptamer for ocular vascular disease. *Nature Reviews Drug Discovery,* 5**,** 123-132.

NIAZI, J. H., LEE, S. J. & GU, M. B. 2008. Single-stranded DNA aptamers specific for antibiotics tetracyclines. *Bioorganic & Medicinal Chemistry,* 16**,** 7245-7253.

NICOLAZZI, C., VENARD, V., LE FAOU, A. & FINANCE, C. 2002. In vitro antiviral efficacy of the ganciclovir complexed with beta-cyclodextrin on human cytomegalovirus clinical strains. *Antiviral Research,* 54**,** 121-127.

NOBLE, R. L., BEER, C. T. & CUTTS, J. H. 1958. Further biological activities of vincaleukoblastine - an alkaloid isolated from Vinca rosea (L). *Biochemical Pharmacology,* 1**,** 347-348.

NOGALES, E. 2001. Structural insights into microtubule function. *Annual Review of Biophysics and Biomolecular Structure,* 30**,** 397-420.

NOGALES, E., WOLF, S. G., KHAN, I. A., LUDUENA, R. F. & DOWNING, K. H. 1995. Structure of tubulin at 6.5 A and location of the taxol-binding site. *Nature,* 375**,** 424-427.

O'KEEFE, D. S., BACICH, D. J. & HESTON, W. D. 2004. Comparative analysis of prostate-specific membrane antigen (PSMA) versus a prostate-specific membrane antigen-like gene. *Prostate,* 58**,** 200-210.

OBBARD, D. J., GORDON, K. H., BUCK, A. H. & JIGGINS, F. M. 2009. The evolution of RNAi as a defence against viruses and transposable elements. *Philosophical Transactions of the Royal Society B: Biological Sciences,* 364**,** 99-115.

OCHSNER, U. A., GREEN, L. S., GOLD, L. & JANJIC, N. 2014. Systematic selection of modified aptamer pairs for diagnostic sandwich assays. *Biotechniques,* 56**,** 125-133.

OSBORN, M. J., FREEMAN, M. & HUENNEKENS, F. M. 1958. Inhibition of dihydrofolic reductase by aminopterin and amethopterin. *Proceedings of the Society for Experimental Biology and Medicine,* 97**,** 429-432.

OSBORN, M. J. & HUENNEKENS, F. M. 1958. Folic acid coenzymes and active one-carbon units .7. Enzymatic reduction of dihydrofolic acid. *Journal of Biological Chemistry,* 233**,** 969-974.

OSTROFF, R., FOREMAN, T., KEENEY, T. R., STRATFORD, S., WALKER, J. J. & ZICHI, D. 2010. The stability of the circulating human proteome to variations in sample collection and handling procedures measured with an aptamer-based proteomics array. *Journal of Proteomics,* 73**,** 649-666.

PAN, Y., JIA, T., ZHANG, Y., ZHANG, K., ZHANG, R., LI, J. & WANG, L. 2012a. MS2 VLP-based delivery of microRNA-146a inhibits autoantibody production in lupus-prone mice. *International Journal of Nanomedicine,* 7**,** 5957-5967.

PAN, Y., ZHANG, Y., JIA, T., ZHANG, K., LI, J. & WANG, L. 2012b. Development of a microRNA delivery system based on bacteriophage MS2 virus-like particles. *FEBS Journal,* 279**,** 1198-1208.

PANG, B., QIAO, X., JANSSEN, L., VELDS, A., GROOTHUIS, T., KERKHOVEN, R., NIEUWLAND, M., OVAA, H., ROTTENBERG, S., VAN TELLINGEN, O., JANSSEN, J., HUIJGENS, P., ZWART, W. & NEEFJES, J. 2013. Drug-induced histone eviction from open chromatin contributes to the chemotherapeutic effects of doxorubicin. *Nature Communications,* 4**,** 1908.

PANG, L., NOWOSTAWSKA, U., RYAN, J. N., WILLIAMSON, W. M., WALSHE, G. & HUNTER, K. A. 2009. Modifying the surface charge of pathogen-sized microspheres for studying pathogen transport in groundwater. *Journal of Environmental Quality,* 38**,** 2210-2217.

PAO, W., MILLER, V., ZAKOWSKI, M., DOHERTY, J., POLITI, K., SARKARIA, I., SINGH, B., HEELAN, R., RUSCH, V., FULTON, L. 2004. EGF receptor gene mutations are common in lung cancers from 'never smokers' and are associated with sensitivity of tumors to gefitinib and erlotinib. *Proceedings of the National Academy of Sciences of the United States of America,* 101**,** 13306–13311.

PATCH, M. G. & CARRANO, C. J. 1981. The origin of the visible absorption in metal transferrins. *Inorganica Chimica Acta-Bioinorganic Chemistry,* 56**,** L71-L73.

PATEL, D. J., SURI, A. K., JIANG, F., JIANG, L. C., FAN, P., KUMAR, R. A. & NONIN, S. 1997. Structure, recognition and adaptive binding in RNA aptamer complexes. *Journal of Molecular Biology,* 272**,** 645-664.

PEER, D., KARP, J. M., HONG, S., FAROKHZAD, O. C., MARGALIT, R. & LANGER, R. 2007. Nanocarriers as an emerging platform for cancer therapy. *Nature Nanotechnology,* 2**,** 751-760.

PETERS, G. J., VAN DER WILT, C. L., VAN MOORSEL, C. J. A., KROEP, J. R., BERGMAN, A. M. & ACKLAND, S. P. 2000. Basis for effective combination cancer chemotherapy with antimetabolites. *Pharmacology & Therapeutics,* 87**,** 227-253.

PETRE, C. E. & DITTMER, D. P. 2007. Liposomal daunorubicin as treatment for Kaposi's sarcoma. *International Journal of Nanomedicine,* 2**,** 277-288.

PLUK, H., DOREY, K. & SUPERTI-FURGA, G. 2002. Autoinhibition of c-Abl. *Cell,* 108**,** 247-259.

POON, R. T. & BORYS, N. 2011. Lyso-thermosensitive liposomal doxorubicin: an adjuvant to increase the cure rate of radiofrequency ablation in liver cancer. *Future Oncology,* 7**,** 937-945.

PRATT, W. & RUDDON, R. 1979. *The anticancer drugs*, New York: Oxford University Press.

PUN, S. H. & DAVIS, M. E. 2002. Development of a non-viral gene delivery vehicle for systemic application. *Bioconjugate Chemistry,* 13**,** 630-639.

QIAN, Z. M., LI, H., SUN, H. & HO, K. 2002. Targeted drug delivery via the transferrin receptor-mediated endocytosis pathway. *Pharmacological Reviews,* 54**,** 561-587.

QIN, L., XIONG, B., LUO, C., GUO, Z. M., HAO, P., SU, J., NAN, P., FENG, Y., SHI, Y. X., YU, X. J., LUO, X. M., CHEN, K. X., SHEN, X., SHEN, J. H., ZOU, J. P., ZHAO, G. P., SHI, T. L., HE, W. Z., ZHONG, Y., JIANG, H. L. & LI, Y. X. 2003. Identification of probable genomic packaging signal sequence from SARS-CoV genome by bioinformatics analysis. *Acta Pharmacologica Sinica,* 24**,** 489-496.

QU, F. & MORRIS, T. J. 1997. Encapsidation of turnip crinkle virus is defined by a specific packaging signal and RNA size. *Journal of Virology,* 71**,** 1428-1435.

RAJU, R. K., HILLIER, I. H., BURTON, N. A., VINCENT, M. A., DOUDOU, S. & BRYCE, R. A. 2010. The effects of perfluorination on carbohydrate-pi interactions: computational studies of the interaction of benzene and

hexafluorobenzene with fucose and cyclodextrin. *Physical Chemistry Chemical Physics,* 12**,** 7959-7967.

REGINO, C. A., WONG, K. J., MILENIC, D. E., HOLMES, E. H., GARMESTANI, K., CHOYKE, P. L. & BRECHBIEL, M. W. 2009. Preclinical evaluation of a monoclonal antibody (3C6) specific for prostate-specific membrane antigen. *Current Radiopharmaceuticals,* 2**,** 9-17.

RENAN, M. J. 1993. How many mutations are required for tumorigenesis? Implications from human cancer data. *Molecular Carcinogenesis,* 7**,** 139-146.

RIVIERE, K., KIELER-FERGUSON, H. M., JERGER, K. & SZOKA, F. C., JR. 2011. Anti-tumor activity of liposome encapsulated fluoroorotic acid as a single agent and in combination with liposome irinotecan. *Journal of Controlled Release,* 153**,** 288-296.

ROBERT, J. 1993. Epirubicin. Clinical pharmacology and dose-effect relationship. *Drugs,* 45 Suppl 2**,** 20-30.

ROBERTSON, D. L. & JOYCE, G. F. 1990. Selection in vitro of an RNA enzyme that specifically cleaves single-stranded DNA. *Nature,* 344**,** 467-468.

ROCKEY, W. M., HERNANDEZ, F. J., HUANG, S. Y., CAO, S., HOWELL, C. A., THOMAS, G. S., LIU, X. Y., LAPTEVA, N., SPENCER, D. M., MCNAMARA, J. O., ZOU, X., CHEN, S. J. & GIANGRANDE, P. H. 2011. Rational truncation of an RNA aptamer to prostate-specific membrane antigen using computational structural modeling. *Nucleic Acid Therapeutics,* 21**,** 299-314.

ROLFSSON, O., TOROPOVA, K., MORTON, V., FRANCESE, S., BASNAK, G., THOMPSON, G. S., HOMANS, S. W., ASHCROFT, A. E., STONEHOUSE, N. J., RANSON, N. A. & STOCKLEY, P. G. 2008. RNA

packing specificity and folding during assembly of the bacteriophage MS2. *Computational and Mathematical Methods in Medicine,* 9**,** 339-349.

ROUS, P. 1911. A sarcoma of the fowl transmissible by an agent from the tumor cells. *Journal of Experimental Medicine,* 13**,** 397-411.

ROWE, J. M. & LOWENBERG, B. 2013. Gemtuzumab ozogamicin in acute myeloid leukemia: a remarkable saga about an active drug. *Blood,* 121**,** 4838-4841.

RUCKMAN, J., GREEN, L. S., BEESON, J., WAUGH, S., GILLETTE, W. L., HENNINGER, D. D., CLAESSON-WELSH, L. & JANJIC, N. 1998. 2'-Fluoropyrimidine RNA-based aptamers to the 165-amino acid form of vascular endothelial growth factor (VEGF165). Inhibition of receptor binding and VEGF-induced vascular permeability through interactions requiring the exon 7-encoded domain. *Journal of Biological Chemistry,* 273**,** 20556-20567.

SAFARI, J. & ZARNEGAR, Z. 2014. Advanced drug delivery systems: Nanotechnology of health design A review. *Journal of Saudi Chemical Society,* 18**,** 85-99.

SAKUMA, T., BARRY, M. A. & IKEDA, Y. 2012. Lentiviral vectors: basic to translational. *Biochemical Journal,* 443**,** 603-618.

SAMRA, Z. Q., AHMAD, S., JAVEID, M., DAR, N., ASLAM, M. S., GULL, I. & AHMAD, M. M. 2013. Anticancer medicines (Doxorubicin and methotrexate) conjugated with magnetic nanoparticles for targeting drug delivery through iron. *Preparative Biochemistry & Biotechnology,* 43**,** 781-797.

SARRIS, A. H., HAGEMEISTER, F., ROMAGUERA, J., RODRIGUEZ, M. A., MCLAUGHLIN, P., TSIMBERIDOU, A. M., MEDEIROS, L. J., SAMUELS, B., PATE, O., OHOLENDT, M., KANTARJIAN, H., BURGE, C. & CABANILLAS, F. 2000. Liposomal vincristine in relapsed non-Hodgkin's

lymphomas: early results of an ongoing phase II trial. *Annals of Oncology,* 11**,** 69-72.

SCHIFF, P. B., FANT, J. & HORWITZ, S. B. 1979. Promotion of microtubule assembly in vitro by taxol. *Nature,* 277**,** 665-667.

SCHRAMA, D., REISFELD, R. A. & BECKER, J. C. 2006. Antibody targeted drugs as cancer therapeutics. *Nature Reviews Drug Discovery,* 5**,** 147-159.

SCHWABER, J. & COHEN, E. P. 1973. Human X mouse somatic-cell hybrid clone secreting immunoglobulins of both parental types. *Nature,* 244**,** 444-447.

SEIDMAN, A., HUDIS, C., PIERRI, M. K., SHAK, S., PATON, V., ASHBY, M., MURPHY, M., STEWART, S. J. & KEEFE, D. 2002. Cardiac dysfunction in the trastuzumab clinical trials experience. *Journal of Clinical Oncology,* 20**,** 1215-1221.

SENIOR, J., DELGADO, C., FISHER, D., TILCOCK, C. & GREGORIADIS, G. 1991. Influence of surface hydrophilicity of liposomes on their interaction with plasma protein and clearance from the circulation: studies with poly(ethylene glycol)-coated vesicles. *Biochimica et Biophysica Acta,* 1062**,** 77-82.

SEYMOUR, L. W., FERRY, D. R., ANDERSON, D., HESSLEWOOD, S., JULYAN, P. J., POYNER, R., DORAN, J., YOUNG, A. M., BURTLES, S., KERR, D. J. & CANCER RESEARCH CAMPAIGN PHASE, I. I. I. C. T. C. 2002. Hepatic drug targeting: phase I evaluation of polymer-bound doxorubicin. *Journal of Clinical Oncology,* 20**,** 1668-1676.

SEYMOUR, L. W., FERRY, D. R., KERR, D. J., REA, D., WHITLOCK, M., POYNER, R., BOIVIN, C., HESSLEWOOD, S., TWELVES, C., BLACKIE, R., SCHATZLEIN, A., JODRELL, D., BISSETT, D., CALVERT, H., LIND, M., ROBBINS, A., BURTLES, S., DUNCAN, R. & CASSIDY, J.

2009. Phase II studies of polymer-doxorubicin (PK1, FCE28068) in the treatment of breast, lung and colorectal cancer. *International Journal of Oncology,* 34**,** 1629-1636.

SHAFFER, A. L., EMRE, N. C. T., LAMY, L., NGO, V. N., WRIGHT, G., XIAO, W. M., POWELL, J., DAVE, S., YU, X., ZHAO, H., ZENG, Y. X., CHEN, B. Z., EPSTEIN, J. & STAUDT, L. M. 2008. IRF4 addiction in multiple myeloma. *Nature,* 454**,** 226-231.

SHAH, N. P., NICOLL, J. M., NAGAR, B., GORRE, M. E., PAQUETTE, R. L., KURIYAN, J. & SAWYERS, C. L. 2002. Multiple BCR-ABL kinase domain mutations confer polyclonal resistance to the tyrosine kinase inhibitor imatinib (STI571) in chronic phase and blast crisis chronic myeloid leukemia. *Cancer Cell,* 2**,** 117-125.

SHANGGUAN, D., LI, Y., TANG, Z., CAO, Z. C., CHEN, H. W., MALLIKARATCHY, P., SEFAH, K., YANG, C. J. & TAN, W. 2006. Aptamers evolved from live cells as effective molecular probes for cancer study. *Proceedings of the National Academy of Sciences of the United States of America,* 103**,** 11838-11843.

SHEN, C., BUCK, A. K., LIU, X., WINKLER, M. & RESKE, S. N. 2003. Gene silencing by adenovirus-delivered siRNA. *FEBS Letters,* 539**,** 111-114.

SHENDURE, J. & JI, H. 2008. Next-generation DNA sequencing. *Nature Biotechnology,* 26**,** 1135-1145.

SHIGDAR, S., MACDONALD, J., O'CONNOR, M., WANG, T., XIANG, D. X., AL SHAMAILEH, H., QIAO, L., WEI, M., ZHOU, S. F., ZHU, Y. M., KONG, L. X., BHATTACHARYA, S., LI, C. G. & DUAN, W. 2013. Aptamers as theranostic agents: Modifications, serum stability and functionalisation. *Sensors,* 13**,** 13624-13637.

SHUKLA, S., ABLACK, A. L., WEN, A. M., LEE, K. L., LEWIS, J. D. & STEINMETZ, N. F. 2013. Increased tumor homing and tissue penetration

of the filamentous plant viral nanoparticle Potato virus X. *Molecular Pharmaceutics,* 10**,** 33-42.

SIDDIK, Z. H. 2003. Cisplatin: mode of cytotoxic action and molecular basis of resistance. *Oncogene,* 22**,** 7265-7279.

SKJOTH, I. H. & ISSINGER, O. G. 2006. Profiling of signaling molecules in four different human prostate carcinoma cell lines before and after induction of apoptosis. *International Journal of Oncology,* 28**,** 217-229.

SKOMMER, J., BRITTAIN, T. & RAYCHAUDHURI, S. 2010. Bcl-2 inhibits apoptosis by increasing the time-to-death and intrinsic cell-to-cell variations in the mitochondrial pathway of cell death. *Apoptosis,* 15**,** 1223-1233.

SKOVSGAARD, T. & NISSEN, N. I. 1982. Membrane transport of anthracyclines. *Pharmacology & Therapeutics,* 18**,** 293-311.

SLAMON, D. J., GODOLPHIN, W., JONES, L. A., HOLT, J. A., WONG, S. G., KEITH, D. E., LEVIN, W. J., STUART, S. G., UDOVE, J., ULLRICH, A. & ET AL. 1989. Studies of the HER-2/neu proto-oncogene in human breast and ovarian cancer. *Science,* 244**,** 707-712.

SMOLLICH, M., GOTTE, M., YIP, G. W., YONG, E. S., KERSTING, C., FISCHGRABE, J., RADKE, I., KIESEL, L. & WULFING, P. 2007. On the role of endothelin-converting enzyme-1 (ECE-1) and neprilysin in human breast cancer. *Breast Cancer Research and Treatment,* 106**,** 361-369.

STEHELIN, D., VARMUS, H. E., BISHOP, J. M. & VOGT, P. K. 1976. DNA related to the transforming gene(s) of avian sarcoma viruses is present in normal avian DNA. *Nature,* 260**,** 170-173.

STEINMETZ, N. F., CHO, C. F., ABLACK, A., LEWIS, J. D. & MANCHESTER, M. 2011. Cowpea mosaic virus nanoparticles target surface vimentin on cancer cells. *Nanomedicine (Lond),* 6**,** 351-64.

STEINMETZ, N. F. & MANCHESTER, M. 2009. PEGylated viral nanoparticles for biomedicine: the impact of PEG chain length on VNP cell interactions in vitro and ex vivo. *Biomacromolecules,* 10**,** 784-792.

STEPHANOPOULOS, N., TONG, G. J., HSIAO, S. C. & FRANCIS, M. B. 2010. Dual-surface modified virus capsids for targeted delivery of photodynamic agents to cancer cells. *ACS Nano,* 4**,** 6014-6020.

STOCKLEY, P. G., ROLFSSON, O., THOMPSON, G. S., BASNAK, G., FRANCESE, S., STONEHOUSE, N. J., HOMANS, S. W. & ASHCROFT, A. E. 2007. A simple, RNA-mediated allosteric switch controls the pathway to formation of a T=3 viral capsid. *Journal of Molecular Biology,* 369**,** 541-552.

STRAUSS, J. H., JR. & SINSHEIMER, R. L. 1963. Purification and properties of bacteriophage MS2 and of its ribonucleic acid. *Journal of Molecular Biology,* 7**,** 43-54.

STREBHARDT, K. & ULLRICH, A. 2008. Paul Ehrlichs magic bullet concept 100 years of progress. *Nature Reviews Cancer,* 8**,** 473-480.

SUBRAMANIAN, N., RAGHUNATHAN, V., KANWAR, J. R., KANWAR, R. K., ELCHURI, S. V., KHETAN, V. & KRISHNAKUMAR, S. 2012. Target-specific delivery of doxorubicin to retinoblastoma using epithelial cell adhesion molecule aptamer. *Molecular Vision,* 18**,** 2783-2795.

SUZUKI, R., TAKIZAWA, T., KUWATA, Y., MUTOH, M., ISHIGURO, N., UTOGUCHI, N., SHINOHARA, A., ERIGUCHI, M., YANAGIE, H. & MARUYAMA, K. 2008. Effective anti-tumor activity of oxaliplatin encapsulated in transferrin-PEG-liposome. *International Journal of Pharmaceutics,* 346**,** 143-150.

SVOBODOVA, M., BUNKA, D. H., NADAL, P., STOCKLEY, P. G. & O'SULLIVAN, C. K. 2013. Selection of 2'F-modified RNA aptamers against prostate-specific antigen and their evaluation for diagnostic and

therapeutic applications. *Analytical and Bioanalytical Chemistry,* 405**,** 9149-9157.

SWIFT, S. L., RIVERA, G. C., DUSSUPT, V., LEADLEY, R. M., HUDSON, L. C., MA DE RIDDER, C., KRAAIJ, R., BURNS, J. E., MAITLAND, N. J. & GEORGOPOULOS, L. J. 2013. Evaluating baculovirus as a vector for human prostate cancer gene therapy. *PLoS One,* 8**,** e65557.

TABATA, T., MURAKAMI, Y. & IKADA, Y. 1998. Tumor accumulation of poly(vinyl alcohol) of different sizes after intravenous injection. *Journal of Controlled Release,* 50**,** 123-133.

TABERNERO, J., SHAPIRO, G. I., LORUSSO, P. M., CERVANTES, A., SCHWARTZ, G. K., WEISS, G. J., PAZ-ARES, L., CHO, D. C., INFANTE, J. R., ALSINA, M., GOUNDER, M. M., FALZONE, R., HARROP, J., WHITE, A. C., TOUDJARSKA, I., BUMCROT, D., MEYERS, R. E., HINKLE, G., SVRZIKAPA, N., HUTABARAT, R. M., CLAUSEN, V. A., CEHELSKY, J., NOCHUR, S. V., GAMBA-VITALO, C., VAISHNAW, A. K., SAH, D. W., GOLLOB, J. A. & BURRIS, H. A., 3RD 2013. First-in-humans trial of an RNA interference therapeutic targeting VEGF and KSP in cancer patients with liver involvement. *Cancer Discovery,* 3**,** 406-417.

TARTARONE, A., LAZZARI, C., LEROSE, R., CONTEDUCA, V., IMPROTA, G., ZUPA, A., BULOTTA, A., AIETA, M. & GREGORC, V. 2013. Mechanisms of resistance to EGFR tyrosine kinase inhibitors gefitinib/erlotinib and to ALK inhibitor crizotinib. *Lung Cancer,* 81**,** 328-336.

TEMIN, H. M. & MIZUTANI, S. 1970. RNA-dependent DNA polymerase in virions of Rous sarcoma virus. *Nature,* 226**,** 1211-1213.

TIWARI, G., TIWARI, R. & RAI, A. K. 2010. Cyclodextrins in delivery systems: Applications. *Journal of Pharmacy And Bioallied Sciences,* 2**,** 72-79.

TOFFOLI, G., SIMONE, F., GIGANTE, M. & BOIOCCHI, M. 1994. Comparison of mechanisms responsible for resistance to idarubicin and daunorubicin in multidrug resistant LoVo cell lines. *Biochemical Pharmacology,* 48**,** 1871-1881.

TRUJILLO, C. A., NERY, A. A., ALVES, J. M., MARTINS, A. H. & ULRICH, H. 2007. Development of the anti-VEGF aptamer to a therapeutic agent for clinical ophthalmology. *Journal of Clinical Ophthalmology,* 1**,** 393-402.

TUCKER, C. E., CHEN, L. S., JUDKINS, M. B., FARMER, J. A., GILL, S. C. & DROLET, D. W. 1999. Detection and plasma pharmacokinetics of an anti-vascular endothelial growth factor oligonucleotide-aptamer (NX1838) in rhesus monkeys. *Journal of Chromatography B: Biomedical Sciences and Applications,* 732**,** 203-212.

TUERK, C. & GOLD, L. 1990. Systematic evolution of ligands by exponential enrichment: RNA ligands to bacteriophage T4 DNA polymerase. *Science,* 249**,** 505-510.

UEDA, H., OU, D., ENDO, T., NAGASE, H., TOMONO, K. & NAGAI, T. 1998. Evaluation of a sulfobutyl ether beta-cyclodextrin as a solubilizing/stabilizing agent for several drugs. *Drug Development and Industrial Pharmacy,* 24**,** 863-867.

UEKAMA, K. 2004. Design and evaluation of cyclodextrin-based drug formulation. *Chemical & Pharmaceutical Bulletin,* 52**,** 900-915.

VAIL, D. M., AMANTEA, M. A., COLBERN, G. T., MARTIN, F. J., HILGER, R. A. & WORKING, P. K. 2004. Pegylated liposomal doxorubicin: Proof of principle using preclinical animal models and pharmacokinetic studies. *Seminars in Oncology,* 31**,** 16-35.

VALLE, J. W., ARMSTRONG, A., NEWMAN, C., ALAKHOV, V., PIETRZYNSKI, G., BREWER, J., CAMPBELL, S., CORRIE, P., ROWINSKY, E. K. & RANSON, M. 2011. A phase 2 study of SP1049C, doxorubicin in P-

glycoprotein-targeting pluronics, in patients with advanced adenocarcinoma of the esophagus and gastroesophageal junction. *Investigational New Drugs,* 29**,** 1029-1037.

VAN BEIJNUM, J. R., DINGS, R. P., VAN DER LINDEN, E., ZWAANS, B. M., RAMAEKERS, F. C., MAYO, K. H. & GRIFFIOEN, A. W. 2006. Gene expression of tumor angiogenesis dissected: specific targeting of colon cancer angiogenic vasculature. *Blood,* 108**,** 2339-2348.

VAN DUIN, J. 1988. Single-stranded RNA bacteriophages. *In:* CALENDAR, R. (ed.) *The Bacteriophages.* Springer US.

VAN MIERLO, G. J. D., DEN BOER, A. T., MEDEMA, J. P., VAN DER VOORT, E. I. H., FRANSEN, M. F., OFFRINGA, R., MELIEF, C. J. M. & TOES, R. E. M. 2002. CD40 stimulation leads to effective therapy of CD40(-)tumors through induction of strong systemic cytotoxic T lymphocyte immunity. *Proceedings of the National Academy of Sciences of the United States of America,* 99**,** 5561-5566.

VARKOUHI, A. K., SCHOLTE, M., STORM, G. & HAISMA, H. J. 2011. Endosomal escape pathways for delivery of biologicals. *Journal of Controlled Release,* 151**,** 220-228.

VARMUS, H. E. 1990. Retroviruses and oncogenes .1. *Angewandte Chemie International Edition,* 29**,** 707-715.

VASCONCELOS, M. H., LIMA, R. T. & GUIMARÃES, J. E. 2007. Overcoming K562Dox resistance to STI571 (Gleevec) by downregulation of P-gp expression using siRNAs. *Cancer Therapy,* 5**,** 67-76.

VASEY, P. A., KAYE, S. B., MORRISON, R., TWELVES, C., WILSON, P., DUNCAN, R., THOMSON, A. H., MURRAY, L. S., HILDITCH, T. E., MURRAY, T., BURTLES, S., FRAIER, D., FRIGERIO, E., CASSIDY, J. & COMM, C. R. C. P. I. I. 1999. Phase I clinical and pharmacokinetic study of PK1 [N-(2-hydroxypropyl)methacrylamide copolymer doxorubicin]:

First member of a new class of chemotherapeutic agents - Drug-polymer conjugates. *Clinical Cancer Research,* 5**,** 83-94.

VASQUEZ-VIVAR, J., MARTASEK, P., HOGG, N., MASTERS, B. S., PRITCHARD, K. A., JR. & KALYANARAMAN, B. 1997. Endothelial nitric oxide synthase-dependent superoxide generation from adriamycin. *Biochemistry,* 36**,** 11293-11297.

VATER, A., JAROSCH, F., BUCHNER, K. & KLUSSMANN, S. 2003. Short bioactive Spiegelmers to migraine-associated calcitonin gene-related peptide rapidly identified by a novel approach: Tailored-SELEX. *Nucleic Acids Research,* 31**,** e130.

VOGELSTEIN, B., PAPADOPOULOS, N., VELCULESCU, V. E., ZHOU, S., DIAZ, L. A., JR. & KINZLER, K. W. 2013. Cancer genome landscapes. *Science,* 339**,** 1546-1558.

VOLKOVA, M. & RUSSELL, R., 3RD 2011. Anthracycline cardiotoxicity: prevalence, pathogenesis and treatment. *Current Cardiology Reviews,* 7**,** 214-220.

WADA, H., MIZUTANI, S., NISHIMURA, J., USUKI, Y., KOHSAKI, M., KOMAI, M., KANEKO, H., SAKAMOTO, S., DELIA, D., KANAMARU, A. & KAKISHITA, E. 1995. Establishment and molecular characterization of a novel leukemic cell line with Philadelphia chromosome expressing p230 BCR/ABL fusion protein. *Cancer Research,* 55**,** 3192-3196.

WAN, Y., HAN, J., FAN, G., ZHANG, Z., GONG, T. & SUN, X. 2013. Enzyme-responsive liposomes modified adenoviral vectors for enhanced tumor cell transduction and reduced immunogenicity. *Biomaterials,* 34**,** 3020-3030.

WANG, L. H., DUESBERG, P. H., KAWAI, S. & HANAFUSA, H. 1976. Location of envelope-specific and sarcoma-specific oligonucleotides on RNA of

Schmidt-Ruppin Rous sarcoma virus. *Proceedings of the National Academy of Sciences of the United States of America,* 73**,** 447-451.

WANG, R. E., WU, H., NIU, Y. & CAI, J. 2011. Improving the stability of aptamers by chemical modification. *Current Medicinal Chemistry,* 18**,** 4126-4138.

WANG, R. H., ZHAO, J. J., JIANG, T. S., KWON, Y. M., LU, H. G., JIAO, P. R., LIAO, M. & LI, Y. B. 2013. Selection and characterization of DNA aptamers for use in detection of avian influenza virus H5N1. *Journal of Virological Methods,* 189**,** 362-369.

WARWICK, O. H., DARTE, J. M. M. & BROWN, T. C. 1960. Some Biological Effects of Vincaleukoblastine, an Alkaloid in Vinca-Rosea Linn in Patients with Malignant Disease. *Cancer Research,* 20**,** 1032-1040.

WEBER, G. 2007. *Molecular Mechanisms of Cancer*, Springer Netherlands.

WEINSTEIN, I. B. 2002. Cancer: Addiction to oncogenes - The Achilles heal of cancer. *Science,* 297**,** 63-64.

WEINSTEIN, I. B. & JOE, A. 2008. Oncogene addiction. *Cancer Research,* 68**,** 3077-3080.

WEISBERG, E., MANLEY, P. W., COWAN-JACOB, S. W., HOCHHAUS, A. & GRIFFIN, J. D. 2007. Second generation inhibitors of BCR-ABL for the treatment of imatinib-resistant chronic myeloid leukaemia. *Nature Reviews Cancer,* 7**,** 345-356.

WEISS, R. B. 1992. The anthracyclines - will we ever find a better doxorubicin. *Seminars in Oncology,* 19**,** 670-686.

WILLS, L., CLUTTERBUCK, P. W. & EVANS, B. D. 1937. A new factor in the production and cure of macrocytic anaemias and its relation to other

haemopoietic principles curative in pernicious anaemia. *Biochemical Journal,* 31**,** 2136-2147.

WILSON, R. C. & DOUDNA, J. A. 2013. Molecular mechanisms of RNA interference. *Annual Review of Biophysics,* 42**,** 217-239.

WOHLBOLD, L., VAN DER KUIP, H., MIETHING, C., VORNLOCHER, H. P., KNABBE, C., DUYSTER, J. & AULITZKY, W. E. 2003. Inhibition of bcr-abl gene expression by small interfering RNA sensitizes for imatinib mesylate (STI571). *Blood,* 102**,** 2236-2239.

WONGANAN, P. & CROYLE, M. A. 2010. PEGylated adenoviruses: from mice to monkeys. *Viruses,* 2**,** 468-502.

WOOD, M. J. A., BYRNES, A. P., PFAFF, D. W., RABKIN, S. D. & CHARLTON, H. M. 1994. Inflammatory effects of gene-transfer into the CNS with defective Hsv-1 vectors. *Gene Therapy,* 1**,** 283-291.

WU, M., BROWN, W. L. & STOCKLEY, P. G. 1995. Cell-specific delivery of bacteriophage-encapsidated ricin A chain. *Bioconjugate Chemistry,* 6**,** 587-595.

WU, M., SHERWIN, T., BROWN, W. L. & STOCKLEY, P. G. 2005. Delivery of antisense oligonucleotides to leukemia cells by RNA bacteriophage capsids. *Nanomedicine: Nanotechnology, Biology and Medicine,* 1**,** 67-76.

WU, W., HSIAO, S. C., CARRICO, Z. M. & FRANCIS, M. B. 2009. Genome-free viral capsids as multivalent carriers for taxol delivery. *Angewandte Chemie,* 48**,** 9493-9497.

XIONG, X. B., FALAMARZIAN, A., GARG, S. M. & LAVASANIFAR, A. 2011. Engineering of amphiphilic block copolymers for polymeric micellar drug and gene delivery. *Journal of Controlled Release,* 155**,** 248-261.

YAN, R., HALLAM, A., STOCKLEY, P. G. & BOYES, J. 2014. Oncogene dependency and the potential of targeted RNAi-based anti-cancer therapy. *Biochemical Journal,* 461**,** 1-13.

YANG, Y., GREENOUGH, K. & WILSON, J. M. 1996. Transient immune blockade prevents formation of neutralizing antibody to recombinant adenovirus and allows repeated gene transfer to mouse liver. *Gene Therapy,* 3**,** 412-420.

YI, Y., HAHM, S. H. & LEE, K. H. 2005. Retroviral gene therapy: safety issues and possible solutions. *Current Gene Therapy,* 5**,** 25-35.

YILDIZ, I., LEE, K. L., CHEN, K., SHUKLA, S. & STEINMETZ, N. F. 2013. Infusion of imaging and therapeutic molecules into the plant virus-based carrier cowpea mosaic virus: cargo-loading and delivery. *Journal of Controlled Release,* 172**,** 568-578.

YITBAREK, E. 2011. *Characterization and analytical applications of dye-encapsulated zwitterionic liposomes*, BiblioBazaar.

YUE, H., ZHAO, Y., MA, X. & GONG, J. 2012. Ethylene glycol: properties, synthesis, and applications. *Chemical Society Reviews,* 41**,** 4218-4244.

YVON, A. M., WADSWORTH, P. & JORDAN, M. A. 1999. Taxol suppresses dynamics of individual microtubules in living human tumor cells. *Molecular Biology of the Cell,* 10**,** 947-959.

ZAHR, A. S., DAVIS, C. A. & PISHKO, M. V. 2006. Macrophage uptake of coreshell nanoparticles surface modified with poly(ethylene glycol). *Langmuir,* 22**,** 8178-8185.

ZHANG, N., KLEGERMAN, M., DENG, H., SHI, Y., GOLUNSKI, E. & AN, Z. 2013. Trastuzumab-doxorubicin conjugate provides enhanced anti-cancer potency and reduced cardiotoxicity. *Journal of Cancer Therapy,* 4**,** 308-322.

ZHANG, Y., YANG, M., PORTNEY, N. G., CUI, D., BUDAK, G., OZBAY, E., OZKAN, M. & OZKAN, C. S. 2008. Zeta potential: a surface electrical characteristic to probe the interaction of nanoparticles with normal and cancer human breast epithelial cells. *Biomedical Microdevices,* 10**,** 321-328.

ZHONG, Y., MENG, F., DENG, C. & ZHONG, Z. 2014. Ligand-directed active tumor-targeting polymeric nanoparticles for cancer chemotherapy. *Biomacromolecules,* 15**,** 1955-1969.

An electronic version of this thesis is included on the CD attached

(Yan 2015.pdf).